Dynamic Interactions between Bicycles and Rumble Strips

Marko Bajic

A Thesis

in

The Department

of

Mechanical Engineering

Presented in Partial Fulfillment of the Requirements
For the Degree of Master of Applied Science at
Concordia University
Montreal, Quebec, Canada

January 2005

Your file Votre référence
ISBN: 0-494-04413-6
Our file Notre référence
ISBN: 0-494-04413-6

ABSTRACT

DYNAMIC INTERACTIONS BETWEEN BICYCLES AND RUMBLE STRIPS

Marko Bajic

The rumble strips have proven to provide a good protection against the run-off-the-road type of accidents. However, installing them on the local and community roads has raised many concerns among the cyclists. The cyclists occasionally cross over the rumble strip patterns in order to avoid obstacles or debris on the road shoulders or pass a slower moving rider. The majority of the reported concerns are those regarding the ride comfort and controllability of a bicycle traversing the rumble strip patterns.

The ride discomfort and controllability of a bicycle traveling on the rumble strips are experimentally investigated by considering a comprehensive test matrix involving: (1) the conventional and suspended bicycles; (2) different rumble strip patterns and traversing speeds; (3) oblique angle of approach to rumble strip; (4) multiple trials and (5) seven test subjects. The objective assessment of the ride comfort on the rumble strip patterns is carried out by measuring the acceleration responses of the bicycle frame at the handle bar and the seat post while the controllability of the bicycle is assessed in terms of the measured yaw oscillations of the handle bar. The cyclist's sensation of the rumble strip patterns is further investigated through subjective measurements where the riders rated each test based on different criteria involving the ride comfort and controllability.

The dynamic properties of the coupled bicycle-rider system are studied utilizing an in-plane 5-DOF and 6-DOF models representing the Touring and Hybrid bicycle-rider systems, respectively. Also, a model of dynamic interaction between the rumble strip and the bicycle tire has been developed in order to study the influence of the rumble strip geometry and the on the acceleration response of the coupled bicycle-rider system.

The acceleration responses measured on the instrumented bicycle traversing different rumble strip patterns were assessed relative to the responses acquired on the flat pavement. The results showed considerable increase in the acceleration levels on the strip patterns, while the patterns with wider grooves resulted in considerably higher magnitudes of vertical acceleration at the seat post and the handle bar. The same patterns were also perceived to be harsh by the subjects, which was evident from the subjective comfort and control ratings, irrespective of the bicycle type and the traversing speed. The results attained from the analyses of the coupled bicycle-rider model revealed a nearly linear relationship between the width of the grooves and the RMS vertical and pitch acceleration responses of the bicycle. The simulation results also showed that the center-to-center distance of the grooved portions in the strip patterns of 0.425 meters could provide improved performance from the point of view of vertical acceleration responses of the bicycle-rider system, and thus the rider comfort.

ACKNOWLEDGEMENTS

The author wishes to express his sincere appreciation to his thesis supervisors, Dr. S. Rakheja and Dr. R. Bhat for initiating the study topic and providing guidance throughout the course of the research.

The author also wishes to thank to the faculty members and staff of CONCAVE (Concordia Center for Advance Vehicle Engineering) Research Center, Department of Mechanical Engineering, Concordia University, for their time and the assistance.

The financial and technical support provided by the Ministère des Transportation du Québec are gratefully acknowledged.

This thesis is dedicated to the author's parents and his sister for their encouragement and support throughout the course of this research. The thesis is also dedicated to the author's grandfather who died during the course of this research.

TABLE OF CONTENTS

LIST OF FIGURES

LIST OF TABLES

NOMENCLATURE

C	Damping matrix of the bicycle model
c_h	Damping coefficient of the rider's hip (Ns/m)
c_{ha}	Damping coefficient of the rider's hand-arm system (Ns/m)
c_{rot}	Damping coefficient of the rider's hinge (Nms/rad)
c_v	Damping coefficient of the rider's visceral mass stiffness (Ns/m)
c_t	Damping coefficient of the bicycle tier (Ns/m)
c_{t1}, c_{t2}	Equivalent vertical damping coefficient of the tire at the trailing and leading edge of the groove (Ns/m)
c_{vd}	Damping coefficient of the Hybrid bicycles front suspension (Ns/m)
F'	The tire foot-print force resulting from the tire-groove interaction occurring in front of the wheel center (N)
F_c	Magnitude of the friction force in the front suspension (N)
F'_v	The vertical component of the tire foot-print force resulting from the tire-groove interaction occurring at an in-coming edge (N)
F''_v	The vertical component of the tire foot-print force resulting from the tire-groove interaction occurring behind the wheel center (N)
F'''_v	The total vertical force developed at the tire-groove interface (N)
f_u	Natural frequency of the unsprung mass (Hz)
H	Vertical distance between the c.g. and imaginary line connecting the centers of the front and rear wheel (m)
I_b	Pitch mass moment of inertia of the bicycle (kgm^2)
I_t	Pitch mass moment of inertia of the rider's torso (kgm^2)
K	Stiffness matrix of the bicycle model
k_e	The equivalent stiffness of the tire in the experiment set up (kN/m)
k_h	Stiffness coefficient of the rider's hip (kN/m)

k_{ha}	Stiffness coefficient of the rider's hand-arm system (kN/m)
k_{rot}	Stiffness coefficient of the rider's hinge (kN/rad)
k_{sus}	Stiffness coefficient of the Hybrid bicycles front suspension (kN/m)
k_v	Stiffness coefficient of the rider's visceral mass stiffness (kN/m)
k_t	Stiffness coefficient of the bicycle tier (kN/m)
k_{t1}, k_{t2}	Equivalent vertical stiffnesses coefficient of the tire at the trailing and leading edge of the groove (kN/m)
k_{spI}	Stiffness coefficient of the seat post suspension (operational range) (kN/m)
k_{spII}	Stiffness coefficient of the seat post suspension (bump stop) (kN/m)
L	Wheelbase (m)
L_f	Horizontal distance between the front tire and bicycle c.g. (m)
L_r	Horizontal distance between rare tire and bicycle c.g. (m)
L_{brf}	Horizontal distance between the handle bar and bicycle c.g. (m)
L_{brr}	Horizontal distance between the seat and bicycle c.g. (m)
L_{rf}	Distance between the rider's hand-arm system and rider's torso c.g. (m)
L_{rr},	Distance between the rider's hip and the torso c.g. (m)
L_v	Distance between the visceral mass and the c.g. of the rider's torso (m)
M	Mass matrix of the bicycle model
m_a	Mass of the rider's arms (kg)
m_b	Total bicycle mass (kg)
m_l	Mass of the rider's lags (kg)
m_u	Bicycle unsprang mass (kg)
m_s	Bicycle sprung mass (kg)

m_t	Mass of the rider's Torso (kg)
m_v	Rider's visceral mass(kg)
q	The vector of generalized coordinates
R'	Deflected radii of the wheel (m)
R_v	Wheel radius (m)
V	Forward velocity of the bicycle (m/s)
W_f	Front wheel load (N)
W_r	Rear wheel load (N)
x'	The longitudinal distance between the tire contact point and the center of the wheel (m)
Z	Amplitude of motion of the suspension unit (m)
z(t)	Random road profile (m)
z'_d	The vertical distance between the reference ground profile and the center of the wheel (m)
$\ddot{z}_h$	Vertical acceleration of the handle bar (m/s^2)
z_f, z_r	Road profile elevation at the front and rear wheels, respectively (m)
$\ddot{z}_s$	Vertical acceleration of the seat post (m/s^2)
$z_1,\ldots, z_4$	Generalized coordinate characterizing vertical displacement of the bicycle frame, rider's torso, visceral mass and unsprung mass, respectively (m)
α_t	Inclination angle of the rider's torso with the respect to horizontal 9degrees)
γ'	The instantaneous angle of the radial spring-damping element of the wheel (rad)
Δ_h, Δ_{ha}	Static deflection of the rider's hip and hand-arm system, respectively (m)
Δ_f, Δ_r	Static deflection of the front and rear wheels, respectively (m)
Δ_{sus}	Static deflection of the front suspension (m)
Δ_v	Static deflection of the visceral mass (m)

ψ	Yaw angle of the bicycle's handle bar (rad)
$\dot{\psi}$	Yaw rate of the bicycle's handle bar (rad/s)
θ_1, θ_2	Generalized coordinate characterizing pitch angular displacement of the bicycle frame and rider's torso, respectively (rad)
$\ddot{\theta}$	Pitch acceleration of the bicycle frame (rad/s^2)
$\xi(t)$	White noise signal (m)
δ'	The deflection of the wheel (m)
$\dot{\delta}'$	Relative velocity between the wheel center and the groove (m/s)

CHAPTER 1

REVIEW OF RELEVANT LITERATURE

1.1 INTRODUCTION

Rumble Strips are raised or grooved patterns, placed between the driving lanes and shoulders of highways, for the purpose of providing audible and tactile stimuli to inattentive drivers if they happen to drive away from the driving lanes. Over the years the rumble strips have shown to be a good method for reducing number of accidents on the highways. When first introduced by some highway agencies in the U.S. in an attempt to reduce the number of accidents on the highways, in a short period of time after the installation, statistics have shown a significant decline in the number of run-off-the-road (ROR) accidents. Since drowsy and inattentive drivers are usual cause of the ROR accidents, rumble strips provide necessary level of vibrations and noise warnings to alert the driver and allow enough lead time for safely regaining the control of the vehicle.

Placement of rumble strips on local and community roads have raised many concerns among community residents with regards to the noise generated by the tire-strip interactions. The rumble strips have also raised concerns among the cyclists regarding the ride discomfort and poor controllability, caused when forced to traverse across the rumble strips in order to avoid debris or other kind of obstacles on the road shoulders. In the recent years, a few transportation agencies have explored different designs of rumble strips to achieve bicycle friendly designs. These studies have invariably reported that the cyclists experience uncomfortable level of vibration and difficulties in control when traversing the rumble strip (Khan and Baccus, 1994; Garder, 1995; Elefteriadou et al.,

2000; Outcalt, 2001). Increased awareness of potential danger of rumble strips to cyclists, coupled with the increasing use of rumble strips on more and more roads in order to enhance safety, has raised the need for creating a rumble strip pattern that will be "Bicycle Friendly" and at the same time produce sufficient vibration and noise cues for the motorists to prevent ROR accidents.

This theses research focuses on the methods for assessing the bicycle friendliness of the shoulder rumble strips in view of the transmitted vibration and rider's ability to retain the control of the bicycle. Experimental and analytical methods are used to identify rumble strip designs with enhanced bicycle friendliness.

1.2 Review of the Relevant Literature

The study of bicycle friendliness of shoulder rumble strips encompasses many challenges related to methods of measurement and assessment of the friendliness, and dynamic interaction among the bicycle, rider and the rumble strip. The reported relevant studies are thus reviewed to build sufficient knowledge on the experimental and analytical methods, and to formulate the scope of the dissertation research.

1.2.1 An Overview of Rumble Strips Design

According to definition provided by the U.S. Department of Transportation Federal Highway Administration (2001), shoulder rumble strip is a longitudinal design feature installed on a paved roadway shoulder near the travel lane. It is made of a series of indented or raised elements intended to alert inattentive drivers through vibration and sound cues generated by the dynamic interactions between the tires and the rumble strip patterns, when the vehicle deviates from the travel lane. The audible warning is provided by the noise generated by the vehicle tire interaction with the rumble strip and the tactile

warning coming from the vibration responses of the vehicle system, transmitted to the driver through contact with the seat and the steering wheel. On divided highways, rumble strips are typically installed on the median side of the roadway as well as on the outside (right) shoulder (U.S. Department of Transportation, 2001). Typical shapes of rumble strips on asphalt shoulders include rounded, rectangular, v-shaped and tapered, while on Portland Cement Concrete (PCC) rectangular and "wave-like" or corrugated shapes are formed. Figure 1.1 illustrates some of the rumble strip patterns.

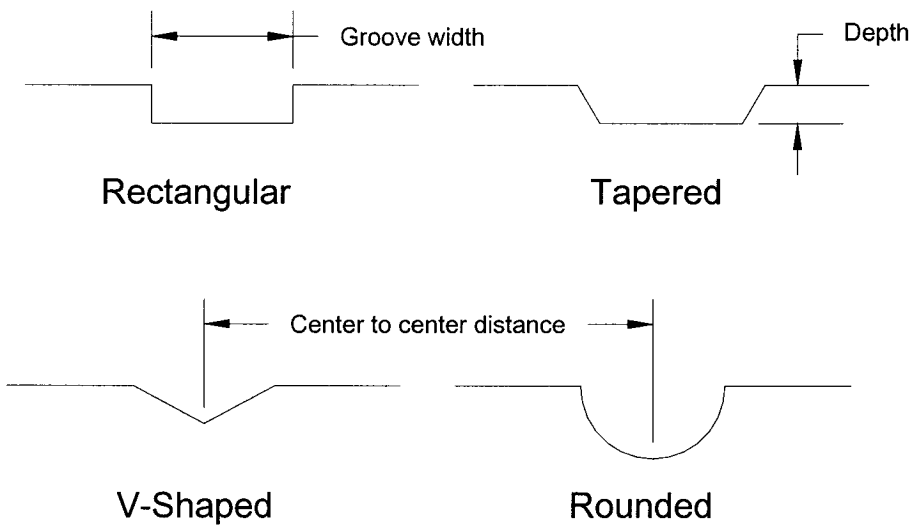

Figure 1.1: Types of rumble strips.

Shoulder rumble strips can either be continuous or intermittent. Continuous rumble strips are patterns formed on the shoulder rumble strips along the entire length of the roadway where they are used, while the intermittent rumble strips are formed with periodical gaps in the patterns, as shown in Figure 1.2. The concern about continuous shoulder rumble strips is the aptness of their placement, either across bridge decks, acceleration and deceleration lanes or narrowing lateral clearance on roadways. Many

States it the U.S. have their own requirements on the placement of these strips depending upon factors, such as: the width of the shoulder, community noise concerns and the commuters using the roadway (Elefteriadou et al., 2000). Placing the rumble strips further from the traveled way results in less frequent interaction and therefore fewer noise complaints. This approach, however, would reduce the space needed for the bicycle lanes and the lead-time of the motorists warning for regaining path control of the vehicle.

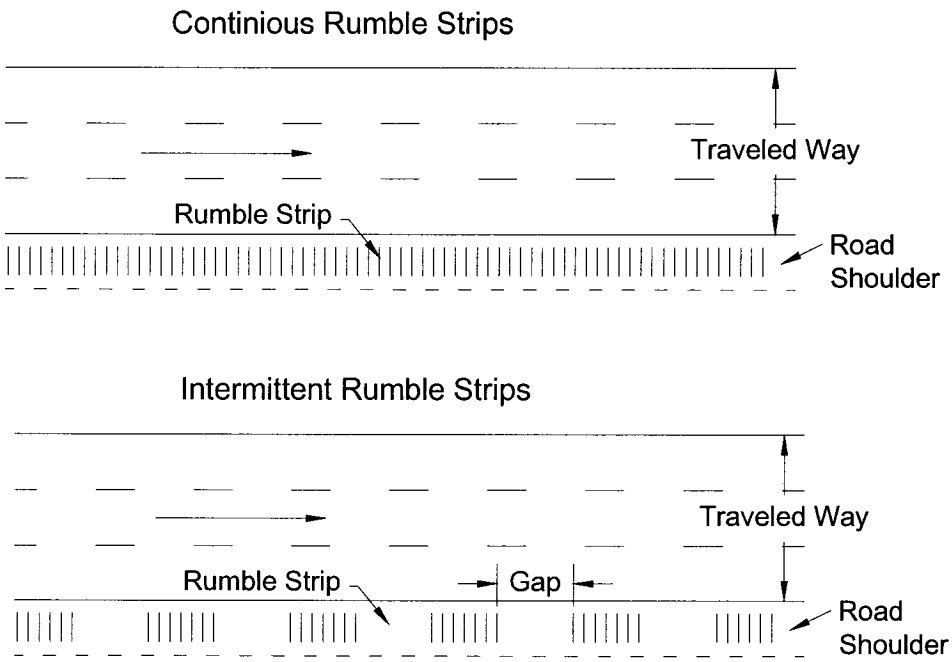

Figure 1.2: Continuous and intermittent shoulder rumble strip.

Noel et al. (1989) studied the continuous rumble strip patterns used to alert drivers at stop signs at rural intersections and concluded that longer continuous rumble strips were more effective in increasing compliance with the stop signs and in reducing accidents. However there were indications that long continuous rumble strips caused distraction for the drivers and some drivers had difficulty with braking. In some

circumstances, Intermittent Rumble Strip patterns have been reported to be more effective than the continuous ones, since they provide a repetitive or series of stimuli to the driver. Morgan and McAuliffe (1997) argued that the data acquired by various agencies suggested that the continuous shoulder rumble strips are more effective than the intermittent ones. Combination of intermittent and continuous rumble strips has also been proposed in an effort to provide better stimuli and warnings to the drivers (Noel et al., 1989).

Transverse Rumble Strips are also used to alert the drivers of upcoming changes in the roadway, such as lane mergers and sharp turns. They are typically placed on approaches to intersections, toll plazas, horizontal curves and work zones. The transverse rumble strips are known to cause severe ride vibration among the bicyclists and motorcyclists, especially at higher speeds when the strips become hazardous to the riders (Noel et al., 1989). Centerline rumble strips are placed on the centerline of rural roadways in order to prevent crossover crashes. This type of rumble strip is usually milled in and then painted over. Outcalt (2001) reported significant decline in the number of cross over type of accidents in the areas where the centerline rumble strips were installed. The study further reported that the number of head-on accidents per million declined by 34 percent, while the sideswipe accidents decline by 36.5 percent.

The rumble strips can be milled, rolled and formed on the roadways and shoulders. The design of various rumble strips used on different roads can differ considerably in view of their sizes, shapes and spacing patterns. The noise and vibration cues generated by different strips thus differ considerably. Milled rumble strips can be installed on existing, new or reconstructed asphalt shoulders. They are produced using a

mechanical device with a rotary cutting head which is used to mill in the rumble strips that result in a smooth, uniform, and consistent cut (Perrillo, 1998). The resulting debris is removed from the site soon after the cut, as it tends to melt back the asphalt due to the heat produced by the cutting action. Because milled rumble strips are directly cut into the pavement, they yield longer life, and do not wear and smoothen out as easily as the rolled or formed strips. The impressions are usually made at a predetermined offset distance from the outer edge of the roadway. Installation cost of milled rumble strips has decreased over the years with the improvement in technology, from $6.18 per linear meter in 1990 to $0.49 per linear meter in 1998 (as reported by the New York State Department of Transportation) (Perrillo, 1998).

Rolled rumble strips, unlike the milled rumble strips which can be installed at any time, can only be installed on new or reconstructed hot asphalt. In this process the grooves are made by a roller with steel pipes uniformly welded to a drum. The roller presses narrow depressions into the asphalt where the excess pavement is pushed to the sides of the newly formed strip (Perrillo, 1998). Rolled rumble strips pose substantial maintenance and construction problems since they are not cut but pressed into place. Some examples of the reported problems are: increased voids formed along the joint trigger premature degradation of the shoulder; and inconsistent depth of the indentations due to variations in temperature and asphalt density. Rolled rumble strips also wear out more easily revealing long sections of smoothened patterns, which reduce the effectiveness in generating the noise and vibration cues for the drivers (Perrillo, 1998). It has been further reported that the roller does not track a straight path along the roadway

edge line, which causes the rumble strip pattern to wander laterally across the shoulder (Richard, 1999).

Formed Rumble Strips were implemented on several roadways during the 1980's. These strips, installed on Portland Cement Concrete (PCC) pavements and shoulders, produced higher magnitudes of noise and vibration for the motorist. The formed rumble strips, however, are less common at the present time, which is mostly attributed to the increasing use of asphalt pavements over PCC pavements. The life span of rumble strips installed on asphalt pavements is in the range of 7 to 8 years, while those on Portland cement pavements offer life span of 25 years and more (Harwood, 1993).

A survey of transportation agencies across the United States and Canada, conducted by Morgan and McAuliffe (1997), showed that the milled-in rumble strips have been used by twelve highway agencies. Six of those agencies employed identical designs of milled-in rumble strips: 400 mm long, 175 mm wide and 13 mm deep. The other three agencies employed rumble strips with the same depth while the lengths varied from 600 mm to 700 mm to the length of the full shoulder and width ranged from 100 mm to 175 mm. All the agencies specify 300 mm center to center spacing with the exception of a single agency, which allows 1500 mm spacing (Morgan and McAuliffe, 1997). The offset from the pavement edge varied from 100 to 450 mm. The only major complaint about milled-in rumble strips was the higher associated costs. Thirteen of the surveyed agencies employed alternate rumble strips, such as roughened shoulders, surface mounted features and thermoplastic rumble strips or surface treatments. Six of the agencies used rumble strips prior to intersections, and five of these used milled-in or rolled-in rumble strips as in-lane warning devices, while the sixth agency used

polyurethane raised strips developed by the Strategic Highway Research Program (Morgan and McAuliffe, 1997).

Various shapes of rumble strips are used in order to produce different levels of sound and vibration cues. The most widely used rolled-in strips is of the semi-circular shape. This shape results in very little tearing of the material during placement and provides a good finishing appearance. For rolling operation, this shape is easiest to weld onto the drum and relatively easy to keep wet during placement. The 'V' shaped rumble strips are easier to roll in than the other shapes, since the process can be carried out at cooler temperatures. This shape, however, tends to tear the material during the placement. The rectangular shape is also considered suitable for the milling-in process but tends to tear the material during the rolling operation, as in the case of V-shaped strips. The rectangular shape with side slopes (rounded-rectangular) combines attributes of both the triangular and rectangular cross-sections and thus can be milled or rolled without any adverse effects (Khan and Baccus, 1994).

1.2.2 Assessment of Rumble Strips and Bicycles Considerations

A wide range of shoulder rumble strips with varying patterns and geometries have been employed in the USA and Canada. The primary goal of such shoulder strips is to reduce the occurrences of ROR accidents, which have been attributed to less attentive and drowsy drivers. The dynamic interactions of vehicle tires with rather rough rumble strips causes loud noise and large magnitude whole-body vibration to warn the drivers of the onset of a potential ROR accident.

Wood (1994) proposed an innovative type of shoulder rumble strips to enhance the road safety. The proposed design was called the "Sonic Alert Pattern" (SNAP), and used an indentation spacing of 305 mm (one foot) along the direction of travel. The proposed pattern was 406.4 mm (16 inch) wide, transverse to the direction of travel, with a depth of 12.7 mm (0.5 inch). The pattern depth of 12.7 mm was considered to provide sufficient tire drop and relatively high magnitude of the resulting sound. The noise measurements performed on rumble strips of varying depths (Table 1.1) revealed that 50.8 mm (2 inch) wide grooves did not produce sufficiently loud sound warning to be heard over a 79 decibels noise level in a truck's cab, while the 101.6 mm (4 inch) and 203.2 mm (8 inch) wide grooves produced a sound audible in both the cars and the trucks.

Table 1.1: SNAP test patterns (Wood, 1994).

Pattern	*Length [mm]*	*Spacing (center to center) [mm]*	*Width [mm]*	*Depth [mm]*
1	406.4	304.8	101.6	9.5
2	406.4	304.8	101.6	6.4
3	406.4	304.8	50.8	6.4
4	406.4	304.8	50.8	12.7
5	406.4	304.8	101.6	12.7

The resulting noise level of 86 decibels was measured in a truck's cab at a forward speed of 105 km/h. Table 1.2 summarizes the mean sound pressure levels measured in the cars and trucks traversing the rumble strips at different speeds. Owing to the high noise levels in the truck cab, the measured levels above 79 dB alone were reported for one of the patterns. The results in general show increase in the sound pressure with increasing speed and rumble strip width. The study further reported that the milled-in SNAP does not show wear of the strips after use, while the rolled in or

impressed patterns show smoothing out. Present specifications for SNAP call for milling or grinding the 177.8 mm (7 inch) openings. Such a modified design produces a 3 decibels louder sound than the original rolled-in openings of 106.6 mm (4 inch) (Hickey, 1997).

Table 1.2: Measured mean noise level in cars and trucks (Wood, 1994).

Pattern	*Mean Noise Level (dB)*			
	Speed			
	64 km/h	80 km/h	97km/h	105 km/h
1	74	77	80	-
2	70	75	76	-
3	68	74	74	-
4	71	73	74	-
5	75	78	80	-
5 (Trucks)*	-	82	82	86

"-" Not recordable over 79 dB noise level in the truck cab.

*The data measured inside truck's cab.

Gupta (1993) conducted noise experiments for both cars and trucks traversing the rumble strips at average speeds of 105 km/h (65 mph), to asses the community noise. The noise levels were measured at a distance of 3.05 m (10 foot) away from the shoulder, while four different rumble strip patterns were used. The geometrical dimensions of the test rumble strip patterns are presented in Table 1.3. The mean values of the measured noise levels arising from cars and trucks are summarized in Table 1.4. The study concluded that pattern A with larger width of 101.6 mm (4 inch) produced higher community noise when compared to the other patterns, since its wider grooves allowed for relatively larger tire drop. Moreover, the sharp edges of the patterns seemed to provide better excitation than the V-shaped or sloping grooves used in patterns B and D. The results also revealed higher community noise due to trucks.

Despite the concerns over the increased community noise due to shoulder rumble strips, the transportation agencies have invariably recognize the high effectiveness of rumble strips in preventing ROR accidents (Elefteriadou et al., 2000; Hickey, 1997; Outcalt, 2001). Owing to their proven effectiveness, many agencies have implemented similar rumble strips to separate the cars and bicycle lanes within the urban and rural roadways in recent years. The primary purpose of such strips is to reduce the car-bicycle accidents, while discouraging the bicycle riders to ride in the car lanes.

Table 1.3: Rumble strip patterns (Gupta, 1993).

Pattern	*Length (transverse to direction of travel)*	*Spacing (center to center)*	*Width (parallel to direction of travel)*	*Depth*
A	406.4	254.0	101.6	12.7
B*	406.4	254.0	101.6	12.7
C	406.4	228.6	76.2	12.7
D*	406.4	228.6	76.2	12.7

All units are in mm

*Edges of the grooves were at an angle, sloping inwards.

Table 1.4: Mean noise level arising from cars and trucks (Gupta, 1993).

Pattern	*Mean Noise Level (dB) - Cars*		*Mean Noise Level (dB) - Trucks*	
	Bare asphalt	Rumble Strips	Bare asphalt	Rumble Strips
Pattern A	72.8	79	80.5	86.3
Pattern B	73.2	76.3	77.7	82.2
Pattern C	73.15	77.3	80.6	86.1
Pattern D	68.5	73.6	78.6	82.5

The bicycle riders, however, are often forced to ride on the rumble strips in order to pass a slower rider or to avoid an obstacle/debris on the bicycle lane. The interaction of the bicycle tires with the rumble strips patterns not only transmit harsh vibration to the rider but also pose a serious safety concern due to excessive handle bar vibration (Outcalt, 2001). The high magnitude vibration may cause the rider to fall off the bicycle or lose the

guidance control. The outcome could be quite severe when the rider falls in the car lane or when the bicycle drifts into the car lane. A few studies have thus attempted to quantify the resulting bicycle rider discomfort and controllability using subjective and objective means.

Garder (1995) performed assessment of rider's comfort and handling abilities, while traversing two different rumble strip patterns. The first pattern comprised of 180 mm (7 inches) long round grooves with 410 mm (16 inches) width and 12.5 mm (0.5 inches) deep. The pattern was designed with center to center distance of 300 mm (12 inches). The second pattern comprised of rectangular grooves with identical dimensions. A total of 20 riders participated in the experiment, while the assessments were based upon subjective responses of the participants. The riders did not report any tendency to lose control of the bicycle irrespective of the speed or angle of approach, even when not holding on to the handle bar. The riders, however, felt uncomfortable when riding on the rumble strips. The study thus concluded that the rumble strips do not pose any danger for the bicyclist. Other reported studies, however, contradict this finding (Elefteriadou et al., 2000; Outcalt, 2001).

Ardekani et al. (1996) performed experiments to assess the ride comfort of four different types of rumble strip patterns for the cyclists. The study included five bicycle riders, riding the Touring and the Mountain bicycles. The riders rated each pattern for comfort on a scale from 1 to 10, where 10 being the most comfortable. Table 1.5 summaries the geometry of tested rumble strips, while the subjective ratings of the strips and the bicycle are presented in Table 1.6. The test patterns involved variations in the depth (2.5 to 5.0 mm), width (107-152 mm), as shown in Table 1.5. An alternate design

with sloping pattern of 150x150 mm square bottom was also included in the study. The results suggested that the pattern 3 with longest flat segment (457 mm) and 152 mm width caused most discomfort for the Touring bicycle riders. The comfort rating for this pattern ranged from 6 to 7 with mean value of 6.6. The same pattern resulted in most discomfort for the Mountain bicycle riders, which was attributed to the long flat segment. This led to the conclusion that sensation and perception of smoothness appeared to be linked to length of the smooth surface and the width of the grooves. The results reported for the Mountain bicycle also revealed poor comfort performances of pattern 1 (mean rating of 7.2), which had much smaller flat segment of 198 mm. The results thus suggest that the comfort performance is related to length, width, depth and the shape in a complex manner.

Table 1.5: Rumble strip patterns (Ardekani et al., 1996).

Pattern	*Rumble Strip Geometry*		
	Flat portion (mm)	*Grooved portion (mm)*	*Depth (mm)*
1	198	107	2.5
2	183	122	5
3	457	152	5
4	150 mm by 150 mm square bottoms, 35 mm high at one end and 25 mm at the other and placed 200 mm center to center		

Table 1.6: Subjective comfort ratings of the test patterns (Ardekani et al., 1996).

Pattern	*Cyclist 1*	*Cyclist 2*	*Cyclist 3*	*Cyclist 4*	*Cyclist 5*	*Mean Score*
The Touring Bicycle						
1	4	4	5	5	7	5.0
2	1	2	3	2	5	2.6
3	7	7	7	6	6	6.6
4	2	4	5	4	6	4.2
The Mountain Bicycle						
1	6	6	7	8	9	7.2
2	4	4	5	5	6	4.0
3	8	8	9	7	8	8.0
4	4	5	7	6	7	5.8

Elefteriadou et al. (2000) investigated rumble strip patterns to identify patterns that are safe for bicyclists and effective enough for the motorists on non-freeway roads. Six different test patterns of rumble strips (Table 1.7) were installed and tested. All of the patterns had a transverse width of 406 mm and each stretch was approximately 38 meters long. Each test subject was asked to ride the bicycle along a 203 mm wide and 13.7 m long straight smooth pavement path to assess their riding abilities. The measurements on the rumble strips were performed for three different speed ranges: 5 - 15 km/h, 16 - 25 km/h and 26 km/h and above, with approach angles: 0, 10 and 45 degrees.

Table 1.7: Patterns installed at the test track (Elefteriadou et al., 2000).

Test Pattern	*Groove Width (mm)*	*Flat portion (mm)*	*Depth (mm)*
1	178	127	13
2	127	178	13
3	127	178	10
4	127	152	13
5	127	152	10
6	127	178	6.3

The types of bicycles used in tests were: mountain, touring, hybrid and tandem bicycles. Rider's sensation of comfort and controllability on the rumble strips was assessed through subjective as well as objective measurements. The subjective assessment of rumble strip patterns were obtained through questionnaires, where subjects ranked different patterns for discomfort experienced in different parts of the body as well as the over all comfort, on a scale from 0 to 25. Objective measures included measurements of the vertical and pitch angular accelerations. The controllability was assessed in terms of the percent time the rider deviated from the rumble strip through analyses of video recordings. The RMS values of the vertical and pitch angular accelerations were used to

assess the comfort and control performance of the rumble strips. On the basis of the data obtained for percent time the rider spent off-line, each pattern was ranked on a scale of 1 to 6, where 1 represented the best pattern. The data suggested that the riders spent nearly 8% of the time off-line on a smooth flat pavement, while this time increased to 25% for the worst pattern (pattern #1; 178 mm wide and 13 mm deep). These results are summarized in Table 1.8.

Table 1.8: Ranking of test configuration based on objective overall control level (Elefteriadou et al., 2000).

	Rank	*Test Pattern*	*Percentage of Time spent off the Line*
		Smooth	8.1
Best	1	3	12.3
	2	6	12.6
	3	4	15.4
	4	5	19.2
	5	2	19.6
Worst	6	1	25.4

The subjective assessment of comfort further confirmed that the same pattern was judged to be most uncomfortable in view of rider comfort and controllability ranked between 0 and 25 (Table 1.9). The objective measurements, however, revealed higher magnitudes of RMS vertical and pitch accelerations for pattern 1 and 4 (Table 1.10) for all bicycles. The study also performed measurements on motor vehicles, traversing the test patterns. The vibration and noise levels inside the passenger compartment were measured at speeds of 72 and 88 km/h, and departure angle of approximately 3 to 5 degrees. A-weighted sound pressure levels measured inside a 1998 Plymouth Grand Voyager are shown in Table 1.11 together with the rankings of the test patterns in the 1 to

6 range on the basis of the effectiveness of the pattern. The effectiveness of the rumble strip configurations for alerting the drowsy/inattentive drivers was also evaluated using the: vertical and pitch acceleration of the chassis and peek sound level in the passenger compartment.

Table 1.9: Ranking of test configuration based on subjective overall comfort level (Elefteriadou et al., 2000).

Test Pattern	*Average overall comfort level*[*]	*Average overall control level*[**]
1	7.3	7.4
2	11.0	10.8
3	14.5	13.4
4	10.0	9.5
5	12.1	11.5
6	14.8	14.3

[*]Comfort scale: very uncomfortable - 0; very comfortable - 25
[**]Control scale: uncontrollable - 0; no effect on handling - 25

Table 1.10: Ranking of test configuration based on objective comfort level (Elefteriadou et al., 2000).

Test Pattern	*Average for: Mountain, road, and hybrid bicycles*	
	RMS-Vertical Acceleration (m/s^2)	*RMS-Pitch Acceleration (rad/s^2)*
1	21.91	30.59
2	16.95	21.23
3	13.18	15.81
4	21.94	21.71
5	19.32	18.99
6	11.32	13.29
Tandem bicycle		
1	16.80	22.00
2	12.45	16.40
3	10.36	13.17
4	19.08	17.83
5	17.97	15.41
6	8.97	10.91

From bicyclist's perspective, pattern 6 was the most bicycle-friendly but it generated the least amount of noise in the passenger compartment at both speeds. The pattern 6 was thus judged as least effective for the motorists. Pattern 3 was found to be the second most bicycle-friendly pattern and also ranked second in the high speed testing for the motor vehicle. This pattern, however, was found to be less effective under lower speed, as it only produced 7 dB(A) above the ambient noise. The results suggested that a bicycle-friendly pattern would result in poor performance in warning the motorist. The study suggests the pattern 5 as a better compromise.

Table 1.11: Ranking of test configuration based on the noise levels inside car (Elefteriadou et al., 2000).

	Ranking	*Pattern*	*Speed (km/h)*	*Sound Level dB (A)*
Best	1	4	72	83.6
	2	1	72	80.0
	3	5	72	79.3
	4	2	72	78.4
	5	3	72	75.2
Worst	6	6	72	74.7
		Smooth	72	68.4
Best	1	1	88	88.9
	2	2	88	83.7
	3	3	88	81.3
	4	4	88	81.2
	5	5	88	79.1
Worst	6	6	88	78.2
		Smooth	88	65.2

Outcalt (2001) conducted a study on five different rumble strip configurations with groove depths of 19, 12.7, 9.5, 6.4, 3.2 mm (3/4, 1/2, 3/8, 1/4 and 1/8 inch). The variation in the groove depth was also coupled with changing in the groove width and the length of the flat portion, while the center to center distance was kept constant. A new 50 mm groove rumble strip design was used for this experiment. Owing to considerable

variations in the depth of each groove, due to the coarse teeth of the grinding operation, the measured data were averaged and summarized in Table 1.12. A total 29 of riders were employed in the experiment, where each rider rode over each section at speeds of 8, 16, 24 and 32 km/h (5, 10, 15 and 20 mph). However, some of the riders felt unsafe and uncomfortable while riding on rumble strip pattern number 5, at speeds of 8 and 16 km/h. The riders were asked to rate each section, for both comfort and controllability, on a scale from 1 to 5, where 1 referred to as "No Effect" and 5 as "Uncomfortable/Uncontrollable".

Table 1.12: List of rumble strip dimensions (Outcalt, 2001).

Rumble Strip Pattern				
Section	*Groove Width [mm]*	*Flat Width [mm]*	*Rumble Strip/Gap [m]*	*Depth [mm]*
1	50.8	254	Continues	12.7
1A	50.8	254	3.7/1.8	12.7
2	50.8	127	Continues	12.7
2A	50.8	127	3.7/1.8	12.7
3	50.8	127	3.7/1.8	9.5
4	50.8	76	Continues	12.7
4A	50.8	76	3.7/1.8	12.7
5	266.7	114	14.6/3.7	19.0
6	165	140	Continues	12.7
7	152	152	Continues	9.5
8	140	165	Continues	6.4
9	127	178	Continues	3.2

The tenth section of a continuous rolled strip was 457 mm (18 inch) wide (perpendicular to the direction of travel) with a 60 mm (2-3/8 inch) wide grooves, 41 mm (1-5/8 inch) flat and 12.7 mm (1/2 inch) depth.

If the cyclists were unwilling to ride over specified section at a specified speed, that particular section was rated as 5. The mean values of the ratings for comfort and controllability are shown in Table 1.13. The study also attempted objective assessment of the selected patterns through measurements of vibration levels on a test bicycle, Schwinn Varsity with 685 x 31 mm (27 x 1 1/4 inch) tires, inflated at 344.7 kPa (50 psi). The

bicycle was instrumented with an accelerometer, which was connected by a lightweight cable to a computer installed on the bed of a small pick up truck. Table 1.14 shows the reported peak acceleration values, in decibels, for each section of the rumble strips along with their corresponding predominant frequencies. The study further reported noise and vibration levels measured in a motor vehicle traversing the selected rumble strip patterns, while the vibration was measured on the floor and the steering wheel.

Table 1.13: Control and comfort ratings of different sections of rumble strips based on subjective responses (Outcalt, 2001).

Section	*Average Control Rating*	*Average Comfort Rating*
1	1.8	2.3
2	2.3	2.9
3	2.1	2.6
4	2.4	3.0
5	4.4	4.7
6	4.2	4.6
7	3.9	4.3
8	3.4	4.0
9	2.9	3.5
10	1.4	1.4

Table 1.15 summarizes the peak accelerations and frequencies measured on the floor and the steering wheel of the motor vehicle. Assuming that a gain of 6 dB in the sound pressure level with reference to that measured on a smooth pavement would be generally accepted as a "clearly noticeable change", Outcalt (2001) concluded that sections 5, 6 and 7 produced the best sound and vibration cues for the motorist. These sections, however, were ranked poorly by the cyclists. Sections 10, 1 and 3 were ranked as the best from the cyclist's point of view, which provided least gains in the noise levels. Sections 2, 4, 8, 9 were rated near the mid range for all three tests.

Table 1.14 Measured peak acceleration levels on a test bicycle traveling different sections of rumble strips (Outcalt, 2001).

Peak acceleration in dB and frequency (indicated in parenthesis)				
Section	Speed			
	8 km/h	16 km/h	24 km/h	32 km/h
Section 1, 1A	8 (31.5)	21 (25)	21 (20)	23 (25)
Section 2, 2A	11 (12.5)	18 (20)	27 (31.5)	26 (40)
Section 3, 4, 4A	10 (12.5)	25 (31.5)	34 (10)	21 (63)
Section 5	12 (20)	28 (12.5)	35 (20)	NA
Section 6	13 (25)	25 (25)	33 (20)	35 (25)
Section 7	11 (31.5)	26 (25)	32 (20)	33 (25)
Section 8	10 (25)	24 (25)	31 (16)	33 (25)
Section 9	6 (31.5)	21 (25)	26 (20)	31 (25)
Section 10	8 (31.5)	18 (40)	15 (63)	12 (20)

Table 1.15: Measured vibration of the GMC Safari minivan (Outcalt, 2001).

Peak acceleration in dB and frequency (indicated in parenthesis)				
Acceleration at:	Floor		Steering Wheel	
Section \ Speed	89 km/h		105 km/h	
Section 1	-6 (80)	-9 (100)	89 km/h	105 km/h
Section 1A	-9 (80)	-11 (200)	5 (80)	-5 (40)
Section 2	-8 (125)	-6 (160)	5 (80)	-5 (100)
Section 2A	-9 (125)	-8 (160)	0 (80)	-6 (40&160)
Section 3	-10 (125)	-9 (160)	-3 (125)	-4 (160)
Section 4	-9 (200)	-1 (250)	-5 (125)	-6 (160)
Section 4A	-17 (25)	-4 (250)	-6 (80)	-**
Section 5	6 (80)	3 (100)	-4 (80)	-**
Section 6	8 (80)	3 (100)	11 (80)	7 (100)
Section 7	8 (80)	3 (100)	8 (80)	21 (100)
Section 8	5 (80)	2 (100)	9 (80)	3 (100)
Section 9	-2 (160)	-1 (100)	5 (80&160)	5 (100)
Section 10	3 (630)	8 (100)	2 (80&160)	7 (100)

** Data at or below background acceleration
Negative decibel levels occurred since the reference acceleration is $1 m/s^2$.

It was found that the proposed 50 mm groove rumble strip did not produce a "noticeable increase" in the sound level for the dump truck. The "standard design" alone produced sufficient noticeable gain (6 dB) in the sound pressure level. The study concluded that the

strips 2, 8 and 9 would provide the best compromise, while the pattern 8 alone could provide the noise level close to 6 dB in the dump truck at 105 km/h (65 mph). The recommended design thus consisted of a pattern with depth of 9.5 ± 3.2 mm (3/8 ± 1/8 inch) with 305 mm (12 inch) center to center distance in 4.6 m (48 feet) long pattern of rumble strip followed by 3.65 m (12 feet) of gap. It was also noted that 12.5 mm (1/2 inch) deep rumble strips are too severe for the cyclists and that warnings should be given prior to the rumble strips.

Moeur (1999) attempted to design rumble strips that are more bicycle friendly by analyzing the gap patterns and determining the optimum length to allow cyclists to cross the rumble strip without having to enter into the rumble strip pattern. At first it was thought that changing the spacing of the individual grooves might be beneficial but a further analysis showed that the problem was the vertical motion of the bicycles and not necessarily the location or period of the motion. It was then suggested to reduce the depth of grooves from 13 mm to 10 mm. Another approach of developing bicycle-friendly rumble strip patterns suggested by Moeur (1999) was to create periodic and sufficiently long gaps in the rumble strip patterns, so that the bicyclists may cross the strips without touching the rumble strip pattern, and at the same time being short enough so that a vehicle may not cross the gap without entering the grooved portion at a typical ROR angle of departure.

The American Association of State Highway and Transportation Officials (AASHTO, 1999) performed many evaluations and recommended the designs of rumble strip patterns for speeds up to 32 km/h. The bicyclists, however, can reach speeds of above 40 km/h on downgrades. The study involved tests with 28 subjects, divided into 5

different groups. The tests were conducted using different simulated rumble strips consisting of raised markers so that the length of the gap could be easily changed, and also the types of bicycles. Comparing to ground-in rumble strips, raised markers had greater visibility but field surveys have indicated that the ground-in shoulder grooves are easily visible under conditions typical for bicycle travel on state highways. The study found that the total lateral movement of the cyclists crossing the gaps was about 1.2 meters, which was significantly larger than the width of the tested rumble strip. It was thus concluded that movement across the rumble strip was governed by the length of the gap and not by the width of the gap. The test results suggested a placing of 3.7 meters gap in a 18.3 or 12.2 meters cycle, resulting in 80% or 70% coverage of the total shoulder length, respectively. Such an arrangement would perform acceptably to permit bicyclists to cross ground-in rumble strip patterns. Both the 18.3 and 12.2 meters cycle were judged to be equally acceptable, on the basis of the frequency of the gaps encountered by the rider, which would be 1.8 and 2.7 seconds, respectively, at a speed of 24 km/h. This period was judged to be enough to allow the bicyclists to move freely across the rumble strip patterns. The recommended design also considered the motor vehicles drift off the roadway data reported for the Portland Cement Concrete shoulders (Illinois Division of Highways, 1970), which suggests that the departure angle for ROR crashes is approximately 3 degrees. At an angle of 3 degrees, the center of tire will travel 190 mm laterally for every 3.7 meters longitudinally thus making it impossible for the tire to completely miss the rumble strip grooves.

According to the recommendation by the U.S. Federal Highway Administration (FHWA) (2001) the rumble strips should only be installed when an adequate

unobstructed width of paved surface remains available for bicycle use. The study suggested that rumble strips should not be used when their installation would leave a clear shoulder pathway of less than 1.2 m (4 feet) wide or less than 1.5 m (5 feet) wide in the presence of an obstruction, such as a curb or guardrail to the right of the rumble strip. At locations where such space does not exist to the right of the rumble strip, a rumble strip may be installed if it is at least 0.3 meters (1 foot) to the right of the edge line. In this case, a bicyclist would be expected to ride to the left of the rumble strip, essentially along the outside edge of the traffic lane.

The reported studies on the design and performance of rumble strips have been mostly based upon field measurements of the bicycles and motor vehicles, while only minimum efforts have been made to seek bicycle-friendly design of patterns using modeling and simulation techniques (Elefteriadou et al., 2000). Owing to the high cost and complexities associated with fabrication of rumble strips patterns, the field studies have been limited to either a few patterns or a few variations in the geometry, and limited types of bicycles. These studies clearly show that a pattern considered most suited for the bicycle would provide poor warning cues for the motorist. The design of bicycle-friendly rumble strips thus involves a complex compromise between the rider comfort and controllability, and vibration and noise cues for the motorist. The development and analysis of analytical models of the bicycles subject to excitation from various rumble strip patterns, could provide considerable knowledge leading to the compromise design. Although such simulation based studies have not yet been attempted, a few studies have developed analytical models of the bicycles and the rider to analyze the rider vibration responses (Waechter et al., 2001; Wang and Hull, 1994; Wang and Hull, 1997;

Elefteriadou et al., 2000). These reported studies are reviewed and discussed in order to gain knowledge for developing the analytical models and methods of analyses.

1.2.3 Mathematical Modeling of Bicycle-Rider System

Waechter et al. (2001) developed a mathematical model of a bicycle-rider system with wheel suspension, for the purpose of predicting vibrational stress on the rider due to surface irregularities. The bicycle-rider system was modeled as a system of four rigid bodies: the rider, the front swing arm system, the rear swing arm system and the central bicycle frame. The rigid bodies were linked together by rotational and linear joints and suspended by linear spring and damping elements. The spring and damping elements were used for modeling of the rider hand-arm system in contact with the handle bar, saddle support, and the wheel suspensions. Each bicycle tire was modeled as a parallel combination of a linear spring and a damping element, assuming point contact with the terrain surface. Figure 1.3 illustrates a schematics of the model, where the components 1 to 8 refer to the rider; central frame; front swing arm system; rear swing arm system; hand-arm system; saddle; suspension spring and damper; and tire spring and damper, respectively.

Owing to the complexities associated with modeling of the biological system, the rider was modeled as a single rigid body, representing the rider's trunk, supported on the bicycle saddle through a pivot, and a linear spring and damping element. The rigid body representation of the rider is further suspended at the shoulder by a spring and a damping element, representing the hand-arm system coupled with the handle bar. The masses due to the legs and the feet were lumped together with the rider's trunk. The tires contact

spring and damping elements were allowed to leave the ground when the distance between the wheel hub and the ground level exceeded the given undeformed wheel radius.

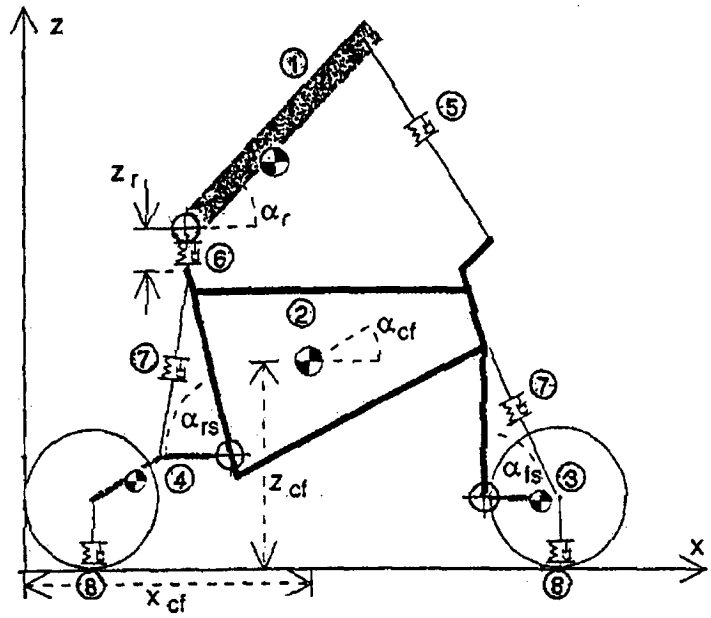

Figure 1.3: Model of the bicycle-ride system (Waechter et al., 2001).

The study further validated developed bicycle-rider model against measured acceleration data obtained at the bicycle's handle bar and the seat. Noticeable differences between the measured data and simulation results in the region above 10 Hz were observed. The differences in the measured and model handle bar spectra, however, were smaller than that in the seat acceleration spectra. The study suggested that further improvements of the model should include more advanced models of the human body and the bicycle tire. The study, however, concluded that the developed model was sufficiently precise for predicting the vibrational stresses on the bicycle.

Modern bicycles are frequently designed with wheel and seat suspension to enhance the vibration comfort of the rider. While a number of studies have investigated the role of suspension damping on the ride dynamics of motorcycles, only minimal efforts have been made for the bicycles. Basso et al. (1998) studied the influence of front suspension damping on the motorcycle ride responses, using a two degree of freedom in-plane model. The sprung mass represented the mass of the rider together with the body of the motorcycle, while the unsprung mass considered the mass of the wheel along with the suspension components. To describe the motion of the sprung and the unsprung masses, linear coordinate y_u was chosen to indicate the vertical displacement of the unsprung mass, while angular coordinate θ denoted the pitch rotation of the sprung mass about point A, as shown in Figure 1.4. The model involved a number of simplifying assumptions. The distance BA between the handle bar and the center of the rear wheel was considered to be constant, while the rear wheel was allowed motion only in the horizontal direction. Moreover, a constant forward velocity was assumed. The two-degree-of-freedom (DOF) system model was subject to base excitations, while the derived equations of motion were solved using the fourth-order Runge-Kutta numerical integration method. The study concluded that it is possible to carry out a dynamic analysis of motorcycle's front suspension by using a simplified two-DOF model.

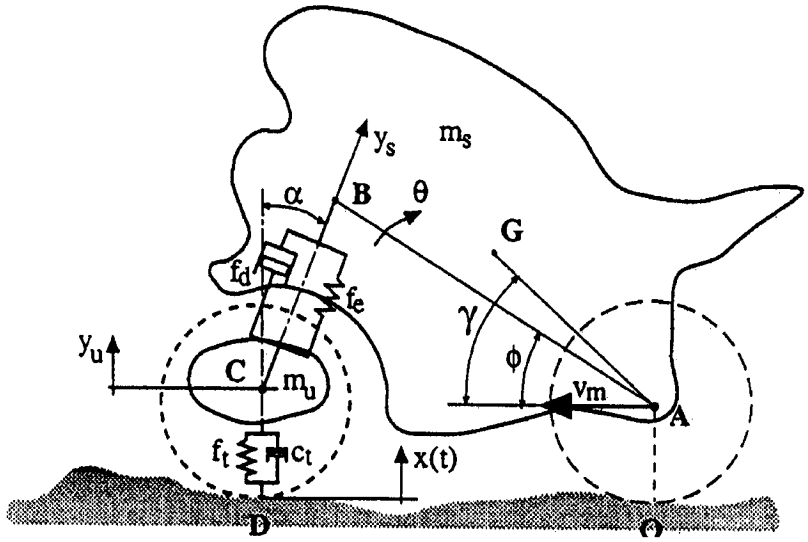

Figure 1.4: A two - DOF model of the motorcycle with rider (Basso et al., 1998).

Wang and Hull (1996) studied rider induced energy loss due to the bicycle suspension system. A two-dimensional dynamic model of a seated rider on an off-road bicycle, pedaling at a constant mean velocity on a smooth road, was developed for the purpose of the study. It was assumed that, all of the suspension motion would be rider induced in the absence of the terrain irregularities. As shown in the Figure 1.5, the developed bicycle-rider model consisted of six rigid bodies: the rider (R), main triangle (MT), rear triangle (RT), fork (FK), front wheel (FW) and rear wheel (RW). The equations of motion for the model were developed using five degrees of freedom: rotation of the rear wheel (Q1), rotation of the rear triangle (Q2), linear displacement of the rear tire (Q3), rotation of the main triangle relative to the rear triangle (Q4) and displacement of the fork (Q5).

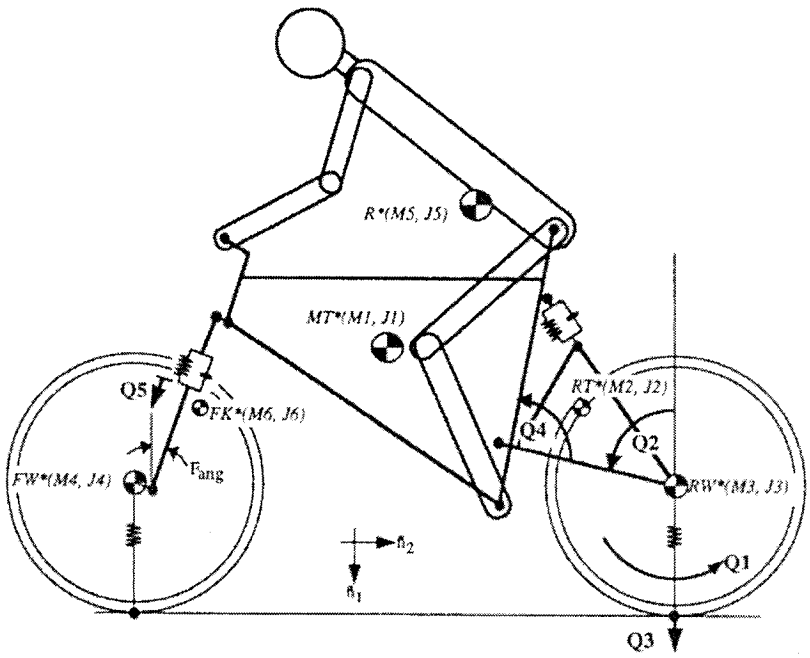

Figure 1.5: The bicycle-rider model (Wang and Hull 1996).

The rider was modeled as a single rigid body, where the location of the rider's center of gravity and the pitch mass moment of inertia were calculated from the body segmental masses and moments of inertia. The relative positions of the rider body segments were calculated relative to the bicycle seat. The displacement of the fork and rear suspension was experimentally measured with linear transducers for a ride at speed of 6.5 m/s. The dissipated power was computed from the known stiffness and dissipative characteristics of the suspension elements. The results obtained from the simulation model were compared with the experimentally measured suspension deflections. The study reported that fork motion could not be observed in both the experiment data and the simulation results. For the rear suspension, the experiment results revealed mean deflection of 6.6 mm. The power dissipation by the rear suspension was calculated to be 6.9 Watts. Based on the results of the simulations, the study concluded that for a

commercially available dual suspension bicycle, the rider induced power losses were 1.3 percent of the total rider input power.

Elefteriadou et al. (2000) used a commercial software package "Dynamic Analysis and Design of Systems" (DADS) to simulate for the dynamic responses of the bicycle-rider system traversing a rumble strip. The bicycle-rider system was modeled as a system comprised of seven rigid bodies, as shown in the Figure 1.6. The bicycle model consisted of the bicycle frame, and the front and the rear wheels, while the rider was modeled by including: rigid mass for the head and torso, upper and lower arms, lower legs, and feet and thighs. Rider's torso, thighs and lower legs were connected with revolute joints. The upper and lower arms were treated as a single rigid body assuming that the rider arms remain straight with negligible rotational motion. The revolute joints were used to represent the connection between the rider's hands and the handle bar, as well as between the rider feet and bicycle pedals.

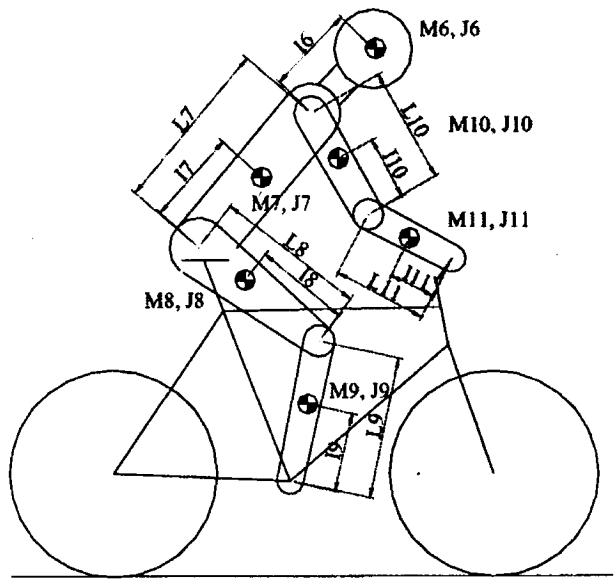

Figure 1.6: Bicycle-rider model (Elefteriadou et al., 2000).

The connection between rider's hip and bicycle seat was modeled as a revolute-translation joint, allowing rider's torso to undergo rotational and vertical motions, while suspended on a spring and damper in the vertical direction. The contact force between the bicycle tire and the rumble strips was considered to be proportional to the tire radial deformation pointing to the center of the wheel. The study further validated the developed bicycle-rider model against measured data. The study concluded that the model simulation results showed a good comparison with the measured data, however, it was noted that compared to the measured data the model showed lower magnitudes for frequencies around 10 Hz.

Wilczynski and Hull (1994) developed a model of the bicycle-rider system for analyzing the loads on the bicycle frame during off-road cycling. The study involved measurements of the frame loads at the rider's contact points with the bicycle using three strain gage dynamometers. One dynamometer was fixed to the pedals, while the other two were attached to the handle bar and the seat. The off-road track was simulated by a series of six square obstacles of a side length of 38 mm. A computer simulation program of the bicycle-rider system was developed and analyzed using the commercial software package DADS. The bicycle frame, as shown on the Figure 1.7, was modeled as a single rigid body. The front fork was connected to the bicycle fame by a linear spring and a damping element. The wheel was modeled by two linear springs assuming that the tire could have more than one point of contact when traversing the obstacles. Rider's trunk, in the seated position was modeled as a rigid body with the head rigidly connected to it. The trunk was connected to the bicycle frame at one end to the seat with a revolute joint and a linear spring and damping element. At the other end, the trunk was also connected to the

frame through a linear spring and a damping element and a revolute joint, representing the hand-arm system. Rider's legs were modeled with two rigid bodies, representing the thighs and the lower legs, rigidly connected to the pedals, while the crank arm was modeled as a spring element.

In order to minimize the differences between the experimental and the simulation results, a parameter optimization was conducted to determine relevant stiffness and damping coefficients. Prior to optimization, a set of parameters was defined which was thought to have the most influence on the responses of the model, when varied. The study reported the model parameters on the basis of the optimization, which are presented in Table 1.16. Measured dynamic forces were reported in the study relative to their respective static loads. The ratio for dynamic loads for both the handle bar and the seat in the horizontal direction was in the range of 6 to 8, and maximum magnitudes were comparable at about 200 N. Although the dynamic to static load ratios for vertical forces were lower than those observed for horizontal forces, the maximum magnitudes were comparable with both the vertical handle bar and seat forces reaching 200 N.

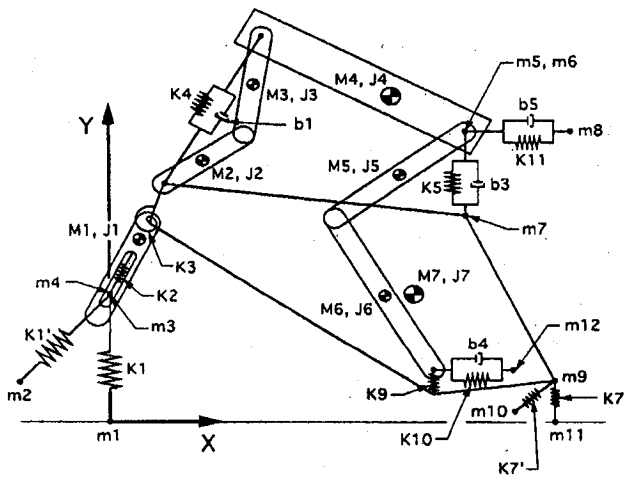

Figure 1.7: Bicycle-rider model (Wilczynski and Hull, 1994).

Table 1.16: Bicycle-rider model system parameters (Wilczynski and Hull, 1994).

Location	*Model Parameter*	*Initial Value*	*Adjusted Value*
Saddle	Stiffness	46700 N/m	48650 N/m
	Damping	1000 Ns/m	1007 Ns/m
Arm	Stiffness	14400 N/m	14980 N/m
	Damping	202 Ns/m	214 Ns/m
Leg	Stiffness	74000 N/m	75200 N/m
	Damping	1350 Ns/m	1273 Ns/m

Wang and Hull (1997) conducted a study in order to optimize the performance of off-road bicycle suspension. To develop the rider model, they measured the stiffness and damping constants for the arms, legs, and visceral mass for seven subjects in three cycling positions: seated, standing and downhill. The study measured the frequency responses of the arms and legs, of a total of seven experienced off-road cyclists, by conducting a series of vibration tests on the bicycle simulator. A band-limited random vibration signal up to 12 Hz and peak-to-peak amplitude of 12 mm served as the vibration excitation. Two different computational models were developed to simulate the laboratory tests involving the arms and the legs. A dynamic model of the cyclist was developed for simulating measured responses of the arms, which is illustrated in Figure 1.8. The model considers the arms as two rigid bodies connected through revolute joints, and linear spring and damping elements spanning the handle bar and the shoulders. The hands were modeled as point masses attached to the end of the lower arms. For the dynamic model used to simulate the legs, each leg was modeled as two rigid segments, as presented in Figure 1.9, connected by revolute joints with linear spring and damping elements connecting the hip and the crank spindle.

In both the models, rider's torso was represented as a single rigid body pivoted at the seat, with head being rigidly connected. The visceral mass (internal organs), was

modeled as a point mass located inside the torso, and attached at the midpoint between the shoulders and the hips by a spring and damper allowing motion perpendicular to the long axis of the torso. The system parameters were identified by minimizing the error function between the experimental data and the simulation results. Identified model parameters for arms, legs and visceral mass, for the seven test subjects are presented in Table 1.17.

The comparisons between the experimental data and the simulation results showed good agreement for the frequencies at which the resonance peaks occurred. The study further reported that the resonant frequency for the legs in the downhill position was between 1 and 2.5 Hz, while for the standing position it was between 2 and 4 Hz. The resonant frequencies for the arms in the seated position occurred between 2 and 3.5 Hz while in the standing position the resonance was between 2.5 and 3.5 Hz. Finally, the visceral mass was found to have the peak frequency in the band of 6 to 8.5 Hz.

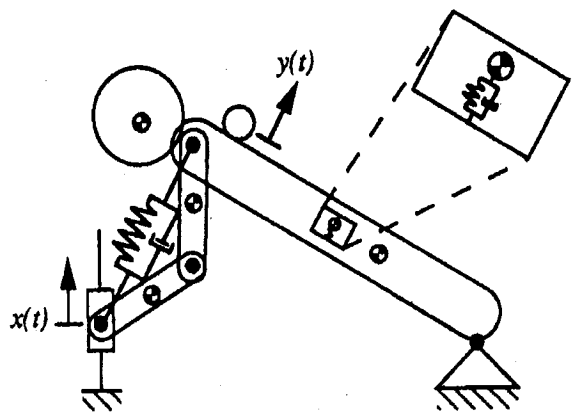

Figure 1.8: Seated bicycle-rider model (Wang and Hull, 1997).

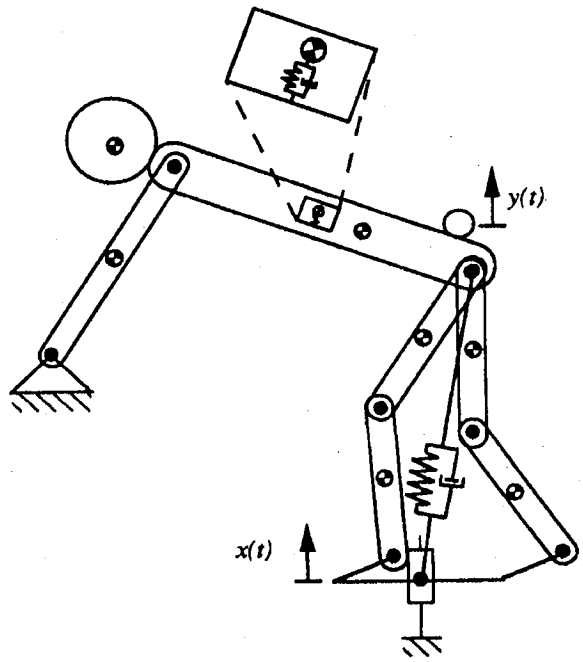

Figure 1.9: Standing bicycle-rider model (Wang and Hull, 1997).

Table 1.17: Bicycle-rider system model parameters (Wang and Hull, 1997).

	Arms				*Legs*				*Visceral mass*	
	seated		*standing*		*standing*		*downhill*			
Subject	stiffness (kN/m)	damping (Ns/m)	stiffness (kN/m)	damping (Ns/m)	stiffness (kN/m)	damping (Ns/m)	stiffness (kN/m)	damping (Ns/m)	stiffness (kN/m)	damping (Ns/m)
1	14.5	595	14.68	659	88.54	1136	55.07	977	20.99	29.4
2	12.32	997	14.20	1044	49.40	1029	37.26	739	18.30	43.1
3	15.15	782	15.20	843	115.39	755	29.02	442	20.99	13.1
4	12.96	565	8.30	775	46.33	909	27.16	444	16.80	77.9
5	7.65	509	8.93	728	46.54	1298	20.18	611	19.29	290.3
6	11.45	428	12.98	532	52.93	998	19.01	474	17.22	115.9
7	8.47	651	14.70	916	74.00	1121	26.51	776	18.48	53.9

Hull et al. (1997) further performed experiments to study the radial force versus deflection behavior of an off-road bicycle tire for a range of cylindrical bump radii. A single off-road bicycle tire, Specialized Ground /S 66 cm x 4.95 cm (26 x 1.95 inch), inflated at 344.7 kPa (50 psi) was used for collecting the load-deflection data for fourteen different surfaces, spanning from 584 mm convex to 584 mm concave. A power-law

formulation was proposed as an empirical model of the tire load-deflection behavior. It was proposed that the relationship between the compressive force and deflection was governed by the equation: $F = A \cdot x \cdot B$, where F is the compressive force in N, x is the compression in cm, and the coefficients A and B were given as:

$$\begin{aligned} A &= 550.9 - 337.8e^{(-2519 \cdot R_b)} \quad \text{for convex radii} \\ A &= 550.9 - 7822 \cdot e^{(0.1398 \cdot R_b)} \quad \text{for concave radii} \\ B &= 1.422 - 0.2469 \cdot e^{(-0.01651 \cdot R_b)} \quad \text{for convex radii} \\ B &= 1.422 - 0.2128 \cdot e^{(-0.0289 \cdot R_b)} \quad \text{for concave radii} \end{aligned} \tag{1.1}$$

where R_b is the radius of curvature of the surface.

The percentage error between the measured data and the data obtained from the model was 4.2% for the concave surfaces, and 13.5% for the convex surfaces. The study concluded that the developed tire model was capable of predicting the radial force-deflection behavior of an off-road bicycle tire. The model, however, could not be applied for terrains with a discontinuous radius of curvature, such as corners, edges and steps.

1.3 SCOPE AND OBJECTIVE OF THE DISSERTATION RESEARCH

From the review of the published literature, it is apparent that the shoulder rumble strips are most effective in preventing the run-off-the-road type of accidents. The use of rumble strips has thus been suggested for separating the bicycle and automotive lanes in the urban areas. The studies show that the current designs provide adequate vibration and noise cues for the motorist but yield uncomfortable ride and a potential for loss of control for the bicycle rider. The designs of bicycle-friendly rumble strips involve complex

compromise between the rider's vibration, and the magnitudes of noise and vibration cues for the motorist. The experimental studies have shown that riding on the rumble strips could generate considerable amount of vibrational stress to cyclists, which causes ride discomfort and poor controllability. Some of the reported investigations of the rumble strip geometry indicate that it is possible to achieve the bicycle-friendly design of the rumble strips. The reported studies on the rumble strips are invariably based on experimental data acquired from limited designs of rumble strips. The analytical techniques involving modeling and analysis of the bicycle-rider system subject to tire interactions with arbitrary rumble strip geometry, have not yet been applied to derive compromise designs. The overall objective of this thesis research is thus formulated to establish relationships between the geometry of the rumble strips and the measures of ride discomfort and controllability through systematic measurements and analytical development. The specific objectives of the theses research are as follows:

1. To experimentally measure the vibrations transmitted to the cyclist while traversing a number of different rumble strips at different speeds and record the subjective responses.
2. Analyze the measured data in an attempt to quantify the effect of rumble strips on the rider's ride comfort and controllability performance.
3. To develop a mathematical model of the bicycle-rider system in order to conduct computer based simulation of the ride dynamics subject to the tire interactions with the rumble strip.
4. To developed a dynamic wheel-groove interaction model suitable for simulating the dynamic interaction between the bicycle and the rumble strip.

5. To validate the simulation model using the measured data.

6. To carry out computer based simulations in order to illustrate the influence of the rumble strip geometry on the ride dynamics of the bicycle-rider system.

1.3.1 Organization of the Thesis

In Chapter 2, the field measurement methodology and data acquisition process during the rumble strips tests is described. A comprehensive test matrix is described, involving multiple rumble strip configurations, traversing speeds, different bicycle types and angles of approach to rumble strips. The chapter also provides the back ground information on test subject populations as well as the technical information on the data acquisition process and equipment.

In Chapter 3, the analysis of the experimentally measured data is conducted. The measured acceleration levels were expressed in terms of overall root mean square accelerations values, are discussed to assess the severity of transmitted vibration. Also the Fourier analysis of the measured data is conducted to examine the frequency components of the measured signals.

In Chapter 4, the dynamic properties of the test bicycle components are characterized in the laboratory, which includes the measurements of the total bicycle masses and pitch mass moment of inertia, and the force-deflection characteristic of bicycle tires and the suspension units. The measure data are applied to formulate a mathematical model of the bicycle. A rider model reported in the literature is modified and integrated to bicycle model to derive the coupled bicycle-rider system model. The differential equations of motion are derived using Langrangian formulation. The point

contact dynamic wheel-terrain model was considered for applying the excitation to the system.

In Chapter 6, the bicycle-rider model is validated by comparing the simulation results with respective to the measured data. The ride dynamics responses of the bicycle-rider system traversing the rumble strips are evaluated for varying geometric parameters of the rumble strip patterns. A parametric sensitivity analysis is conducted to study the influence of front suspension properties on the ride dynamics response of the bicycle-rider system.

In Chapter 7, the conclusions drawn from the study and the recommendation for the future work are presented.

CHAPTER 2

EXPERIMENTAL ASSESSMENTS OF RUMBLE STRIPS

2.1 INTRODUCTION

During the occasional contact with the rumble strips, cyclists experience a sudden increase in the level of vibration. This increase in vibration has a negative impact on the riding comfort, and controllability and, thus the rider's safety. In an effort to estimate the influence of rumble strips on cyclist's comfort and controllability, and to seek designs of bicycle-friendly rumble strips, it is essential to investigate cyclist's experience while traversing different rumble strip patterns. Although the bicyclists may ride on the strips occasionally, the measurements of vibration magnitudes transmitted to the bicycle-rider contact locations, are often performed under continuous riding on the rumble strips to obtain continuous signals of reasonable duration for assessment of objective measures related to comfort and controllability (Elefteriadou et al., 2000; Outcalt, 2001).

Apart from the objective measures, it is also important to investigate rider's subjective sensation of ride comfort and controllability. Both objective and subjective measurements are thus needed in order to achieve better understanding of the impact of rumble strips on the riders. Subjective measurements concentrate on rider's perception of transmitted vibrations and handling. In case of rumble strip tests, the subjects are asked to rate each design and test condition in view of the ride comfort and controllability perception. Garder (1997), Ardekani et al. (1996) performed tests on different rumble strip configurations to assess riders, comfort and controllability on the basis of subjective responses alone. Considering that the rider perceptions are strongly influenced by many

factors, such as individual factors and riding skills, the subjective responses in general yield large inter subject variability and often contradictory responses. Alternatively, objective measurements of vibration levels on instrumented bicycle have been preformed by Elefteriadou et al. (2000) and Outcalt (2001). These studies also acquired the subjective reactions of only a smaller sample of the test subject population. In the present study, both objective and subjective responses are acquired for a total of 7 adult male subjects, while riding two different bicycles on four different rumble strips. The test methodology and the experiment design are described together with the developments in the measurement and data recording system.

2.2 TEST MATRIX

The experiments were designed in a way to include a wide range of parameters, such as different test subjects, bicycle types, riding speeds, approach angles, rumble strip configurations and multiple trials. The analysis of the acquired data could thus enable the assessment of the influence of the different strips designs, riding speeds, types of bicycle and the rider's skill. Table 2.1 summarizes the test matrix, while the components of the matrix are described in details in the following subsections.

2.2.1 Test Subject Population

A total of seven adult male subjects took part in the experiments designed to evaluate the effects of rumble strip patterns on the cyclist's comfort and controllability. Table 2.2 summarizes the age, weight, and riding skills of the subject population. These subjects were within the age group of 25 to 60 years with mean body mass of 78.6 kg and

standard deviation of 11.0 kg. All subjects were in a good physical health. Subjects expressed their riding skills either as occasional bicycle riders or as experienced bicycle riders. All subjects were informed on the content of the experiment prior to the testing, and provided their consent for participation. Each subject was advised of his right to discontinue the experiment for whatever reason at any time. They were also encouraged to stop the testing at any point, if they felt the test as either too dangerous or too uncomfortable.

Table 2.1: Rumble strip test matrix.

Rumble Strip Configuration	*Bicycle Type*		*Trials*	*Speeds (km/h)*				*Angle of Approach*	*Number of Subjects*
	Touring	*Hybrid*		*10*	*15*	*20*	*30*		
Round I	X	X	3	X	–	X	X	–	2
				X	X	X	–	X*	5
Round II	X	X	3	X	X	X	–	–	2
Rectangular I	X	X	3	X	–	X	X	–	2
Rectangular II	X	X	3	X	–	X	X	–	2
Flat Pavement	X	X	2	X	–	X	X	–	2
				X	X	X	–	–	5

*Only four subjects participated in angle of approach tests.

2.2.2 Test Bicycles

Two most commonly used types of bicycles among recreational cyclists, who ride usually on the open roads, are the Touring bicycle and the Hybrid bicycle. Considering the bicycle interaction with the rumble strips would depend upon the type of bicycle, these two types of bicycle were selected for the experiments. The Touring bicycle, shown in Figure 2.1, is a non suspended bicycle with 685 mm (27 inch) wheel size. The bicycle

was equipped with 700x28C tubeless tires, while tire inflation pressure was kept at 655 kPa (95 psi), as recommended by the manufacturer.

Table 2.2: Age, Weight and Riding Skills of the Test Subject Population.

Subject	*Age (Years)*	*Weight [kg]*	*Riding Skills*
1	42	86.0	Experienced
2	53	89.6	Occasional
3	26	69.0	Occasional
4	50	61.0	Occasional
5	27	75.8	Occasional
6	60	75.0	Occasional
7	30	90.0	Occasional
Mean	41.1	78.6	-
Std. Dev.	13.7	11.0	-

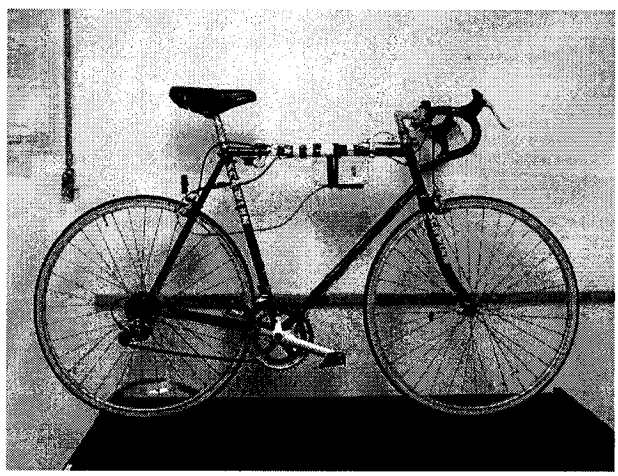

Figure 2.1: A pictorial view of the Touring bicycle.

The Hybrid bicycle, shown on Figure 2.2, is a suspended bicycle comprising the front wheel and the seat post suspension and 685 mm (27 inch) wheel size, identical to that used for the Touring bicycle. The bicycle was equipped with KENDA 700x38C tires and the tire inflation pressure during the tests was kept at the recommended value of 517 kPa (75 psi).

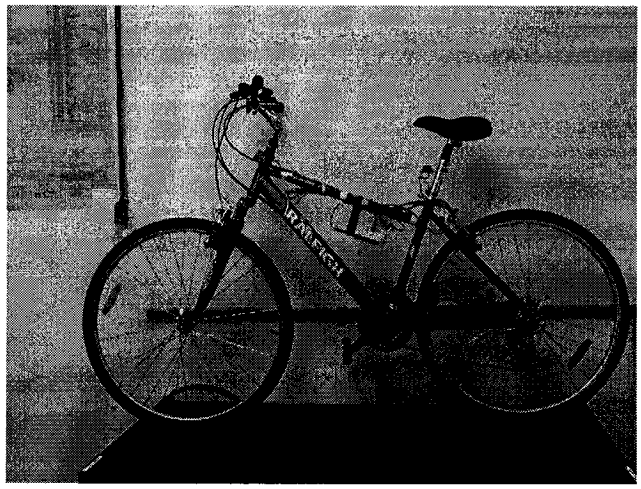

Figure 2.2: A pictorial view of the Hybrid bicycle.

2.2.3 Rumble Strip Configurations

The primary focus of the study is to identify bicycle-friendly rumble strip designs in view of the vibration transmitted to the rider and the handling abilities of the rider. A number of prototype rumble strip designs were fabricated by the Ministère des Transportation du Québec on the basis of the design used in the USA and intuition. A total of six different milled in rumble strip configurations, installed along side a highway stretch, were considered for the study. All of the rumble strip configurations were milled in asphalt pavement with an asphalt grinder, as shown on Figure 2.3. A total of three rumble strips patterns were initially fabricated, which included a rounded pattern (Round

I) following the configurations used in a few studies (Wood, 1994; Ardekani et al., 1996; Elefteriadou et al., 2000), and two rectangular designs (Rectangular I and II). The groove lengths of the two rectangular strips were 30 and 15 mm, respectively, with center to center distance of 120 mm and 105 mm and, depths of 15 mm. The grove width of the round strips was 115 mm with center-to-center distance of 300 mm and depth of 10 mm.

Three additional strips of round profiles denoted as Round II, Round III and Round IV were fabricated at a later stage to study the influences of variations in the groove depth and length. Both these strips were fabricated with center-to-center distance of 445 mm and groove length of 200 mm, while the depths were 5, 8 and 10 mm, respectively for the Round II, Round III and Round IV strips. Figures 2.4 and 2.5 illustrate the geometry of the round and rectangular patterns. Table 2.3 summarizes the dimensions of the prototype patterns. It should be noted that the reported dimensions represent the mean dimensions, which varied considerably from the target or desired dimensions due to inaccuracies in the rumble strip fabrication process. In order to illustrate the magnitude of the scatter of the grooved patterns, Table 2.4 presents the measured dimensions of the rumble strip pattern "Round I" conducted on a randomly chosen sample of 10 consequent grooves.

Figure 2.3: Installation of rumble strips in asphalt pavement.

Table 2.3: Nominal dimensions of the prototype rumble strip configurations.

Rumble Strip Configuration	*Center to Center Distance [mm]*	*Groove Length [mm]*	*Groove Depth [mm]*	*Width of Pattern [mm]*
Rectangular I	120	30	15	300
Rectangular II	105	15	15	300
Round I	300	115	10	300
Round II	445	200	5	1130
Round III	445	200	8	1130
Round IV	445	200	10	1130

Table 2.4: Measured geometric dimensions of rumble strip pattern "Round I".

Measurement	*Groove Depth [mm]*	*Center to Center Distance [mm]*	*Grooved Length [mm]*
1	9.08	280.00	110.00
2	9.80	292.00	114.00
3	10.30	307.00	113.90
4	10.10	301.00	114.50
5	10.52	293.00	115.07
6	9.43	308.00	110.77
7	9.08	300.00	118.15
8	10.08	291.00	117.63
9	9.27	275.00	103.40
10	9.45	280.00	140.60
Mean	9.71	292.70	115.80
St. Dev.	0.52	11.55	9.69

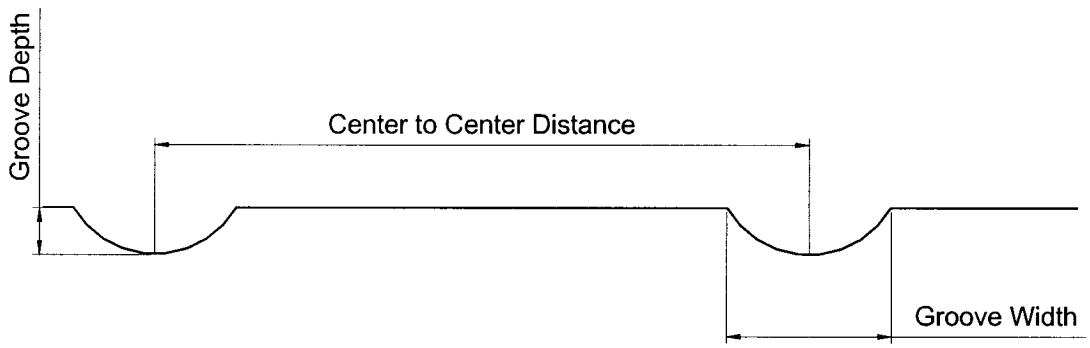

Figure 2.4: Geometry of the round rumble strip profiles.

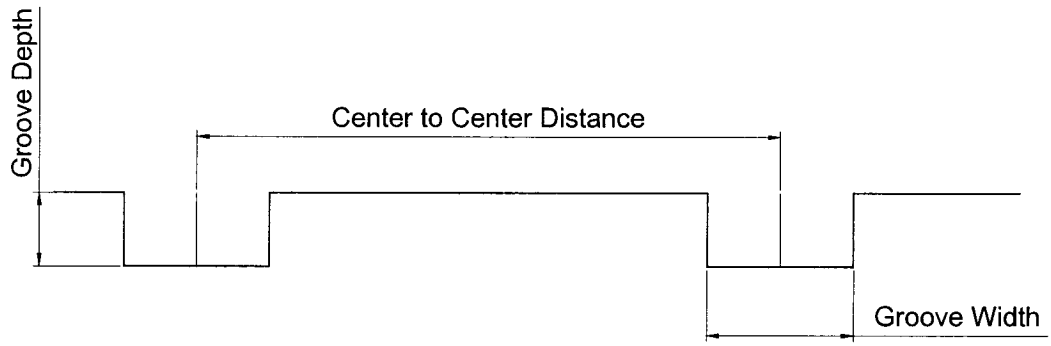

Figure 2.5: Geometry of the rectangular rumble strip profiles.

2.2.4 Traversing Speeds

Each rumble strip configuration was tested at three different traversing speeds. During the first phase of the testing, speeds were selected as at 10 km/h, 20 km/h and 30 km/h. After a few initial trials with selected subjects, it was observed that a number of subjects had difficulty in maintaining the higher speed of 30 km/h, while riding on the rounded rumble strips. The subjects felt very uncomfortable and had difficulty in controlling the bicycle. Some of the subjects also reported that the riding at 30 km/h was physically demanding for them, since they had to maintain the same speed for the entire

length of the test. Test speed was thus limited to 20 km/h to ensure subject safety and consistent speed during a given trial. Further tests were thus performed at riding speeds at 10 km/h, 15 km/h and 20 km/h. During the tests, subjects were able to monitor the forward speed using the display from the Cat-Eye CC-ST200 speed-o-meter installed on both test bicycles. Figure 2.6, illustrates a pictorial view of the speed indicator that was attached on the bicycle's handle bar. Each subject was advised to maintain the speed close to the desired speed for a trial.

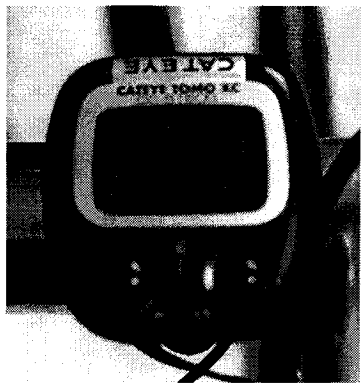

Figure 2.6: A pictorial view of the Cat-Eye CC-ST200 speed-o-meter.

2.2.4 Angle of Approach

The rumble strips are designed to separate the bicycle lanes from the automobile lanes to provide safer environment for the bicycle riders. The addition of a rumble strip, however, could considerably reduce the width of the bicycle lane and may encourage the riders to ride on the rumble patterns. Moreover, the riders would be expected to ride on the strips to avoid some obstacle on the path or pass a slower moving bicycle. In these situations, the rider would approach the strips at a certain angle, and may even cross over the rumble strips, depending upon the speed and controllability of the rider. The bicycle

response, and the rider's perception and reaction to such responses would strongly depend upon angle of approach. The experiments were thus conducted using an angle of approach of 10 degrees with respect to the direction of the rumble strip, as shown in Figure 2.7. A total of four subjects were employed in this experiment, which further involved three different speeds and three trials.

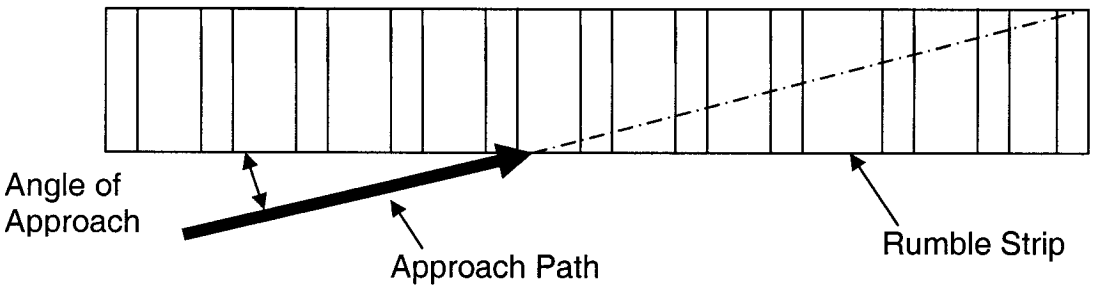

Figure 2.7: Bicycle Angle of Approach to Rumble Strips.

2.3 TEST METHODOLOGY

The tests were conducted on six different types of milled in rumble strip configurations installed by the Ministère des Transportation du Québec (MTQ), on an unused paved road section besides a local highway. Each rumble strip pattern was approximately seventy meters long. All of the tests were conducted during the months of August and September, and the temperature varied between twenty and twenty five degrees that would correspond to a typical weather for cycling. The evaluation of rumble strips for rider's comfort and controllability were performed using both objective and subjective measurements. Objective measurements were conducted using the instrumented Touring and Hybrid bicycles, while the subjects rode them across different

rumble strip configurations. A questionnaire was designed to document the subjective responses of all the subjects after a few selected trials.

Test subjects who participated in the study were volunteer bicycle riders. The purpose of the experiment as well as the test procedure was described to each participant prior to the experiments. At the same time, the subjects were asked to provide background information on their body weight, age and bicycle riding skills. Each subject participated in the experiments involving two bicycles, selected rumble strips and three trials of each combination. Prior to the experiments, each subject was asked to perform preliminary trials and become familiar with the bicycles and the strips while maintaining nearly constant speed. They were also instructed to practice riding bicycles at constant speed, while monitoring the speed using the speed-o-meter installed on the bicycle's handle bar. At the same time heights of the seat post and the handle bar were adjusted to ensure comfortable ride for every subject, as judged by the subject. Since the data logger was attached to the bicycle's frame, it was rider's responsibility to turn it on at the beginning of each trial, when it reached the desired test speed, and to turn it off at the end of the trial.

Each subject was initially asked to ride the bicycle on the flat asphalt pavement, in a straight line path for duration of approximately fifteen seconds. These tests were conducted at three different speeds, and two trials were performed at each speed. The results attained from these tests served as the reference values for assessing the role of the rumble strips using both the subjective and objective methods. The participants were then asked to ride the selected bicycle across a rumble strip at a selected speed. Subjects traversed each rumble strip configuration at three different speeds by making three

independent trials for each speed. Each subject was asked to rest for a few minutes after every three trials. Each participant was further asked to respond to the questionnaire after completing the tests for a particular bicycle and strip configuration, while the responses were documented by the experimenter. For this purpose, the participants were asked to describe their ride sensation and ability to guide the bicycle, as experienced during the previous test. At the same time, the functioning of the instrumentation was verified in order to ensure the alignment of the transducers as well as the positioning of the potentiometer used for measuring yaw oscillations of the handle bar. The files stored within the multi-channel data logger were downloaded and the data was verified using digital signal processor software (DADiSP) on an on-site laptop computer.

The final stage of tests involved riding the bicycle at an angle of approach and crossing the selected rumble strips. Test subjects approached the rumble strip configuration, Round I, at an angle of 10 degrees at three different speeds by making three independent trials for every speed.

2.4 OBJECTIVE MEASUREMENTS

Objective evaluations of rumble strips included measurements of ride vibration transmitted to the rider and measurements related to controllability of the rider. The most commonly used method for objective assessment of ride comfort is based on the measured vibration magnitudes transmitted to the rider. The acceleration due to vibration has been directly related to human perception of vibration. According to ISO-2631 (1997) standard, the primary quantity of vibration magnitude should be acceleration. According to the same standard, vibration shall be measured along a coordinate system

originating at a point from which the vibration is considered to enter the human body. In case of a bicycle, when the rider is in the seated position, it is considered that predominant entry points of vibration to the rider are through the seat and through the handle bar. Therefore for the purpose of assessing the vibration comfort of the rider, each bicycle was instrumented with two acceleration transducers to measure the vibration at the seat and handle bar. Transducers were mounted on the bicycles close to the handle bar and the seat post. The exact mounting locations of the seat post and the handle bar transducers on the Hybrid bicycle and the Touring bicycle are shown on Figures 2.8 and 2.9, respectively. Measurements of controllability of rider were conducted by measuring the yaw angle of the bicycle's handle bar. The reported studies have suggested the use of pitch motion of the bicycle as a measure of rider's controllability (Elefteriadou et al., 2000). It has also been shown that the controllability performance of the rider, while riding over the rumble strips, could be best described by the lateral deviation of the bicycle path with respect to the target path.

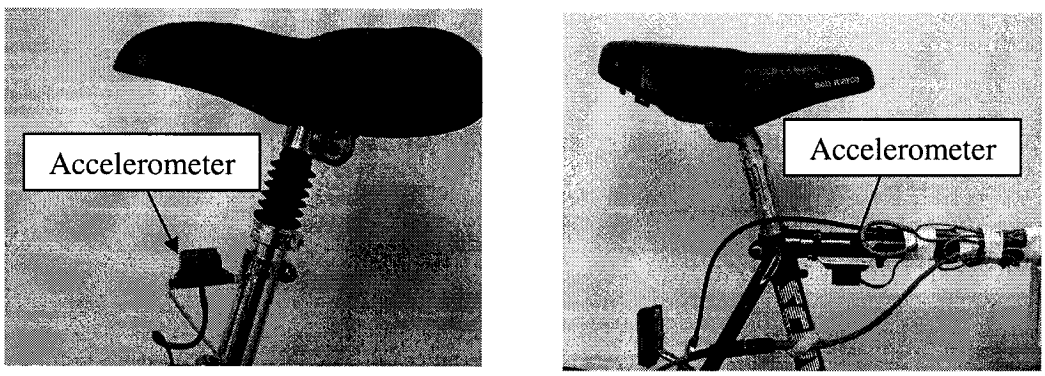

a.) Hybrid bicycle b.) Touring bicycle

Figure 2.8: Mounting locations of the seat post acceleration transducers.

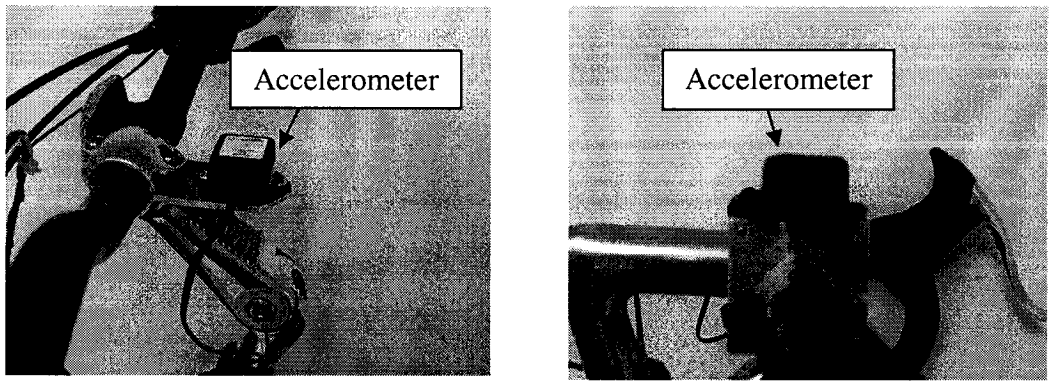

a.) Hybrid bicycle b.) Touring bicycle

Figure 2.9: Mounting locations of the handle bar acceleration transducers.

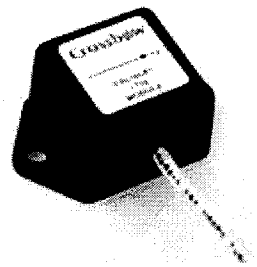

Figure 2.10: Crossbow CXL25LP1Z accelerometer.

In some studies video cameras were employed to capture the path followed by the rider and the deviations with respect to the target path (Elefteriadou et al., 2000). It is believed that the bicycle tires interaction with the rumble strips cause undesirable steering of the tires and excessive vibration of the handle bar. The rider tends to control or guide the bicycle along the desired path by steering the handle bar. The yaw deflection of the handle bar and the yaw rate of the handle bar could thus provide a measure of the involuntary steering effect of the handle bar and the effort expended by the rider. The yaw angle and yaw rate responses of the handle bar are thus considered as objective

measures. The instantaneous values of the yaw angle were measured with a rotary servo potentiometer. The bottom of the potentiometer was rigidly attached to the bicycle's frame while its slider end was free to slide in a circular path along the handle bar and thereby measuring relative angle between the bicycle's frame and the handle bar, as shown on Figure 2.11.

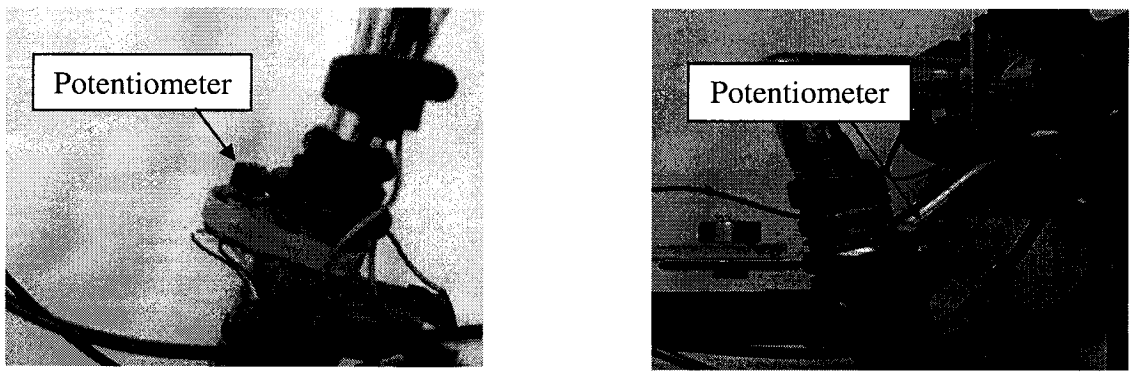

a.) Hybrid bicycle

b.) Touring bicycle

Figure 2.11: Mounting of servo potentiometers at the bicycle's handle bar.

Acceleration transducers used in this study are single-axis Crossbow micro-accelerometers, model CXL25LP1Z, shown in Figure 2.10. These accelerometers are silicon micro-machined capacitive beam type with sensitivity of 80±4 mV/g and an input range of ±25g. The analog signals from the transducers were digitized and recorded using a compact data logger, which was attached to the bicycle frame. The portable four-channel data logger, shown in Figure 2.12, was developed at CONCAVE Research Center, Concordia University. The data logger was designed to continuously store the data acquired through input channels at a maximum sampling frequency of 2 kHz/channel. Considering that the ride dynamics of a bicycle-rider system occur at

frequencies below 100Hz (Elefteriadou et al., 2000; Waechter et al., 2002), the sampling frequency was set at 256 Hz/channel. The data logger provides 16-bit analog to digital data conversion with an input range of ±10V. A power supply circuit is also integrated within the recorder to supply a 5 VDC power to the transducers through interface connections. The data logger is equipped with the connectors through which it can either monitor the incoming transducer signals or accept ± 10 volt bipolar analog input signals. The power supply for the data logger and the transducers is provided by a 9-V lithium battery providing continuous data acquisition for duration of 8 hours. The acquired sampled data are stored on an on-board 32Mb Flashcard. The data stored on the Flashcard can be easily read by a Flashcard reader.

In order to start the data acquisition, the start switch has to be switched to the "open" position, which will open a new file on the Flashcard. The file names on the Flashcard have numerical values indicating the sequential number of the file in series. Each further records the time. The LED flashes every second as the data is written to the file indicating that the data acquisition is in process. To finish the data acquisition, the start switch has to be switched back to "close" position which will automatically close the file on the Flashcard. The file name will then automatically be incremented with each acquisition.

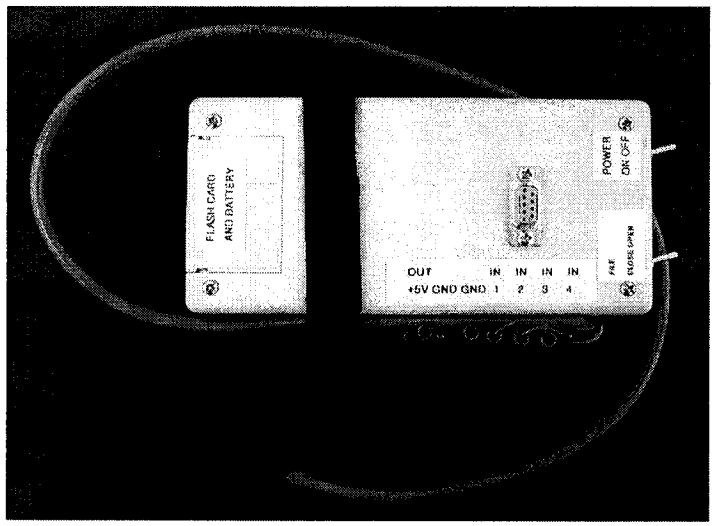

Figure 2.12: Portable Data Logger.

2.5 SUBJECTIVE MEASUREMENTS

In order to carry out the subjective assessment of the rider's comfort and controllability, the test subjects were asked to provide ratings on a series of different questions. The questions were assembled to emphasize on rider's subjective sensation of the rumble strip configurations. After riding each set of three trials over designated rumble strip configuration and speed, the subjects rated every question on the scale from 1 to 10. The scale was set up in a way that, the smoothest riding sensation, as if riding on a flat pavement, was denoted as 1, and the roughest riding sensation, under which the subject would not be able to continue riding the bicycle, as 10. All of the questions were organized in a questionnaire, which contained two different parts. The first part emphasized the subject's sensation of riding comfort, while the second part contained questions on the subject's sensation of controllability. Each question was followed by a brief explanation to ensure that the rating is given in relation to the sensation experienced while riding on the flat pavement.

The questions regarding bicycle riding comfort level were set up in a way to address sensation of comfort of different body parts as well as the overall riding comfort level. The selection of the body parts, on which subjects provided comfort ratings, was based on the study by Christiaans et al. (1998), which identifies the most affected body segments, such as wrist, fingers, elbow, back, bottom and knees. Since there have been reports about cyclist's fear of damaging their bicycles, while riding over the rumble strips (Outcalt, 2001), an additional question was added to this group of questions with an intention to examine rider's subjective sensation of danger that rumble strips are imposing to the their bicycles. It was felt that this issue is also very important from the traffic safety point of view, since it might provide a better understanding of cyclist's willingness to ride over the rumble strips. A total of six questions regarding the riding comfort level, were assembled for subjects to provide rating of:

- Overall comfort

  Rate overall ride comfort level on the scale from one to ten, where one is a comfort level of riding on a flat pavement and ten is a comfort level which would relate to conditions where it would not be possible to continue to ride the bicycle.

- Comfort in the area of arms and hands

  Rate comfort level in the wrist, fingers and elbows on a scale from one to ten, where one is a comfort level of riding on a flat pavement and ten relates to extremely uncomfortable ride where you would not be able to hold on to the handle bar.

- Comfort in the area of neck and shoulders

  Rate comfort in the area of neck and shoulders on a scale from one to ten, where one is a comfort level of riding on a flat pavement and ten relates to comfort level where it would not be possible to continue to ride the bicycle.

- Comfort in the back and spine

  Rate comfort in the area of back and spine on a scale from one to ten, where one is a comfort level of riding on a flat pavement and ten refers to excessive spine loading that would not permit you to continue to ride the bicycle.

- Comfort in the seat area

  Rate comfort in seat area on a scale from one to ten, where one is a comfort level of riding on a flat pavement and ten is the most uncomfortable level which would make it impossible to ride the bicycle.

- Potential damage to bicycle

  Rate level of danger for damaging the bicycle on a scale from one to ten, where one would be no danger, as if riding on flat pavement and ten would refer to the risk of severely damaging the bicycle.

In most of the previous studies (Gardet, 1997; Ardekani et al., 1996; Meuer, 1999; Elefteriadou at al., 2000; Outcalt, 2001), the overall controllability was subjectively assessed. The controllability of the rider, however, is a complex function of many factors, such as foot pressure constancy, ability to pedal with sufficient force, ability to hold the handle bar firmly, and perform corrective steering (Outcalt, 2001). The second part of the questionnaire was thus formulated to include following four questions:

- Overall controllability rating

  Rate overall controllability level (difficulty to control)on a scale from one to ten, where one is a controllability level of riding on a flat pavement and ten refers to extreme difficulty in guiding the bicycle, which would make the riding too dangerous.

- Ability to retain feet on the pedals

  Rate ability to keep feet on the pedals due to vibrations felt in the area of feet and knees on a scale from one to ten, where one represents a constant contact between feet and the pedals and ten would be a absolute lack of ability to keep feet on the pedals during the ride.

- Ability to see straight

  Rate ability to see straight and guide the bicycle on a scale from one to ten, where one is no influence to vision and guidance ability and ten refers to riding condition under which subject's vision is blurred and ability to guide diminishes.

- Ability to keep balance

  Rate ability to keep balance on a scale from one to ten, where one represents an ability to keep balance as if riding on a flat pavement and ten relates to condition under which subject would lose ability to balance and fall-off the bicycle.

2.6 SUMMARY

The measurement methods and data collection process during the rumble strip tests are described in this chapter. The tests included both the objective and subjective assessment of the rumble strips for the rider's comfort and controllability. The test methodology is described in details and the technical details concerning the test bicycle and the instrumentation are presented. The analysis of the collected data is conducted in the following chapter.

CHAPTER 3

ANALYSIS OF THE RUMBLE STRIP TEST DATA

3.1 INTRODUCTION

The data collected during the rumble strips tests, described in Chapter 2, need to be analyzed to derive measures that would provide the vital knowledge for design of bicycle-friendly rumble strips. The measured data are thus analyzed to quantify the amount of the vibrations experienced by the rider while traversing the rumble strips, and to examine the subjective sensation of the ride and controllability of the bicycle. In general, the purpose of the data analysis is to examine certain aspects of the measured data that are of particular interest. The traditional way of analyzing a dynamic signal is by observing its magnitudes in time, which can effectively describe the variations in a performance measure under the conditions or parameters considered. The bicycle's interactions with rough road surfaces or rumble strips would yield random vibration signal, which can be analyzed to determine the amplitude and frequency compositions of its acceleration time-history. The acceleration amplitude is the characteristic which describes the severity of the vibration exposure (Griffin, 1996). Human perception of vibrations is invariably assessed in terms of the magnitude of acceleration, expressed in terms of root mean square (RMS) values, and spectral contents (ISO-2631, 1997; Griffin 1996). The reported studies on assessment of bicycle interaction with rumble strips also consider RMS accelerations along the vertical and pitch axis to assess the rider's comfort and control performances (Elefteriadou et al., 2000; Outcalt, 2001). The peak values of

accelerations may also be considered to assess the severity of vibrations under repetitive or intermittent interactions with rumble strips.

3.2 METHODS OF DATA ANALYSIS

During the rumble strip tests, the accelerations of the bicycle frame were measured using two acceleration transducers attached to the handle bar, and the seat post, both oriented vertically upwards (Figure 3.1). The pitch acceleration response of the bicycle frame was derived from the measured vertical accelerations using the kinematics relations and assuming small angular motions:

$$\ddot{\theta} = \frac{\ddot{z}_h - \ddot{z}_s}{L_t} \tag{3.1}$$

where $\ddot{z}_h$ and $\ddot{z}_s$ are the vertical accelerations measured at the handle bar and the seat post, respectively, L_t is the horizontal distance between the two transducers, and $\ddot{\theta}$ is the pitch acceleration of bicycle frame.

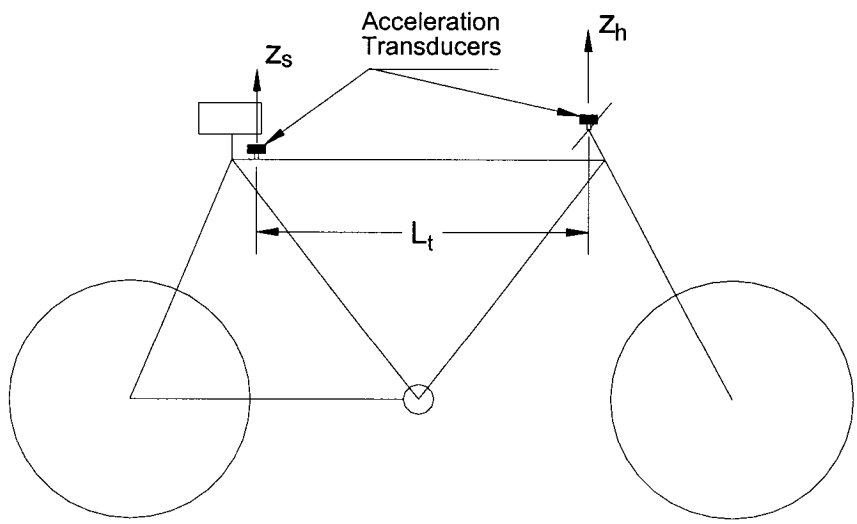

Figure 3.1: Acceleration transducers mounted on the bicycle.

The Root-Mean-Square (RMS) value of acceleration has been widely used to assess the magnitudes of transmitted vibrations in automobiles and machine structures (Wong, 1993), which directly relate to the energy content of the vibration. Several experimental studies have shown that the RMS acceleration values often provide good correlation with the subjective sensation of vibration related discomfort (Griffin, 1996). The RMS acceleration value can be computed from the measured time history in the following manner (ISO-2631, 1997):

$$a_{rms} = \left[\frac{1}{T} \int_0^T a_w^2(t) dt \right]^{1/2} \tag{3.2}$$

where a_{rms} is the RMS value of the translational or rotational acceleration in m/s^2 or rad/s^2 and T is duration of measurement. The measure based on RMS accelerations, however, tends to smoothen the contributions due to intermittent shock motion, when present in the signals. For the bicycle-rumble strip interactions considered in the study, considerable shock motions of repetitive nature would be expected, which are known to cause far more discomfort and control difficulties. For analysis of vibration signals comprising either intermittent or repetitive shock motion, the International Standard (ISO-2631, 1997) on assessment of human response to vibration recommends the use of Vibration Dose Value (VDV). The VDV measure tends to emphasize the contributions due to intermittent peaks by considering the fourth power of the acceleration, such that:

$$VDV = \left[\int_0^T [a_w^4(t)] dt \right]^{1/4} \tag{3.3}$$

where VDV is expressed in $m/s^{1.75}$ or $rad/s^{1.75}$.

The peak value of the measured acceleration signal may also be considered to assess the severity of vibration associated with short duration shocks. The data acquired for each bicycle, rider, strip and speed combination, are thus analyzed to derive the following for the seat post and handle bar vertical accelerations, and bicycle pitch acceleration:

- Power spectral density of the measured signal to identify dominant frequencies of vibration, and the frequency range of predominant vibration.
- Overall RMS accelerations to assess the relative roles of bicycle, strip configuration and operating conditions.
- RMS acceleration spectra in the 1/3 - octave frequency bend to identify the important frequency bands.

Apart from the measured acceleration signals, the yaw oscillations (ψ) of the handle bar are analyzed to study the bicycles tendency to deviate from the desired path coupled with rider's effort to guide the bicycle along the desired path.

3.3 INTER-SUBJECT VARIABILITY

The dynamic responses of the bicycle and its interactions with the rumble strips are strongly dependent upon many factors, such as rumble strip pattern, and seat post and bicycle suspension. Apart from these, the responses would be strongly influenced by many individual factors, such as subjects' mass, height, build and general physical fitness, as it has been reported in many studies on human responses to vibration (Griffin, 1996; Lundstrom and Holmlund, 1998; Paddan and Griffin, 1998). The riding styles and postures assumed during a trial may further affect the nature of the responses. Owing to

the strong effect of various rider factor, the measured data are expected to reveal significant inter and intra-subject variabilities. A higher degree of inter-subject variability would be expected due to considerably different riding skills of the selected test subjects.

The measured data acquired for seven subjects, riding the Touring and Hybrid bicycles on selected strip configuration are analyzed to examine the inter-subject variability of the data. The subjects invariably found that riding the strips, Round II, III, and IV, was extremely demanding and unsafe, while the rectangular strips provided a very smooth ride comparable to the flat pavement. The experiments on these strips were thus discontinued after the trials with only 2 subjects. The analysis of the inter-subject variability is thus limited to flat pavement and "Round I" pattern. The data acquired during each trial are analyzed to derive RMS accelerations in the 1/3-octave frequency band. The data attained for three trials involving each bicycle, pattern and speed combination are averaged to describe the mean responses for each subject. The mean and standard deviations of accelerations in each 1/3-octave band are than evaluated on the basis of mean data obtained for the seven subjects. Figures 3.2 and 3.3 illustrate the mean RMS spectra of the Touring and Hybrid bicycles responses, while riding on the flat pavement. The figures illustrate the mean spectra of vertical accelerations measured on the seat post ($\ddot{z}_s$) and the handle bar ($\ddot{z}_h$) together with the standardized deviations, corresponding to three test speeds.

The results show high magnitudes of accelerations in the 12.5 to 50 Hz bends for the Touring bicycle, and in the 10 to 40 Hz bands for the Hybrid bicycle, irrespective of the speed. The handle bar acceleration response for the Touring bicycle reveals peaks in the 16 to 20 Hz and 31.5 to 50 Hz bands, which may be attributed to the vertical and

pitch frequencies of the bicycle. For the Hybrid bicycle, these peaks are observed near 16 and 31.5 Hz for all three speeds. The RMS acceleration levels tend to increase with increasing vehicle speed for both the bicycles. The results further show considerable standard deviations of the means, specifically in the frequency bands, where the vibration levels tend to be high. The coefficients of variation for both bicycles correspond to each 1/3-octave band are summarized in Tables 3.1 and 3.2, respectively, for all three speeds.

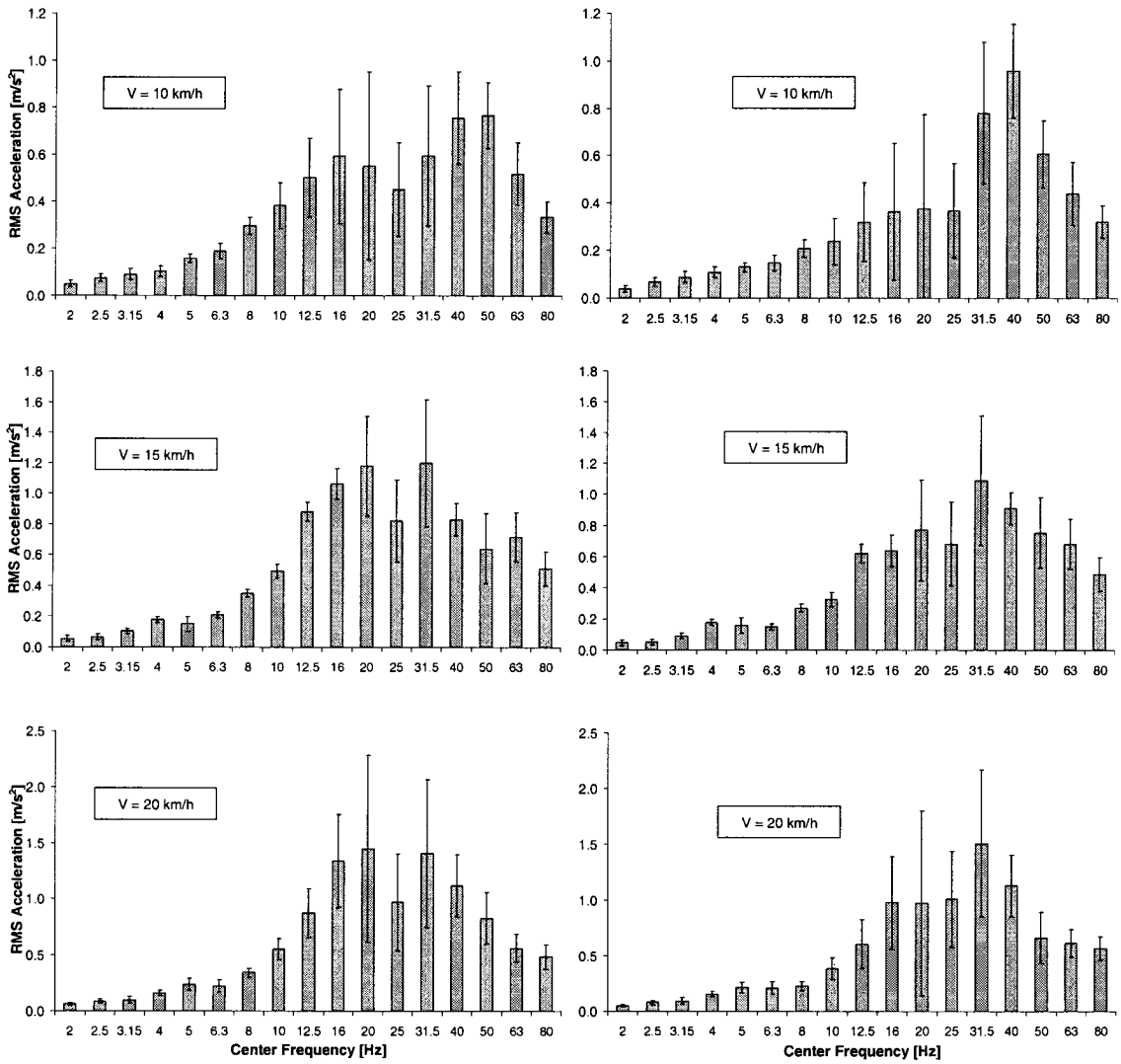

(a) Handle bar acceleration

(b) Seat post acceleration

Figure 3.2: Mean and standard deviation of the (a) handle bar and (b) seat post RMS vertical acceleration in 1/3-octave frequency bands (bicycle: Touring; pattern: Flat).

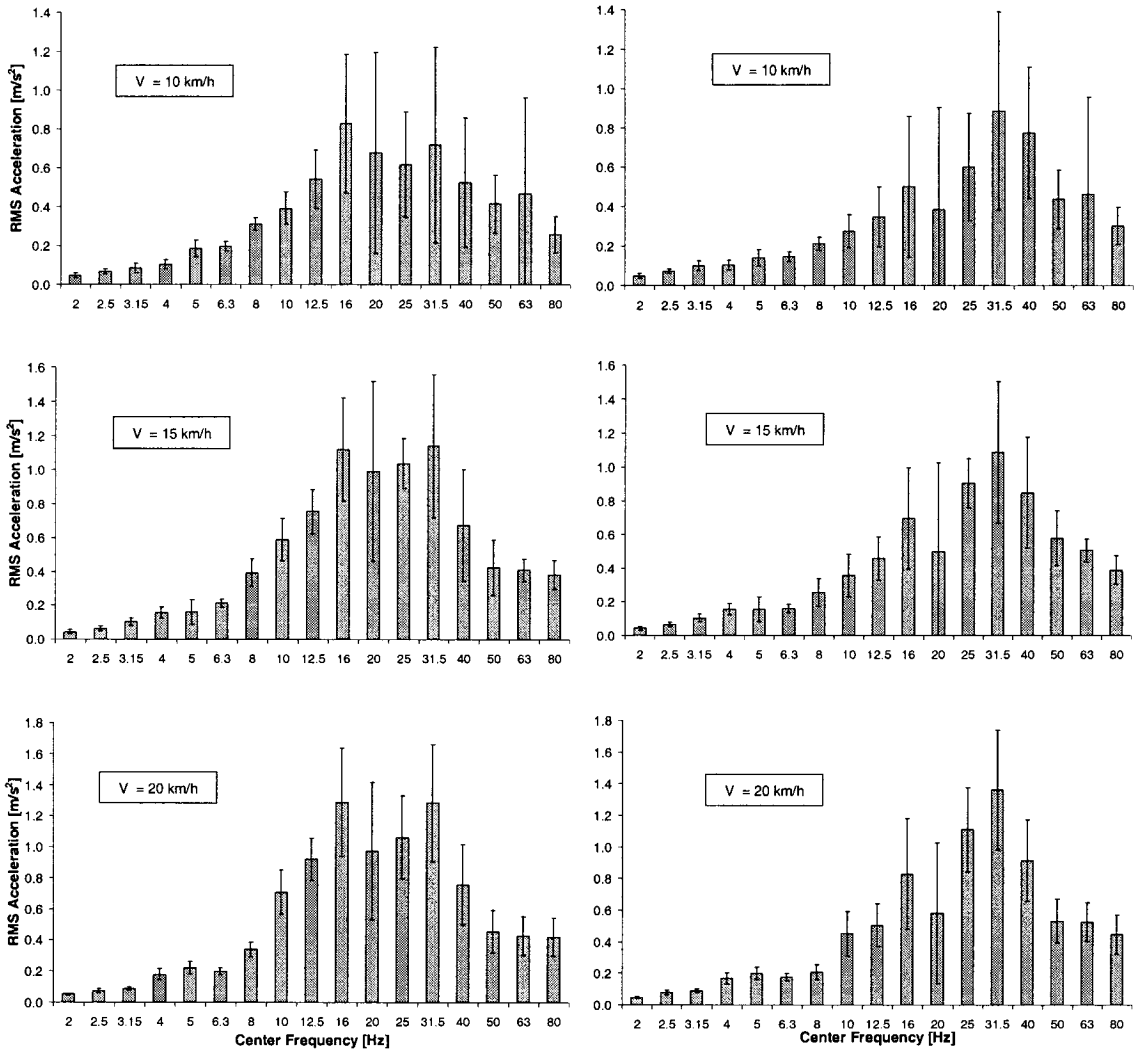

(a) Handle bar acceleration

(b) Seat post acceleration

Figure 3.3: Mean and standard deviation of the (a) handle bar and (b) seat post RMS vertical acceleration in 1/3-octave frequency bands (bicycle: Hybrid; pattern: Flat).

The coefficients of variation, considered as measures of the inter-subject variability, tend to be highest in the 20 Hz band for the Touring bicycle at speeds of 10 and 20 km/h. The peak variations at 15 km/h tend to occur in the 1.6 to 2.5 Hz and 20 to 31.5 Hz bands. For the Hybrid bicycle, the peak variabilities occur in the 20 Hz band, irrespective of the speed and location of measurement. The results also show significant variabilities in the 2.5 to 4 Hz bands, which is most likely attributed to the whole body

vibration modes of the rider. The inter-subject variability for riding speed of 15 km/h appears to be the lowest, while the highest variability occurs for speed of 20 km/h.

Table 3.1: Inter-subject variability corresponding to each third octave band (Touring Bicycle; Pattern: Flat).

Coefficient of Variation [%]						
Central Frequency [Hz]	Handle Bar			Seat Post		
	10 km/h	15 km/h	20 km/h	10 km/h	15 km/h	20 km/h
0.5	13.0	19.9	22.0	15.7	16.4	17.2
0.6	23.8	12.2	29.1	23.1	13.3	22.0
0.8	27.3	25.2	20.2	24.9	11.2	25.4
1.0	25.9	32.5	15.4	20.7	25.3	18.1
1.3	27.9	27.3	28.2	14.7	21.4	14.7
1.6	29.6	35.7	32.6	17.4	26.1	27.4
2.0	27.7	31.9	17.4	15.1	21.7	22.0
2.5	23.1	28.0	21.9	14.8	30.7	28.0
3.2	26.8	16.5	31.9	19.7	13.8	45.3
4.0	21.9	11.0	15.3	16.6	11.6	11.8
5.0	11.9	32.7	21.4	16.0	31.6	12.4
6.3	17.6	10.0	25.1	25.4	12.7	23.6
8.0	12.6	7.0	11.3	19.5	5.7	13.5
10.0	25.7	9.0	17.1	40.3	15.5	18.9
12.5	33.4	7.0	24.8	40.8	9.2	28.2
16.0	48.7	9.6	31.0	45.9	18.3	25.6
20.0	72.4	27.5	57.6	60.0	23.5	60.1
25.0	44.4	32.6	44.3	37.2	26.0	38.3
31.5	50.1	34.7	46.9	13.6	14.4	38.3
40.0	26.1	12.6	25.0	20.9	16.6	32.5
50.0	18.5	35.5	27.6	21.9	22.7	24.1
63.0	25.8	22.3	22.3	14.4	15.3	14.5
80.0	20.4	21.0	22.2	16.1	9.3	13.0
Overall RMS Acceleration	19.5	12.5	29.9	12.9	8.2	27.0

Table 3.2: Inter-subject variability corresponding to each third octave band (Hybrid bicycle; Pattern: Flat).

Coefficient of Variation [%]						
Central Frequency [Hz]	Handle Bar			Seat Post		
	10 km/h	15 km/h	20 km/h	10 km/h	15 km/h	20 km/h
0.5	37.9	20.0	19.4	40.7	9.0	23.1
0.6	41.8	18.0	30.7	38.4	14.6	29.2
0.8	35.0	23.6	19.3	33.9	17.5	21.7
1.0	33.6	17.8	19.7	33.6	17.2	24.2
1.3	30.8	15.2	18.0	36.4	24.1	21.6
1.6	32.9	37.1	15.1	31.2	20.3	15.9
2.0	27.6	26.9	10.9	23.1	11.1	12.2
2.5	19.3	23.0	18.5	13.4	24.4	18.8
3.2	28.9	22.8	11.7	51.9	29.4	19.2
4.0	23.2	21.5	19.8	17.0	19.0	14.1
5.0	22.3	46.2	17.7	28.4	37.2	18.5
6.3	12.1	11.1	11.1	22.1	17.8	16.8
8.0	10.4	20.8	13.9	18.4	19.7	7.9
10.0	21.2	21.2	20.0	26.8	31.3	18.8
12.5	27.9	17.2	14.8	30.0	13.7	13.3
16.0	43.2	26.8	27.0	52.5	31.9	19.4
20.0	76.3	53.5	45.6	58.5	40.3	31.3
25.0	44.1	14.0	25.1	42.4	19.3	22.5
31.5	69.9	36.6	29.5	32.4	23.6	23.3
40.0	63.4	48.8	34.1	24.6	26.8	26.9
50.0	36.2	38.7	30.5	29.3	9.7	18.9
63.0	105.6	16.7	29.0	73.3	12.6	16.4
80.0	36.5	22.4	29.6	47.5	28.9	21.2
Overall RMS Acceleration	28.5	13.9	34.2	25.2	11.3	31.1

Figures 3.4 and 3.5 illustrate the mean RMS acceleration responses of the two bicycles traversing rumble strip Round I at three different speeds. The results also show standard deviation of the means attained for seven subjects. The coefficients of variation corresponding to each frequency band are summarized in Tables 3.3 and 3.4, respectively, for the Touring and Hybrid bicycles. The peak responses for the Touring bicycle handle bar tend to occur in the 10 and 20 Hz bands at 10 km/h, 12.5 and 25 bands

at 15 km/h, and 20 and 40 Hz bands at 20 km/h. The results for the Hybrid bicycle show peak handle bar and seat post responses in the 20 and 40 Hz bands for 10 km/h, 25 and 40 Hz bands for 15 km/h, and 16-20 and 31.5 Hz bands for 20 km/h. These frequencies are comparable with those observed on the flat pavement for the Touring bicycle, but are lower for the Hybrid bicycle, which is most likely attributed to the suspension travel and damping.

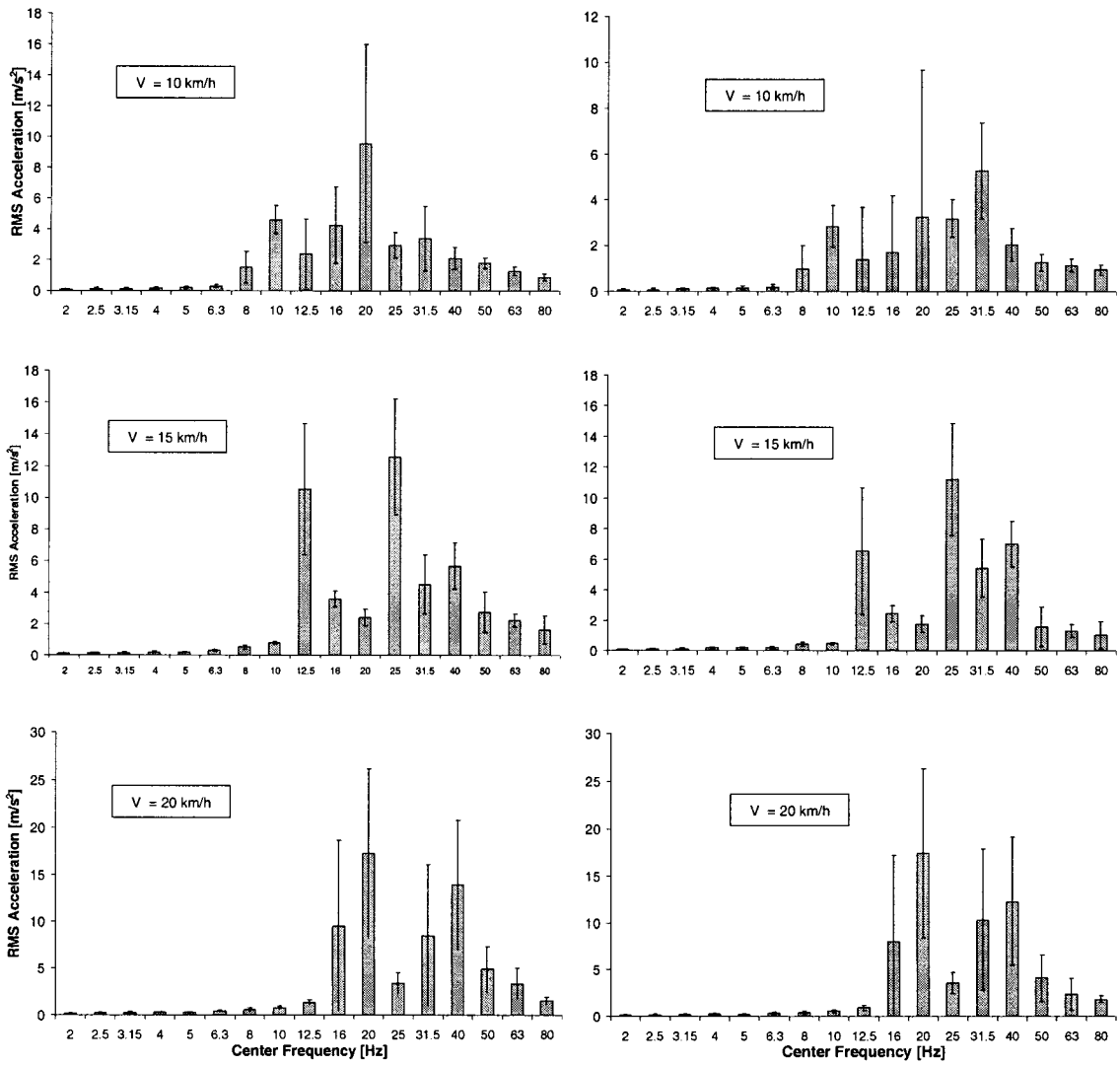

(a) Handle bar acceleration

(b) Seat post acceleration

Figure 3.4: Mean and standard deviation of the (a) handle bar and (b) seat post RMS vertical acceleration in 1/3-octave frequency bands (bicycle: Touring; pattern: Round I).

The magnitudes of vibration, however, are significantly higher for the Round I pattern, when compared to those attained for the flat pavement. The Touring bicycle tends to yield higher levels of vibration than the Hybrid bicycle, while a higher speed yields higher magnitudes of vibration. Both bicycles exhibit higher variability at lower frequencies compared to the flat asphalt pavement, while the inter-subject variability is quite high in the entire frequency range. Such variability is most likely attributed to variations in the riding skills of the subjects, as more skilled riders generally revealed lower magnitudes of vibration. Moreover, the magnitudes of vibration are observed to be considerably lower for the Hybrid bicycle, as evident in Table 3.4.

Table 3.3: Inter-subject variability corresponding to each third octave band (Touring Bicycle; Pattern: Round I).

Coefficient of Variation [%]						
Central Frequency [Hz]	Handle Bar			Seat Post		
	10 km/h	15 km/h	20 km/h	10 km/h	15 km/h	20 km/h
0.5	68.0	56.1	76.4	43.2	77.2	57.3
0.6	67.0	51.1	78.6	46.0	82.2	72.0
0.8	60.0	25.3	60.0	59.6	62.3	72.3
1.0	76.5	30.4	55.8	54.5	55.1	78.4
1.3	96.8	42.3	47.7	50.5	57.4	47.0
1.6	80.6	23.0	60.7	41.1	85.4	42.8
2.0	56.8	50.2	56.8	45.1	53.6	58.2
2.5	60.5	28.6	52.7	33.4	51.7	57.5
3.2	44.3	38.8	50.3	13.9	63.8	62.3
4.0	41.5	27.9	26.2	22.8	38.1	45.5
5.0	40.5	22.7	13.9	20.6	39.4	31.2
6.3	34.8	23.1	36.3	19.0	56.4	40.3
8.0	69.0	26.8	34.3	62.6	25.6	28.9
10.0	19.7	8.6	21.4	22.1	29.3	24.8
12.5	96.3	39.4	21.3	86.6	18.7	23.1
16.0	58.9	14.3	95.1	26.3	23.8	103.6
20.0	67.4	22.2	51.8	24.2	16.6	52.1
25.0	28.1	29.1	33.8	33.2	28.7	31.8
31.5	62.1	41.6	88.2	54.3	13.3	64.9
40.0	34.6	26.1	48.9	26.9	19.5	43.7
50.0	19.7	46.7	51.5	14.5	22.2	61.0
63.0	20.6	18.6	50.0	14.3	14.4	46.6
80.0	25.7	54.8	22.9	15.9	11.1	18.3
Overall RMS Acceleration	28.4	9.1	22.4	23.3	20.1	25.7

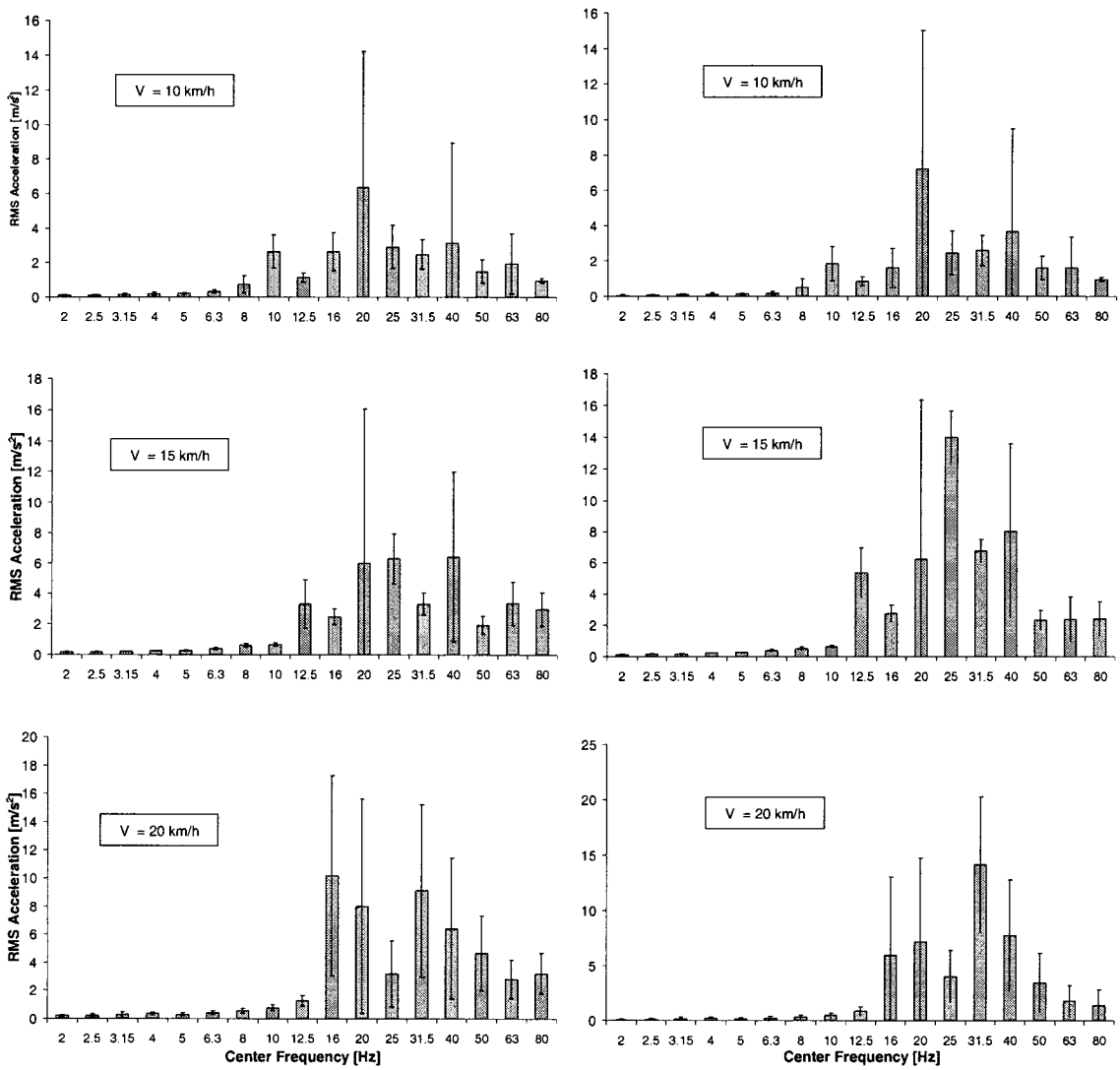

(a) Handle bar acceleration

(b) Seat post acceleration

Figure 3.5: Mean and standard deviation of the (a) handle bar and (b) seat post RMS vertical acceleration in 1/3-octave frequency bands (bicycle: Hybrid; pattern: Round I).

The measured responses of the yaw angle are analyzed to examine the inter-subject variability of the measured data in term of rider's handling performance. The analyses are performed for every combination of bicycle, speed and selected strip pattern. The mean responses derived from three trials for each subject are applied to compute the mean response and standard deviation for seven subjects. The results are expressed in terms of coefficients of variation in Table 3.5 for every combination of bicycle, speed and

selected pattern (Flat and Round I). The results indicate lower degree of inter-subject variability for the rumble strip than for the flat pavement. It can possibly be attributed to the absence of target path for guidance control when traveling on the flat pavement, as the rider followed an imaginary straight line. The riding on the rumble strip, on the other hand, required the rider to follow the defined path of the rumble strip. The Touring bicycle exhibits less variability on the flat pavement at all three speeds, while on the rumble strip the Hybrid bicycle shows leer variability for speeds of 10 and 15 km/h.

Table 3.4: Inter-subject variability corresponding to each third octave band (Hybrid bicycle; Pattern: Round I).

Coefficient of Variation [%]						
Central	Handle Bar			Seat Post		
Frequency [Hz]	10 km/h	15 km/h	20 km/h	10 km/h	15 km/h	20 km/h
0.5	84.5	26.8	42.3	75.9	110.8	45.4
0.6	61.9	23.4	44.6	84.0	128.5	20.9
0.8	56.6	24.7	33.5	73.5	129.2	20.0
1.0	64.0	42.4	31.7	75.0	144.6	35.6
1.3	56.0	38.3	32.8	54.4	143.2	41.7
1.6	44.1	34.3	46.1	31.7	118.8	32.1
2.0	57.7	27.1	36.2	47.9	85.5	24.4
2.5	35.2	13.0	43.9	40.3	91.1	15.9
3.2	40.2	15.9	63.3	28.9	88.8	80.7
4.0	50.9	10.9	32.0	21.5	78.8	39.2
5.0	27.4	11.9	35.2	23.9	106.2	27.1
6.3	36.8	19.1	27.4	27.7	126.3	36.3
8.0	67.6	21.7	30.7	64.2	76.3	26.7
10.0	36.5	15.7	29.6	37.3	63.4	16.4
12.5	22.5	48.0	29.8	34.5	92.5	29.5
16.0	41.9	21.2	69.7	59.6	71.4	90.0
20.0	123.9	169.1	95.1	103.4	159.8	115.1
25.0	43.2	26.1	73.8	44.6	47.4	62.8
31.5	34.6	22.2	67.3	51.1	45.1	48.3
40.0	184.8	86.7	78.5	135.1	76.6	56.4
50.0	45.1	30.3	57.7	41.6	76.2	55.2
63.0	90.9	42.4	49.0	35.9	64.7	35.1
80.0	12.3	37.0	45.5	36.6	95.7	18.8
Overall RMS Acceleration	15.4	17.2	12.6	9.5	9.5	31.0

Table 3.5: Inter-subject variability in the handle bar yaw angle response.

Coefficient of Variation [%]						
Test Bicycle	Touring			Hybrid		
Speed	10 km/h	15 km/h	20 km/h	10 km/h	15 km/h	20 km/h
Flat pavement	32.9	40.7	37.8	55.0	47.1	63.8
Round I pattern	22.9	23.5	17.4	8.7	7.0	22.7

3.4 INTRA-SUBJECT VARIABILITY

The measured data acquired for the seven subjects, riding the Touring and Hybrid bicycles on rumble strip configuration Round I, are analyzed to examine the intra-subject variability of the data. The analyses of the measured data are performed for each bicycle and speed combination to derive the overall RMS acceleration and RMS yaw angle. The data attained for each subject performing three trials on each bicycle, and speed combination are averaged to describe the mean responses and standard deviation for each subject. Tables 3.6 to 3.8 summarize the mean and coefficient of variation of handle bar and seat post RMS acceleration, and yaw angle, respectively, attained for seven subjects. The results show that majority of the riders exhibit less variability with the Hybrid bicycle for all three speeds. Subject number one, whose riding skill is classified as experienced bicycle rider exhibits least variability in the handle bar and seat post acceleration with the Hybrid bicycle. The same subject revealed higher variability in yaw angle oscillations, which can be attributed to extensive steering in order to stay on the narrow rumble strip (300 mm). Subject number two on the Touring bicycle shows the highest level of variability for both the vertical acceleration and the yaw angle

oscillations at speeds of 10 and 20 km/h. The intra-subject variability for riding speed of 15 km/h appears to be the highest with both bicycles compared to the inter-subject variability which is the lowest for the same speed, as described in section 3.3.

Table 3.6: Mean RMS handle bar acceleration and coefficient of variation of the trials undertaken with each subject and particular combination of speed and bicycle.

Mean Handle Bar RMS Acceleration in m/s^2 (% CV)							
Subject	1	2	3	4	5	6	7
Speed (km/h)	Touring bicycle						
10	9.8 (7.6)	14.8 (81.9)	20.7 (6.6)	21.2 (3.7)	12.5 (2.3)	15.2 (8.1)	12.1 (9.7)
15	-	-	25.9 (7.7)	22.3 (39.0)	21.8 (6.9)	19.6 (2.5)	22.2 (8.0)
20	15.6 (13.3)	21.8 (54.6)	27.3 (10.3)	27.6 (14.3)	32.2 (0.7)	28.2 (3.3)	32.1 (0.8)
	Hybrid bicycle						
10	5.7 (4.0)	5.6 (4.9)	8.2 (10.1)	7.9 (4.2)	7.2 (5.2)	8.2 (9.1)	7.4 (3.5)
15	-	-	15.6 (13.3)	11.5 (17.2)	12.3 (5.5)	10.3 (15.1)	10.8 (6.8)
20	17.0 (4.3)	17.5 (8.5)	21.9 (4.2)	16.3 (3.6)	21.2 (7.0)	20.9 (5.5)	17.1 (6.1)

Table 3.7: Mean RMS seat post acceleration and coefficient of variation of the trials undertaken with each subject and particular combination of speed and bicycle.

Mean Seat Post RMS Acceleration in m/s^2 (% CV)							
Subject	1	2	3	4	5	6	7
Speed (km/h)	Touring bicycle						
10	9.3 (4.2)	13.1 (96.0)	9.7 (10.2)	14.1 (12.0)	10.3 (5.0)	9.1 (16.5)	7.2 (4.7)
15	-	-	17.8 (7.9)	23.6 (15.8)	16.0 (2.7)	15.2 (8.7)	15.2 (5.5)
20	18.3 (12.1)	15.7 (56.3)	27.7 (11.5)	35.4 (7.6)	26.8 (16.8)	26.0 (0.6)	27.7 (4.6)
	Hybrid bicycle						
10	6.5 (0.3)	6.9 (5.1)	8.2 (13.7)	7.7 (7.0)	6.6 (11.6)	6.5 (8.1)	7.4 (4.7)
15	-	-	18.3 (12.1)	18.7 (17.9)	15.1 (7.4)	15.8 (12.2)	18.0 (8.5)
20	16.9 (2.3)	17.2 (12.1)	22.9 (0.6)	23.16 (2.8)	21.9 (2.9)	23.0 (2.3)	23.5 (3.1)

Table 3.8: Mean RMS yaw angle and coefficient of variation of the trials undertaken with each subject and particular combination of speed and bicycle.

Mean Yaw Angle RMS Acceleration in rad(10^{-3}) (% CV)							
Subject	1	2	3	4	5	6	7
Speed (km/h)	Touring bicycle						
10	30.6 (11.7)	35.8 (33.6)	47.7 (13.6)	58.9 (10.9)	44.8 (10.0)	44.8 (2.5)	32.4 (7.7)
15	-	-	32.8 (9.6)	49.6 (22.4)	29.4 (15.9)	39.8 (7.4)	29.8 (7.5)
20	39.2 (17.1)	33.1 (28.0)	27.5 (10.9)	40.6 (29.8)	35.9 (2.6)	34.3 (4.5)	26.1 (4.7)
	Hybrid bicycle						
10	46.4 (15.3)	48.3 (11.2)	51.4 (9.4)	53.1 (9.8)	48.5 (6.9)	58.5 (13.1)	44.1 (28.1)
15	-	-	39.2 (17.2)	37.2 (11.6)	38.2 (1.4)	37.3 (16.4)	32.5 (7.7)
20	35.2 (29.4)	23.6 (7.8)	41.8 (15.0)	42.2 (17.4)	28.8 (32.3)	33.2 (7.8)	25.8(18.2)

3.5 RESPONSES TO INTERACTION WITH FLAT PAVEMENT

The measured data attained during operations of the bicycle on a flat asphalt pavement is initially analyzed to study the response characteristics of the coupled bicycle-rider system as functions of forward speed. The results are examined to identify some important insight into dynamic properties of the system in terms of its frequency components and amplitudes. The vertical accelerations measured at the handle bar ($\ddot{z}_h$) and seat post ($\ddot{z}_s$) are expressed in terms of their power spectral densities for the Touring and Hybrid bicycles, as illustrated in Figures 3.6 and 3.7, respectively. The figures show the PSD of accelerations attained for all seven subjects corresponding to two different speeds, 10 km/h and 20 km/h. Figures 3.8 and 3.9 present mean PSD acceleration responses for all seven subjects along with the standard deviations for the Touring and Hybrid bicycles, respectively. The results also show PSD of pitch acceleration of the bicycle frame, as derived from Equation (3.1).

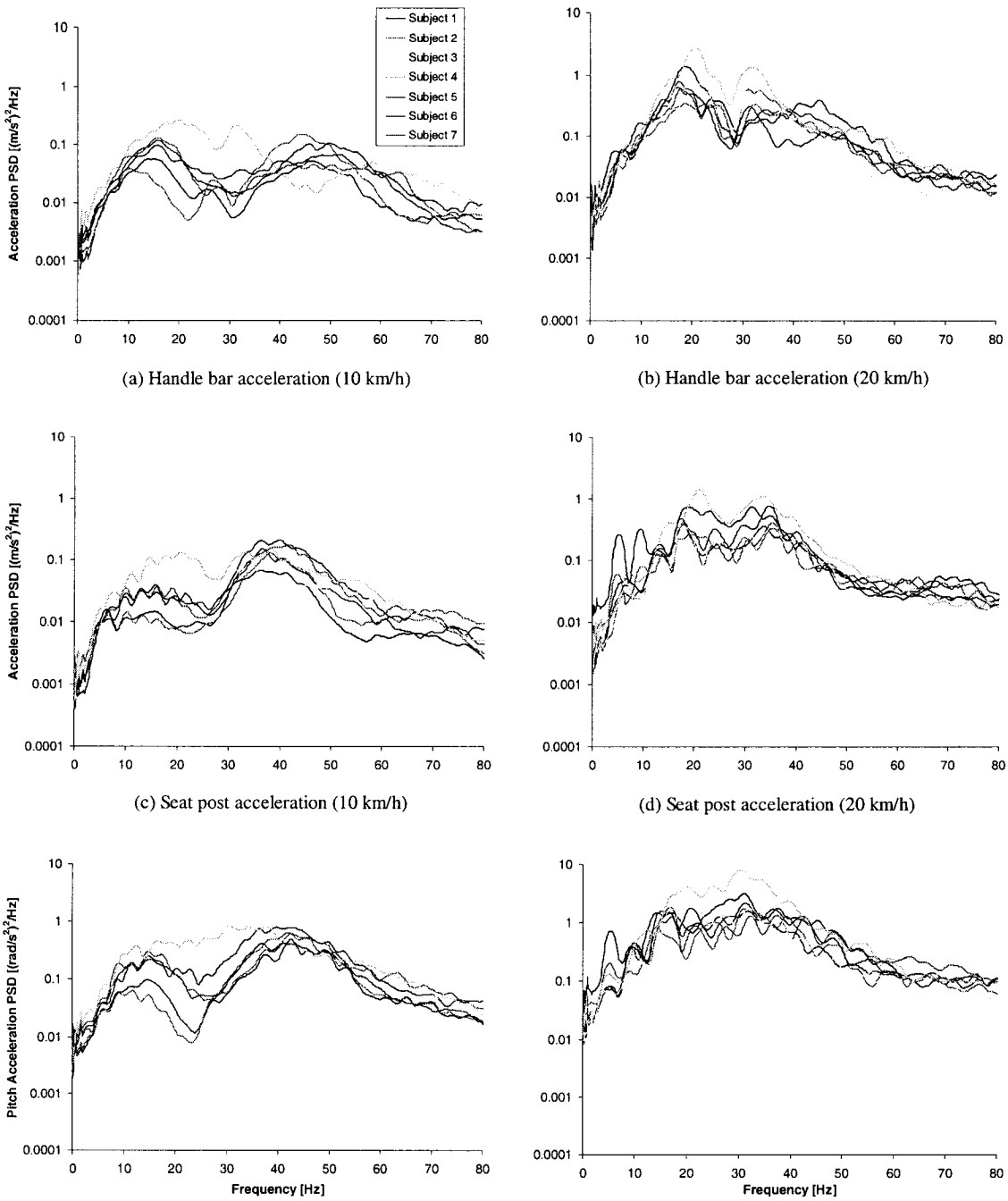

(a) Handle bar acceleration (10 km/h)

(b) Handle bar acceleration (20 km/h)

(c) Seat post acceleration (10 km/h)

(d) Seat post acceleration (20 km/h)

(e) Pitch acceleration (10 km/h)

(f) Pitch acceleration (20 km/h)

Figure 3.6: Comparison of vertical and pitch acceleration PSD spectra of the Touring bicycle attained with seven subjects (Speeds: 10 and 20 km/h; Pattern: Flat).

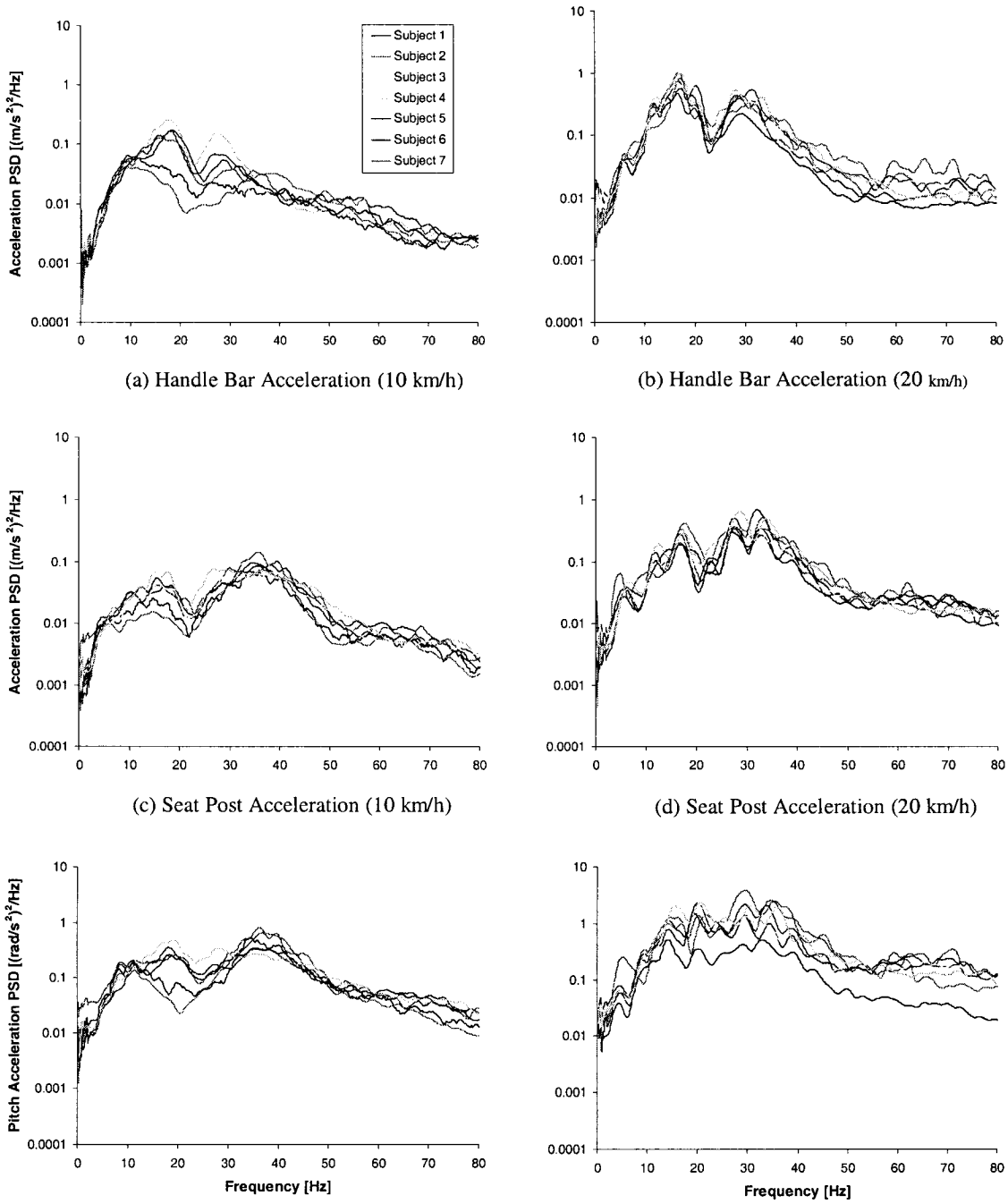

(a) Handle Bar Acceleration (10 km/h)

(b) Handle Bar Acceleration (20 km/h)

(c) Seat Post Acceleration (10 km/h)

(d) Seat Post Acceleration (20 km/h)

(e) Pitch Acceleration (10 km/h)

(f) Pitch Acceleration (20 km/h)

Figure 3.7: Comparison of vertical and pitch acceleration PSD spectra of the Hybrid bicycle attained with seven subjects (Speeds: 10 and 20 km/h; Pattern: Flat).

The figures show very similar trends for all seven subjects, in terms of the spectral components and magnitudes of acceleration PSD. Considerable variations in the

magnitudes of accelerations PSD's, however, are evident among the different subjects, which are attributed to relatively high inter-subject variabilities, as described in section 3.3. Irrespective of the riding speed, and the bicycle type, the responses show two predominant peaks in the frequency spectra of the handle bar and the seat post accelerations. The handle bar and seat accelerations tend to peak in the 12 to 15 Hz range at a speed of 10 km/h for all subjects. This frequency tends to increase slightly at the higher speed of 20 km/h and lies in the 15 to 18 Hz range. The second peak in the handle bar acceleration spectra appears to be more dependent on the type of bicycle. For the Touring bicycle at 10 km/h the second peak occurs in the vicinity of 45 Hz, except for subject number three and four where it is around 33 Hz. For the Hybrid bicycle, this second peak corresponding to 10 km/h is clustered around 27 Hz, and increases to nearly 30 Hz at 20 km/h. The Touring bicycle, on the other hand, exhibits handle bar acceleration peak in the vicinity of 30 Hz at 20 km/h.

The seat post acceleration spectra, exhibits peak in the 10 to 15 Hz (as in the case of the handle bar) and 30 to 35 Hz ranges for both bicycles and speeds. The inter-subject variations in the seat post accelerations are relatively less than those observed for the handle bar accelerations. The magnitudes of PSD of $\ddot{z}_h$ and $\ddot{z}_s$ appear to be comparable for both bicycles. In case of the Hybrid bicycle, the frequency of the second peak in the seat post acceleration spectrum shows considerable scatter. It seems to be more dependent on the test subject. An increase in the speed generally yields considerably larger levels of vertical acceleration at the handle bar and the seat post. Moreover, the inter-subject variability tends to be higher at higher speeds, which may be attributed to variations in the riding skills of subjects and individual factors (Tables 3.1 to 3.4).

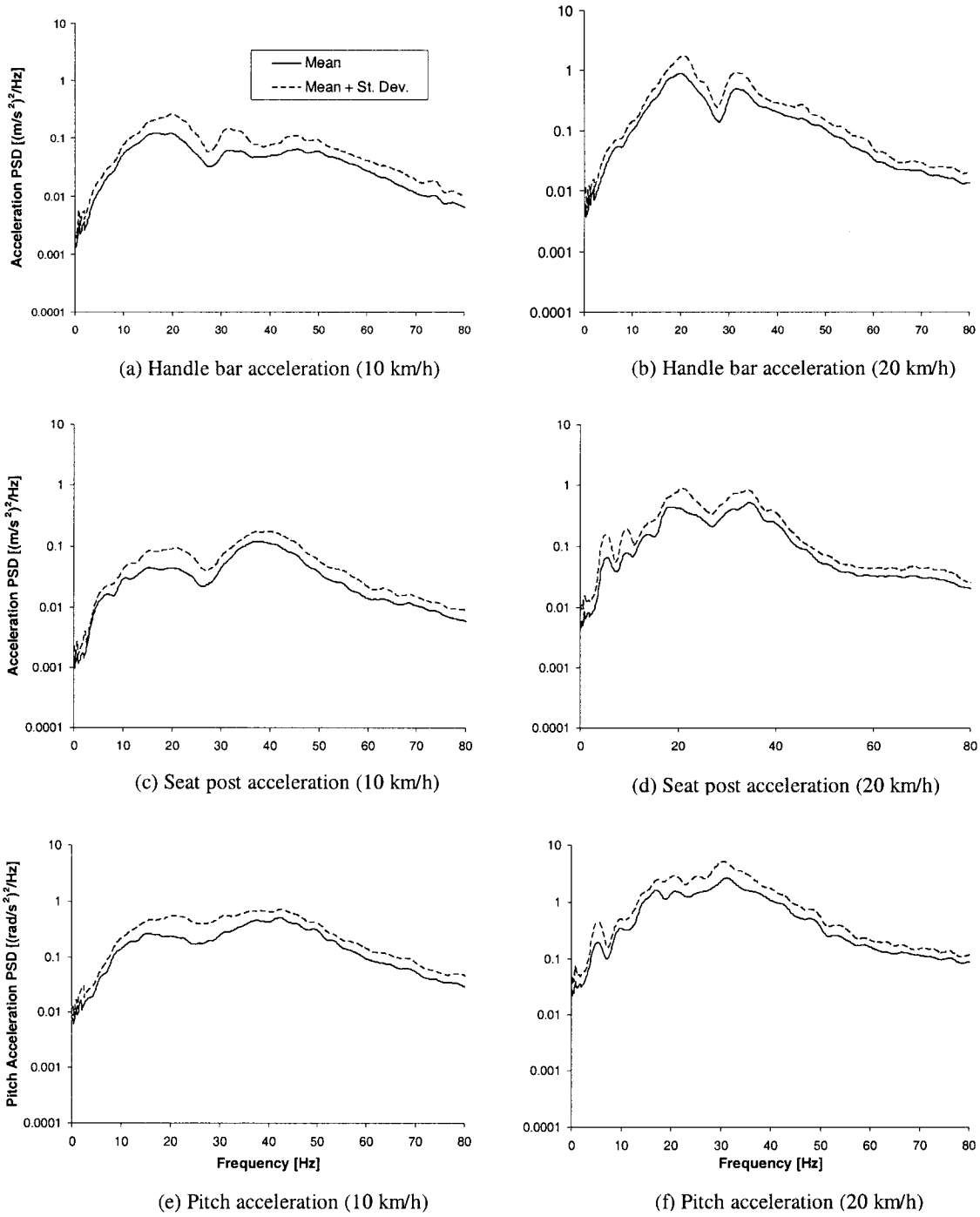

(a) Handle bar acceleration (10 km/h)

(b) Handle bar acceleration (20 km/h)

(c) Seat post acceleration (10 km/h)

(d) Seat post acceleration (20 km/h)

(e) Pitch acceleration (10 km/h)

(f) Pitch acceleration (20 km/h)

Figure 3.8: Mean and standard deviation of vertical and pitch acceleration PSD spectra of the Touring bicycle attained with seven subjects (Speeds: 10 and 20 km/h; Pattern: Flat).

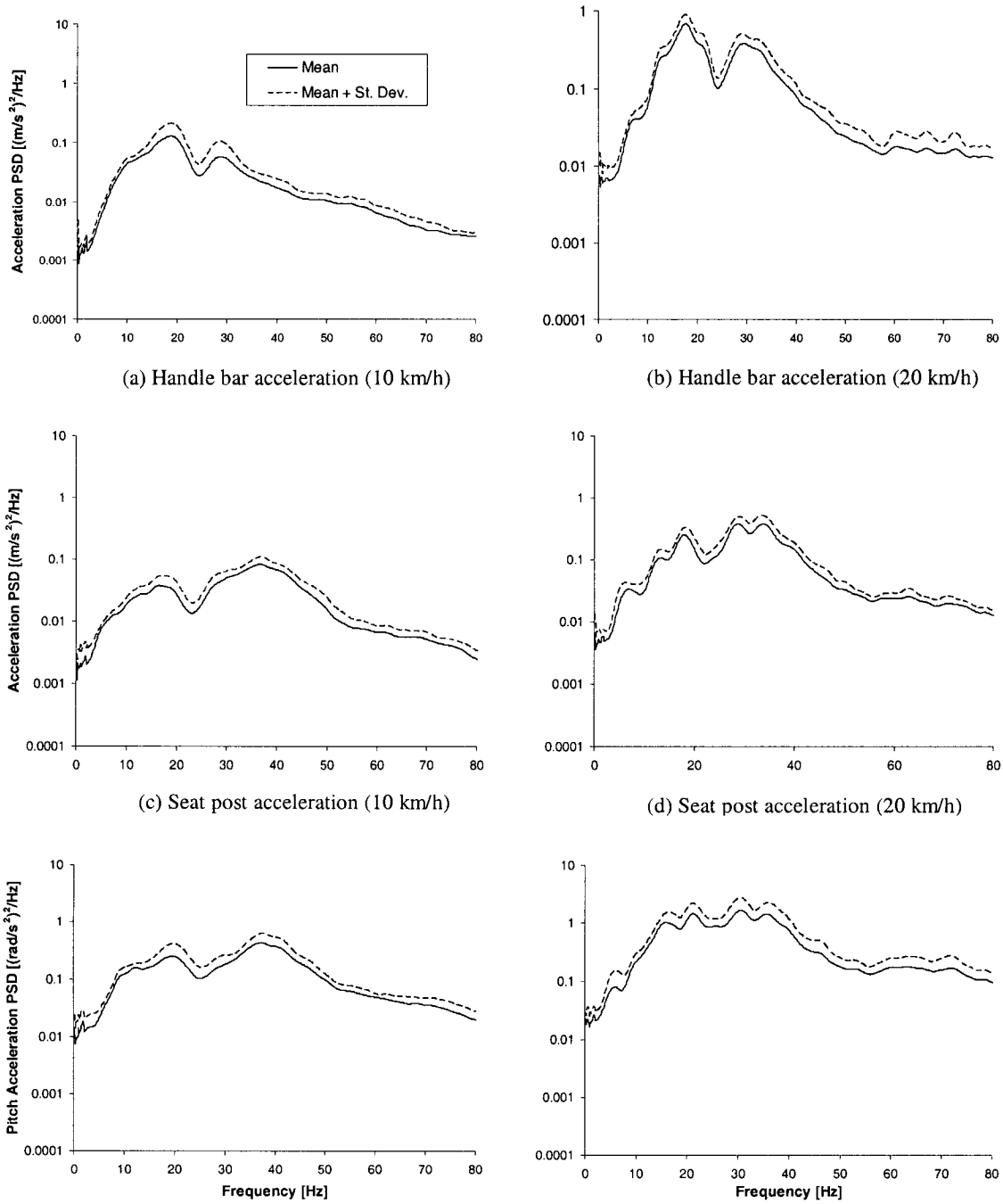

(a) Handle bar acceleration (10 km/h)

(b) Handle bar acceleration (20 km/h)

(c) Seat post acceleration (10 km/h)

(d) Seat post acceleration (20 km/h)

(e) Pitch acceleration (10 km/h)

(f) Pitch acceleration (20 km/h)

Figure 3.9: Mean and standard deviation of vertical and pitch acceleration PSD spectra of the Hybrid bicycle attained with seven subjects (Speeds: 10 and 20 km/h; Pattern: Flat).

The PSD of pitch acceleration responses of both bicycles also show two predominant peaks at a speed of 10 km/h, in the vicinity of 12 Hz and 40 Hz for the Touring bicycle, and 10 to 18 Hz and near 34 Hz for the Hybrid bicycle. The pitch acceleration PSD increases with increase in speed and reveals considerable variations in the spectrum attained for different subjects.

The time history of the measured data obtained with seven subjects are analyzed to derive overall RMS and VDV values of the acceleration, and the RMS yaw angle. The data attained for three trials involving each bicycle, pattern and speed combination, are averaged to derive the mean response for each subject. The mean data sets are than applied to derive mean and standard deviations of the mean response for seven subjects. Tables 3.9 and 3.10 summarize the mean and standard deviations of the RMS and VDV values of the vertical and pitch acceleration, and RMS yaw angle attained for seven subjects, while riding the Touring and Hybrid bicycles, respectively, on flat pavement at three different speeds.

Table 3.9: Mean and standard deviation of RMS and VDV values of vertical and pitch acceleration and RMS yaw angle of the Touring bicycle on the flat pavement.

Speed	*Measure*	*Mean and Standard Deviation*			
		Handle bar acceleration	Seat post acceleration	Pitch acceleration	Yaw angle
10 kh/h	RMS*	2.05±0.40	1.85±0.17	4.19±0.01	0.0372±0.0120
	VDV**	8.52±2.79	7.12±1.77	16.15±4.57	-
15 km/h	RMS	2.94±0.37	2.37±0.19	5.62±0.66	0.0251±0.0102
	VDV	15.39±2.02	12.24±2.03	26.88±4.53	-
20 km/h	RMS	3.86±0.85	3.29±0.66	7.49±1.74	0.0192±0.0069
	VDV	17.33±5.25	15.32±4.41	31.46±10.23	-

* in m/s^2 or rad/s^2 or rad; ** in $m/s^{1.75}$ or $rad/s^{1.75}$

Table 3.10: Mean and standard deviation of RMS and VDV values of vertical and pitch acceleration and RMS yaw angle of the Hybrid bicycle on the flat pavement.

Speed	*Measure*	*Mean and Standard Deviation*			
		Handle bar acceleration	Seat post acceleration	Pitch acceleration	Yaw angle
10 km/h	RMS*	1.87±0.34	1.76±0.26	3.91±0.66	0.0415±0.0152
	VDV**	7.34±1.78	6.03±1.39	13.84±3.06	-
15 km/h	RMS	2.77±0.39	2.32±0.26	5.42±0.79	0.0276±0.0130
	VDV	10.73±0.57	8.91±0.51	20.43±0.73	-
20 km/h	RMS	3.75±0.90	3.24±0.71	7.37±1.81	0.0240±0.0124
	VDV	13.22±1.93	12.86±2.45	28.24±4.54	-

* in m/s^2 or rad/s^2 or rad; ** in $m/s^{1.75}$ or $rad/s^{1.75}$

The results show that the Touring bicycle yields higher magnitudes of RMS vertical and pitch accelerations at all three speeds, when compared with those of the Hybrid bicycle. Lower magnitudes of RMS acceleration response of the Hybrid bicycle could be attributed to its front and seat post suspension, and its relatively softer tires. The Touring bicycle yields highest mean RMS values for the handle bar and seat post vertical accelerations (3.86 and 3.29 m/s^2), and bicycle pitch acceleration (7.49 rad/s^2) at the higher speed of 20 km/h. The corresponding acceleration values for the Hybrid bicycle are obtained as 3.75 and 3.24 m/s^2, and 7.34 rad/s^2. Irrespective of the traversing speed, both bicycles exhibit higher overall RMS acceleration at the handle bar ($\ddot{z}_h$) compared to that of the seat post ($\ddot{z}_s$).

The influence of intermittent peak acceleration responses, assessed in terms of VDV, appears to follow the same trend as the RMS with respect to the bicycle, and the speed. The VDV values, however, tend to be considerably larger than the RMS values. The Touring bicycle operating at a speed of 20 km/h yields mean VDV values of 17.33

and 15.32 m/s$^{1.75}$ for the handle bar and seat post acceleration, respectively, and 31.46 rad/s$^{1.75}$ for the pitch acceleration. The Hybrid bicycle yields lowest values of VDV at the lower speed of 10 km/h: 1.87 and 1.76 m/s$^{1.75}$ for the $\ddot{z}_h$ and $\ddot{z}_s$, respectively, and 3.91 rad/s$^{1.75}$ for $\ddot{\theta}$. The corresponding values at 20 km/h are 13.22 m/s$^{1.75}$, 12.86 m/s$^{1.75}$ and 28.24 rad/s$^{1.75}$. Comparison of the RMS as well as VDV values of the Touring and Hybrid bicycle vibration suggests that the Hybrid bicycle tends to suppress the intermittent acceleration peaks. While the RMS responses of the two bicycles are quite comparable, the VDV responses of the Hybrid bicycle are considerably lower than those of the Touring bicycle. The Hybrid bicycle, however, yields slightly larger yaw angle response.

Figures 3.10 and 3.11 illustrate the influence of riding speed on the acceleration spectra and RMS yaw responses of the Touring and Hybrid bicycles, respectively. The figures show the mean RMS spectra of the vertical and pitch accelerations, and RMS values of the handle bar yaw angle and yaw rate at speeds of 10, 15 and 20 km/h. The results clearly show higher magnitudes of vertical and pitch acceleration at higher speeds in most of the frequency range, for both the Touring and Hybrid bicycles. These results confirm the trends in overall RMS and VDV of the accelerations, presented in Tables 3.9 and 3.10, respectively. The effect of speed is more evident in the vicinity of the peak responses, which occur in the 18 to 20 Hz band and near 33 Hz for the Touring bicycle. The vertical and pitch acceleration PSD responses of the Hybrid bicycle also show similar effect of speed, where the peak responses occur in the 16 to 20 Hz and 30 to 40 Hz ranges. The results also reveal vertical and pitch acceleration peaks around 5 Hz, irrespective of the type of bicycle, which is most likely attributed to the human body

vibration mode. Wang and Hull (1997) reported that the rider dynamics mostly occurs at frequencies below 10 Hz.

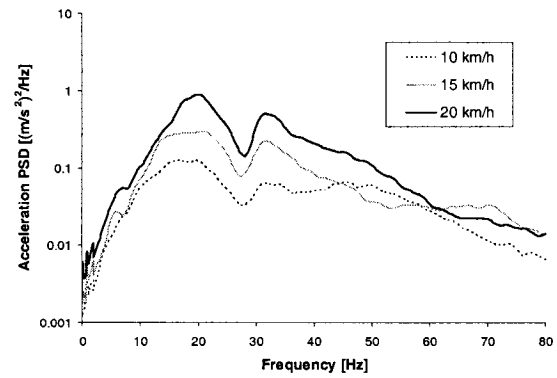

(a) Handle bar acceleration

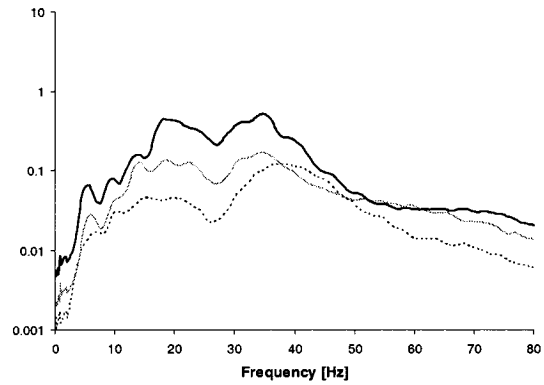

(b) Seat post acceleration

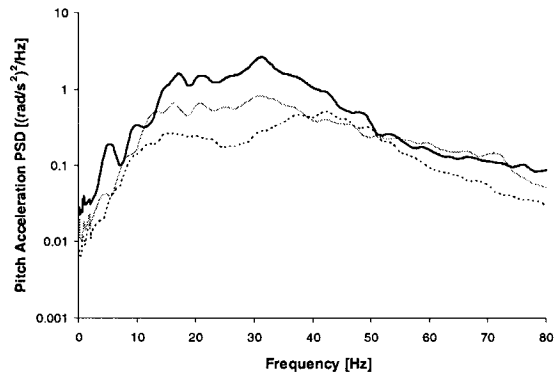

(c) Pitch acceleration

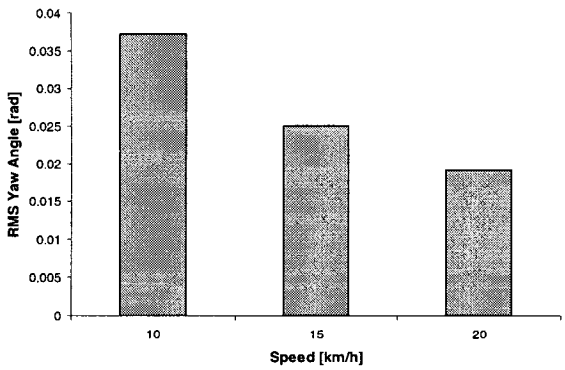

(d) Yaw angle

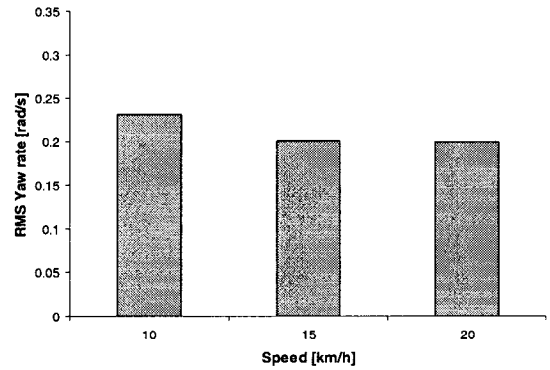

(e) Yaw rate

Figure 3.10: Comparison of mean vertical and pitch acceleration, yaw angle responses and the rate of change of the yaw angel for the Touring bicycle (Speeds: 10, 15 and 20 km/h; Pattern: Flat).

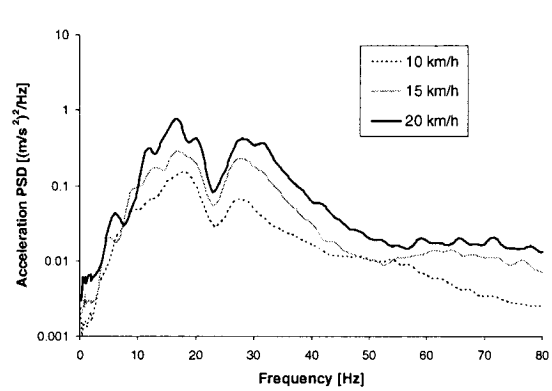

(a) Handle bar acceleration

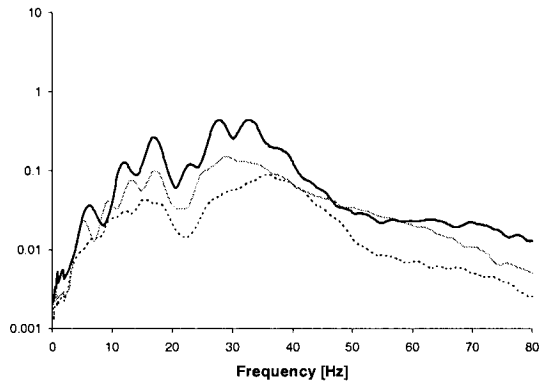

(b) Seat post acceleration

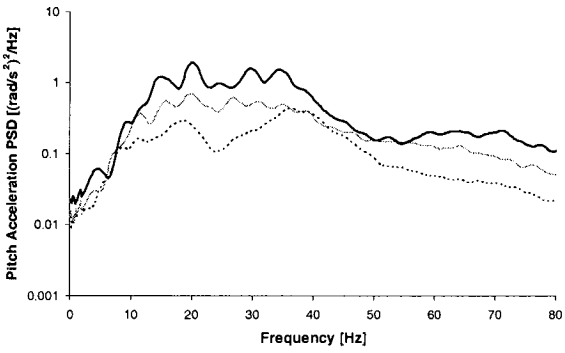

(c) Pitch acceleration

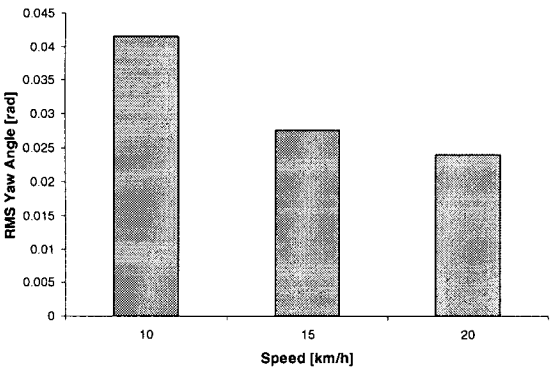

(d) Yaw angle

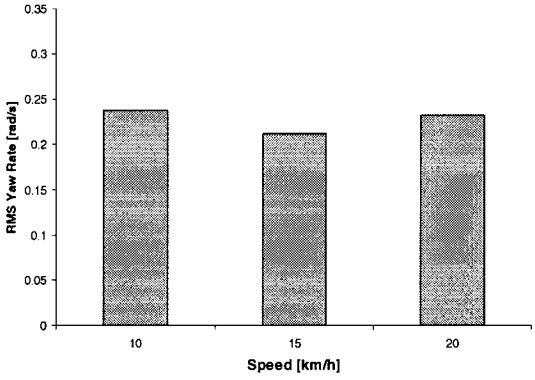

(e) Yaw rate

Figure 3.11: Comparison of mean vertical and pitch acceleration, yaw angle responses and the rate of change of the yaw angle of the Hybrid bicycle (Speeds: 10, 15 and 20 km/h; Pattern: Flat).

Contrary to the acceleration responses, the RMS yaw angle response decreases with the speed, for both bicycles. This trend is expected since the bicycle-rider system gains stability with a higher speed, which requires lesser steering effort from the rider at higher speeds. The rate of change of the yaw angle may thus be considered as a measure of the rider's steering effort. The influences of forward speed on the RMS values of the yaw angle and rates for the Touring and Hybrid bicycles are also illustrated in Figures 3.10 and 3.11, respectively. The results indicate that less intense steering is needed at higher speeds than that at the lower speed of 10 km/h, irrespective of the type of the bicycle. The yaw rate response of the Hybrid bicycle at 20 km/h, however, forms an exception to the general trend. Higher yaw rate responses of the Hybrid bicycle at 20 km/h is most likely attributed to significantly higher high inter-subject variability under this condition, as evident from Table 3.5.

3.6 RESPONSES TO INTERACTION WITH RUMBLE STRIPS

The data acquired during bicycles tests performed on the different patterns of the rumble strips are analyzed to study the response characteristics of the coupled bicycle-rider system as a function of the bicycle, rumble strip geometry and forward speed. The analyses are performed for Round I and II and Rectangular I and II patterns. The mean responses for Round I pattern are obtained from data acquired for seven subjects, while those for the remaining patterns are based on the data for only two subjects. Table 3.11 summarizes the geometry of the rumble strip patterns along with the size of the test subject population. The table also presents the computed fundamental frequencies of the interaction between bicycle's wheel and the grooved portions of the rumble strips,

computed from the ratio of the traversing speed and the center to center distance, and referred to as the strip frequency. The data attained for different patterns are examined to identify some important insights into the dynamic properties of the system in terms of the frequency components and amplitudes of the vertical and pitch acceleration. The acquired data are also evaluated in term of RMS and VDV of the vertical and pitch accelerations, and RMS yaw angle.

Table 3.11: The geometry of different patterns and the strip frequencies corresponding to different traversing speeds.

Pattern	*Center to Center Distance (mm)*	*Speed (km/h)*	*Strip Frequency (Hz)*	*Number of Subjects*
Round I	300	10	9.3	7
		15	13.9	
		20	18.5	
Round II	445	10	6.2	2
		15	9.4	
		20	12.5	
Rectangular I	120	10	23.1	2
		-	-	
		20	46.3	
Rectangular II	105	10	26.5	2
		-	-	
		20	52.9	

3.6.1 Rumble Strip Pattern Round I

The measured data acquire for seven subjects on rumble strip pattern Round I are analyzed to derive average acceleration responses from three trials for each subject, and combination of bicycle and speed. The vertical acceleration measured at the handle bar ($\ddot{z}_h$) and seat post ($\ddot{z}_s$), on the Touring and Hybrid bicycles, are expressed in terms of their power spectral densities, as illustrated in Figures 3.12 and 3.13, respectively. The figures show the PSD of accelerations attained for all seven subjects corresponding to

two different speeds, 10 km/h and 20 km/h. The results also show PSD of pitch acceleration of the bicycle frame, as derived from Equation (3.1).

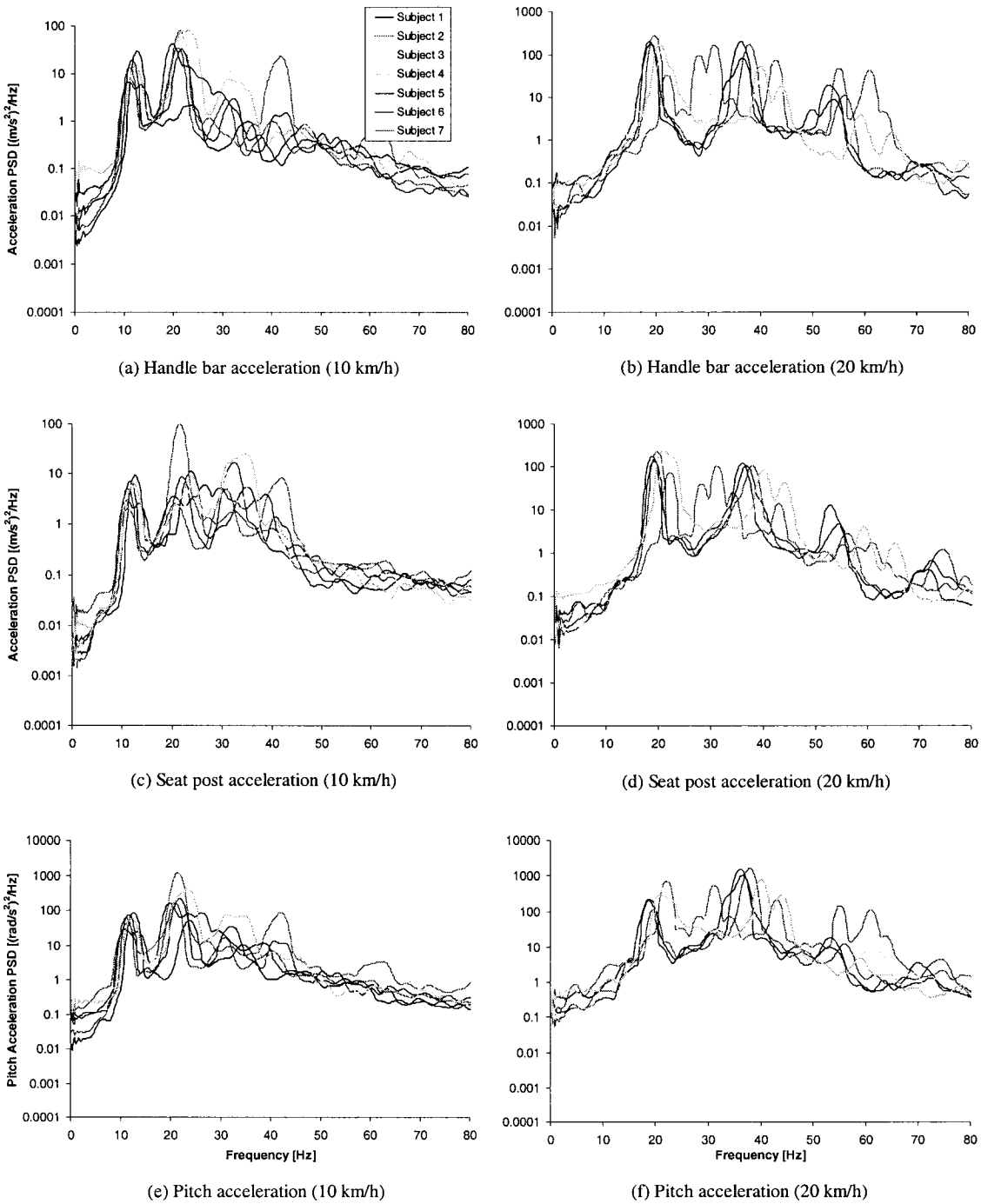

(a) Handle bar acceleration (10 km/h)

(b) Handle bar acceleration (20 km/h)

(c) Seat post acceleration (10 km/h)

(d) Seat post acceleration (20 km/h)

(e) Pitch acceleration (10 km/h)

(f) Pitch acceleration (20 km/h)

Figure 3.12: Comparisons of the vertical and pitch acceleration responses of the Touring bicycle attained with seven subjects (Speeds: 10 and 20 km/h; Pattern: Round I).

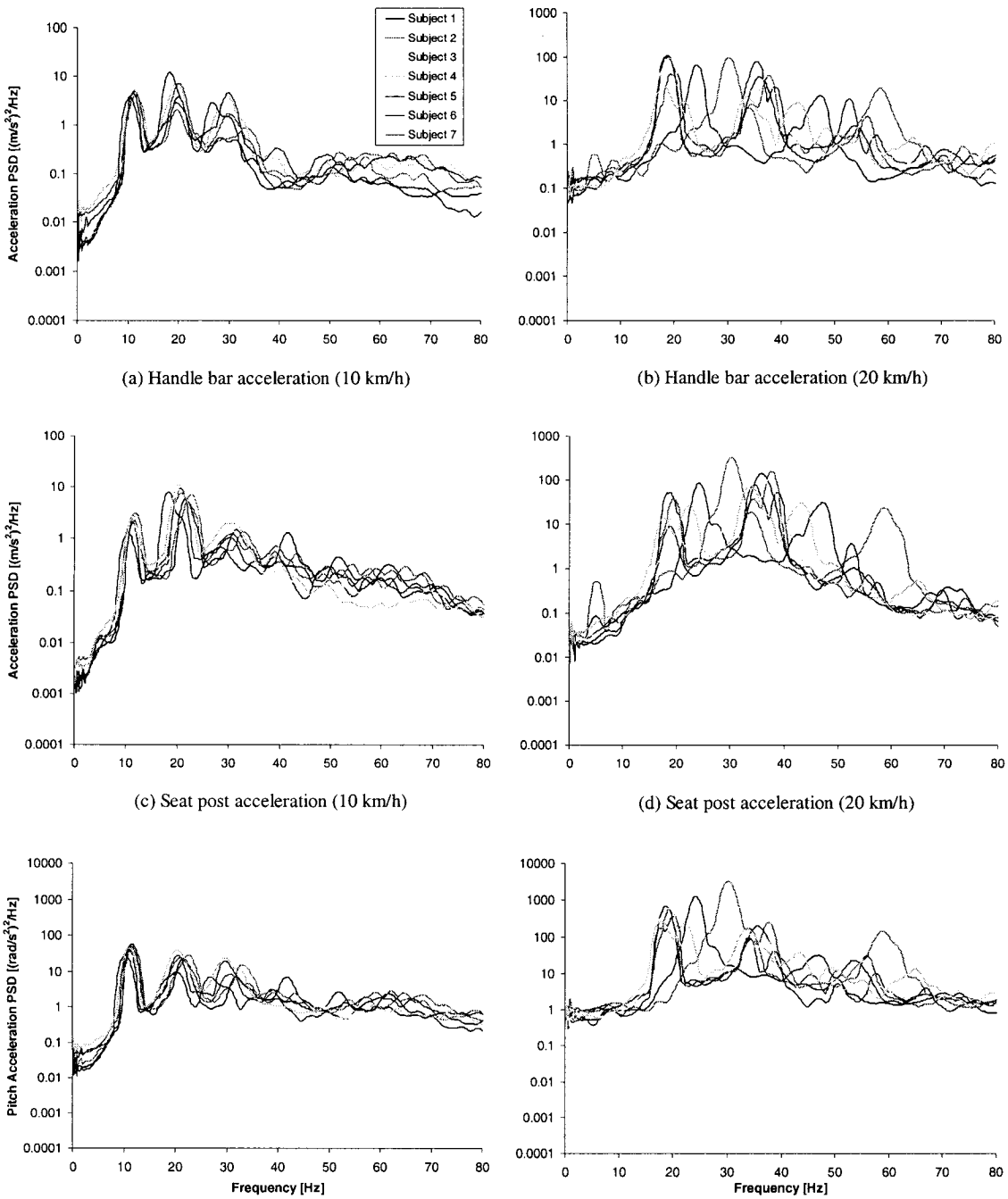

(a) Handle bar acceleration (10 km/h)

(b) Handle bar acceleration (20 km/h)

(c) Seat post acceleration (10 km/h)

(d) Seat post acceleration (20 km/h)

(e) Pitch acceleration (10 km/h)

(f) Pitch acceleration (20 km/h)

Figure 3.13: Comparisons of the vertical and pitch acceleration responses of the Hybrid bicycle attained with seven subjects (Speeds: 10 and 20 km/h; Pattern: Round I).

The figures show comparable trends for all seven subjects, in terms of the spectral components and magnitudes of acceleration PSD. However, considerable variations in

the spectral components and magnitudes are also evident among different riders, especially at the higher speed of 20 km/h, which are attributed to relatively higher inter-subject variability. Irrespective of the bicycle type, all three acceleration responses ($\ddot{z}_h$, $\ddot{z}_s$ and $\ddot{\theta}$) at 10 km/h show peaks in the 10-12 Hz, 18-22 Hz and 30-32 Hz frequency bands. The responses at 20 km/h show peaks in the 18-21 Hz, and 35-40 Hz bands. The lower frequencies are close to the strip frequencies of 9.3 and 18.5 Hz at 10 and 20 km/h, respectively, as shown in Table 3.14. It should be noted that the majority of the subjects traversed the strips at speeds slightly higher than the desired 10 km/h speed, which resulted in slightly higher frequencies. Furthermore, considerable variations were observed in center to center distances of the fabricated prototype rumble strip patterns, as evident from Table 2.4.

Figures 3.14 and 3.15 illustrate the mean acceleration PSD responses of the Touring and Hybrid bicycles, respectively, while traversing the Round I pattern at: 10 and 20 k/h. The results also show standard deviation of the means attained for all seven subjects. The mean responses of the Touring bicycle exhibit first peak in the 10-12 Hz range, and near 20 Hz at 10 and 20 km/h, respectively, which are close to the fundamental strip frequencies. The vertical handle bar and seat post acceleration spectra, and pitch acceleration responses show peaks in the 22 to 23 Hz and 30 to 35 Hz bands while traversing at 10 km/h, and in the 38 to 40 Hz band at 20 km/h. The results for the Hybrid bicycle at 10 and 20 km/h show peak handle bar and seat post responses in the 10-12 Hz and 19-21 Hz bands, which are attributed to the strip frequencies. The results also show peak responses near 20 and 30 Hz at 10 km/h and near 35 Hz at 20 km/h. The

pitch acceleration PSD responses of both bicycles also show peaks in the similar frequency ranges.

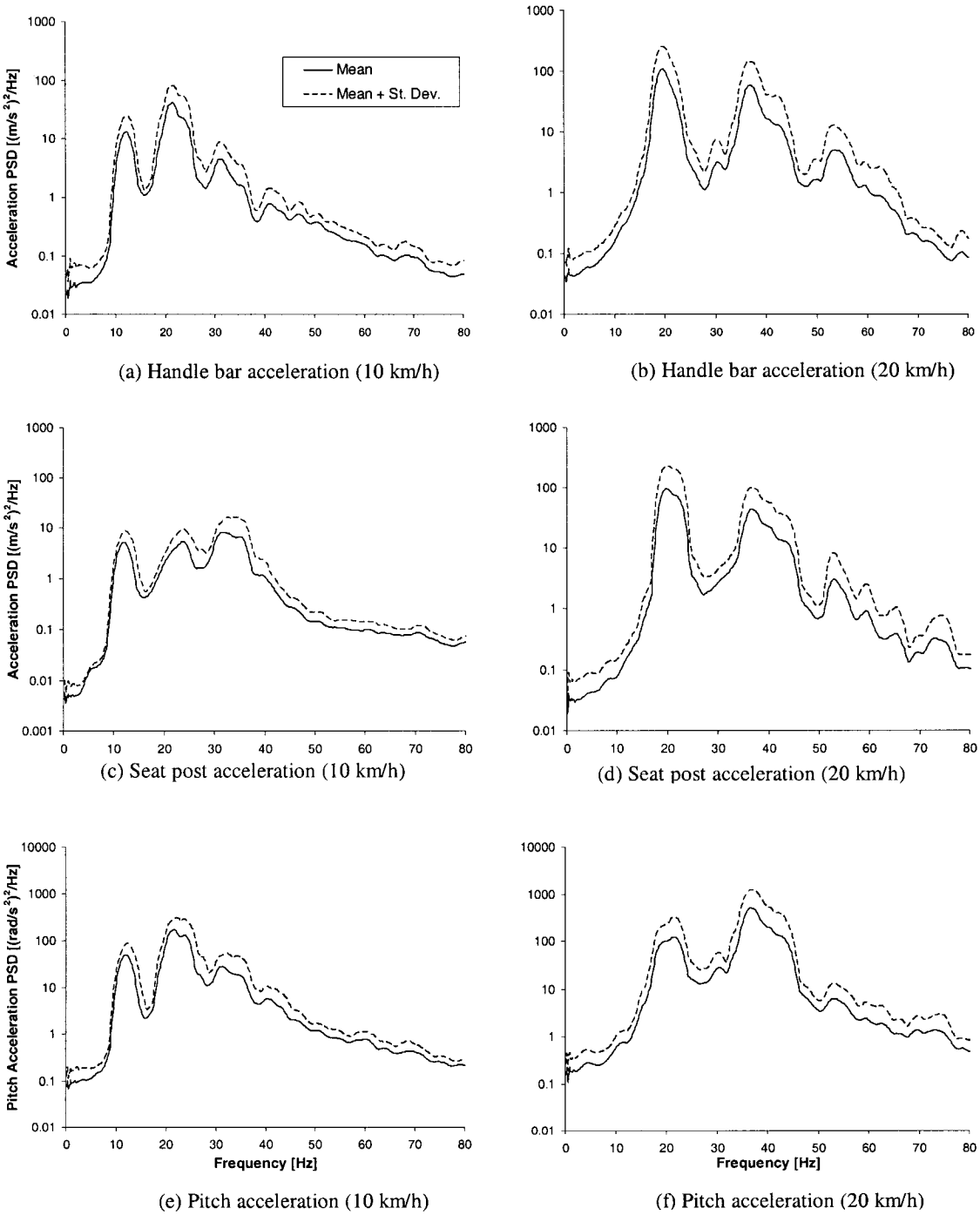

(a) Handle bar acceleration (10 km/h)

(b) Handle bar acceleration (20 km/h)

(c) Seat post acceleration (10 km/h)

(d) Seat post acceleration (20 km/h)

(e) Pitch acceleration (10 km/h)

(f) Pitch acceleration (20 km/h)

Figure 3.14: Mean and standard deviation of the vertical and pitch acceleration responses of the Touring bicycle (Speeds: 10 and 20 km/h; Pattern: Round I).

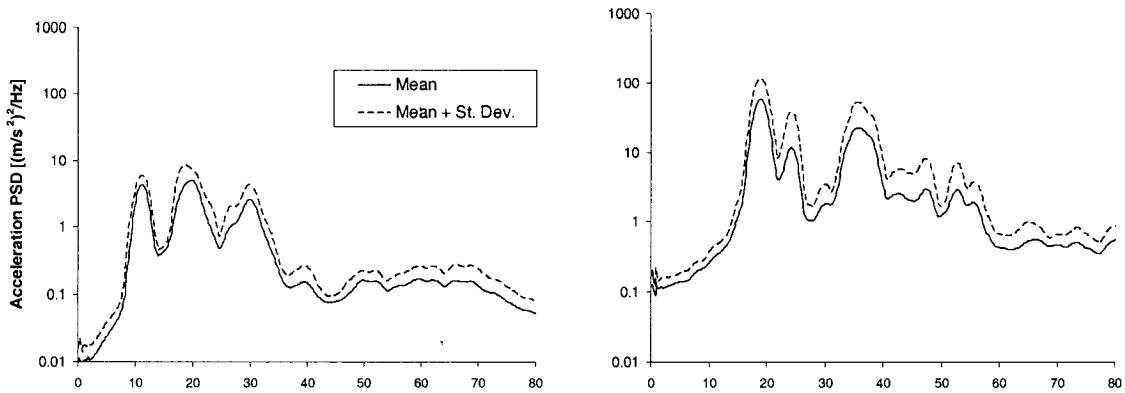

(a) Handle bar acceleration (10 km/h)

(b) Handle bar acceleration (20 km/h)

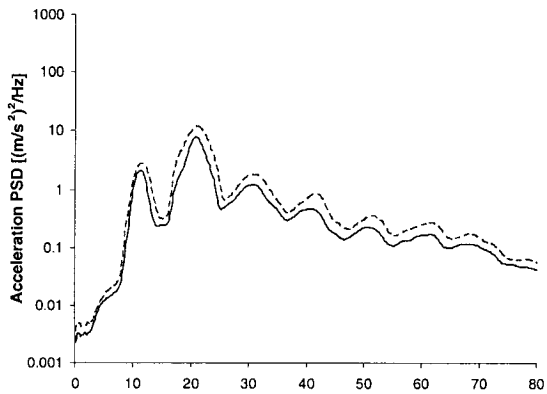

(c) Seat post acceleration (10 km/h)

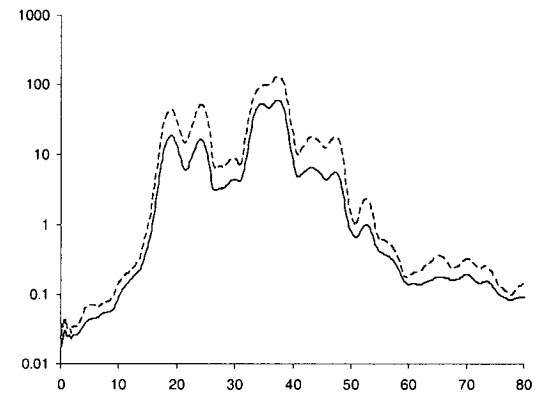

(d) Seat post acceleration (20 km/h)

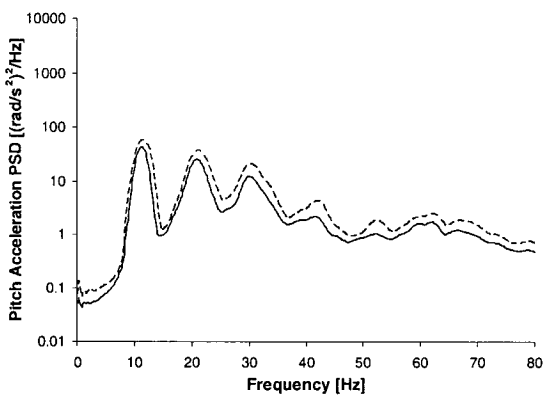

(e) Pitch acceleration (10 km/h)

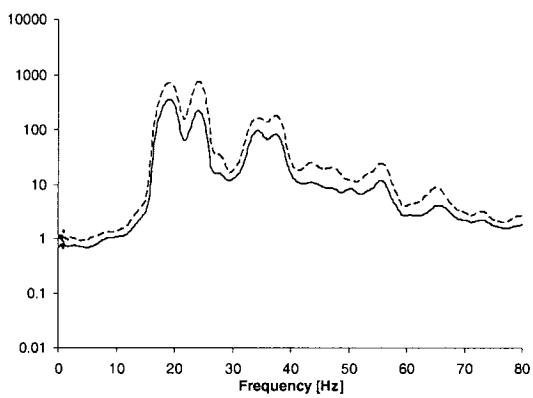

(f) Pitch acceleration (20 km/h)

Figure 3.15: Mean and standard deviation of the vertical and pitch acceleration responses of the Hybrid bicycle (Speeds: 10 and 20 km/h; Pattern: Round I).

Figures 3.16 and 3.17 illustrate the influence of forward speed on the mean acceleration PSD responses of the Touring and Hybrid bicycles, respectively. The figures also show the RMS values of the yaw angle and yaw rates of the two bicycles as a function of the forward speed. It can be observed that the peak responses shift to higher frequencies as the forward speeds is increased. This could be attributed to higher strip frequency and stiffening of the rider's musculature as it tries to adjust to higher level of vibration magnitude, while imparting higher pedaling effort to achieve higher speed. An increase in the speed generally yields higher peak magnitudes of the vertical and pitch accelerations of both bicycles, while the Touring bicycle yields higher magnitudes than the Hybrid bicycle, as observed for the responses to flat pavement.

The magnitudes of vertical and pitch accelerations are significantly higher than those encountered on the flat pavement. The RMS yaw angles of both bicycles tend to decrease with increasing speed, as observed for the flat pavement. The Hybrid bicycle, however, exhibits higher magnitudes of yaw oscillations than the Touring bicycle at all three speeds, which agrees with the trend observed for the flat pavement. Both of the bicycle exhibit highest yaw rate at the lowest speed of 10 km/h, suggesting higher degree of steering effort. The yaw rates tend to be lowest at 15 km/h and highest at 20 km/h.

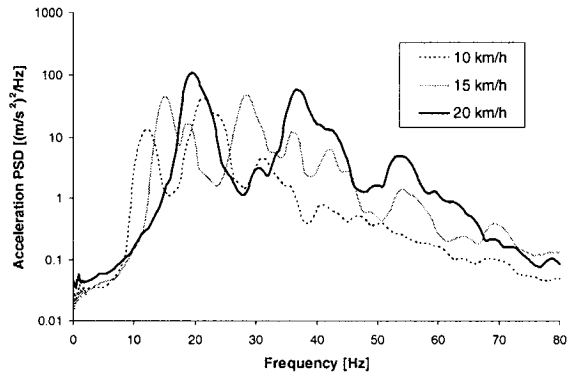

(a) Handle bar acceleration

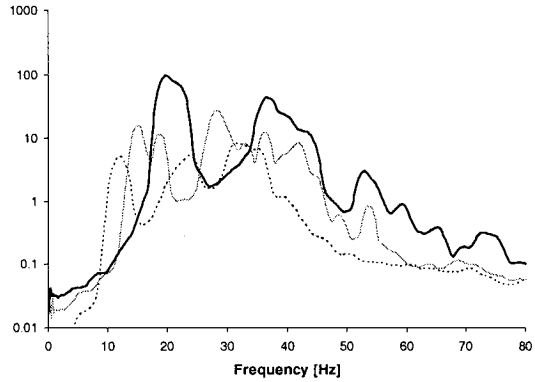

(b) Seat post acceleration

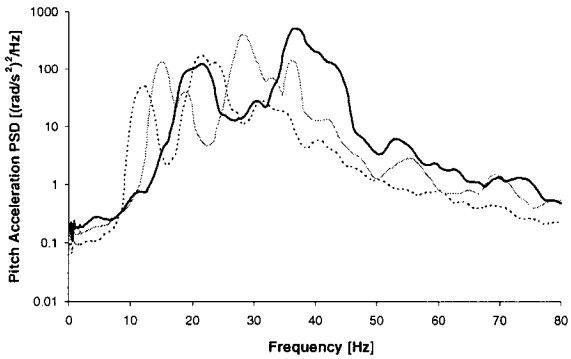

(c) Pitch acceleration

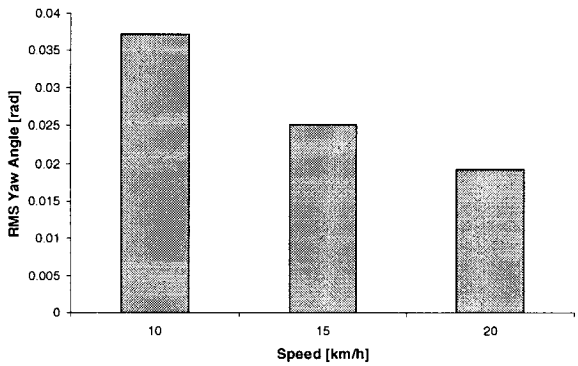

(d) Yaw angle

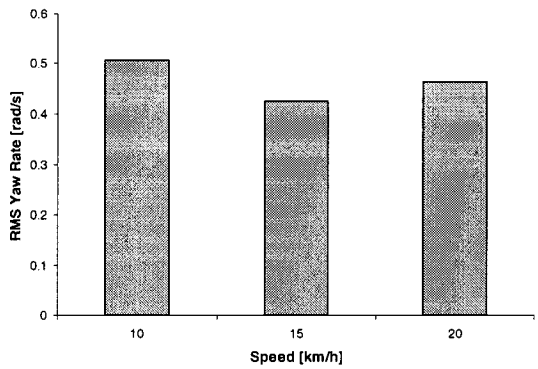

(e) Yaw rate

Figure 3.16: Influence of forward speed on the mean vertical and pitch accelerations, and RMS yaw angle and yaw rate response of the Touring bicycle (Pattern: Round I).

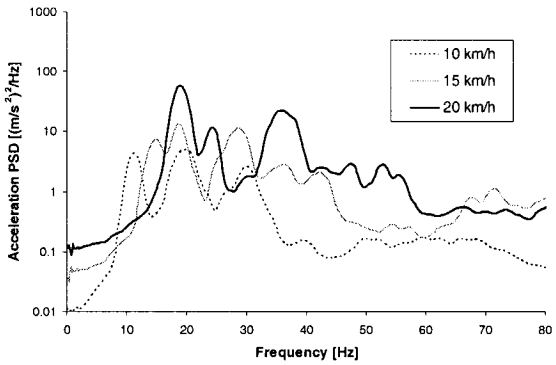

(a) Handle bar acceleration

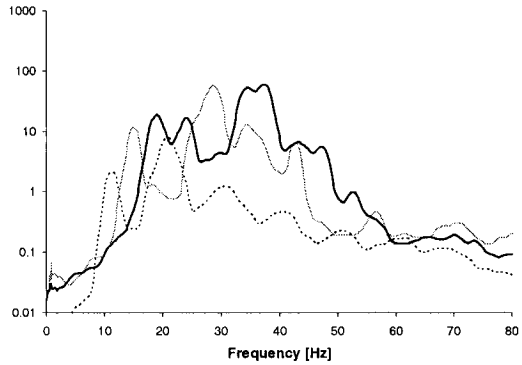

(b) Seat post acceleration

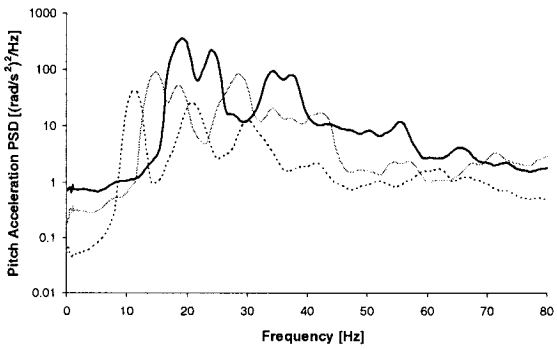

(c) Pitch acceleration

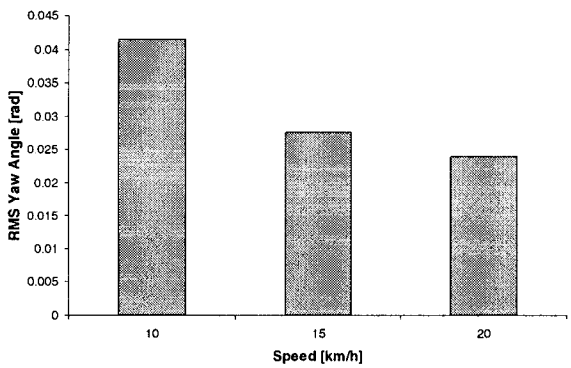

(d) Yaw angle

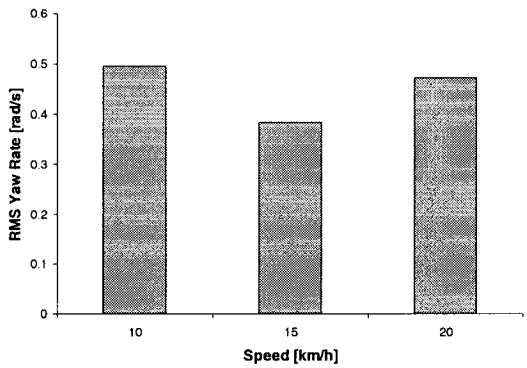

(e) Yaw rate

Figure 3.17: Influence of forward speed on the mean vertical and pitch accelerations, and RMS yaw angle and yaw rate response of the Hybrid bicycle (Pattern: Round I).

3.6.2 Rumble Strip Patterns Round II and Rectangular I

Figure 3.18 illustrates the mean vertical and pitch acceleration PSD responses of the Touring and Hybrid bicycles traversing the Round II pattern at speeds of 10 and 20 km/h. Figure 3.19 presents the results attained for the Rectangular I pattern. The results clearly show peaks in the vicinity of the strip frequencies, which are at 6.2 and 12.5 Hz for the Round II pattern, and 23.1 and 46.3 Hz for Rectangular I at speeds of 10 and 20 km/h, respectively. The peak magnitudes of vertical and pitch accelerations are considerably smaller than those obtained for the Round I pattern. Apart from the strip frequencies, the Touring bicycle responses reveal peaks in the 14-18 Hz ranges at 10 km/h and in the 20-46 Hz range at 20 km/h, while traversing the Round II pattern. The Hybrid bicycle responses reveal peaks near 15 Hz and in the 30 to 32 Hz range at 10 km/h, and near 12.5 Hz, and in the 21 to 25 Hz ranges at 20 km/h.

The responses under Rectangular I pattern show higher magnitude peak responses in the 32-35 Hz and near 50 Hz for the Touring bicycle at 10 and 20 km/h, respectively. The corresponding peak responses of the Hybrid bicycle occur in the 26-28 Hz for both speeds. The Hybrid bicycle also exhibits peak response in the 40-50 Hz range, which are most likely attributed to vibration models of the bicycle. A higher forward speed in general yields higher magnitudes of vertical and pitch accelerations for both bicycles and patterns. The trend with the respect to the effect of the bicycle type could not be clearly established for both patterns, which is most likely attributed to small subject sample and their significantly different riding skills.

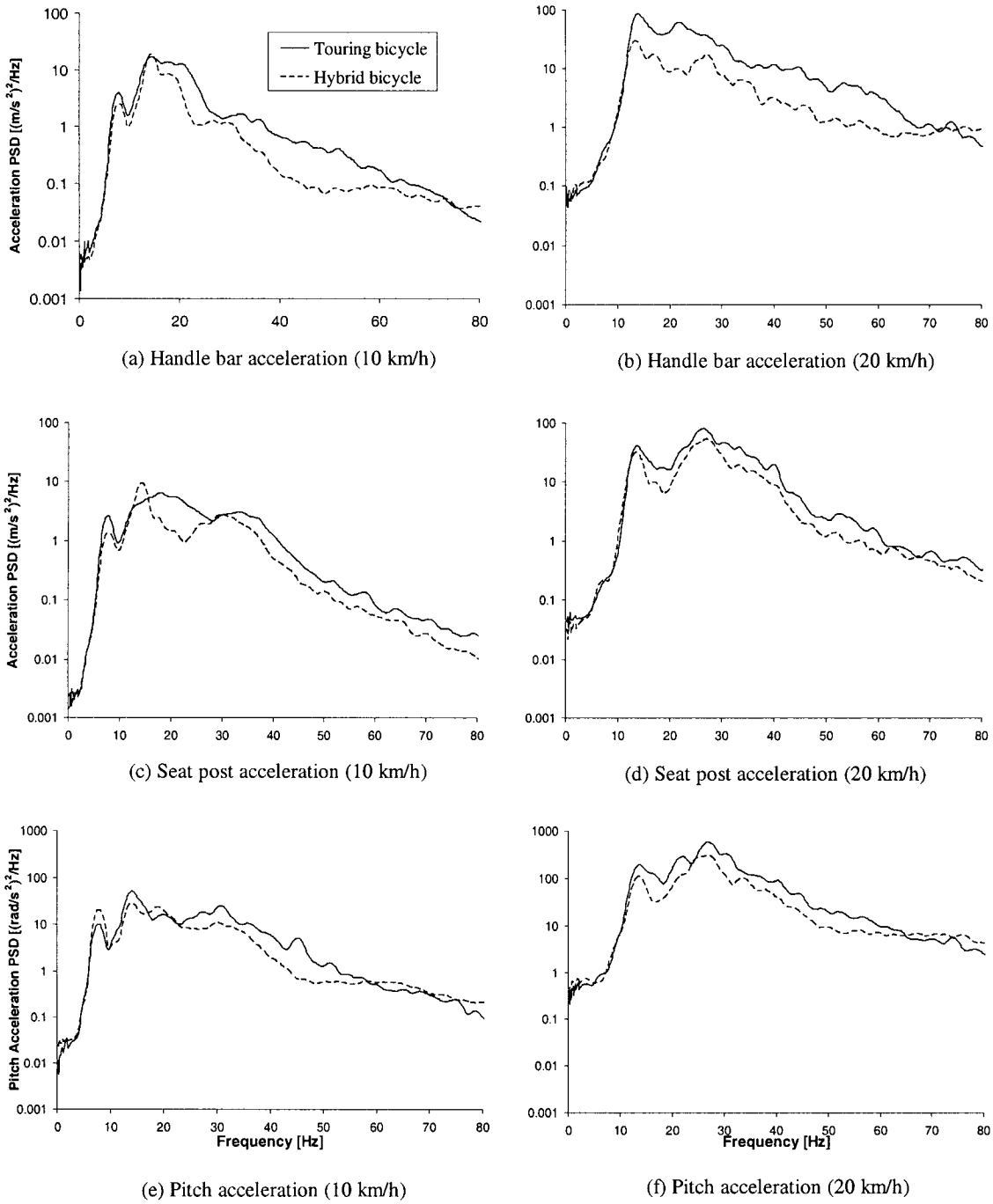

(a) Handle bar acceleration (10 km/h)

(b) Handle bar acceleration (20 km/h)

(c) Seat post acceleration (10 km/h)

(d) Seat post acceleration (20 km/h)

(e) Pitch acceleration (10 km/h)

(f) Pitch acceleration (20 km/h)

Figure 3.18: Mean vertical and pitch acceleration responses of the Touring and Hybrid bicycles (Speeds: 10 and 20 km/h; Pattern: Round II).

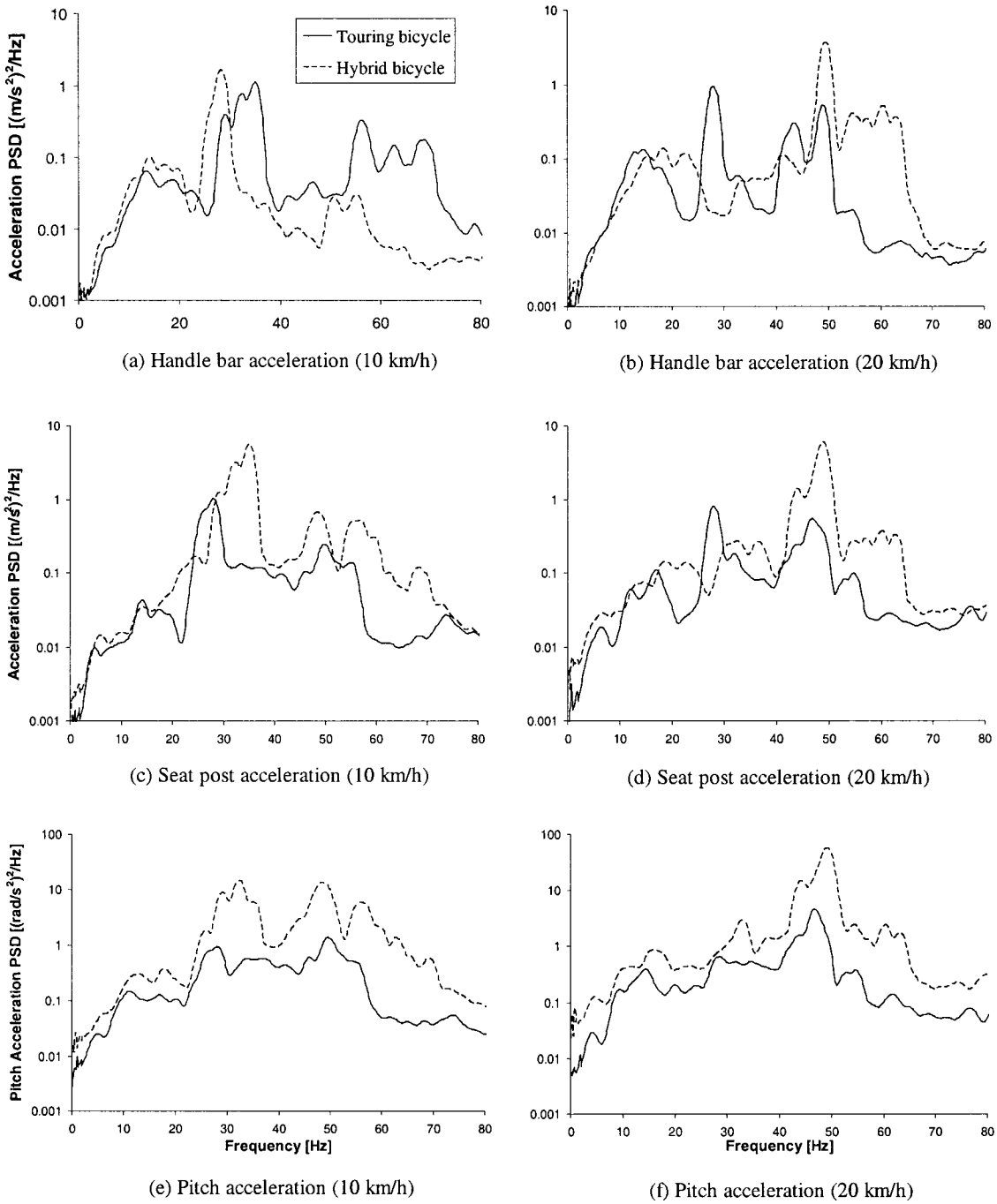

(a) Handle bar acceleration (10 km/h)

(b) Handle bar acceleration (20 km/h)

(c) Seat post acceleration (10 km/h)

(d) Seat post acceleration (20 km/h)

(e) Pitch acceleration (10 km/h)

(f) Pitch acceleration (20 km/h)

Figure 3.19: Mean vertical and pitch acceleration responses of the Touring and Hybrid bicycles attained with two subjects (Speeds: 10 and 20 km/h; Pattern: Rectangular I).

3.6.3 Comparative analysis of the tested rumble strip patterns

The ride comfort and controllability of the tested rumble strip patterns is assessed in terms of RMS and VDV values of the vertical and pitch accelerations, and RMS values of the yaw angle and the yaw rate. The mean responses of both of the bicycles on the rumble strip patterns Round I, Round II, Rectangular I and Rectangular II, are compared with the respective mean responses under the flat pavement. Tables 3.15 and 3.16 present comparisons of RMS values of the accelerations, yaw angles and yaw rates of the Touring and Hybrid bicycle, respectively, while traversing different patterns and flat pavement at three different speeds. The VDV values of the vertical and pitch accelerations attained under different patterns are compared in Tables 3.14 and 3.15, respectively, for two bicycles

The results indicate that overall the greatest ride discomfort occurs on the rumble strip pattern Round II, for both bicycles and at all three speeds. Overall, pattern Round II shows highest RMS and VDV vertical and pitch accelerations, when compared to the other strip patterns. Pattern Round II exhibits lower RMS values for the handle bar acceleration on the Touring bicycle at 10 km/h and on the Hybrid bicycle at 20 km/h and for the seat post acceleration on the Hybrid bicycle at 15 km/h, compared to those of the Round I pattern. This can be attributed to considerable inter-subject variability of the measured data on the pattern Round I (as described in section 3.3) as well as to small subject sample on the Round II pattern. The influence of intermittent acceleration peaks on ride discomfort, assessed in term of VDV, also exhibits the highest values for the pattern Round II. The same trend is observed for each combination of bicycle and speed, except for the handle bar acceleration of the Hybrid bicycle at 20 km/h, which can be

attributed to considerable scatter of the data from the mean response measured for the Round I pattern, as discussed in section 3.3.

Pattern Round I produces a significant increase in both the RMS and VDV values of the vertical and pitch accelerations, when compared with those observed for the flat pavement and Rectangular I and Rectangular II patterns, for both bicycle and at three different speeds. However, it can be also observed that the VDV values for the Touring bicycle at 10 and 20 km/h for the Round I pattern are comparable to those observed on the pattern Rectangular I, for the both vertical and pitch accelerations. On the other hand, Rectangular I and Rectangular II patterns produce small increase in RMS and VDV accelerations when compared with the results obtained for the flat pavement for the Touring and Hybrid bicycles (Tables 3.9 and 3.10, respectively) at all three speeds. Moreover, the results for the Touring and Hybrid bicycle at 20 km/h indicate that RMS accelerations for the Rectangular II pattern are lower than those measured for the flat pavement, however, it could be attributed to small subject sample for the Rectangular II pattern.

Irrespective of the traversing speed and the strip pattern, the Touring bicycle yields higher magnitudes of vertical and pitch accelerations than the Hybrid bicycle. Such a trend is attributed to front and seat post suspension and to relatively softer tire of the Hybrid bicycle. It can be also observed that irrespective of the bicycle or the traversing speed, the results reveal a relationship between the length of the grooved portions of the rumble strip patterns, and the magnitudes of the vertical and pitch accelerations. The patterns that exhibit the highest RMS and VDV values of the vertical and pitch accelerations are Round II and Round I, which at the same time have the largest groove

lengths (115 and 200 mm, respectively). Also, the increase in the groove lengths from 15 to 30 mm yield a significant increase in acceleration magnitudes between the Rectangular II and Rectangular I patterns, respectively, which is most evident for the Touring bicycle.

The RMS values of the yaw angle responses for the Touring and Hybrid bicycle presented in Tables 3.12 and 3.13, respectively, show that ride on all four tested rumble strip patterns exhibit a decrease of the RMS values with the increase of traversing speed, irrespective of the bicycle type. Such a trend corresponds with the trend observed for the flat pavement, as discussed in section 3.5. The results show that Rectangular II pattern, yields lowest levels of the RMS values of the yaw angle that are close to those attained for the flat pavement. The RMS values of yaw angle for this pattern appear to be slightly lower than those of the flat pavement, which can be attributed to high inter-subject variability of the measured yaw oscillations for the flat pavement, as evident from Table 3.5, and to small subject sample for the Rectangular II pattern.

Patterns Round I and Round II exhibit considerably higher values of the RMS yaw rate when compared with those obtained for the flat pavement, irrespective of the bicycle or the traversing speed. The results also indicate that riding speed of 10 km/h yields the largest RMS values of the yaw rare, except for the Round II pattern and for the Touring bicycle for the flat pavement. However, the results for the RMS yaw rate for the Touring and the Hybrids bicycle, presented in Table 3.12 and 3.13, respectively, do not show a consistent trend neither regarding the traversing speed nor the bicycle type.

Table 3.12: Comparison of mean RMS responses of the Touring bicycle traversing different strip pattern.

Speed (km/h)	Pattern	*Mean RMS values*				
		$\ddot{z}_h$ (m/s^2)	$\ddot{z}_s$ (m/s^2)	θ (rad/s^2)	ψ (rad)	$\dot{\psi}$ (rad/s)
10	Round I	16.35	10.08	35.41	0.0456	0.5069
	Round II	14.00	10.36	38.05	0.0593	0.5016
	Rect. I	4.81	5.47	12.12	0.0481	0.2180
	Rect. II	2.44	1.85	4.91	0.0218	0.1932
	Flat	**2.05**	**1.85**	**4.19**	**0.0372**	**0.2003**
15	Round I	22.25	17.54	52.69	0.0363	0.4249
	Round II	26.36	19.98	69.91	0.0475	0.5122
	Rect. I	-	-	-	-	-
	Rect. II	-	-	-	-	-
	Flat	**2.94**	**2.37**	**5.62**	**0.0251**	**0.2373**
20	Round I	29.50	28.72	62.27	0.0328	0.4639
	Round II	34.30	34.17	98.75	0.0419	0.5786
	Rect. I	6.96	5.63	15.56	0.0258	0.2039
	Rect. II	3.19	2.72	6.71	0.0147	0.1848
	Flat	**3.86**	**3.29**	**7.49**	**0.0192**	**0.1944**

Table 3.13: Comparison of mean RMS responses of the Hybrid bicycle traversing different strip pattern.

Speed (km/h)	Pattern	*Mean RMS values*				
		$\ddot{z}_h$ (m/s^2)	$\ddot{z}_s$ (m/s^2)	θ (rad/s^2)	ψ (rad)	$\dot{\psi}$ (rad/s)
10	Round I	7.78	7.30	17.97	0.0511	0.4951
	Round II	10.47	8.52	19.93	0.0549	0.3969
	Rect. I	3.01	2.82	5.28	0.0376	0.2573
	Rect. II	1.89	1.82	3.82	0.0383	0.2608
	Flat	**1.87**	**1.76**	**3.91**	**0.0415**	**0.2372**
15	Round I	11.12	17.18	32.45	0.0369	0.3838
	Round II	17.31	15.13	41.06	0.0427	0.4191
	Rect. I	-	-	-	-	-
	Rect. II	-	-	-	-	-
	Flat	**2.77**	**2.32**	**5.42**	**0.0276**	**0.2113**
20	Round I	19.48	22.90	43.32	0.0343	0.4724
	Round II	18.25	22.91	54.01	0.0289	0.3503
	Rect. I	3.78	3.10	6.76	0.0228	0.1923
	Rect. II	2.30	2.11	4.64	0.0204	0.1620
	Flat	**3.75**	**3.24**	**7.37**	**0.0240**	**0.2324**

Table 3.14: Comparison of mean VDV responses of the Touring bicycle traversing different strip pattern.

Speed (km/h)	Pattern	*Mean VDV values*		
		$\ddot{z}_h$ (m/s$^{1.75}$)	$\ddot{z}_s$ (m/s$^{1.75}$)	θ (rad/s$^{1.75}$)
10	Round I	37.93	27.00	85.78
	Round II	41.19	35.13	112.87
	Rect. I	12.40	13.87	31.68
	Rect. II	7.24	6.58	14.51
	Flat	**8.52**	**7.12**	**16.15**
15	Round I	57.47	44.36	123.24
	Round II	71.29	57.84	185.61
	Rect. I	-	-	-
	Rect. II	-	-	-
	Flat	**15.39**	**12.24**	**26.88**
20	Round I	62.23	58.83	132.78
	Round II	90.41	87.64	255.32
	Rect. I	15.50	13.99	37.87
	Rect. II	11.16	11.67	22.66
	Flat	**17.33**	**15.32**	**31.46**

Table 3.15: Comparison of mean VDV responses of the Hybrid bicycle traversing different strip pattern.

Speed (km/h)	Pattern	*Mean VDV values*		
		$\ddot{z}_h$ (m/s$^{1.75}$)	$\ddot{z}_s$ (m/s$^{1.75}$)	θ (rad/s$^{1.75}$)
10	Round I	20.38	20.55	55.22
	Round II	30.37	27.86	62.96
	Rect. I	9.00	8.84	16.45
	Rect. II	6.36	6.20	13.02
	Flat	**7.34**	**6.03**	**13.84**
15	Round I	31.96	41.11	85.74
	Round II	46.22	43.77	112.63
	Rect. I	-	-	-
	Rect. II	-	-	-
	Flat	**10.73**	**8.91**	**20.43**
20	Round I	46.60	49.37	122.35
	Round II	45.80	61.62	137.67
	Rect. I	10.02	8.94	19.89
	Rect. II	9.40	8.66	17.62
	Flat	**13.22**	**12.86**	**28.24**

3.7 RESPONSE UNDER OBLIQUE ANGLE OF APPROACH

The data acquired for the oblique angle of approach to rumble strip pattern Round I are analyzed to study the ride discomfort and controllability. As described in Chapter 2, a total of four riders traversed the rumble strip patterns Round I approaching it at an angle of 10 degrees at three different speeds (10, 15 and 20 km/h). The total contact duration of the bicycle with the rumble strip depends upon the approach angle, the width of the pattern and the traversing speed. The measured data are thus analyzed to extract the portions of the measured signal acquired while the bicycle was in the contact with the rumble strip, by considering the length of the recorded signal of 0.75 seconds for the speed of 10 km/h and 0.5 seconds for the speeds of 15 and 20 km/h. Figure 3.20 illustrates a sample measurement of the acceleration time history of the handle bar of the Touring bicycle approaching the Round I pattern at an oblique angle of 10 degrees and speed of 10 km/h. The measured data are further analyzed to derive RMS and VDV of the vertical and pitch accelerations, RMS yaw angle and RMS yaw rate responses. The results attained for three trials involving each combination of bicycle and speed are averaged to describe the mean responses for each subject. The mean responses attained for every subject are then averaged to describe the mean response and standard deviation of the means for every combination of bicycle and speed. Tables 3.16 and 3.17 summarizes the mean RMS and VDV of the vertical and pitch accelerations and RMS yaw angle and yaw rate along with standard deviations of the means attained for four subjects, riding the Touring and Hybrid bicycle, respectively.

The results show a considerably higher RMS and VDV values of the vertical and pitch accelerations, when compared to those obtained on the flat pavement (Tables 3.9

and 3.10), for both bicycles. The RMS and VDV values are, however, lower than those obtained for continuous ride on the Round I pattern (Tables 3.15 and 3.16). This can be attributed to relatively short duration of the measured signal considered for the analysis, as evident from Figure 3.20. The results also indicate that the Touring bicycle exhibits higher acceleration magnitudes than the Hybrid bicycle at all three speeds, as observed for the flat pavement and other patterns.

The results for the RMS yaw angle show decrease with speed with an exception of the Hybrid bicycle at 20 km/h. This trend is consistent with that observed on the flat pavement and for the rumble strip patterns. The Hybrid bicycle show higher values of the RMS yaw rate compared to those observed for the Touring bicycle. Moreover, the Hybrid bicycle exhibits increase in the RMS values of the yaw rate with the increase in speed while the Touring bicycle does not exhibits such a trend.

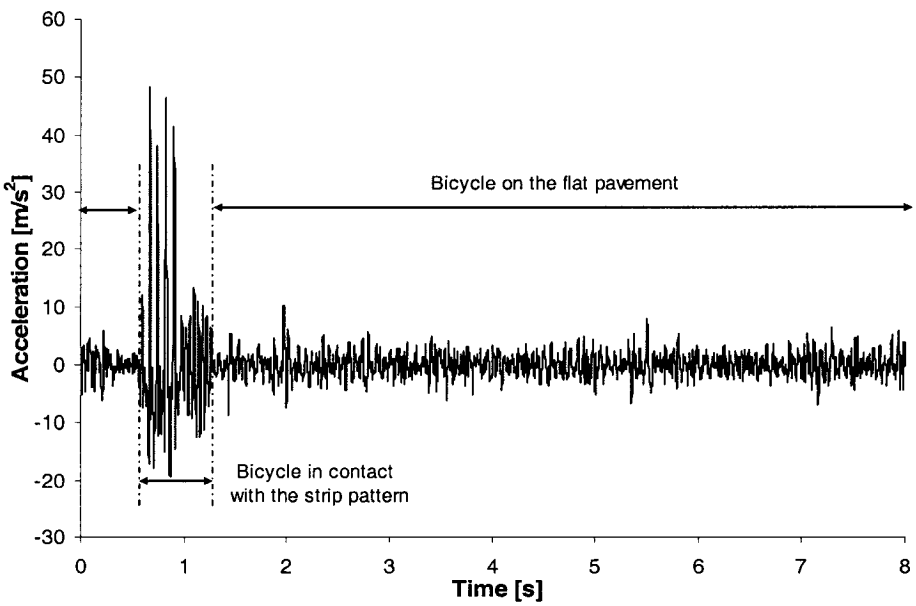

Figure 3.20: Acceleration of the handle bar on the Touring bicycle approaching rumble strips at an angle of 10 degrees (Speed: 10 km/h; Pattern: Round I).

Table 3.16: Mean and standard deviation of the RMS and VDV vertical and pitch acceleration and RMS yaw angle and yaw rate of the Touring bicycle obtained for an oblique angle of approach attained for four subjects (Speeds: 10, 15 and 20 km/h; Pattern: Round I).

Speed	*Measure*	*Mean and Standard Deviation*				
		$\ddot{z}_h$ [m/s^2]	$\ddot{z}_s$ [m/s^2]	$\ddot{\theta}$ [rad/s^2]	ψ [rad]	$\dot{\psi}$ [rad/s]
10 kh/h	RMS	10.9±1.3	8.3±0.9	18.5±1.7	53.7±17.6	200.3±46.6
	VDV	15.6±2.1	11.6±14	24.9±2.4	-	
15 km/h	RMS	17.4±3.3	13.5±3.1	34.4±7.1	31.6±30.1	237.3±175.2
	VDV	21.60±3.7	15.9±3.5	38.0±7.70	-	
20 km/h	RMS	21.4±6.1	17.8±2.0	44.5±8.8	25.4±22.1	194.4±41.1
	VDV	26.1±6.3	21.5±1.6	49.9±8.8	-	

Table 3.17: Mean and standard deviation of the RMS and VDV vertical and pitch acceleration and RMS yaw angle and yaw rate of the Hybrid bicycle obtained for an oblique angle of approach attained for four subjects (Speeds: 10, 15 and 20 km/h; Pattern: Round I).

Speed	*Measure*	*Mean and Standard Deviation*				
		$\ddot{z}_h$ [m/s^2]	$\ddot{z}_s$ [m/s^2]	$\ddot{\theta}$ [rad/s^2]	ψ [rad]	$\dot{\psi}$ [rad/s]
10 kh/h	RMS	9.0±3.3	7.1±1.5	16.9±3.0	43.1±17.1	246.9±86.2
	VDV	12.4±5.3	9.6±1.9	22.7±3.6	-	-
15 km/h	RMS	11.1±1.5	12.1±1.9	39.2±1.7	30.4±8.7	256.2±208.2
	VDV	12.6±0.9	13.6±1.4	40.9±1.2	-	-
20 km/h	RMS	13.2±1.0	12.6±2.3	40.6±5.2	34.3±13.2	290.7±306.0
	VDV	14.4±1.2	14.9±2.9	44.4±3.9	-	-

3.8 SUBJECTIVE MEASUREMENTS

Subjective data collected during the experiments are analyzed to enhance an understanding of the rider's personal sensation of the ride comfort and controllability. Subjective data compiled for the Round I pattern define the comfort and controllability ratings relative to the ride sensation on the flat pavement. Figure 3.21 presents the mean and standard deviation of the subjective overall comfort and controllability ratings, while the mean and standard deviation of subjective ratings of comfort of different body parts are presented in Figure 3.22. Figure 3.23 presents the mean and standard deviation of particular control ratings. The figures provide the data for both the Touring and Hybrid bicycles at three different speeds.

The inter-subject variability of the data attained with seven subjects is evaluated in term of the coefficient of variation of the mean results. Table 3.18 summarizes the coefficients of variation of the subjective measurements for the Touring and Hybrid bicycles. The results show considerable inter-subject variability of the data, irrespective of the bicycle and the speed. The questions regarding overall comfort and controllability as well as the questions regarding the comfort of the arms and hands and in the seat zone exhibit relatively lower variability, for both bicycles. The question that shows the highest inter-subject variability is the ability to see straight at 10 and 15 km/h, for both bicycles.

The results presented in Figures 3.21, 3.22 and 3.23, indicate that the overall comfort and controllability decreases with speed on both bicycles. This can be directly correlated with the observed trends of the RMS and VDV vertical and pitch accelerations of the measured data on the pattern Round I, as discussed in section 3.6.3. Figure 3.22 indicates that the comfort of the arms and hands as well as the comfort in the seat area are

more influenced by the traversing speed than the comforts of the neck and shoulders and the spine and back. The results also indicate that the sensation of comfort in neck and shoulders is worst on the Touring bicycle, while the ride on the Hybrid bicycle provides less comfort to the spine and back. The Touring bicycle exhibits higher mean discomfort and control ratings which also confirms with the higher acceleration magnitudes recorded on the Touring bicycle when compared with those of the Hybrid bicycle.

Table 3.18: Inter-subject variability of the subjective responses for the Touring and Hybrid bicycles at different speeds (Pattern: Round I).

Coefficient of variation [%]						
Bicycle	Hybrid			Touring		
Speed	10 km/h	15 km/h	20 km/h	10 km/h	15 km/h	20 km/h
Overall comfort	21.96	34.31	25.54	21.26	34.93	15.29
Comfort of the arms and hands	27.08	30.21	19.76	34.40	33.15	30.41
Comfort of the neck and shoulders	50.99	32.20	44.08	57.50	33.52	48.66
Comfort in the back and spine	32.32	32.70	40.54	50.78	29.66	46.92
Comfort in the seat area	24.62	16.53	20.20	40.43	15.91	32.24
Overall control	30.62	32.97	20.36	25.91	28.33	24.85
Ability to keep feet on the pedals	46.57	39.03	36.38	52.70	42.59	46.57
Ability to see straight	69.72	66.90	34.40	81.65	64.89	31.42
Ability to keep balance	42.13	52.32	42.38	53.93	54.56	46.48

The results regarding different aspects of the controllability, presented in Figure 3.23, as well as the results for the overall controllability, presented in Figure 3.21, suggest that subject's sensation of control worsens as the forward speed increases.

Moreover, the Hybrid bicycle offers more controllability than the Touring bicycle, irrespective of the speed. This trend is opposite to that of the measured yaw angle oscillations on the rumble strip patterns and on the flat pavement, for both bicycles. However, the measured data show lower magnitudes of the yaw angle oscillations for the Hybrid bicycle, as describes in section 3.6.3. The results regarding the particular issues of the controllability, presented in Figure 3.23, suggest that rider's ability to see straight decreases more on the Touring bicycle than on the Hybrid bicycle. However, the results regarding rider's ability to see straight showed large scatter from the mean values, as evident from Table 3.18. The subjects also felt better feet-pedal contact with the Hybrid bicycle, while little differences were observed in subject's tendency to balance the bicycle.

Figure 3.24 illustrates the rider's sensation of the level of danger for damaging the bicycle while traversing the rumble strip. The results show that sensation of damaging the bicycle is greater on the Touring bicycle than on the Hybrid bicycle. Also, higher speeds of 15 and 20 km/h would generate more potential danger for both of the bicycles.

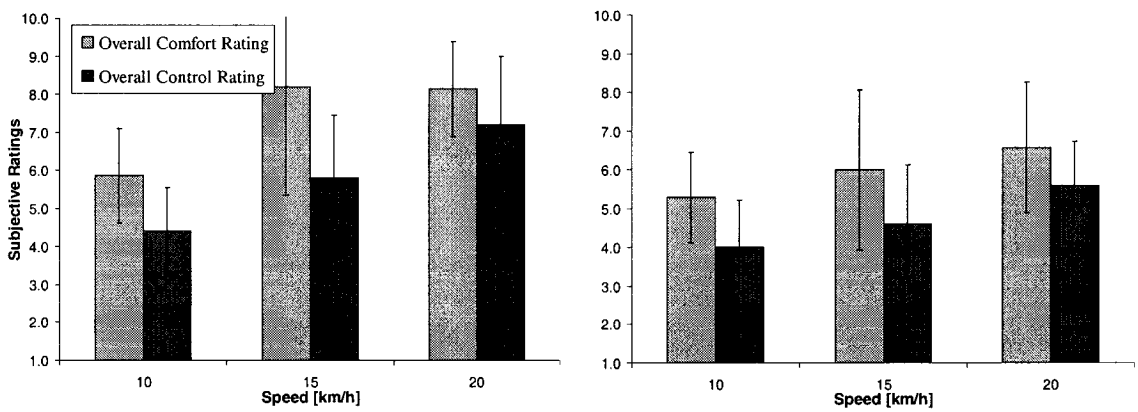

(a) Touring bicycle

(b) Hybrid bicycle

Figure 3.21: Mean and standard deviation of the subjective comfort and controllability ratings as a function of speed (Pattern: Round I): (a) Touring bicycle; (b) Hybrid bicycle.

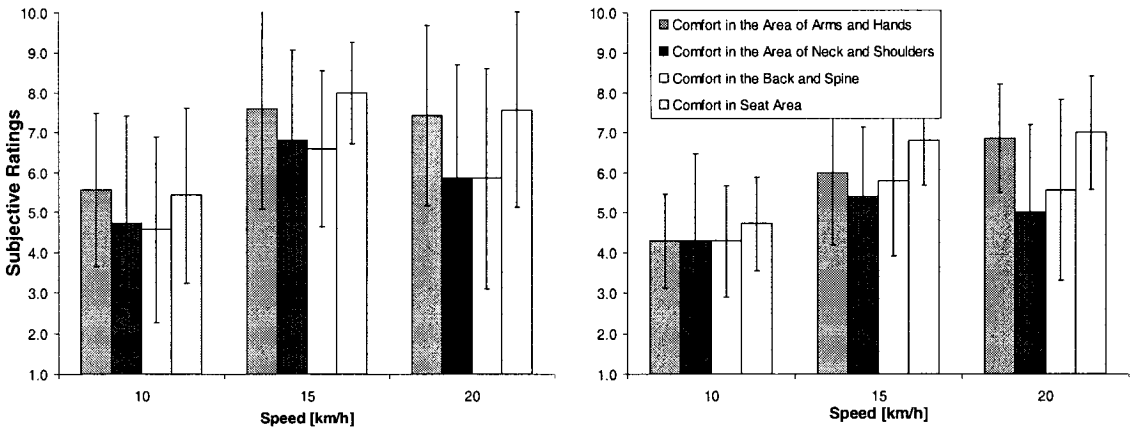

(a) Touring bicycle

(b) Hybrid bicycle

Figure 3.22: Mean and standard deviation of the subjective comfort ratings senses by different body segments as a function of speed (Pattern: Round I): (a) Touring bicycle; (b) Hybrid bicycle.

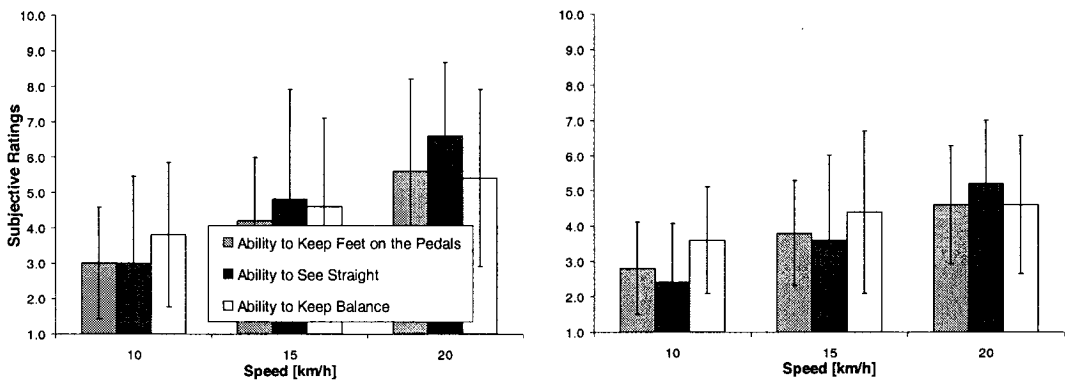

(a) Touring bicycle

(b) Hybrid bicycle

Figure 3.23: Mean and standard deviation of the subjective control ratings as a function of speed (Pattern: Round I): (a) Touring bicycle; (b) Hybrid bicycle.

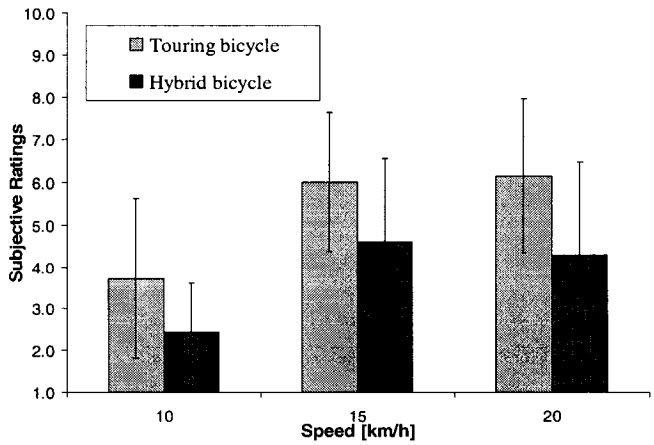

Figure 3.24: Mean and standard deviation of the subjective ratings of potential danger of damaging while traversing the rumble strip (Pattern: Round I).

3.9 SUMMARY

The experimental data for two of the bicycles traversing different rumble strip patterns at different speeds are analyzed to study ride discomfort and controllability as a function of bicycle type, rumble strip geometry and forward speed. The inter-subject and intra-subject variability of the measured data are evaluated in terms of the coefficients of variability of the mean responses. The acceleration responses measured at the handle bar and seat post, as well as the computed pitch acceleration responses, are expressed in terms of the power spectral densities, and overall RMS and VDV values. The yaw responses are expressed in terms of RMS values of the yaw angle and yaw rates. The comfort and controllability characteristics of different patterns are evaluated as relative to the data obtained for the flat pavement in term of respective RMS and VDV values. The data acquired for oblique angle of approach are also expressed in term of RMS and VDV accelerations and yaw oscillations. Subjective ratings of the ride discomfort and the controllability of the bicycles are further discussed. The experimental data are further used to examine the validity of analytical models of bicycles, developed in the following chapters.

CHAPTER 4

BICYCLE COMPONENT CHARACTERIZATION

4.1 INTRODUCTION

The identification of the rider-friendly rumble strip pattern could be more effectively carried our through development and analysis of reliable analytical model of the bicycle-rider system. The development of an analytical model would require a reliable set of systems parameters in order to accurately simulate dynamic behavior of a physical system, such as the bicycle-rider system. In general, the required set of system parameters would depend on the model complexity and the desired level of accuracy. The human body, owing to its complex biological properties, exhibits a complex dynamic response. Furthermore, the differences that occur both between and within subjects can be significant which makes it difficult to accurately measure the dynamic properties of the human body. The majority of the reported studies on human body modeling consider the visco-elastic properties of the human body based on the curve-fitting methods (Griffin, 1996; Wang and Hull, 1997). On the other hand, the geometrical and inertial properties of the bicycle as well as the visco-elastic properties of its suspension units can be more easily determined through laboratory tests. A few studies reported measured mass and pitch mass moment of inertia of the bicycle frame. Depending on the type of bicycle the mass of the bicycle frame is between 8.5 and 12.5 kg, while the pitch mass moment of inertia about the center of gravity varies between 1.25 and 2.62 kgm^2 (Waechter, 2002; Elefteriadou et al., 2000; Wilczynski and Hull, 1994). The conventional bicycle, such as the Touring bicycle, is considered to be suspended on the tires, while the

Hybrid bicycle has additional front fork suspension and the seat post suspension units. The vertical stiffness of a tire can be determined by the slope of the static load-deflection curve. The automobile tires are known to exhibit more or less linear load-deflection characteristic for a given inflation pressure, except at relatively low values of load (Wong, 1993). It is expected that the vertical stiffness of a bicycle tire would depend greatly on the type of the tire and the inflation pressure. A few studies considered vertical stiffnesses of bicycle tires ranging from 90 to 134 kN/m (Waechter, 2002; Wilczynski and Hull, 1994), depending on the type of the tire and the inflation pressure. The front fork suspension units can exhibit different stiffness and damping properties depending on the type of suspension unit. The suspension spring rate would further depend on the type of cycling performance it is used for, such as: road or off-road. For instance, Wilczynski and Hull (1994) considered the front suspension spring rate of 73.6 kN/m for an off-road cycling performance. The suspension damping, again depending on the type of suspension unit and the cycling performance it is used for, can be either Coulomb of viscous type.

4.2 BICYCLE GEOMETRIC AND INERTIAL PROPERTIES

The geometric and inertial properties of the Touring and the Hybrid bicycles are initially measured for development and analysis of the system model. These included: the location of bicycle's center of gravity; the bicycle mass and the pitch mass moment of inertia. The mass of the bicycle was measured using two weighing scales placed under the front and the rear wheel while the bicycle was lightly supported by the hand, in a horizontal position, as shown in Figure 4.1. The measured values of the front and rear

wheel loads (W_f and Wr) were used to compute the total bicycle mass and the longitudinal component of the bicycle's center of gravity (c.g):

$$m_b = (W_r + W_f)/g \tag{4.1}$$

$$L_f = L\frac{W_r}{m_b g};\ L_r = L\frac{W_f}{m_b g} \tag{4.2}$$

where m_b is the mass of the bicycle, L is its wheelbase, and L_f and L_r define the location of the mass center with respect to the front and rear wheel centers, respectively, as shown in Figure 4.1. The mass of the front wheel of the Hybrid bicycle was considered to represent bicycle's unsprung mass (m_u). The front wheel was disassembled from the rest of the bicycle and its weight was measured on the weighing scale. The sprung (m_s) mass was computed from the measured unsprung mass (m_u) and the total measured mass of the Hybrid bicycle (m_b), such as:

$$m_s = m_b - m_u \tag{4.3}$$

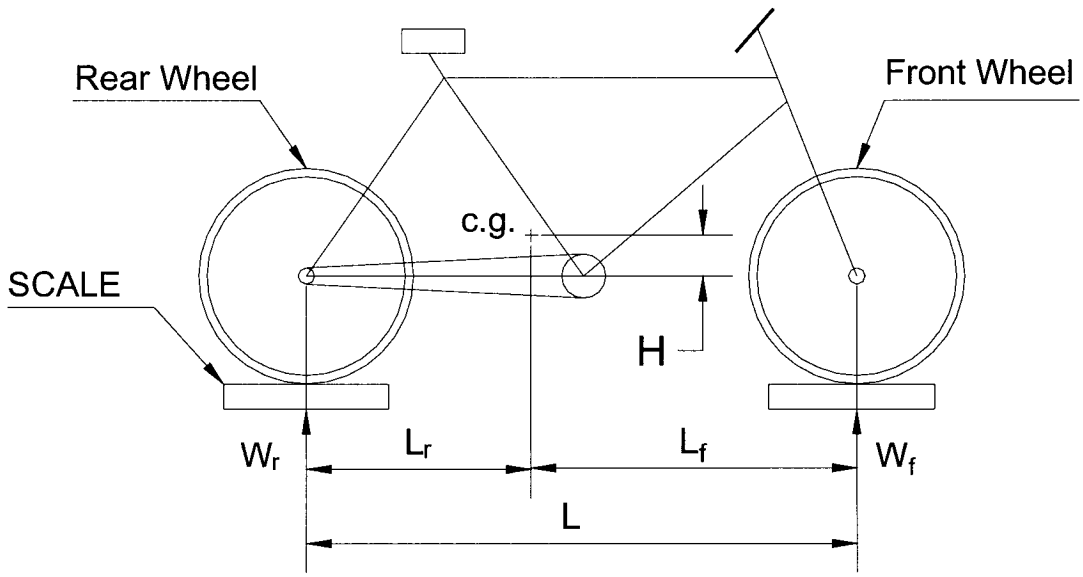

Figure 4.1: Measurement of center of gravity location of the bicycle.

The pitch mass moment of inertia of each bicycle was measured on the basis of the principle of compound pendulum pivoted around a fixed point. The pitch mass moment of inertia thus estimated about the pivot point was transferred to the bicycle's c.g. using the parallel axis theorem. The experimental procedure involved measurement of the period of free oscillations (T) of the bicycle supported around a fixed point. The bicycle was suspended by a string from a rigid frame allowing it to hang freely in the air, as shown in Figure 4.2. In order to keep the bicycle in a horizontal position, the string was attached to the bicycle's frame at a point which lies along a vertical axis passing through the bicycle's c.g., estimated from Equation (4.2), denoted as point "B" in Figure 4.2. To minimize the rotational motion of the bicycle around the attachment point on the rigid frame, denoted as point "A", the string was placed inside a metal pipe with a relatively small inner diameter, therefore restricting the motion of the string in the horizontal direction. Since the length of the string between the free end of the pipe and the attachment point on the bicycle frame was relatively short (about 5 mm), it was considered that the bicycle oscillates about point "B". A single axis accelerometer was installed on the bicycle frame, oriented along the longitudinal direction. Once the bicycle was in its equilibrium position, a small amplitude perturbation was applied to cause free oscillations of the bicycle. The accelerometer signal was recorded and analyzed to determine the period of the oscillation of the bicycle. The period of the oscillation was also measured with a stop-watch by averaging elapsed time for eight full oscillations. Three independent measurements were conducted for each bicycle. The acceleration time history obtained from acceleration transducer was also analyzed using Fast Fourier Transform (FFT) technique.

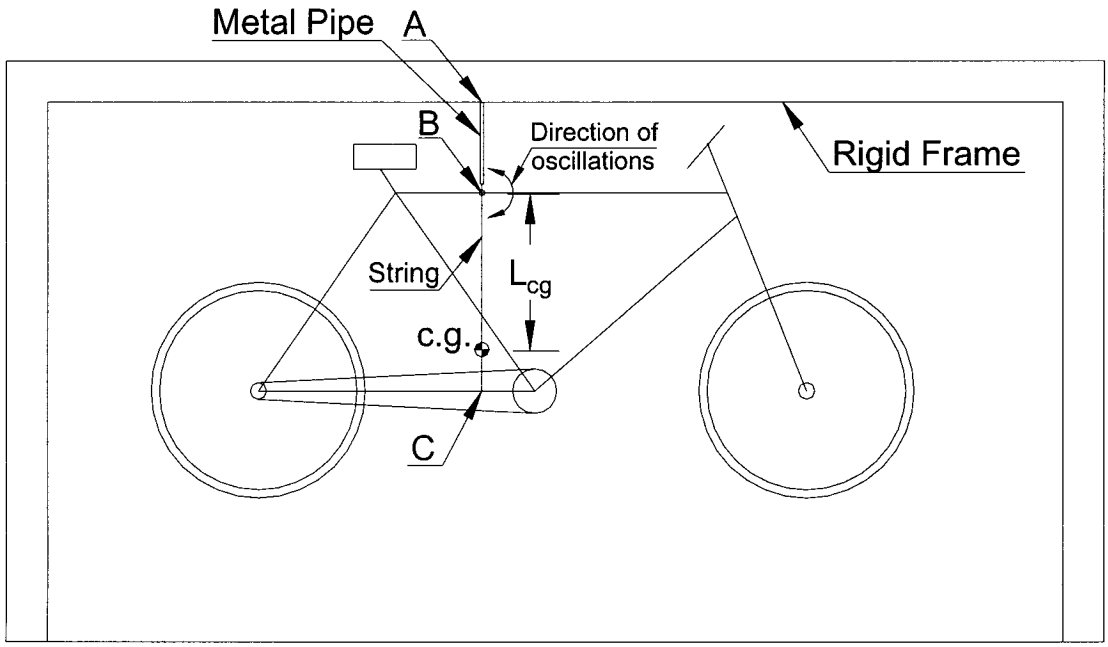

Figure 4.2: Attachment of bicycle to the rigid frame.

The analysis resulted in a single predominant frequency component, while the frequency was very close to that obtained from the stop-watch measurements. The oscillating frequencies of the Touring and Hybrid bicycles were obtained as 0.5 Hz and 0.416 Hz, respectively, resulting in oscillation periods of T = 2.0 s and T = 2.4 s. The vertical component of the c.g. was also measured by suspending the bicycle from different points along the frame. Knowing that the c.g. of the entire bicycle lies along a vertical axis passing through point "B", the string was extended from point "B" in a vertical direction downwards and attached to the frame at point "C". The bicycle was then attached at an alternate point "D" to allow it to suspend in an inclined position, as shown in Figure 4.3. The string was then extended from point "D" vertically downwards until it intersected the string connecting points "B" and "C". The point of intersection (c.g.) was considered as

the bicycle's center of mass. This measurement was repeated three times, which revealed high degree of repeatability.

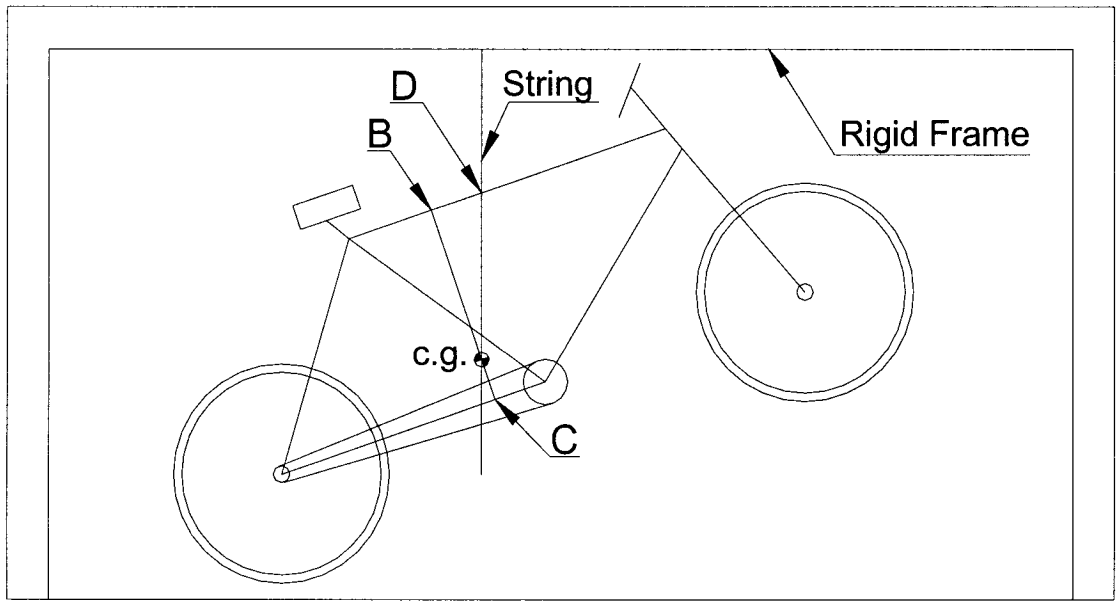

Figure 4.3: Determining location of bicycle's center of gravity.

The bicycle's pitch mass moment of inertia about point "B" was computed from the free oscillations of the compound pendulum, assuming small oscillations, such that:

$$I_B = \frac{m_b g L_{cg}}{(2\pi)^2} T^2 \tag{4.4}$$

where L_{cg} is the length of the pendulum, the distance between the pivot and attachment point on the frame "B", I_B is the pitch mass moment of inertia of the bicycle about the pivot point and m_b is its mass. The pitch mass moment of inertia about the mass center (I_b) of the bicycle is derived from:

$$I_b = I_B - m_b L_{cg}^2 \tag{4.5}$$

The measurements of the pitch mass moment of inertia of the Hybrid bicycle were conducted together with the bicycle's unsprung mass, meaning that during the experiments the front wheel was attached to the bicycle. Tables 4.1 and 4.2 summarize the measured geometric and inertial properties of the Touring and Hybrid bicycles, respectively.

Table 4.1: Geometric and inertial properties of the Touring bicycle.

Symbol	*Value*	*Description*
L	1.016 m	Wheelbase
L_f	0.533 m	Horizontal distance between the front wheel center and the c.g.
L_r	0.483 m	Horizontal distance between rear wheel hub and center of gravity
H	0.480 m	Vertical distance between the c.g. and imaginary line connecting the centers of the front and rear wheel
m_b	12.2 kg	Total bicycle mass
W_f	56.9 N	Front wheel load
W_r	62.8 N	Rear wheel load
I_b	2.755 kgm^2	Pitch mass moment of inertia of bicycle

Table 4.2: Geometric and inertial properties of the Hybrid bicycle.

Symbol	*Value*	*Description*
L	1.092 m	Wheelbase
L_f	0.557 m	Horizontal distance between the front wheel center and the c.g.
L_r	0.535 m	Horizontal distance between rear wheel hub and center of gravity
H	0.400 m	Vertical distance between the c.g. and imaginary line connecting the centers of the front and rear wheel
m_b	14.9 kg	Total bicycle mass
W_f	71.6 N	Front wheel load
W_r	74.6 N	Rear wheel load
m_s	12.9 kg	Sprung mass
m_u	2.0 kg	Unsprung mass - front wheel
I_b	3.518 kgm^2	Pitch mass moment of inertia of bicycle

4.3 CHARACTERISATION OF BICYCLE SUSPENSION COMPONENTS

Dynamic properties of bicycle suspension components, such as bicycle tires, the seat post suspension and the front suspension (incase in of the Hybrid bicycle) were experimentally measured in the laboratory. The experimental setup for measuring component force-deflection characteristics comprised of a reaction frame stand installed around an electro-hydraulic actuator generating the desired force. A strain-gage based load cell was installed between the component and the reaction frame to measure the force imparted on the component. Resulting component deflection was measured using a Linear Variable Differential Transformer (LVDT) displacement transducer integrated within the electro-hydraulic actuator. Figure 4.4 schematically illustrates the test fixture for characterizing the force-deflection properties of the bicycle tire. The same fixture was also used for measurement of force-deflection properties of the seat post and the front suspension as shown in Figure 4.5 and 4.6, respectively.

4.3.1 Bicycle Tires

The force-deflection characteristic of the bicycle tires were measured through a simple static compression. The bicycle wheel together with the tire was placed vertically in a test stand, by clamping the top and bottom edges, as shown in Figure 4.4. The hydraulic actuator was displaced to achieve the desired static force, while the corresponding deflection of the tire and wheel assembly was measured. The actuator displacement was gradually increased in increments of 2.5 mm until the total wheel deformation approached in the 20-25 mm range.

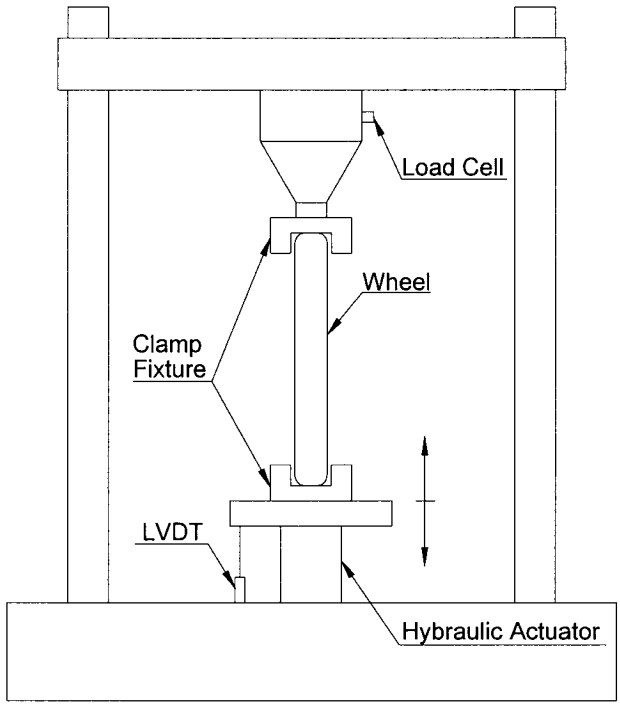

Figure 4.4: The experimental set up for tire characterization.

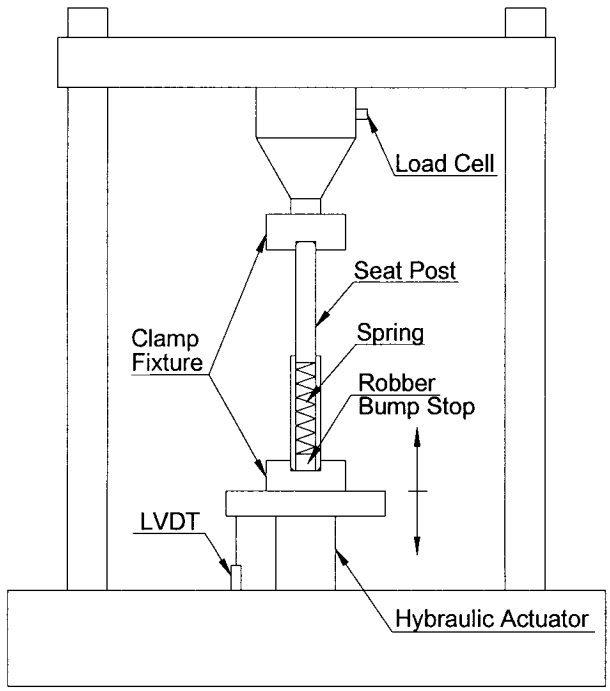

Figure 4.5: The experimental set up for characterizing the seat post suspension.

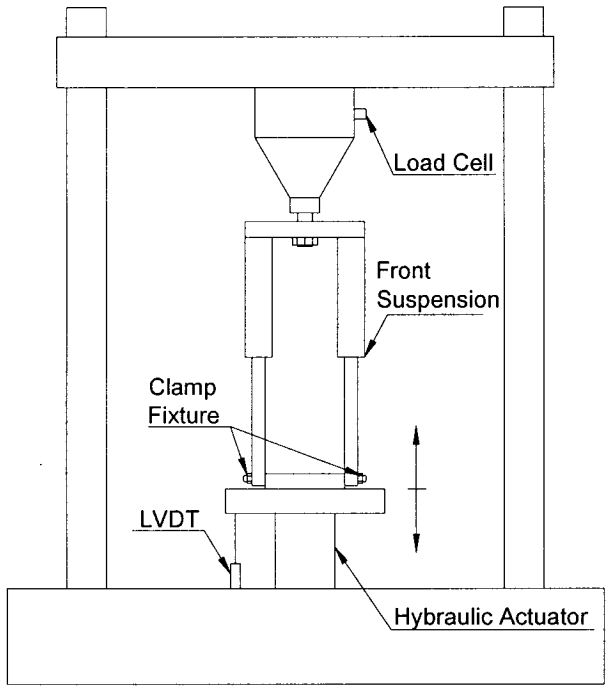

Figure 4.6: The experimental set up for characterizing the front suspension.

The actuator deflection was then gradually decreased until the preload diminished to achieve a complete loading and unloading cycle. The experiment was repeated for three different inflation pressures of the tire to characterize the force-deflection properties as a function of the pressure. For the Touring bicycle tire, the experiments were performed for kPa 482 (70 psi), 586 kPa (85 psi) and 655 kPa (95 psi). The Hybrid bicycle tire was characterized under 413, 482, and 517 kPa (60, 70 and 75 psi). It should be noted that the recommended inflation pressure for the Touring and Hybrid bicycles are 655 kPa (95 psi) and 517 kPa (75 psi), respectively. These pressure values were used during the trials on the prototype rumble strips.

In the above described experimental set up, the applied force acts on the wheel from both sides, resulting in deflections of both sides of the tire, while in reality the tire

makes contact with the ground from only one side. The measured force-defection characteristics are thus considered to provide equivalent wheel spring rate (k_e). In order to calculate tire stiffness (k_t) when loaded only from one side, the wheel in the experimental set up was modeled as a series connection of two independent springs, where each spring represents the top and bottom tire loading, as shown in Figure 4.7. Assuming identical stiffness of the wheel from both sides, the tire and wheel stiffness is estimated from:

$$\frac{1}{k_e} = \frac{1}{k_t} + \frac{1}{k_t} \qquad (4.4)$$

$$k_t = 2 \cdot k_e$$

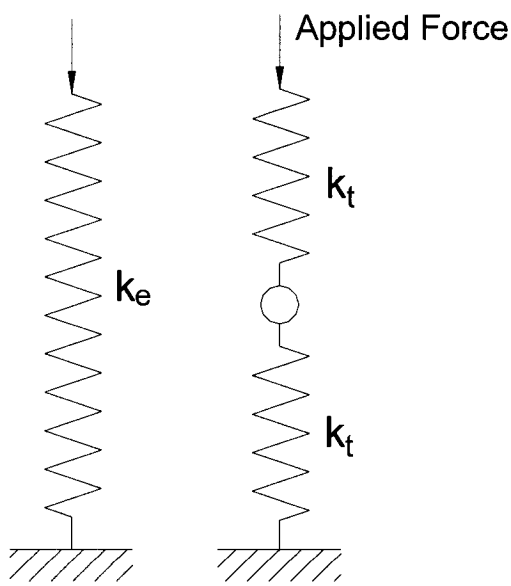

Figure 4.7: Model of the wheel and tire in the experimental set up.

Figures 4.8 and 4.9 present the measured force-deflection characteristics for the Touring and the Hybrid bicycle tires, respectively, for three different inflation pressures considered. It can be observed from the plots that for a given inflation pressure, the force-deflection characteristics for both tires exhibits reasonable level of linearity, except for relatively low values of tire load. The relatively large deflections under light loads around the free tire position is attributed to relatively soft carcass plies. Consequently, it can be assumed that the vertical stiffness of the bicycle tire is independent of load in the range of practical interest, since the tire is normally subject to static loads well above the initial nonlinear range. The static vertical stiffness of each tire is determined from the slope of the mean force-deflection curve, which are summarized in Table 4.3. The results show that the spring rates generally increase with the inflation pressure. The Touring bicycle tire, however exhibits only slight increase in the stiffness values, when the inflation pressure is increased in from 586 kPa (85 psi) to 655 kPa (95 psi).

Table 4.3: Bicycle tire spring rates.

Bicycle	*Tire Inflation Pressure [kPa]*	*Tire Spring Rate [kN/m]*
Touring	482	101.90
	586	112.10
	655	114.13
Hybrid	413	90.38
	482	93.80
	517	97.30

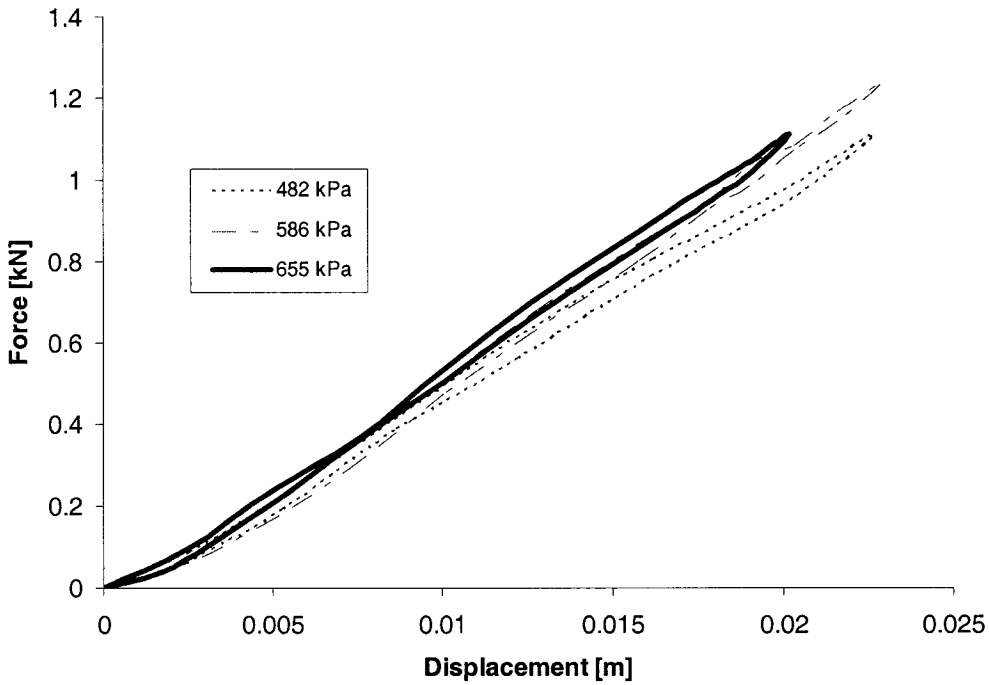

Figure 4.8: Force-displacement characteristics of the Touring bicycle tire.

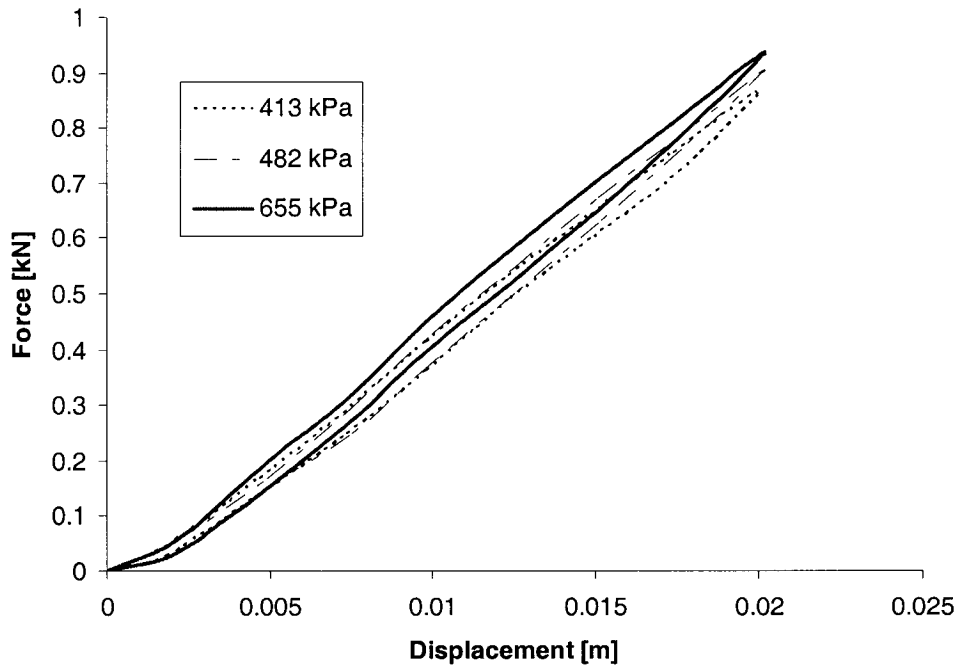

Figure 4.9: Force-displacement characteristics of the Hybrid bicycle tire.

4.3.2 The Seat Post Suspension

The seat post suspension consists of a rectangular cross-section bar which can slide freely inside a hollow cylindrical tube against a suspension spring supported on a rubber bump stop to limit the maximum travel, as illustrated in Figure 4.5. The experiment involved gradual static compression/extension of the seat post assembly by applying discrete deflections in increments of 2.5 mm through the displacement control of the electro-hydraulic actuator. A preload of 43.5 kg was initially applied displacing the servo-hydraulic actuator and monitoring the resulting force, which corresponded to half of the suspension's travel. The suspension was gradually compressed until the contact with the bump stop was attained, which was observed through the rapid increase in the force. The suspension was then gradually unloaded until the zero reading of the load cell, and gradually compressed to its initial preload. Figure 4.10 shows the seat post suspension force-displacement characteristics. The suspension exhibits linear properties prior to making contact with the bump stop, which could be characterized by a high spring rate clearance spring. The spring rate of the seat post suspension, calculated from its force-displacement curve in the linear range was obtained as 20.75 kN/m, while that of the bump was estimated as 2480 kN/m.

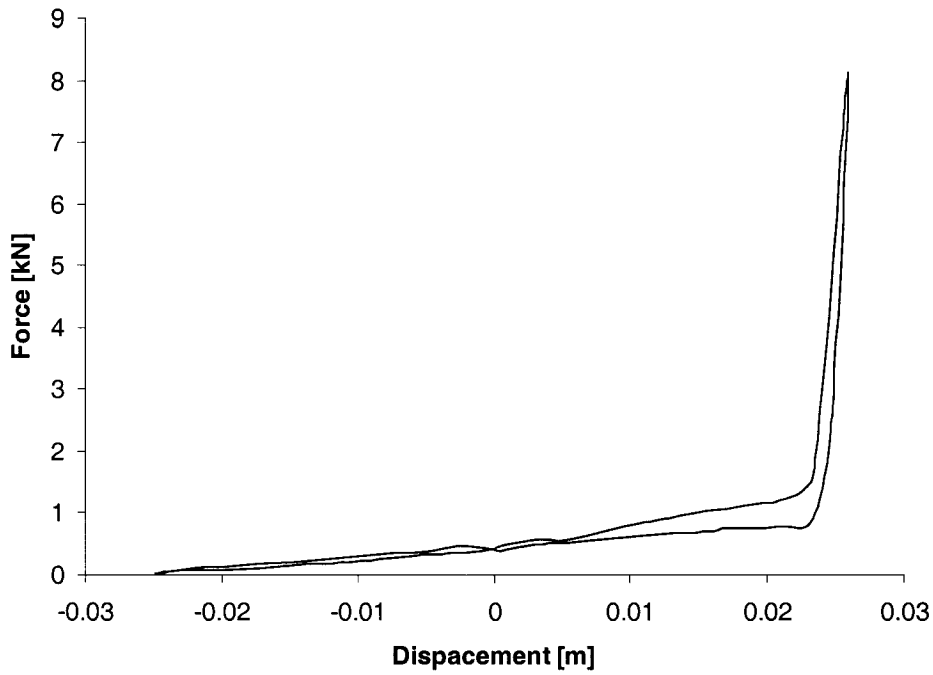

Figure 4.10: Force-deflection characteristics of the seat post suspension (Hybrid bicycle).

4.3.3 Front Suspension

The stiffness of the front suspension of the Hybrid bicycle was measured by applying sinusoidal deflections of 3.125, 6.35 and 10.15 mm amplitude at a frequency of 0.1 Hz. The front suspension of the Hybrid bicycle was mounted as illustrated in Figure 4.6. The suspension was installed between the vibrating platform and the reaction frame through the load cell. The measured force-deflection characteristics of the front suspension, shown in Figures 4.11, 4.12 and 4.13 exhibit a considerable hysteresis due to large Coulomb friction in the suspension. The enclosed area in the force-deflection characteristic plot represents the energy dissipated per cycle. The stiffness of the front suspension was calculated from the slope of the mean force-deflection curve, while the magnitudes of the Coulomb friction force was estimated as one-half the difference in

forces during loading and unloading near zero deflection. The analysis revealed spring rate of 22.12 kN/m and Coulomb friction of 150 N.

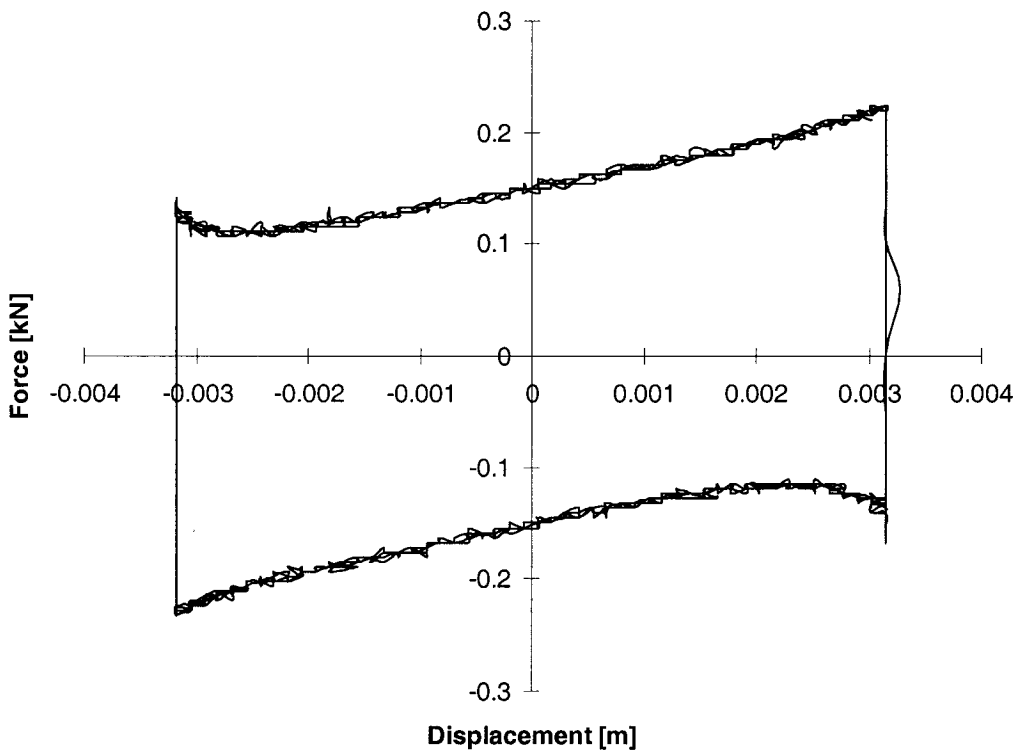

Figure 4.11: Force-deflection characteristics of the front suspension under 3.125 mm amplitude at 0.1 Hz (Hybrid bicycle).

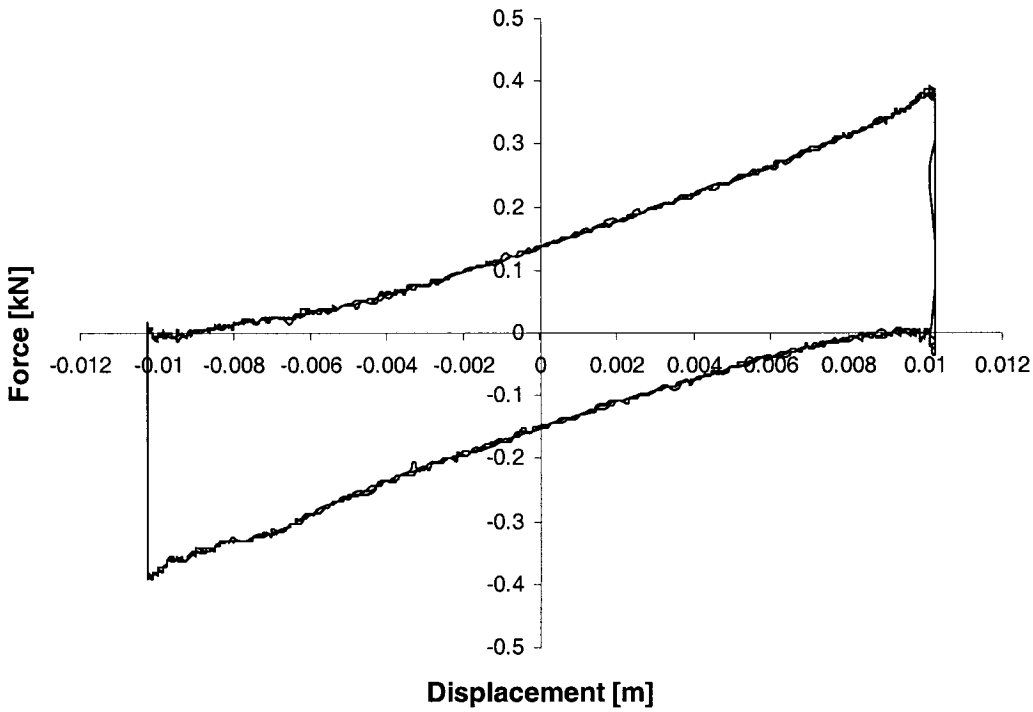

Figure 4.12 Force-deflection characteristics of the front suspension under 10.35 mm amplitude at 0.1 Hz (Hybrid bicycle).

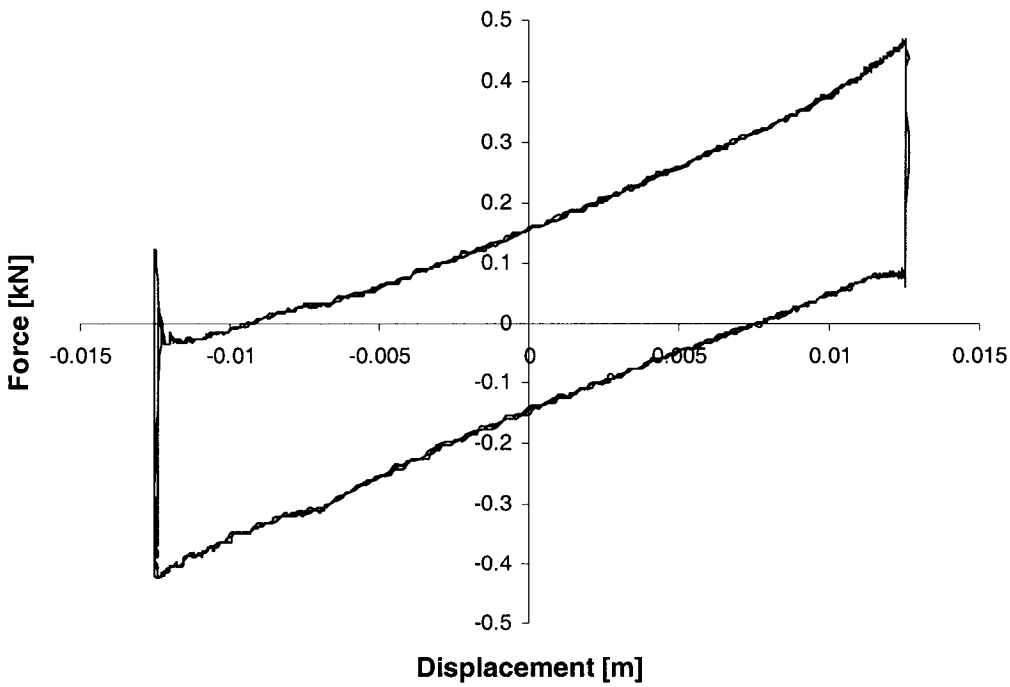

Figure 4.13: Force-deflection characteristics of the front suspension under 12.15 mm amplitude at 0.1 Hz (Hybrid bicycle).

4.4 SUMMARY

The inertial and geometric properties, such as mass, pitch mass moment of inertia and the location of the center of gravity of the Touring and the Hybrid bicycles were experimentally measured, in order to identify the essential parameters for development and analysis of the bicycle-rider models. The force-deflection properties of the suspension components, namely the tires; front suspension and seat post suspension were characterized through measurements in the laboratory. The identified bicycle parameters and component properties are applied to the analytical models of the bicycle and rider system in the following chapter.

CHAPTER 5

ANALYTICAL MODELING OF BICYCLE-RIDER SYSTEM

5.1 INTRODUCTION

The bicycle interaction with the rumble strip pattern is strongly dependent upon many bicycle, rider and pattern related parameters in a highly complex manner. The identification of rider-friendly pattern and the analysis of the impact of bicycle interactions with the rumble strip, specifically in view of the shock and vibration transmitted and controllability, could be evaluated through development and analysis of a bicycle-rider system model. Such a model could not only facilitate the relative analysis of different rumble strip pattern but would also provide considerate insight into the role of the bicycle design parameters and rider behavior.

The term "bicycle-rider system", which is mainly used in this study, refers to a coupled dynamical system consisting of the human rider and the bicycle. The development of an appropriate rider model, however, is a formidable task. The human body is a complex biological system, whose behavior is dependent upon the posture assumed, anthropometric parameters and general physical fitness of the individuals, in a highly complex manner. The human body is known to absorb/dissipate significant amount of vibration energy, and thus expected to strongly influence the dynamic behavior of coupled system. A number of studies conducted on the seated human occupant and suspension seat have clearly established that the human occupant significantly contributes to the overall vibration isolation performance of the coupled human seat system (Griffin, 1995). Other studies on biodynamic responses suggested

several resonances of the biological system in the frequency range of bicycle vibration (up to 50 Hz), as observed from the measured data. Although, a number of biodynamic models of seated human occupant have been developed for applications in the vehicular seating (Boileau, 1995; Tchernychouk, 1999), only minimum effort have been made to derive similar models for postures assumed by the bicycle rider. Moreover, the reported models have been mostly developed under whole-body vibration exposure in the 0.5 to 20 Hz frequency range. The human body responses to vibration also exhibit considerable nonlinear behavior. However, the nonlinearities may be neglected if the model is restricted to small magnitudes of motions (Wang and Hull, 1997). For bicycle applications, contributions due to rider dynamics may be more significant due to considerably larger rider mass compared to that of a bicycle. On the basis of reported studies on the biodynamic models of the seated body and those of the rider, it may be ascertained that rider dynamics may be modeled through equivalent mechanical systems comprising rigid bodies, linear springs and viscous dampers (Waechter et al., 2001; Wilczynski and Hull, 1994; Wang and Hull, 1997).

A conventional bicycle can be represented as a two-degrees-of-freedom dynamic system comprising the sprung mass representing the bicycle body and associated components suspended on the tires, and assuming negligible contributions due to deformations of the frame. In case of the suspended bicycle, the bicycle mass could be represented by a sprung mass and unsprung masses of the wheels supported on the suspension and tires. In this Chapter, the reported models of the rider are reviewed and a simple rider model is proposed. The rider model is integrated to the bicycle model, which

is formulated on the basis of its components and component properties identified in the previous chapter.

5.2 DEVELOPMENT OF THE RIDER MODEL

As opposed to the road and off-road vehicles with human occupants, the dynamic responses of the bicycle-rider system are largely influenced by the dynamics of the rider, due to the larger mass of the rider compared to that of the bicycle. The human body is known to exhibit complex non-linear characteristics in its dynamic response to vibration, which varies greatly between and within individuals (Griffin, 1996). Furthermore, a bicycle rider tends to constantly change body posture in response to varying road conditions, and vary the rate of pedaling depending upon the localized grade of the road surface. Changes in the body posture will cause changes in the muscle tension and thus the dynamic properties on the human body. Different analytical models of the human occupant have been developed for the seated and the standing postures (Boileau, 1995; Tchernychouk, 1999) These models for the seated posture are considered valid for sitting with upright back, supported and unsupported, hands in the lap position, and exposed to vibration in the frequency range (0.5-20 Hz) that is considerably lower than that of vibration encountered on the bicycle. Such models thus can not be applied for the study of bicycle-rider systems. Waechter et al. (2002), Wilczynski and Hull (1994) and Wang and Hull (1997) have proposed mechanical equivalent model of the bicycle riders in the seated position and riding on flat paved roads, and for the standing posture for off-road cycling.

In this study, a rider model is developed to simulate a seated rider pedaling at a constant rate. The structure of the model is conceived on the basis of Waechter et al. (2002), and Wang and Hull (1997). The model is formulated as a combination of a single rigid body representing the rider's torso and thighs, and supported on the handle bar and the seat through linear springs and viscous damping elements. The rider's torso and thighs are modeled as a non-uniform beam, with center of mass closer to the seat support in accordance with mass distribution and anthropometric properties (Wilczynski and Hull, 1994; Wang and Hull, 1997). The beam is modeled as an inclined rigid body to represent the inclined torso of the rider during cycling, as illustrated in Figure 5.1. An inclination angle of α_t, with respect to the horizontal axis is considered. The proposed model considers the rider's head being rigidly connected to the torso. A visceral mass is introduced as a point mass to represent the viscera within the torso. The visceral mass is coupled with the primary torso mass at the midpoint between the shoulders and the hip through a linear spring and damper, constrained to allow visceral mass motion perpendicular to the long axis of the torso (Wang and Hull, 1997). The visceral mass is assumed to be 15 percent of the total body mass (Minetti and Belli, 1994).

The hand-arm system is modeled as a single point mass, attached to the torso at the vicinity of the shoulders, coupled with the handle bar through a parallel combination of a linear spring and damper. The spring and damping elements, representing the visco-elastic properties of the hand-arm structure, are constrained to deform along an axis normal to the longitudinal axis of the torso mass. Rider's legs are modeled as a mass, lumped with the torso mass in the vicinity of the rider hip, since the mass acting on the pedals does not exceed 12 percent of the entire body mass (Pheasant, 1986). The lumped

torso mass is further suspended at the hip by linear spring and damping elements supported by the bicycle seat. This particular spring-damper combination is permitted to deform along the vertical axis of the bicycle or the seat. The rotational flexibility of the rider's hinge-point near the hip-joint is represented by a combination of torsional stiffness and damping (k_{rot}, c_{rot}) at the seat support, as shown in Figure 5.1. The rider model parameters, partially taken from the reported studies (Wilczynski and Hull, 1994; Wang and Hull, 1997), are summarized in Table 5.1. These include the anthropometric parameters, and visco-elastic properties of the hand-arm and visceral mass.

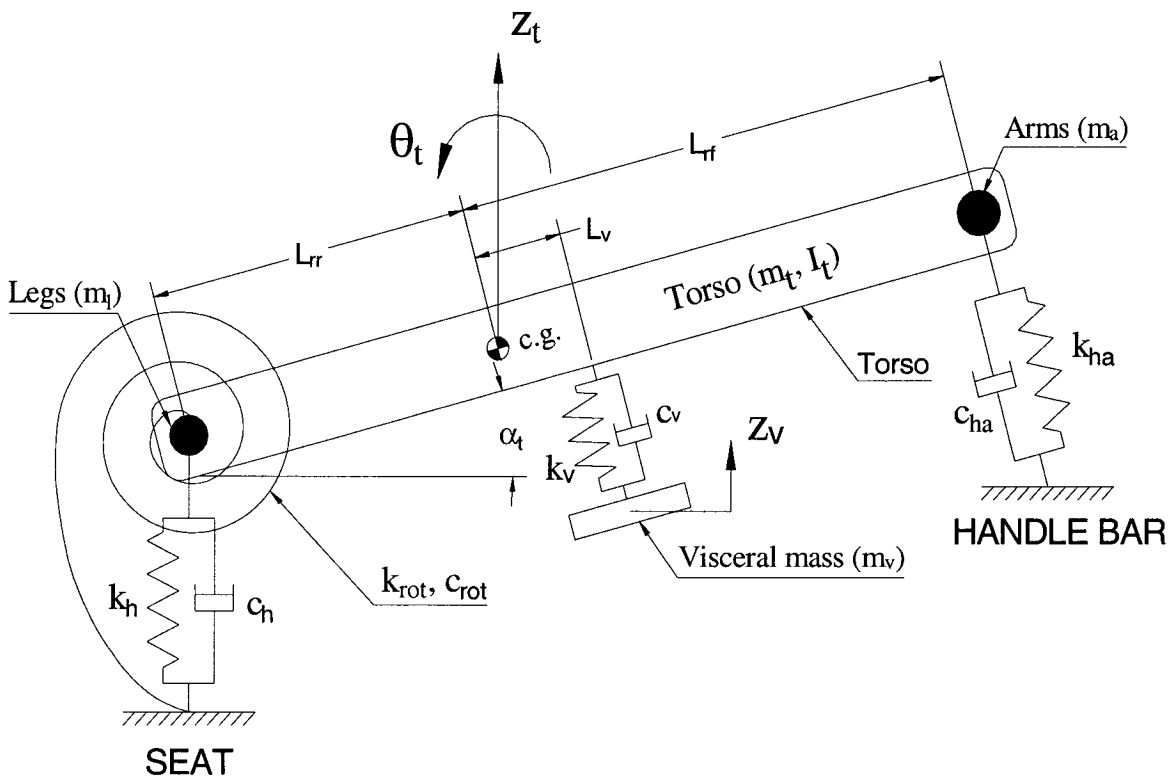

Figure 5.1: A mechanical equivalent representation of the bicycle rider.

The proposed rider model comprises linear elements and three-degree-of-freedom system, namely the vertical motion of the torso mass, z_t; the pitch motion of the torso, θ_t;

and the vertical motion of the visceral mass, z_v. The viscera mass is considered to be 15 percent of the total body mass (Minetti and Belli, 1994), such that:

$$m_v = 0.15 \cdot (m_t + m_l + m_a + m_v) \tag{5.1}$$

where m_v, m_t, m_l and m_a are the masses due to viscera, torso, legs and arms, respectively. The stiffness and the damping properties of the rider's hip and buttocks were selected on the basis of those reported by from Wilczynski and Hull (1994). The damping coefficient, however, was judged to be significantly high resulting in overdamped modes. The damping coefficient c_h was thus reduced to 500 Ns/m to achieve underdamped modes. The torsional stiffness and damping properties of the rotational spring element are selected as 5 kNm/rad and 50 Nms/rad, respectively. The inclination angle, α_t, was defined as the angle between rider's torso and the horizontal plane. The angle was measured on subjects sitting on the Touring and Hybrid bicycle using a protractor. The mean values of the measured angles for the Touring and Hybrid bicycles were obtained as 35 and 45 degrees, respectively.

According to the selected anthropometric model parameters, the total mass of the rider model is 77.48 kg, which is close to the mean body mass of the subject population used in this study (78.6 kg). The model yields the rider mass distribution as 59 and 41 % of the body mass supported on the seat and on the handle bar, respectively. It has been reported that approximately 30 % of the body mass is supported by the hands and arms on the handle bar (Wang and Hull, 1997). The model mass supported on the handle bar (41%) is larger than the reported values of 30%.

Table 5.1: Bicycle rider model parameters.

Model Component	*Parameter*	*Value*	*Source*
Torso	Mass, m_t, [kg]	32.98	[27]
	Mass moment of inertia, I_t, [kgm^2]	1.827	[27]
	L_{rr} [m]	0.31	[27]
	L_{rf} [m]	0.2	[27]
Hand-Arm System	Mass, m_a, [kg]	7.7	[27]
	Stiffness, k_{ha}, [kN/m]	14.5	[27]
	Damping, c_{ha}, [Ns/m]	595	[27]
Legs	Mass, m_l, [kg]	25.18	[27]
Hip	Stiffness, k_h, [kN/m]	47.6	[27]
	Damping, c_h, [Ns/m]	500	Estimated
Hinge Joint	Stiffness, k_{rot}, [kNm/rad]	5	Estimated
	Damping, c_{rot}, [Nms/rad]	50	Estimated
Visceral Mass	Mass, m_v, [kg]	11.62	[28]
	L_v [m]	0.045	[28]
	Stiffness, k_v, [kN/m]	21	[28]
	Damping, c_v, [Ns/m]	29.4	[28]

5.3 DEVELOPMENT OF THE BICYCLE MODEL AND ITS VALIDATION

From modeling point of view, a conventional bicycle can be represented as a dynamic system consisting of the bicycle frame mass suspended on the tires, assuming negligible contributions due to deformations of the bicycle frame. Each bicycle tire is modeled as a parallel combination of linear spring and damping element, assuming point contact with the road surface. The relatively high stiffness and low width of the bicycle tire, in-general, yields small contact patch area with the road surface, which can justifiably be represented as a point-contact with the road in the pitch plane. The Touring bicycle is thus represented by a two-degree-of-freedom (DOF) model in the pitch plane in

Figure 5.2. The analytical model of the Hybrid bicycle however, would differ due to presence of the front-fork suspension and seat post suspension. The Hybrid bicycle considered in this study, however, revealed considerably high Coulomb friction in the front fork suspension, as evident from the measured data presented in Figures 4.11, 4.12 and 4.13. The suspension often exhibits lock-out due to high friction and relatively small mass of the bicycle frame supported on the front fork. The front fork suspension of this bicycle is thus considered as locked out resulting in directly coupling the sprung and unsprung masses. The seat post of the Hybrid vehicle is considered to possess negligible mass, while its elastic properties are directly coupled with the stiffness of the rider model at the seat post support. The Hybrid bicycle model thus reduces to be identical to that of the conventional bicycle (Figure 5.2).

Assuming linear stiffness and damping properties of the tires, and small magnitudes of pitch oscillations, and considering zero road input, the linearized equations of motion of the bicycle alone can be expressed in the following manner:

$$[M]\{\ddot{q}\}+[C]\{\dot{q}\}+[K]\{q\}=0 \tag{5.2}$$

where q is the vector of generalized coordinates: bicycle centroidal bounce motion, z, and bicycle pitch about the centroid, θ:

$$\{q\}=\{z \quad \theta\}^T \tag{5.3}$$

[M], [K] and [C] represent system's mass, stiffness and damping matrices given by:

$$[M]=\begin{bmatrix} m_b & 0 \\ 0 & I_b \end{bmatrix} \tag{5.4}$$

$$[K] = k_t \begin{bmatrix} 2 & (L_f - L_r) \\ (L_f - L_r) & (L_f^2 + L_r^2) \end{bmatrix} \tag{5.5}$$

$$[C] = c_t \begin{bmatrix} 2 & (L_f - L_r) \\ (L_f - L_r) & (L_f^2 + L_r^2) \end{bmatrix} \tag{5.6}$$

The model parameters for the Touring and Hybrid bicycles are summarized in Table 5.2.

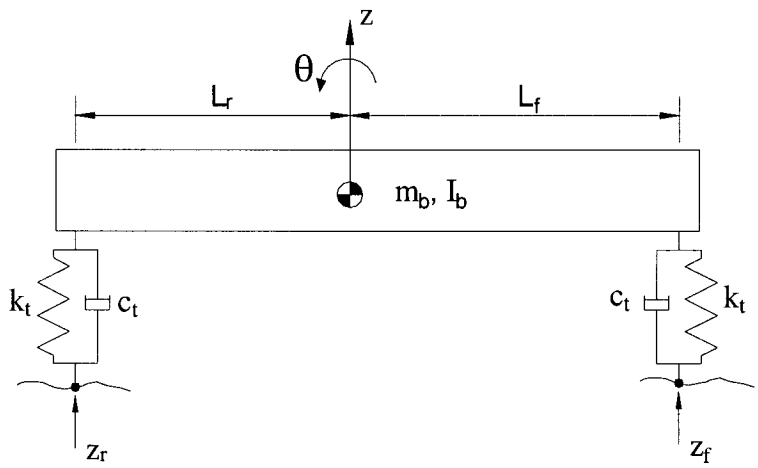

Figure 5.2: 2-DOF in-plane bicycle model.

Table 5.2: Parameters for the Touring and the Hybrid bicycle models.

Parameter	*Touring*	*Hybrid*
Sprung mass, m_b, [kg]	12.2	14.9
Pitch mass moment of inertia, I_b, [kgm^2]	2.755	3.518
Tire stiffness, k_t, [kN/m]	114.0	97.3
Tire damping, c_t, [Ns/m]	85.0	85.0
Front wheel to c.g. distance, L_f, [m]	0.533	0.557
Rear wheel to c.g. distance, L_r [m]	0.483	0.535

In order to validate developed analytical bicycle models, the dynamic responses of the bicycles alone are measured on the smooth flat surface, comprised of plastic tiles, in order to minimize the influence of the road roughness on bicycle vertical and pitch responses. The vertical acceleration responses of the Touring and the Hybrid bicycles are measured at the handle bar and at the seat post, using the instrumentation described in Chapter 2 (section 2.4). In order to obtain the responses of the bicycle alone, during the experiment, the bicycle was lightly supported at the handle bar. The bicycle was pushed forward at an approximate speed of 4 km/h, by monitoring through the speed-o-meter installed on the bicycle's handle bar. Four independent trials are conducted for each bicycle while the duration of the recorded signals for each trial was approximately 12 seconds. Since the weight of the Touring and Hybrid bicycles (12.2 and 14.9 kg, respectively) was not sufficient to provide for the bicycle tires to operate in a linear range, as discussed in Chapter 4 (section 4.3.1), each bicycle was equipped with an additional load of 36.2 kg. The load was in the form of sand bags, rigidly attached to the bicycle frames close to their respective centers of gravity. The inflation pressure inside the Touring and Hybrid tires during the experiment was 655 kPa (95 psi) and 517 kPa (75 psi), respectively. Figures 5.3 and 5.4 present mean measured vertical accelerations at the handle bar and at the seat post expressed in terms of their power spectral densities for the Touring and Hybrid bicycle, respectively. The results also show PSD of pitch acceleration of the bicycle frame, as derived from Equation (3.1). The results for the Touring bicycle show the resonant frequency of the vertical motion at 10.5 Hz, at both the handle bar and the seat post spectra, while the pitch angular acceleration of the Touring bicycle tends to peak in the vicinity of 20 to 22 Hz. The handle bar and the seat

post acceleration spectra on the Hybrid bicycle exhibits peak at 9 Hz while the pitch acceleration spectra reveals a resonant frequency at 19 Hz. It can be noted that the Hybrid bicycle's vertical and pitch motions resonate at lower frequencies compared to those of the Touring bicycle. This can be attributed to the Hybrid bicycle's softer tire spring rates and its higher mass compared to that of the Touring bicycle, as evident from the measured data presented in Chapter 4.

The two damped natural frequencies of the Touring and Hybrid bicycle models are computed from the eigenvalues of their respective model characteristic equations while the dominant deflection modes are identified from the eigenvectors. The masses of the Touring and Hybrid bicycle models are adjusted as 48.4 and 51.1 kg, respectively, in order to account for the loads (36.2 kg) placed on each bicycle during the experiment while the pitch mass moment of inertia of the bicycles remained unchanged, assuming that the loads were placed close to bicycle's respective centers of gravity. The tire stiffness of the Touring and Hybrid bicycles is considered at 655 kPa (95 psi) and 517 kPa (75 psi), respectively. Table 5.3 summarizes damped natural frequencies together with the predominant deflection modes for the Touring and Hybrid bicycle models. The model results show a good overall correlation with the respective measured data for both the Touring and Hybrid bicycles. Both bicycle models show slightly higher bounce frequencies compared to the respective measured data while the pitch frequencies for both models exhibit opposite trends. The difference can be attributed to uncertainties in measured bicycle model parameters, especially in measured values of the bicycles pitch mass moments of inertia.

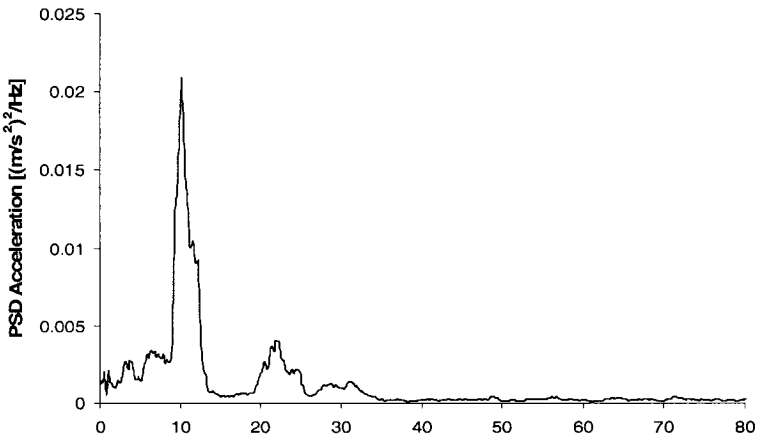

(a) Handle Bar Acceleration

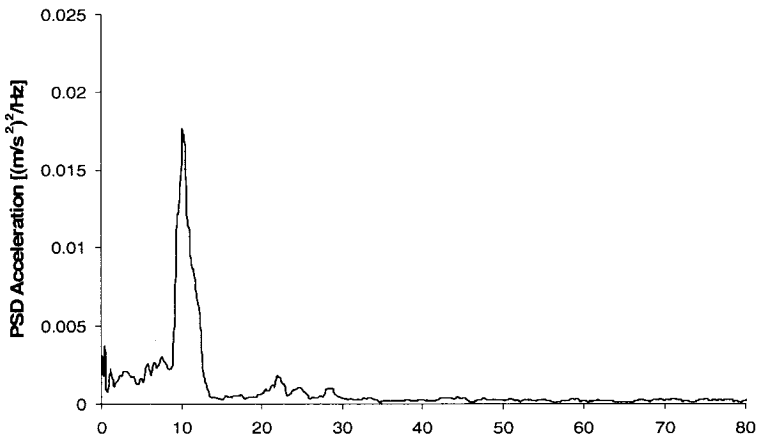

(b) Seat Post Acceleration

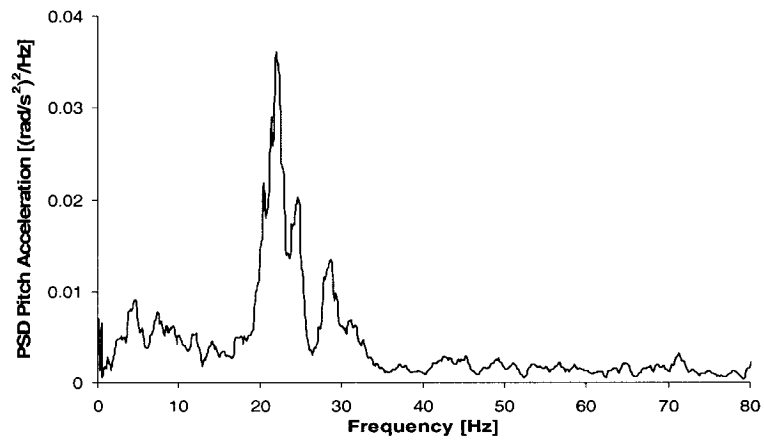

(c) Pitch Acceleration

Figure 5.3: Mean measured vertical and pitch acceleration responses of the Touring bicycle alone acquired on the smooth surface (Speed: 4 km/h): (a) Handle bar acceleration; (b) Seat post acceleration; (c) Pitch acceleration.

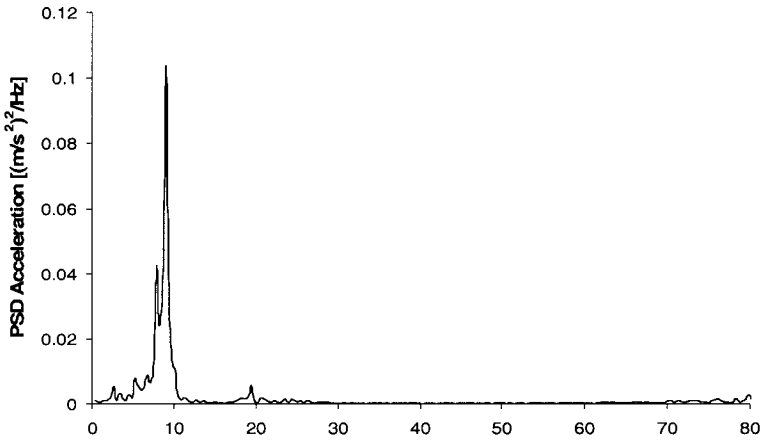

(a) Handle Bar Acceleration

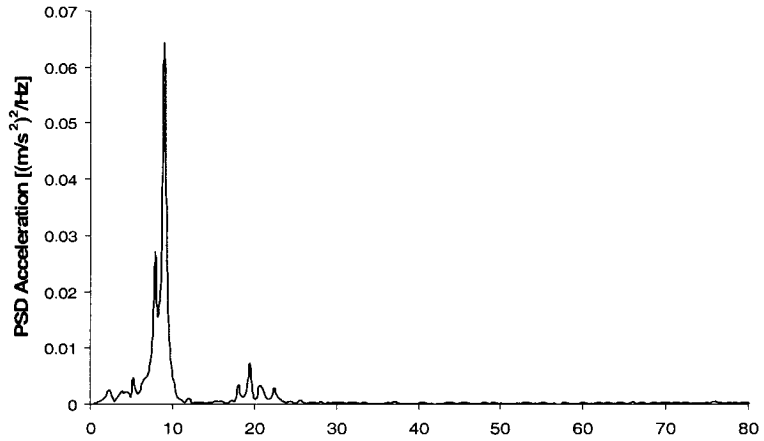

(b) Seat Post Acceleration

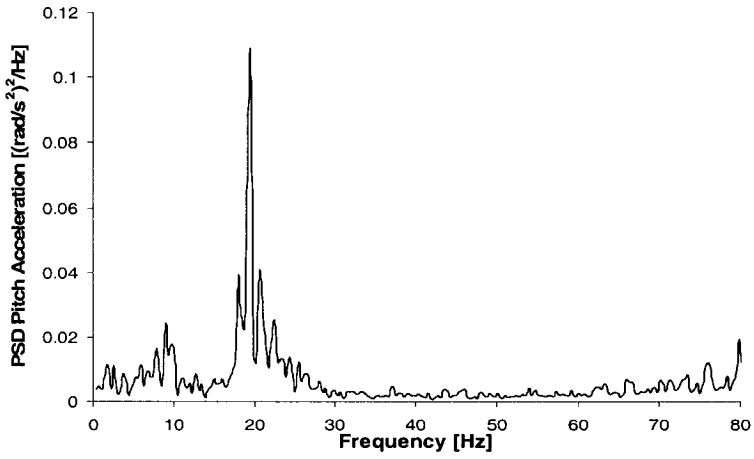

(c) Pitch Acceleration

Figure 5.4: Mean measured vertical and pitch acceleration responses of the Hybrid bicycle alone acquired on the smooth surface (Speed: 4 km/h): (a) Handle bar acceleration; (b) Seat post acceleration; (c) Pitch acceleration.

Table 5.3: Damped natural frequencies and corresponding predominant deflection modes for the Touring and the Hybrid bicycle models.

Bicycle	*Deflection mode*	*Damped natural frequency [Hz]*
Touring	Bounce	10.1
	Pitch	21.5
Hybrid	Bounce	9.8
	Pitch	19

5.4 DEVELOPMENT OF THE BICYCLE-RIDER MODEL

For the purpose of dynamic modeling, the bicycle-rider system can be approximated as a base excited mechanical system consisting of two major subsystems: the human rider and the bicycle, as illustrated in Figure 5.5. The development of human rider model, however, forms the most challenging task. Owing to the complex dynamic behavior of the biological system and its strong dependence on various anthropometric and postural factors, only limited efforts have been made to develop models of the bicycle rider. A number of mechanical equivalent models of the seated and standing individuals exposed to base motion have been proposed, where the model parameters are identified by curve-fitting a measured response, such as driving-point mechanical impedance or apparent mass (Boileau and Boileau, 1995; Griffin, 1996). There is a wide variation in the identified parameters with little association with the properties of the biological system. A few studies have also proposed mechanical equivalent models of the bicycle-riders, as discussed in section 5.1 (Waechter et al., 2001; Wilczynski and Hull, 1994; Wang and Hull, 1997).

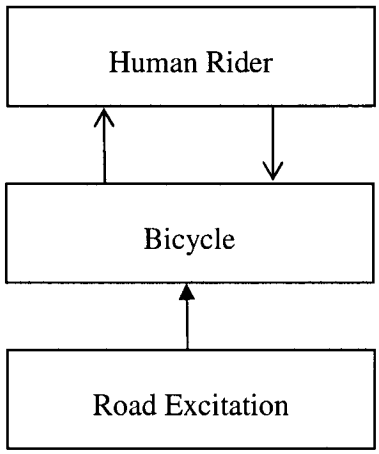

Figure 5.5: Blocks diagram representation of the bicycle-rider system.

The development of an analytical model of the bicycle, on the other hand, requires integration of the component models, such as tires, frame and suspension. While a number of tire models have been developed for the automobiles and heavy vehicles, only a few studies have reported the properties of bicycle tires (Hull et al., 1997; Waechter et al., 2001). Captain et al. (1979) compared four different analytical tire models suitable for dynamic vehicle simulation: the point contact tire model, rigid tread bend tire model, fixed foot print tire model and adaptive footprint tire model. Because of its analytical simplicity, a point contact tire model is most commonly used for vehicle ride evaluations (Dhir and Sankar, 1997). It has been reported that compared to other tire models, the point contact model tends to overestimate the transmitted tire forces. The point contact model is represented as a combination of parallel spring and damper, where the terrain contact occurs through a single terrain point follower located vertically beneath the center of the wheel (Dhir and Sankar, 1997). The vertical foot-print force results from the deflection of the spring and dashpot caused by motion of the wheel relative to the terrain profile. The schematic representation of the point contact model is shown in Figure 5.6. The terrain follower is also capable of leaving the ground to

simulate wheel hop condition. The terrain profile is defined through a look-up table containing horizontal and vertical coordinates of successive terrain profile points. For the purpose of computer simulation, intermediate profile points are determined based on linear interpolation. The automobile tires with their large section height and relatively large inflation pressure yield considerable tire deformation near the contact region, and thus distributed tire force over the contact length. The bicycle tire with its small section height and considerably higher inflation pressure results in significantly smaller contact patch and thus can be accurately represented by a contact point on the pitch plane.

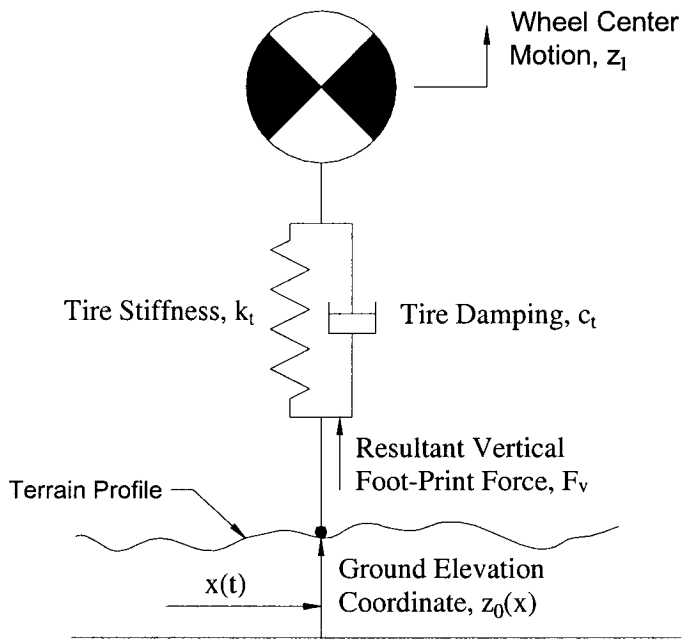

Figure 5.6: The point contact tire model.

Assuming linear stiffness and damping due to tire, and elevation z_0 corresponding to a horizontal location x(t), the foot-print force can be calculated as:

$$F = \int_0^{z_{st}+z_0-z_1} k_t dz + \int_0^{\dot{z}_0-\dot{z}_1} c_t d\dot{z} \tag{5.7}$$

where z_{st} is the static deflection of the tire under a load W, and $\dot{z}_0$ is the rate of change of profile elevation transmitted by the point follower due to the forward motion of the wheel at velocity V. Parameters z_{st} and $\dot{z}_0$ can be calculated as:

$$z_{st} = \frac{W}{k_t} \tag{5.8}$$

$$\dot{z}_0 = V(dz_0 / dx) \tag{5.9}$$

As explained in section 5.3, the vertical and pitch responses of the Touring bicycle can be conveniently derived from the in-plane, two degree-of-freedom linear system model. The Hybrid bicycle can also be considered as a two degrees-of-freedom system, when the relative movement of the front wheel is negligible due to high friction. Coupled with the rider model, the total mass of the bicycle-rider system, however, will be sufficient to produce enough inertial force to overcome the suspension lock-up, specifically when interactions with strip pattern occur. Two different bicycle-rider models are thus developed for the Touring and Hybrid bicycles. The Touring bicycle-rider model is initially developed and used as the base line model. The model is represented by a 5-DOF system by combining the rider model with the Touring bicycle model. Consequently, to account for the bounce motion of the front unsprung mass the Hybrid bicycle-rider model was represented as a 6-DOF system.

Equations of motion for the bicycle-rider system are developed using Langrangian formulation, subject to following assumptions:

- Constant forward velocity of the bicycle.

- No steering input.
- The sprung masses are considered as rigid bodies constrained to move along the vertical and pitch axes.
- Suspension units and tires are modeled as linear springs and dampers.
- Road is assumed to be a rigid surface.
- Excitation to the system is considered to be applied through the tire-road contact points.

5.4.1 5-DOF Touring bicycle-rider model

The Touring bicycle-rider model is developed by combining the 2-DOF, Touring bicycle model, described in section 5.3, with the 3-DOF rider model, resulting in an in-plane, 5-DOF bicycle-rider model. The rider model is coupled to the bicycle frame at the handle bar and the seat through linear spring and damping elements representing rider's hand-arm system and rotational spring and damper element at the hip, respectively. Schematic representation of the 5-DOF bicycle-rider model is shown in Figure 5.7.

Equations of motion for the in-plane, 5-DOF bicycle-rider system are derived around their respective static equilibriums, using Langrangian formulation. Accordingly, using the scalar quantities of kinetic energy, T, potential energy, U, and work, Q, expressed in terms of generalized coordinates, q, the equations of motion are given by:

$$\frac{d}{dt}\left(\frac{\partial T}{\partial \dot{q}}\right)-\frac{\partial T}{\partial q}+\frac{\partial U}{\partial q}=Q_q \tag{5.10}$$

where kinetic and potential energies of the system are expressed in terns of the generalized coordinates as (Thomson, 1998):

$$T=\frac{1}{2}\{\dot{q}\}^T[m]\{\dot{q}\} \tag{5.11}$$

$$U = \frac{1}{2}\{q\}^T [k]\{q\} \tag{5.12}$$

where the generalized coordinate vector $\{q\}^T = \{z_1, z_2, z_3, \theta_1, \theta_2\}$ comprises the axial motion of the bicycle frame (z_1), torso (z_2), and viscera (z_3), and rotational motions of the frame (θ_1) and torso (θ_2).

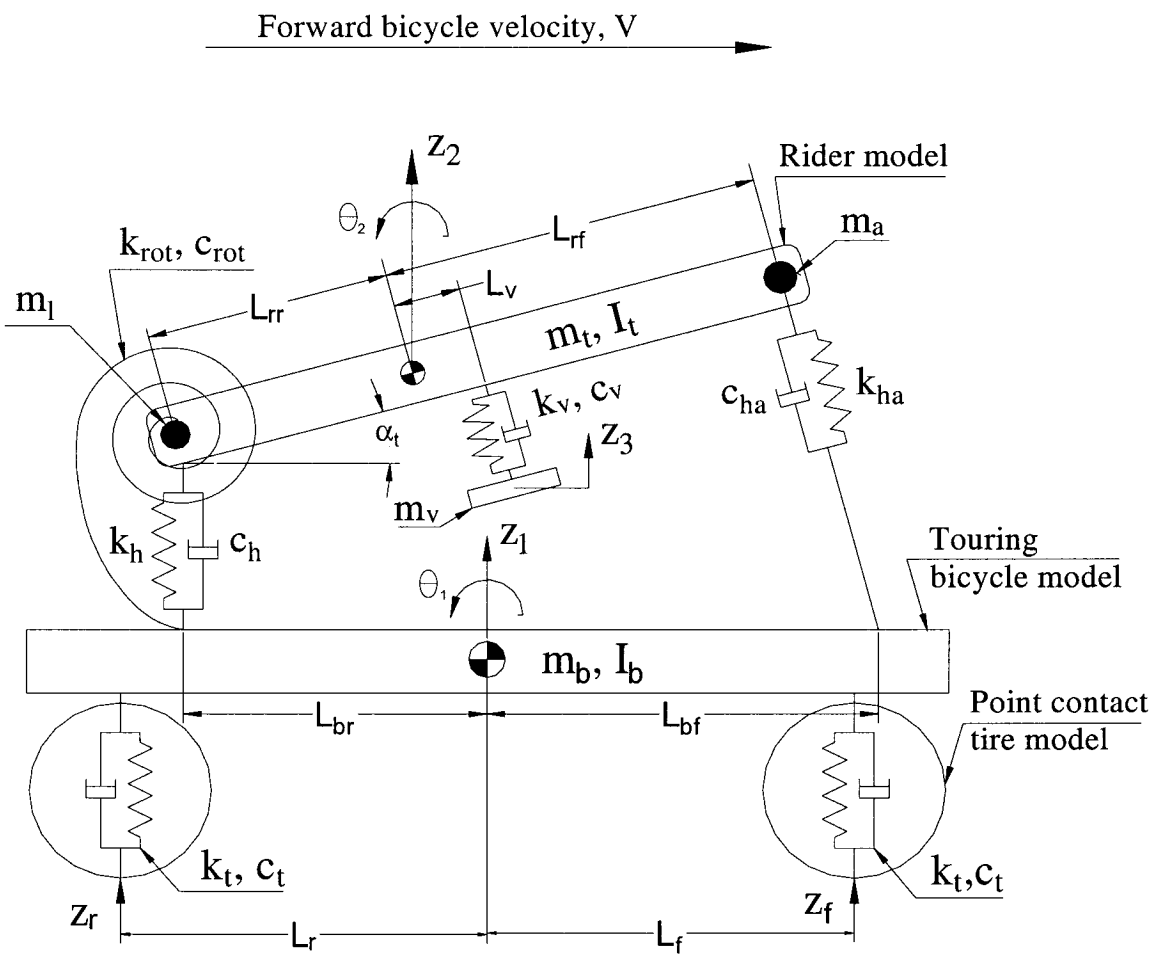

Figure 5.7: The 5-DOF Touring bicycle-rider model.

The generalized force, Q_q, was obtained using the method of virtual work (δW) due to non conservative forces, including the damping forces, such as:

$$\delta W = \sum_i F_i \cdot \delta r_i = \sum_j \sum_i F_i \cdot \frac{\delta r_j}{\delta q_i} \delta q_i = \sum_i Q_i \delta q_i \tag{5.13}$$

where $\vec{F}_i$ are the applied forces excluding all constraint forces and internal forces of frictionless joints and $\delta \vec{r}_i$ are the virtual displacements (Thomson, 1998).

The coupled differential equations of motion for the 5-DOF system are derived in the following form:

$$m_b \ddot{z}_1 + m_b g + F_{tr} + F_{tf} + F_h + F_{ha} = 0 \tag{5.14}$$

$$I_b \ddot{\theta}_1 + F_{tf} L_f - F_{tr} L_r + F_{ha} L_{bf} - F_h L_{br} + k_{rot}(\theta_1 - \theta_2) + c_{rot}(\dot{\theta}_1 - \dot{\theta}_2) = 0 \tag{5.15}$$

$$\begin{aligned}&(m_t + m_l + m_a)\ddot{z}_2 + (m_a L_{rf} - m_l L_{rr})\cos\alpha_t \cdot \ddot{\theta}_2 + (m_t + m_l + m_a)g \\ &- F_h - F_{ha} - F_v = 0\end{aligned} \tag{5.16}$$

$$\begin{aligned}&(I_t + m_l L_{rr}^2 + m_a L_{rf}^2)\ddot{\theta}_2 + (m_a L_{rf} - m_l L_{rr})\cos\alpha_t \ddot{z}_2 + \\ &(m_a L_{rf} - m_l g L_{rr}) g \cos\alpha_t - F_{ha} L_{rf} \cos\alpha_t + F_h L_{rr} \cos\alpha_t + F_v L_v \cos\alpha_t - \\ &k_{rot}(\theta_1 - \theta_2) - c_{rot}(\dot{\theta}_1 - \dot{\theta}_2) = 0\end{aligned} \tag{5.17}$$

$$m_v \ddot{z}_3 + m_v g + F_v = 0 \tag{5.18}$$

where F_{ha} and F_v are the vertical force developed rider-handle bar interface and the force due to viscera mass, respectively:

$$\begin{aligned}F_{ha} = {} & k_{ha}\left(\Delta_{ha} - z_2 - L_{rf}\theta_2 \cos\alpha_t + z_1 + L_{bf}\theta_1\right) \\ & + c_{ha}(\dot{z}_1 + L_{bf}\dot{\theta}_1 - \dot{z}_2 - L_{rf}\dot{\theta}_2 \cos\alpha_t)\end{aligned} \tag{5.19}$$

$$F_v = k_v\left(z_3 - z_2 - L_{rv}\theta_2 \cos\alpha_t - \Delta_v\right) + c_v(\dot{z}_3 - \dot{z}_2 - L_v\dot{\theta}_2 \cos\alpha_t) \tag{5.20}$$

where F_h is the vertical forces developed at the rider-seat interface defined as:

$$F_h = \begin{cases} k_h \delta_{sp} + c_h \dot{\delta}_{sp}; & FOR \quad \delta_{sp} < 0 \\ \\ 0; & FOR \quad \delta_{sp} > 0 \end{cases} \tag{5.21}$$

where δ_{sp} and $\dot{\delta}_{sp}$ are:

$$\delta_{sp} = \Delta_h - z_2 + L_{rr}\theta_2 \cos\alpha_t + z_1 - L_{br}\theta_1 \tag{5.22}$$

$$\dot{\delta}_{sp} = \dot{z}_1 - \dot{z}_2 + L_{rr}\dot{\theta}_2 \cos\alpha_t - L_{br}\dot{\theta}_1 \tag{5.23}$$

where Δ_f, Δ_r, Δ_h, Δ_{ha} and Δ_v are the static deflection of the front and rear wheels, rider's hip, hand-arm and the visceral mass, respectively. Constants L_f, L_r, L_{rf}, L_{rr}, L_v, L_{brf} and L_{brr} define geometric variables of the bicycle-rider mode, presented in Figure 5.7. The bicycle wheels are modeled assuming nonlinear point contact with the road surface, such that:

$$F_{tf} = \begin{cases} k_t(z_1 + L_f\theta_1 - z_f - \Delta_f) \\ + c_t(\dot{z}_1 + L_f\dot{\theta}_1 - \dot{z}_f); & FOR \quad (\dot{z}_1 + L_f\theta_1 - z_f - \Delta_f) < 0 \\ \\ 0; & FOR \quad (\dot{z}_1 + L_f\theta_1 - z_f - \Delta_f) \geq 0 \end{cases} \tag{5.24}$$

$$F_{tr} = \begin{cases} k_t(z_1 - L_r\theta_1 - z_r - \Delta_r) \\ + c_t(\dot{z}_1 - L_r\dot{\theta}_1 - \dot{z}_r); & FOR \quad (\dot{z}_1 - L_r\theta_1 - z_r - \Delta_r) < 0 \\ \\ 0; & FOR \quad (\dot{z}_1 - L_r\theta_1 - z_r - \Delta_r) \geq 0 \end{cases} \tag{5.25}$$

where F_{tf} and F_{tr} are the forces developed at the wheel-road interface. The model parameters are summarized in Table 5.4.

Table 5.4: Touring bicycle-rider model parameters.

Parameter	*Value*
Torso mass, m_t [kg]	32.98
Pitch mass moment of inertia of the torso, I_t, [kgm^2]	1.827
Mass of the legs, m_l [kg]	25.18
Mass of the arms, m_a [kg]	7.7
Hip stiffness, k_h, [kN/m]	47.6
Hip damping, c_h, [Ns/m]	500
Hand-arm stiffness, k_{ha}, [kN/m]	14.5
Hand-arm damping, c_{ha}, [Ns/m]	595
Visceral mass, m_v, [kg]	11.62
Visceral mass stiffness, k_v, [kN/m]	21
Visceral mass damping, c_v, [Ns/m]	29.4
Visceral mass c.g. to torso c.g., L_v, [m]	0.045
Hip to torso c.g. distance, L_{rr}, [m]	0.31
Hand-arm to torso c.g. distance, L_{rf}, [m]	0.2
Hinge stiffness, k_{rot}, [kN/m]	5
Hinge damping, c_{rot}, [Ns/m]	50
Torso inclination angle, α_t, [degrees]	35^o
Bicycle mass m_b, [kg]	12.2
Pitch mass moment of inertia of the bicycle, I_b, [kgm^2]	2.755
Tire stiffness, k_t, [kN/m]	114
Tire damping, c_t, [Ns/m]	85
Front tire to bicycle c.g. distance, L_f, [m]	0.533
Rare tire to bicycle c.g. distance, L_r, [m]	0.483
Handle bar to bicycle c.g. distance, L_{brf}, [m]	0.5
Seat to bicycle c.g. distance, L_{brr} [m]	0.24

5.4.2 6-DOF Hybrid bicycle-rider model

The Hybrid bicycle is developed by considering the bicycle frame suspended on the front wheel suspension and the front wheel mass, m_u. The Hybrid bicycle-rider model is thus modeled as a 6-DOF dynamic system, as illustrated in Figure 5.12, where the front suspension is modeled as a parallel combination of a linear spring and a viscous damper. It should be noted that the measured force-deflection characteristics of the front suspension revealed the presence of high magnitude of Coulomb friction, which is often the case for less expensive Hybrid bicycles where a viscous damper is replaced by a less expensive dry friction mechanism. It is reasonable to expect that the type of bicycle used by recreational cyclists, riding on open roads, would be with somewhat higher performance and therefore with better suspension units. Therefore for the purpose of this study, viscous damping properties of the suspension are considered.

The coefficient of equivalent viscous damping was estimated using the principle of energy similarity (Tchernychouk, 1999). The energy dissipated per cycle by Coulomb damping can be calculated as:

$$\Delta E = 4F_c Z \tag{5.26}$$

where ΔE is energy dissipated per cycle, F_c is the magnitude of the friction force and Z is amplitude of motion of the suspension unit. Equating the energy with that of a viscous damper yields an expression for the equivalent viscous damper coefficient, c_{vd}, as a function of the motion amplitude Z and frequency ω:

$$c_{vd} = \frac{4F_c}{\pi\omega Z} \tag{5.27}$$

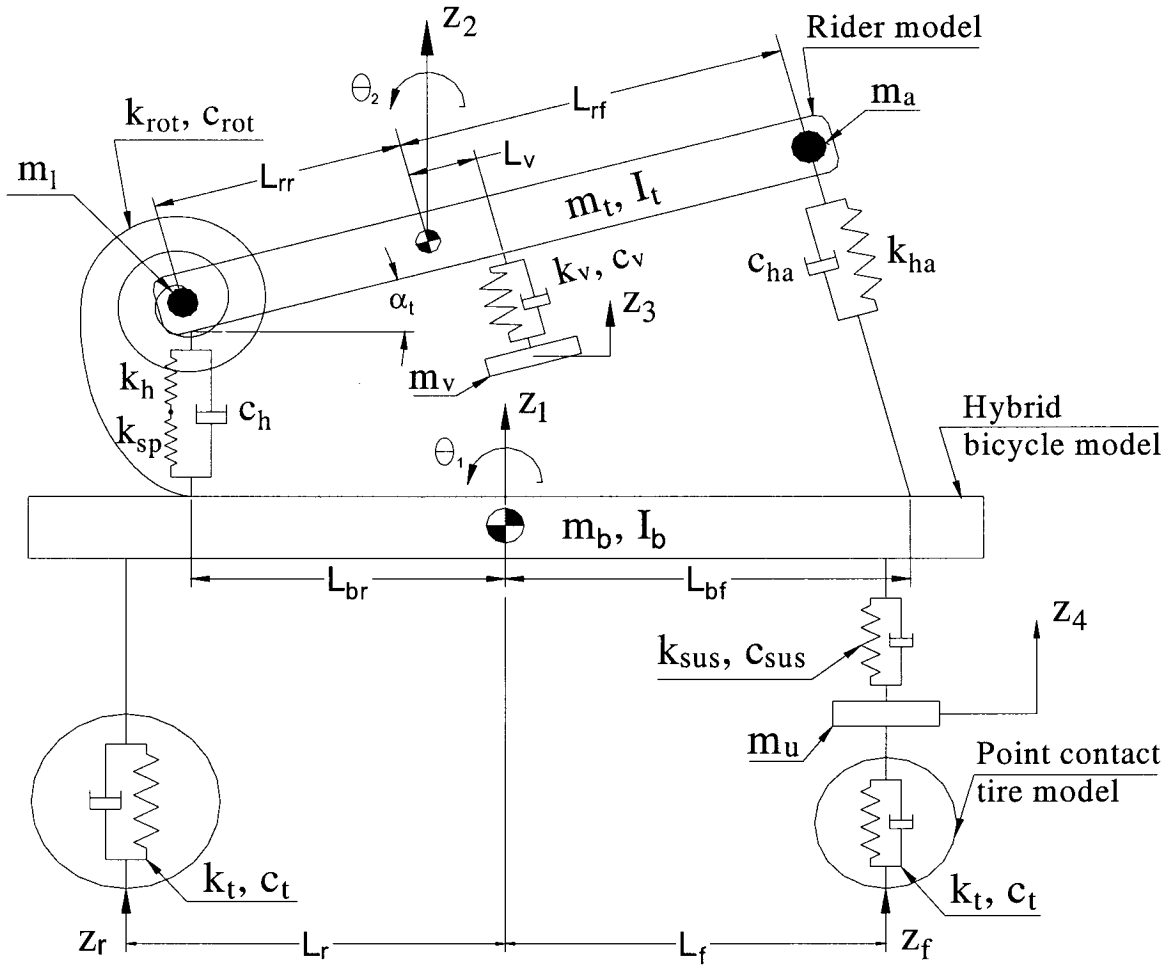

Figure 5.12: The 6-DOF Hybrid bicycle model with the rider.

The seat post suspension was modeled as a spring element connected in series with elastic element representing the rider hip. The stiffness of the seat post suspension is approximated as linear in its operational range, as derived from the measured data, together with high stiffness due to bump stop. A piece-wise linear representation is thus used, as shown in Figure 5.13. The constants k_{spI} and k_{spII} in the figure, characterize the low and high stiffness due to seat post spring and bump stop, respectively.

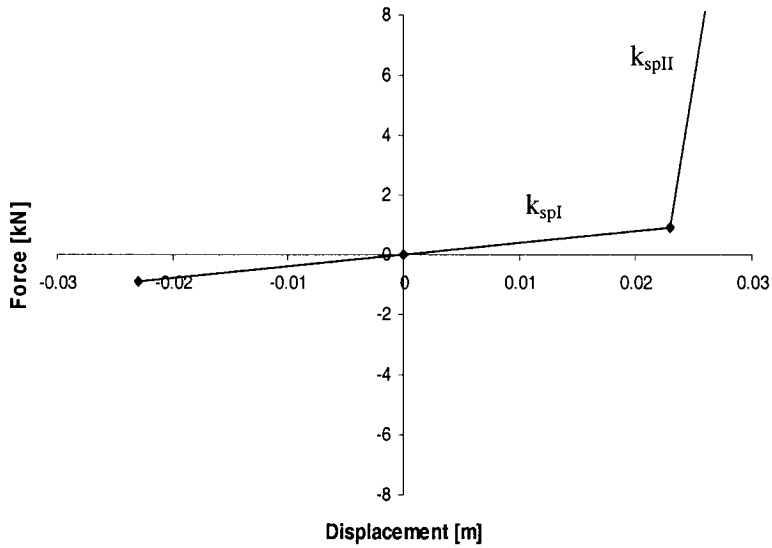

Figure 5.13: Piece-wise linear stiffness properties of the seat post suspension.

The differential equations of motion of the 6-DOF bicycle rider model are derived to describe the vertical and pitch motion of the bicycle frame (z_1 and θ_1), vertical motion of the front wheel (z_4), vertical and pitch motion of the torso (z_2 and θ_2), and vertical motion of the visceral mass (z_3). The forces due to front and rear wheels are derived assuming nonlinear point-contact elements, as described in Equation (5.7), such that:

$$F_{tf} = \begin{cases} k_t(z_4 - z_f - \Delta_f) \\ +c_t(\dot{z}_4 - \dot{z}_f); & FOR \quad (\dot{z}_4 - z_f - \Delta_f) < 0 \\ \\ 0; & FOR \quad (\dot{z}_4 - z_f - \Delta_f) \geq 0 \end{cases} \tag{5.28}$$

$$F_{tr} = \begin{cases} k_t(z_1 - L_r\theta_1 - z_r - \Delta_r) \\ +c_t(\dot{z}_1 - L_r\dot{\theta}_1 - \dot{z}_r); & FOR \quad (\dot{z}_1 - L_r\theta_1 - z_r - \Delta_r) < 0 \\ \\ 0; & FOR \quad (\dot{z}_1 - L_r\theta_1 - z_r - \Delta_r) \geq 0 \end{cases} \tag{5.29}$$

where F_{tf} and F_{tr} are the forces developed at the wheel-road interface. The vertical force developed at rider-seat interface (F_h) is derived from the piecewise-linear force-deflection characteristic shown in Figure 5.13, such that:

$$F_h = \begin{cases} k_{eq}\delta_{sp} + c_h\dot{\delta}_{sp}; & FOR \quad \delta_{sp} < 0 \\ 0; & FOR \quad \delta_{sp} > 0 \end{cases} \tag{5.30}$$

where δ_{sp} and $\dot{\delta}_{sp}$ are:

$$\delta_{sp} = \Delta_h - z_2 + L_{rr}\theta_2\cos\alpha_t + z_1 - L_{br}\theta_1 \tag{5.31}$$

$$\dot{\delta}_{sp} = \dot{z}_1 - \dot{z}_2 + L_{rr}\dot{\theta}_2\cos\alpha_t - L_{br}\dot{\theta}_1 \tag{5.32}$$

where:

$$k_{eq} = \begin{cases} \dfrac{k_h k_{spI}}{k_h + k_{spI}}; & FOR \quad \delta_{sp} < 0.023\,m \\ k_{spII}; & FOR \quad \delta_{sp} \geq 0.023\,m \end{cases} \tag{5.33}$$

The equations of motion of the bicycle-rider system are summarized below:

$$m_s\ddot{z}_1 + m_s g + F_{tr} + F_{sus} + F_h + F_{ha} = 0 \tag{5.34}$$

$$I_b\ddot{\theta}_1 + F_{sus}L_f - F_{tr}L_r + F_{ha}L_{bf} - F_h L_{br} + k_{rot}(\theta_1 - \theta_2) + c_{rot}(\dot{\theta}_1 - \dot{\theta}_2) = 0 \tag{5.35}$$

$$\begin{aligned}&(m_t + m_l + m_a)\ddot{z}_2 + (m_a L_{rf} - m_l L_{rr})\cos\alpha_t \cdot \ddot{\theta}_2 + (m_t + m_l + m_a)g \\ &- F_h - F_{ha} - F_v = 0\end{aligned} \tag{5.36}$$

$$\begin{aligned}&(I_t + m_l L_{rr}^2 + m_a L_{rf}^2)\ddot{\theta}_2 + (m_a L_{rf} - m_l L_{rr})\cos\alpha_t\ddot{z}_2 + \\ &(m_a L_{rf} - m_l g L_{rr})g\cos\alpha_t - F_{ha}L_{rf}\cos\alpha_t + F_h L_{rr}\cos\alpha_t + F_v L_v\cos\alpha_t - \\ &k_{rot}(\theta_1 - \theta_2) - c_{rot}(\dot{\theta}_1 - \dot{\theta}_2) = 0\end{aligned} \tag{5.37}$$

$$m_v\ddot{z}_3 + m_v g + F_v = 0 \tag{5.38}$$

$$m_u \ddot{z}_4 + m_u g + F_{tf} - F_{sus} = 0 \tag{5.39}$$

where F_{ha}, F_v and F_{sus} are the vertical forces developed rider-handle bar interface, the force due to viscera mass and the force developed in the front suspension, respectively:

$$\begin{aligned} F_{ha} &= k_{ha}\left(\Delta_{ha} - z_2 - L_{rf}\theta_2 \cos\alpha_t + z_1 + L_{bf}\theta_1\right) \\ &\quad + c_{ha}(\dot{z}_1 + L_{bf}\dot{\theta}_1 - \dot{z}_2 c - L_{rf}\dot{\theta}_2 \cos\alpha_t) \end{aligned} \tag{5.40}$$

$$F_v = k_v\left(z_3 - z_2 - L_{rv}\theta_2 \cos\alpha_t - \Delta_v\right) + c_v(\dot{z}_3 - \dot{z}_2 - L_v\dot{\theta}_2 \cos\alpha_t) \tag{5.41}$$

$$F_{sus} = k_{sus}(z_1 + L_f\theta_1 - z_4 - \Delta_{sus}) + c_{vd}(\dot{z}_1 + L_f\dot{\theta}_1 - \dot{z}_4) \tag{5.42}$$

where Δ_f, Δ_r, Δ_h, Δ_{ha}, Δ_v and Δ_{sus} are the static deflection of the front and rear wheels, rider's hip, hand-arm, the visceral mass and front suspension, respectively. Constants L_f, L_r, L_{rf}, L_{rr}, L_v, L_{bf} and L_{br} define geometric variables of the bicycle-rider model, presented in Figure 5.7.

The equivalent damping coefficient for the front suspension, c_{vd}, was estimated from Equation (5.26), by considering measured magnitude of Coulomb damping of 150 N and the natural frequency of the unsprung mass of 38.9 Hz, which was approximated according to the relationship:

$$f_u = \frac{1}{2\pi}\sqrt{\frac{k_t + k_{sus}}{m_u}} \tag{5.43}$$

where the values of k_t, k_{sus}, m_{sus}, are presented in Table 5.7. Based on the preliminary simulations, the suspension travel was estimated as 7.5 mm.

Table 5.5: Hybrid bicycle-rider model parameters.

Parameter	*Value*
Torso mass, m_t [kg]	32.98
Pitch mass moment of inertia of the torso, I_t, [kgm^2]	1.827
Mass of the legs, m_l [kg]	25.18
Mass of the arms, m_a [kg]	7.7
Hip stiffness, k_h, [kN/m]	47.6
Hip damping, c_h, [Ns/m]	500
Hand-arm stiffness, k_{ha}, [kN/m]	14.5
Hand-arm damping, c_{ha}, [Ns/m]	595
Visceral mass, m_v, [kg]	11.62
Visceral mass stiffness, k_v, [kN/m]	21
Visceral mass damping, c_v, [Ns/m]	29.4
Visceral mass c.g. to torso c.g., L_v, [m]	0.045
Hip to torso c.g. distance, L_{rr}, [m]	0.31
Hand-arm to torso c.g. distance, L_{rf}, [m]	0.2
Hinge stiffness, k_{rot}, [kN/m]	5
Hinge damping, c_{rot}, [Ns/m]	50
Bicycle sprung mass, m_s, [kg]	12.9
Torso inclination angle, α_t, [degrees]	45^o
Bicycle unsprang mass, m_u, [kg]	2
Pitch mass moment of inertia of the bicycle, I_b, [kgm^2]	3.518
Tire stiffness, k_t, [kN/m]	97.3
Tire damping, c_t, [Ns/m]	100
Front suspension stiffness, k_{sus}, [kN/m]	22.12
Front suspension equivalent viscous damping, c_{vd}, [Ns/m]	104.2
Seat post suspension stiffness (operational range), k_{spI}, [kN/m]	20.75
Seat post suspension stiffness (bump stop), k_{spII}, [kN/m]	2480
Front tire to bicycle c.g. distance, L_f, [m]	0.557
Rare tire to bicycle c.g. distance, L_r, [m]	0.535
Handle bar to bicycle c.g. distance, L_{brf}, [m]	0.49
Seat to bicycle c.g. distance, L_{brr}, [m]	0.23

5.4.3 Free vibration analysis of the analytical bicycle-rider models

A free vibration analysis of the developed analytical models is conducted to identify model's resonant frequencies and dominant deflection modes. An eigenproblem is formulated to compute the damped natural frequencies and dominant deflection modes. Table 6.2 summarizes the damped natural frequencies and corresponding dominant deflection modes identified from the eigenvectors for the Touring and Hybrid bicycle-rider models.

The inspection of the resonant frequencies of the Touring and Hybrid bicycle-rider models reveals that the frequencies of the deflection modes associated with the rider model are in the range from 2 to 7 Hz. This agrees with the study by Wang and Hull (1997) which showed that no significant rider dynamics occurs above 10 Hz. The results for the Touring and Hybrid bicycle-rider models show that the bounce frequency of the rider's torso is at 3.5 or 2.3 Hz while the pitch frequency is at 6.3 or 5 Hz, respectively, for the Touring and Hybrid bicycles. The visceral mass oscillates at 6.8 Hz and 7 Hz, respectively, for the Touring and Hybrid bicycle models. Measured responses of bicycle rider in the seated position showed resonant peaks between 2 and 3.5 Hz, while it was found that the visceral mass resonates in the range between 6 and 8.5 Hz (Wang and Hull, 1997). The bounce and the pitch frequencies of the bicycle frame are 21.7 and 24.4 Hz for the Touring bicycle model and 7.4 and 17.1 Hz for the Hybrid, respectively. Lower natural frequencies of the Hybrid bicycle's frame are expected due to its front suspension and softer tire spring rates.

Table 5.6: Damped natural frequencies and corresponding dominant deflection modes for the Touring and Hybrid bicycle-rider models.

Bicycle	*Damped natural Frequency [Hz]*	*Dominant deflection mode*
Touring	3.5	Rider's Torso, Bounce (z_2)
	6.3	Rider's Torso, Pitch (θ_2)
	6.8	Visceral Mass, Bounce (z_1)
	21.7	Bicycle Frame, Bounce (z_1)
	24.4	Bicycle Frame, Pitch (θ_1)
Hybrid	2.3	Rider's Torso, Bounce (z_2)
	5	Rider 's Torso ,Pitch (θ_2)
	7	Visceral Mass, Bounce (z_1)
	7.4	Bicycle Frame, Bounce (z_1)
	17.1	Bicycle Frame, Pitch (θ_1)
	38.9	Unsprung mass, bounce (z_4)

5.5 SUMMARY

In this chapter, the bicycle-rider system is represented by a nonlinear 5-DOF and 6-DOF in-plane time-domain models, respectively, for the Touring and the Hybrid bicycles. A nonlinear point contact dynamic wheel-terrain model is considered to determine the forces arising from the surface irregularities. The differential equations of motion were derived using Langrangian formulation, assuming linear rider model, constant forward velocity and non-deformable terrain profile. The equations of motion are solved under excitations arising from rumble strips patterns to determine the rider dynamic response of the bicycle-rider models, in the following chapter.

CHAPTER 6

RESPONSE EVALUATION OF THE BICYCLE-RIDER MODELS

6.1 INTRODUCTION

The rider properties of the bicycle-rider system are strongly influenced by the terrain roughness, particularly the geometry of the rumble strip pattern. The analysis of the models to excitations arising from the rumble strip geometry could provide considerable information leading to identification of rider-friendly rumble strip patterns. Furthermore, the analysis could provide significant insight into design of wheel suspension in reducing the magnitudes of vibration transmitted to the rider. In this study, the analytical models are evaluated under excitation arising from a random rough road and a rumble strip pattern. The simulation results are compared with the measured data to examine the validity of the model. Parametric sensitivity analyses are then performed to identify rumble strip geometry that would yield reduced levels of transmitted vibrations.

6.2 CHARACTERIZATION OF INPUTS

The bicycle-rider models are evaluated under excitations arising from randomly distributed surface irregularities and selected rumble strip patterns, including equally spaced rectangular and round grooves. The bicycle-rider model responses to a flat randomly-rough road surface are initially evaluated to examine the model validity, and to establish the baseline values of the responses. The data acquisition from field trials performed on flat road surfaces are used to examine the model validity. Although the

roughness of the road profile used in the field measurements was not characterized, the road roughness is described using the profiles described in ISO-8608 (1984).

6.2.1 Random Road Profile

For the purpose of this study, a random road profile $z(t)$ was generated from a white noise signal $\xi(t)$ by solving the following differential equation (Hac, 1985):

$$\dot{z}(t) + \eta \cdot V \cdot z(t) = \xi(t) \tag{6.1}$$

where V is the forward velocity of the vehicle, and η is the constant coefficient, taken as 0.15 m^2 for the asphalt road (Hac, 1985). The road profile derived from Equation (6.1) is shown in Figure 6.1 in terms of the surface elevation as a function of the longitudinal coordinate of the road. Alternatively, the severity of the road roughness can be expressed in terms of the magnitudes of road elevations and the corresponding frequency components. The ISO-8608 (1984) document describes standardized road profiles in terms of power spectral density of the roughness. The document presents classifications of the road surface in terms of magnitudes of the spatial power spectral density $S_g(\Omega_0)$ corresponding to the spatial frequency $\Omega_0 = 1/2\pi$ (cycles/m). The standard classifies the road surfaces into eight different categories, as summarized in Table 6.1. The random road profiles derived from Equation (6.1) is expressed by its spatial spectral density, $S_g(\Omega)$, using Fast Fourier Transformation (FFT) technique. Figure 6.2 presents the spatial power spectral density (PSD) of the random road profile as a function of the spatial frequency Ω. The magnitude of the road profile PSD at the spatial frequency $\Omega_0 = 1/2\pi$ was estimated as $1.51 \cdot 10^{-5}$ (m^2/cycle/m), which can be classified as a "good" road (Class B) on the basis of the data presented in Table 6.1.

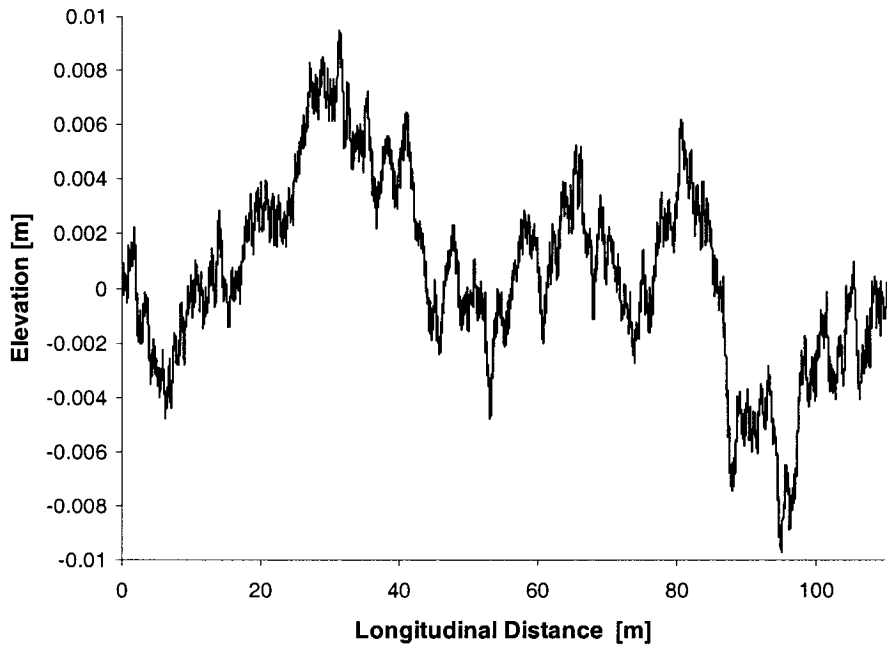

Figure 6.1: Elevation of the road surface.

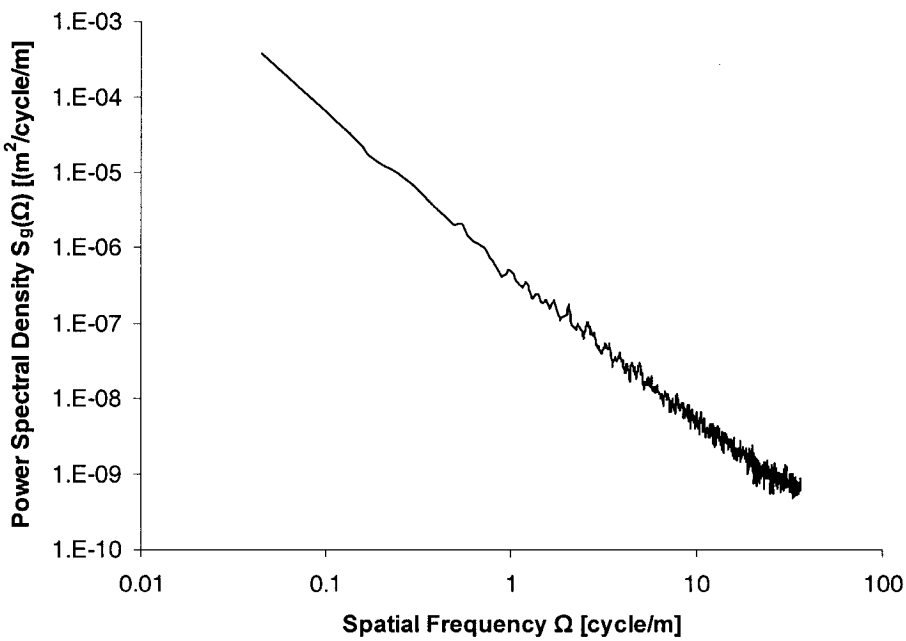

Figure 6.2: Power spectral density of the random road profile.

Table 6.1: Classification of road roughness proposed by ISO (Wong, 1993).

Road Class	*Range* $S_g(\Omega_0)$ *[m^2/cycles/m]*
A (Very good)	$<8 \times 10^{-6}$
B (Good)	$8\text{-}32 \times 10^{-6}$
C (Average)	$32\text{-}128 \times 10^{-6}$
D (Poor)	$128\text{-}524 \times 10^{-6}$
E (Very poor)	$512\text{-}2048 \times 10^{-6}$
F	$2048\text{-}8192 \times 10^{-6}$
G	$8192\text{-}32768 \times 10^{-6}$
H	$>32768 \times 10^{-6}$

6.2.2 Dynamic interaction between the wheel and the rumble strip

The dynamic interaction between the wheel and a rumble strip pattern are evaluated by considering the pattern as an equally spaced deterministic ground profile. Figure 6.3 illustrates the equally-spaced rectangular pattern, as an example. Moreover, the deterministic profile is superimposed by the random distributed pavement roughness, derived from Equation (6.1). The current designs of patterns do not permit for total tire drop that would cause contact between the tire and the bottom of the groove. Assuming partial tire drop, the tire-road contact is considered to occur either at a single point located at the leading or trailing edge or at two contact points located in-front of and behind the tire vertical center line, as shown in Figure 6.4. The tire foot-print force, F', resulting from the tire-groove interaction occurring at an in-coming edge, can be calculated from (Figure 6.5):

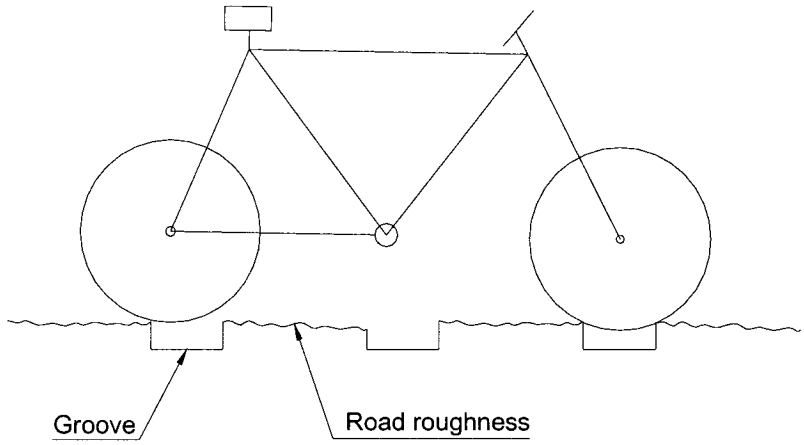

Figure 6.3: Bicycle interaction with a rectangular rumble strip pattern.

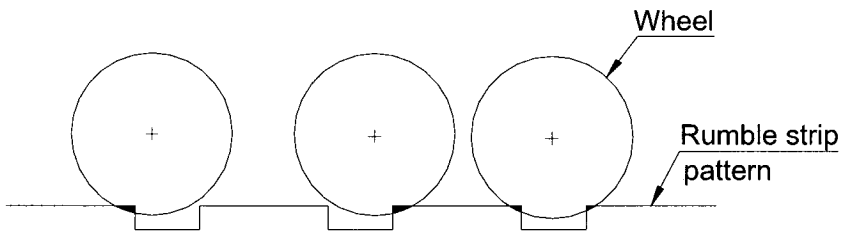

Figure 6.4: The wheel-strip contact points.

$$F' = k_{t1} \cdot \delta' + c_{t1} \cdot \dot{\delta}' \tag{6.2}$$

where constants k_{t1} and c_{t1} are the equivalent vertical stiffness and damping coefficient of the tire, respectively. The deflection of the wheel, δ', can be computed as the difference between the deflected (R') and non-deflected (R_v) radii of the wheel:

$$\delta' = R_v - R' \tag{6.3}$$

The deflected radius of the wheel can be computed from the relationship:

$$R' = \sqrt{z_d'^2 + x'^2} \tag{6.4}$$

where x' is the longitudinal distance between the contact point and the center of the wheel, and z'_d is the vertical distance between the reference ground profile and the center of the wheel, given by:

$$z'_d = z + R_v - \Delta_{st} - z' \tag{6.5}$$

where Δ_{st} (Δ_f or Δ_r) is the static deflection of the wheel on a flat surface calculated from the static equilibrium, z' is the elevation of the terrain profile at the contact location and z is the vertical motion of the wheel center (equal to z_1, for the Touring bicycle, z_4 for the Hybrid bicycle front wheel, and z_1 for the Hybrid bicycle rear wheel).

The relative velocity between the wheel center and the groove edge, $\dot{\delta}'$, can be calculated from the vertical velocity, $\dot{z}$, and the forward velocity, V, of the wheel center as:

$$\dot{\delta}' = \left[\dot{z} - V\frac{dz'}{dx}\right]\cos\gamma' \tag{6.6}$$

where x is the longitudinal coordinate and γ' is the instantaneous angle of the radial spring-damping element of the wheel shown in Figure 6.5, and given by:

$$\gamma' = \tan^{-1}\left(x'/z'_d\right) \tag{6.7}$$

The term dz'/dx defines the slope of the road profile at the contact location on the basis of the random roughness alone. The vertical component (F'_v) of the net foot-print force can be calculated as:

$$F'_V = F' \cdot \cos(\gamma') \tag{6.8}$$

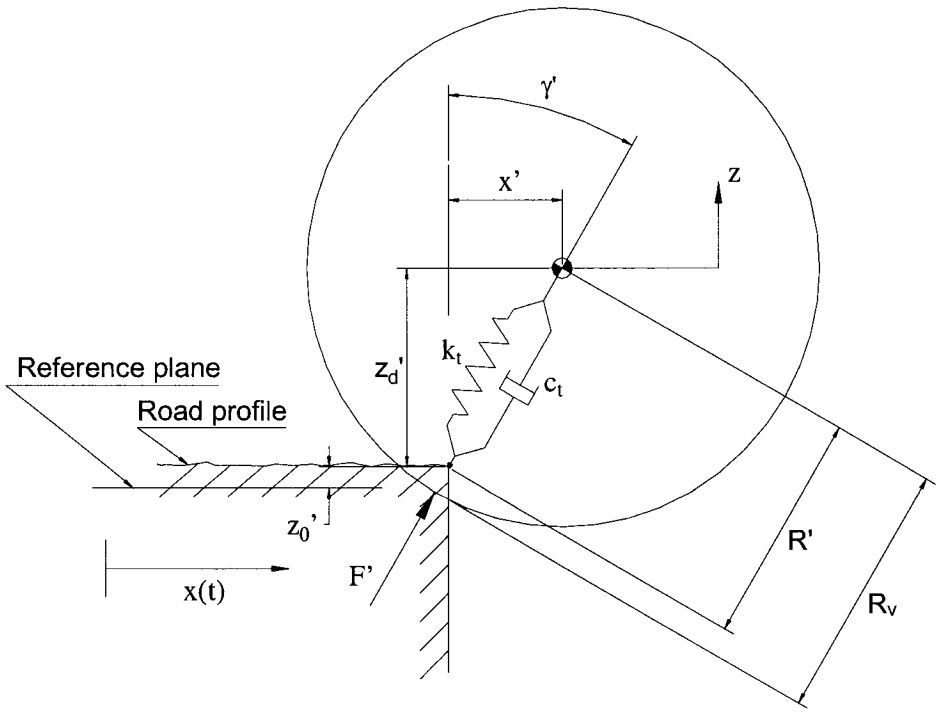

(a) Contact occurring at the leading edge of the groove

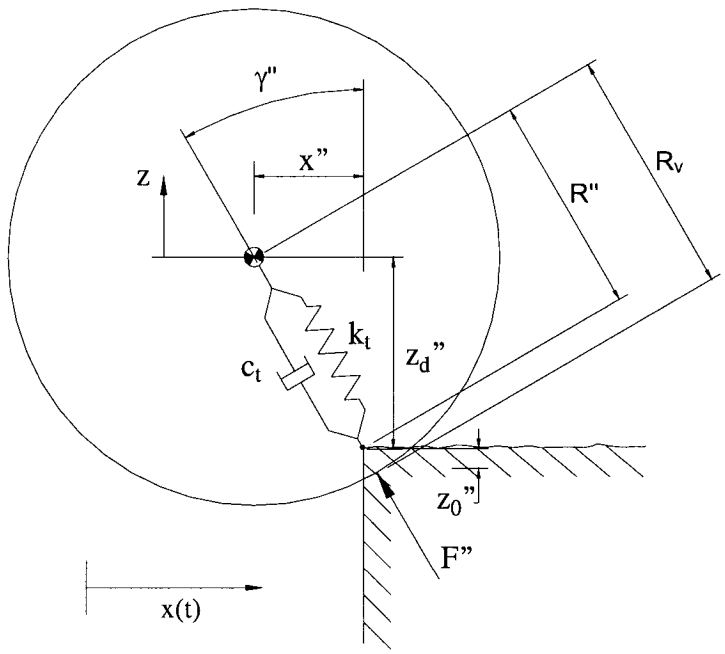

(b) Contact occurring at the trailing edge of the groove

Figure 6.5: Wheel-terrain contact force: (a) Contact occurring at the leading edge of the groove; (b) Contact occurring at the trailing edge of the groove.

The vertical component of the foot print force for the contact point occurring behind the wheel center can be derived in a similar manner, such that:

$$F''_V = F'' \cdot \cos(\gamma'') \tag{6.9}$$

$$F_v'' = k_{t2}\delta'' + c_{t2}\dot{\delta}'' \tag{6.10}$$

$$\delta'' = R_v - \sqrt{(z + R_v - \Delta_{sp} - z'')^2 + x''^2} \tag{6.11}$$

$$\dot{\delta} = \left(\dot{z} - V\frac{dz''}{dx} \right) \cos\gamma'' \tag{6.12}$$

The vertical component of the foot print force, when the contact occurs at two contact points, as illustrated in Figure 6.6, is derived upon summing the two force components:

$$F_v''' = F_v' + F_v'' \tag{6.13}$$

where F_v''' is the total vertical force developed at the tire-terrain interface. In this case, the effective radial stiffness and damping of the tire, at each contact location is considered as one half of the equivalent vertical stiffness and damping, such that:

$$\begin{aligned} k_{t1} &= \frac{k_t}{2};\ k_{t2} = \frac{k_t}{2} \\ c_{t1} &= \frac{c_t}{2};\ c_{t2} = \frac{c_t}{2} \end{aligned} \tag{6.14}$$

where k_t is the tire vertical stiffness of tire derived from the laboratory measured data and c_t is the tire damping coefficient. The forces are developed at the tire-terrain contact point, as described from Equations(6.2) and (6.10), only when the tire-road contact exists,

as described for the Touring bicycle-rider model, Equations (5.24) and (5.25), and the Hybrid bicycle-rider model, Equations (5.28) and (5.29).

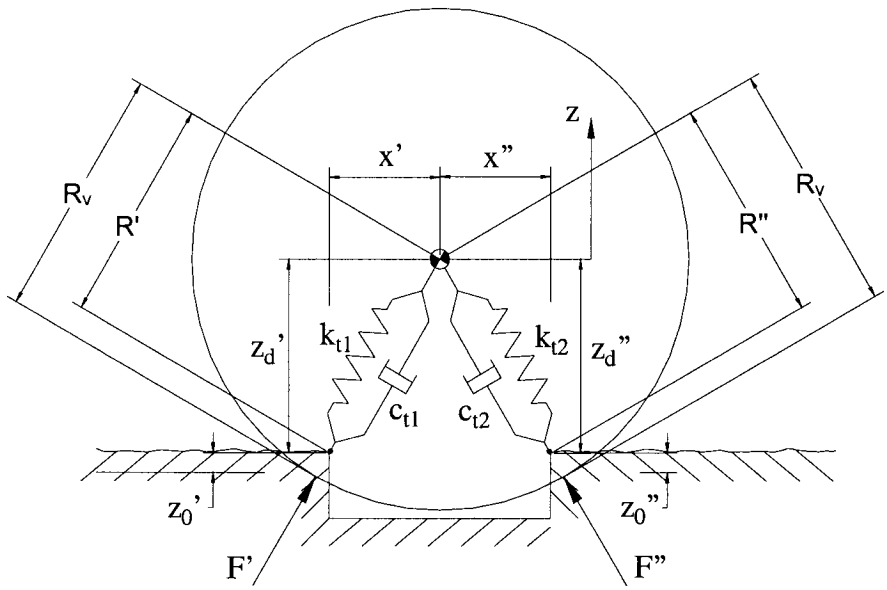

Figure 6.6: Tire contact forces occurring at two contact points.

6.3 VALIDATION OF THE ANALYTICAL MODELS

The validity of the analytical bicycle-rider models, developed in Chapter 5, is examined by comparing the model results with the measured data, presented in Chapter 3. The model validity is initially examined using the model results and measured data for excitations arising from a flat pavement at a speed of 10 km/h. The results obtained from the analytical models are evaluated against the envelope of the measured data in terms of the spectral components and magnitudes of the acceleration PSD. The model results are further validated against the measured data in term of the overall RMS vertical and pitch accelerations for a ride on the flat pavement at speeds of 10, 15 and 20 km/h.

The random responses of the Touring and Hybrid bicycle-rider models are simulated using the computer-based program to solve the model's differential equations

of motion, as described in Chapter 5 (sections 5.4.1 and 5.4.2, respectively). The excitations arising from the road roughness are applied to the models in the computer simulation, with the previously generated random road input, as described in section 6.2. The model results obtained from the computer base program are further transformed to describe the model responses at the handle bar, $\ddot{z}_h$, and at the seat post, $\ddot{z}_s$, as:

$$\begin{aligned} \ddot{z}_h &= \ddot{z}_1 + L_{bf} \cdot \ddot{\theta}_1 \\ \ddot{z}_s &= \ddot{z}_1 - L_{br} \cdot \ddot{\theta}_1 \end{aligned} \tag{6.15}$$

where $\ddot{z}_1$ and $\ddot{\theta}_1$ are the vertical and pitch accelerations of the bicycle frame obtained from the model results and constants L_{bf} and L_{br} are the horizontal distances between the bicycle frame c.g. and the handle bar and seat post, respectively, as obtained from the geometrical properties of the Touring and Hybrid bicycles.

6.3.1 Validation of the bicycle-rider models on the flat pavement

The model results for the Touring and Hybrid bicycle-rider systems are obtained from the computer simulation for a forward speed of 10 km/h, subject to random road input. The vertical accelerations at the handle bar and seat post, computed from Equation (6.15), and the pitch acceleration of the bicycle frame, $\ddot{\theta}_1$, are analyzed to derive the PSD. The acceleration responses obtained from the model results are then compared with the mean measured responses attained with seven subjects on the flat pavement at the speed of 10 km/h. Figures 6.7 and 6.8 illustrate the comparison of the PSD plots obtained from the model results and from the mean and maximum measured responses of the Touring and Hybrid bicycles, respectively.

The results for the Touring bicycle-rider model show a peak response in the 20 to 25 Hz band in the handle bar, seat post and pitch acceleration spectra. These frequencies correspond to the bounce and pitch frequencies of the Touring bicycle frame (21.7 and 24.4 Hz, respectively), as identified from the free vibration analysis of the Touring bicycle-rider model (Table 5.6). The Hybrid bicycle-rider model exhibits a peak response in the 17 to 20 Hz band in both the vertical and pitch accelerations. This frequency corresponds to the bounce frequency of the Hybrid bicycle frame of 17.1 Hz, as identified from the free vibration analysis of the Hybrid bicycle-rider model (Table 5.6). Comparing with the measured data, the Touring bicycle model yields higher magnitudes of the acceleration at the seat post than at the handle bar. The results for the Hybrid bicycle-rider show better agreement with the envelope of the respective measured data with the respect to the magnitudes of acceleration PSD than the Touring bicycle model. However, the results indicate that both bicycle models tend to overestimate the responses in the vicinity of the peak accelerations. These deviations of the model results from the measured data can be attributed to considerable simplicity of the rider model in comparison with the complexity of the human body. The results also reveal that both models fail to predict the second peak in the acceleration spectra of the measured data which occurs in the 30 to 40 Hz band, depending on the bicycle and the location of measurement. This can be attributed to relatively smooth road roughness considered for the computer simulations in comparison with the relatively poor quality of the road surface, as observed during the field measurements. The second peak in the measured data can be attributed as well to structural modes of the bicycle frame which was not considered in the models due to approximation of the bicycle frame as a rigid body.

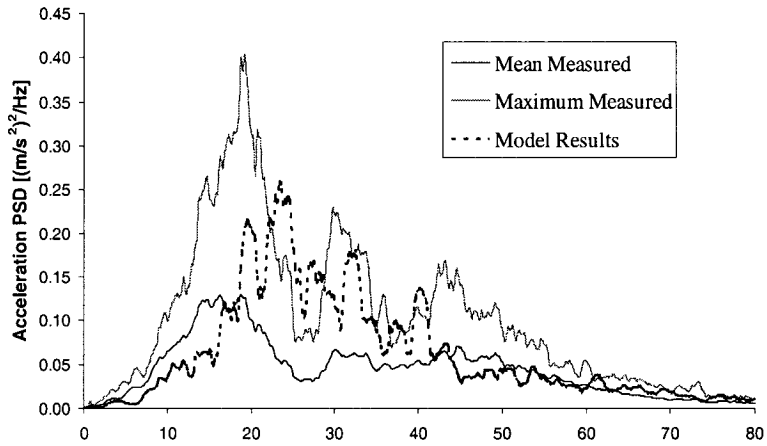

(a) Handle Bar Acceleration

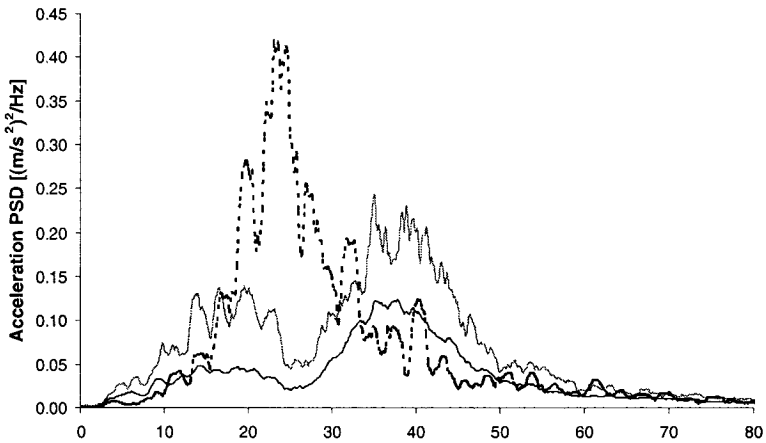

(b) Seat post acceleration

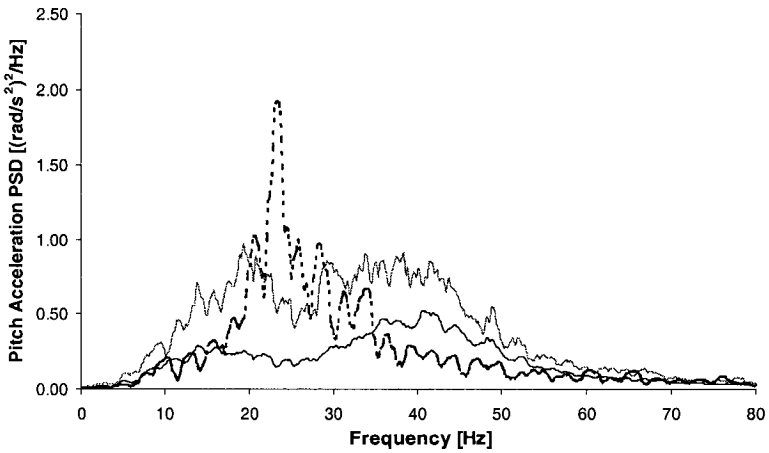

(c) Pitch acceleration

Figure 6.7: Model results vs. mean and maximum measured PSD response of the Touring bicycle (Speed 10 km/h; Pattern: Flat pavement): (a) Handle bar acceleration; (b) Seat post acceleration; (c) Pitch acceleration.

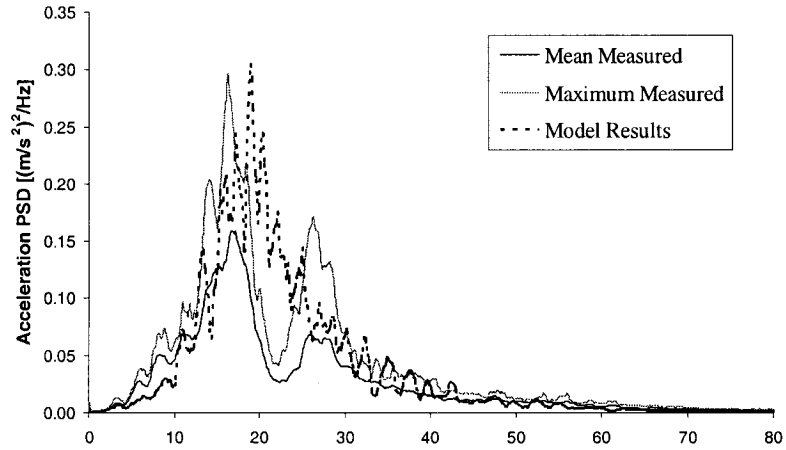

(a) Handle Bar Acceleration

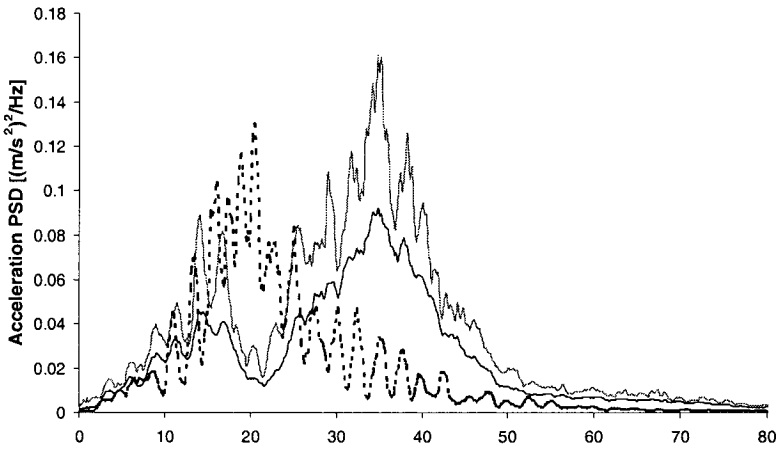

(b) Seat post acceleration

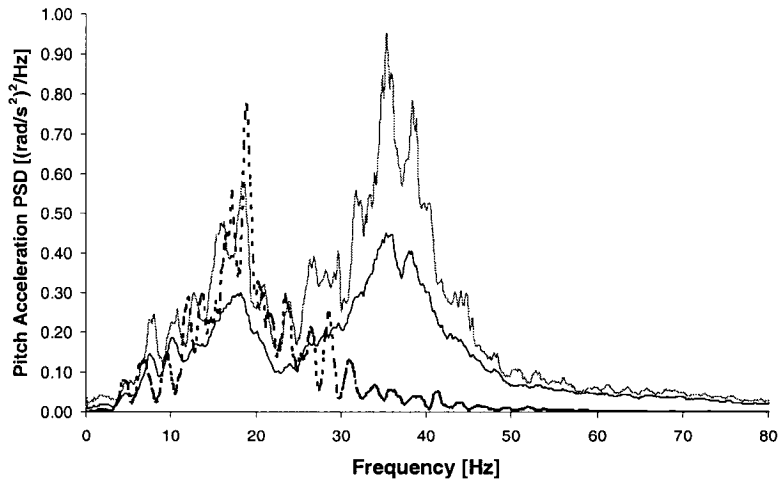

(c) Pitch acceleration

Figure 6.8: Model results vs. mean and maximum measured PSD response of the Hybrid bicycle (Speed 10 km/h; Pattern: Flat pavement): (a) Handle bar acceleration; (b) Seat post acceleration; (c) Pitch acceleration.

The validity of the analytical models is further investigated by comparing the overall RMS vertical and pitch accelerations computed from the model results with those computed from the measured data. The model results obtained for the Touring and Hybrid bicycle-rider models for speeds of 10, 15 and 20 km/h and subject to random road input are compared with the mean measured acceleration responses of the respective bicycles, acquired on the flat pavement with seven subjects. Tables 6.2 and 6.3 summarize the RMS vertical and pitch accelerations of the Touring and Hybrid bicycles obtained from the model results and the measured data, respectively.

The results for the Touring and Hybrid bicycle-rider models show increase in RMS vertical and pitch accelerations with speed. The results also show that the Touring bicycle models yield higher RMS vertical and pitch accelerations than the Hybrid bicycle model, at all the speeds. Both of these trends correspond to the trends observed in the measured data for the Touring and Hybrid bicycles, as evident from the Tables 6.2 and 6.3, respectively. The Touring bicycle-rider model exhibits higher RMS accelerations than the measured data for speeds of 10 and 15 km/h while at 20 km/h the measured data yield higher results. The Hybrid bicycle-rider models, on the other hand, exhibit lower RMS accelerations at all three speeds compared with the respective measured data.

The results suggest that both bicycle-rider models are able to predict the trends of the measured data with respect to the bicycle type and the traveling speed. However, both models exhibit lower increase in the overall RMS accelerations with the speed compared with that of the measured data, especially the pitch acceleration of the Hybrid bicycle-rider model. This can be attributed to lack of ability of the models to predict the second peak in the acceleration spectra of the measured data, as evident from the Figures 6.7.

Moreover, the measured data exhibited higher sensitivity to forward speed in the vicinity of the peak responses, as evident from Figures 3.10 and 3.11.

Table 6.2: Comparison between the RMS vertical and pitch accelerations obtained from the model results and the mean measure data attained for seven subjects (Touring bicycle; Speeds: 10, 15 and 20 km/h).

	Traversing speed					
	10 km/h		15 km/h		20 km/h	
Acceleration	Model	Measured	Model	Measured	Model	Measured
$\ddot{z}_h$ [m/s^2]	2.30	2.05	3.00	2.94	3.60	3.86
$\ddot{z}_s$ [m/s^2]	2.40	1.85	3.10	2.37	3.50	3.59
$\ddot{\theta}$ [rad/s^2]	4.70	4.19	5.80	5.62	6.80	7.49

Table 6.3: Comparison between the RMS vertical and pitch accelerations obtained from the model results and the mean measure data attained for seven subjects (Hybrid bicycle; Speeds: 10, 15 and 20 km/h).

	Traversing speed					
	10 km/h		15 km/h		20 km/h	
Acceleration	Model	Measured	Model	Measured	Model	Measured
$\ddot{z}_h$ [m/s^2]	1.90	1.87	2.20	2.77	2.60	3.75
$\ddot{z}_s$ [m/s^2]	1.20	1.76	1.50	2.32	1.80	3.24
$\ddot{\theta}$ [rad/s^2]	3.10	3.91	3.70	5.42	4.00	7.37

6.3.2 Validation of the bicycle-rider models on the rumble strip pattern

The validity of the analytical bicycle-rider model subject to exaltations arising from the rumble strip pattern is examined through comparison of the model results with

the measured data. A computer based simulation model is developed by incorporating the model of dynamic interaction between the wheel and the rumble strip, as described in section 6.2.2, into previously developed Touring bicycle-rider model. The model results are obtained at forward speed of 10 km/h while the geometry of the prototype rumble strip pattern Round I, described in Table 6.2, is considered for the purpose of model validation. The acceleration response of the Touring bicycle-rider model obtained from the simulation model are manipulated according to Equation (6.15) to compute the accelerations at the handle bar and the seat post. The results are further analyzed to derive the acceleration PSD. The resulting data are then compared with the mean measured responses of the Touring bicycle acquired on the rumble strip pattern Round I with seven subjects. Figure 6.9 illustrate the comparison of the vertical and pitch acceleration PSD obtained from the model results and the mean measured data for the Touring bicycle at 10 km/h.

The results show that the vertical and pitch acceleration responses obtained for the simulation model follow the same trend as the mean measured response. It can also be observed that the model exhibits lower acceleration PSD magnitudes compared to the measured data. However, the model results are obtained for the speed of 10 km/h while it is expected that the speed at which the riders were traversing the rumble strip pattern during the tests varied from its desired value. The measured data revealed that the speed at which the riders traversed rumble strip pattern Round I ranged between 10.8 and 13 km/h, as discussed in Chapter 3 (section 3.6.1). Therefore, model results are compared with the data measured for a single trial that seemed to exhibit the closest response to that of the model results. Figure 6.10 illustrate the comparison between the model results and

measured response of a single trial for subject number four, riding the Touring bicycle at 10 km/h on the rumble strip pattern Round I. As evident from the figure, the model results show a somewhat better agreement in magnitudes of acceleration PSD with the data measured with subject number four. However, the model results still exhibit lower acceleration magnitudes for spectral frequencies above 30 Hz. This can be attributed to the lack of ability of the model to predict the second in the acceleration spectra of the measured data, as discussed in 6.3.1.

Model results are further compared with the measured data in terms of the overall RMS vertical and pitch acceleration. The vertical and pitch acceleration responses obtained from the simulation model are compared with the mean measured acceleration responses acquired with seven subjects on the Rumble strip I for traversing speeds of 10, 15 and 20 km/h. Figure 6.11 illustrate the comparison of RMS vertical and pitch accelerations obtained from the model results and the mean measured acceleration responses on the Touring bicycle. The results show that the RMS accelerations of the model successfully predict the trend of the measured data with respect to speed. However, the model exhibits lower increase in the RMS vertical and pitch accelerations with the speed compared with the measured data. This trend is also observed in the model results for the Touring and Hybrid bicycle-rider models obtained for the flat pavement.

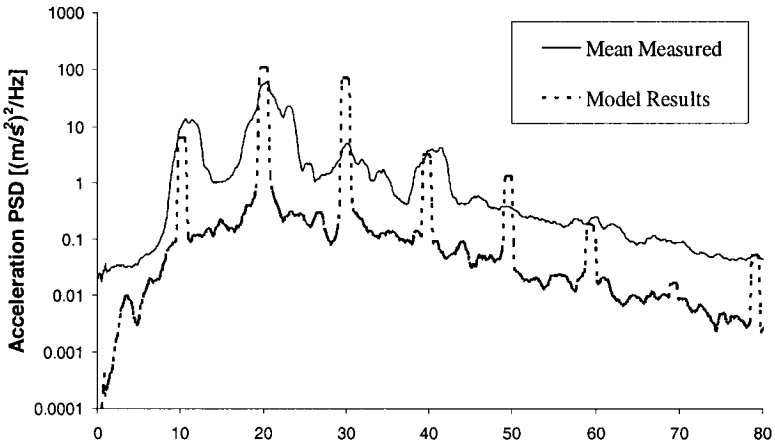

(a) Handle bar acceleration

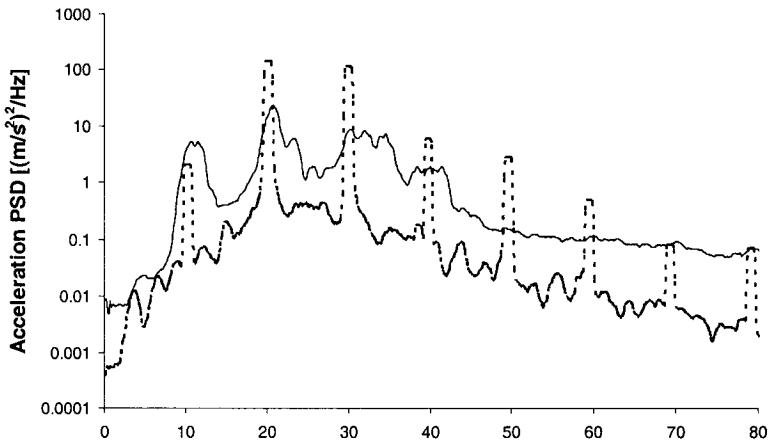

(b) Seat post acceleration

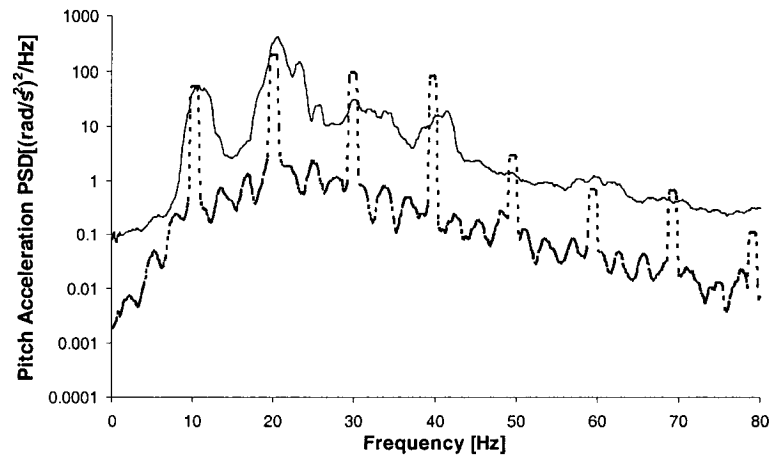

(c) Pitch acceleration

Figure 6.9: Model results vs. mean measured PSD response of the Touring bicycle (Speed: 10 km/h; Pattern: Round I): (a) Handle bar acceleration; (b) Seat post acceleration; (c) Pitch acceleration.

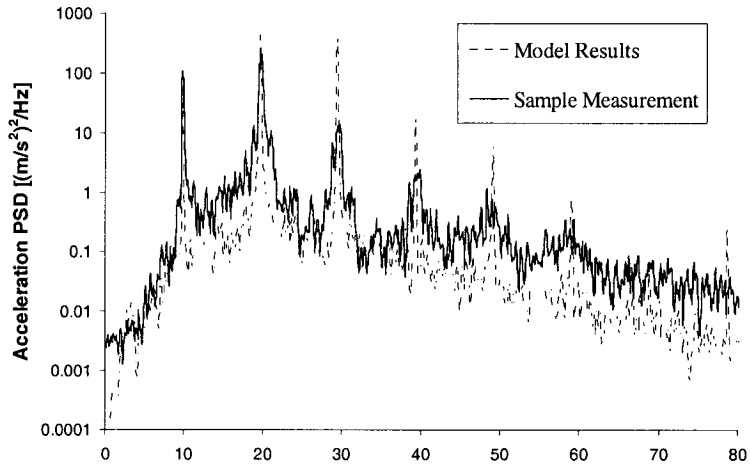

(a) Handle bar acceleration

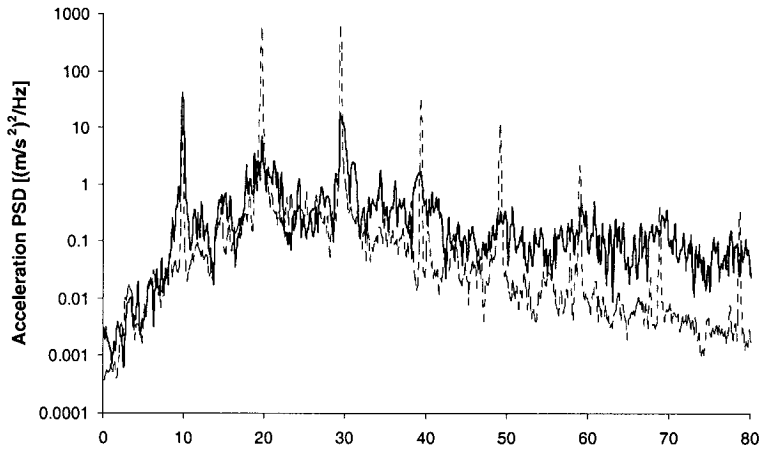

(b) Seat post acceleration

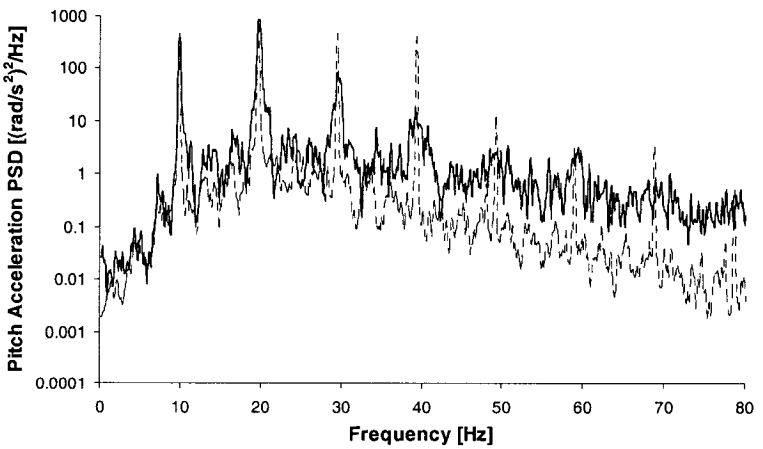

(c) Pitch acceleration

Figure 6.10: Model results vs. measured PSD response for single trial for subject number four on the Touring bicycle (Speed: 10 km/h; Pattern: Round I): (a) Handle bar acceleration; (b) Seat post acceleration; (c) Pitch acceleration.

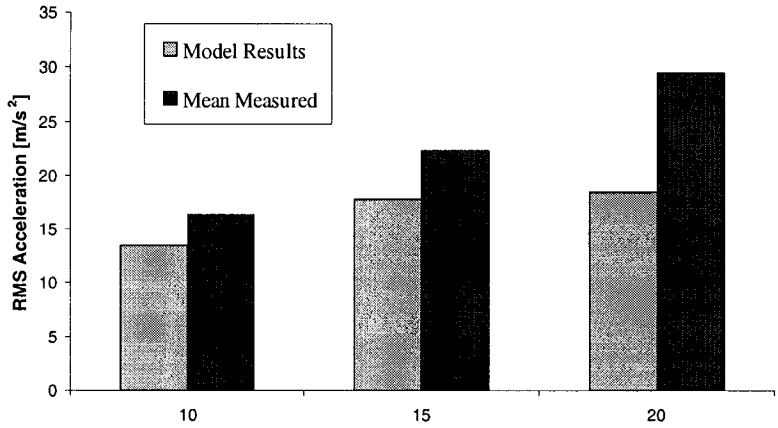

(a) Handle bar acceleration

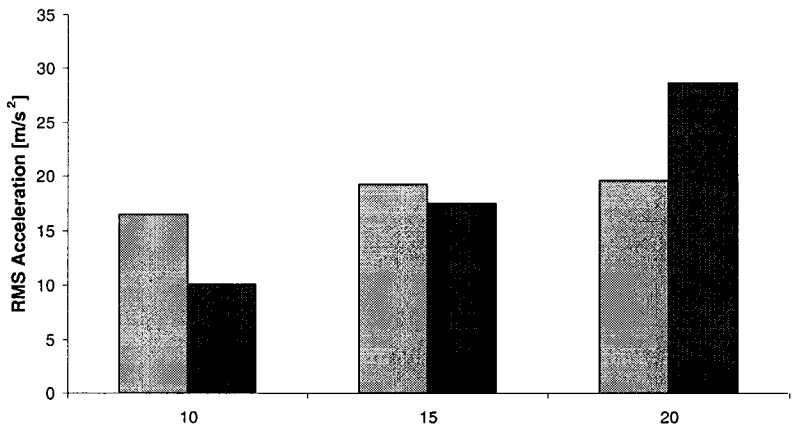

(b) Seat post acceleration

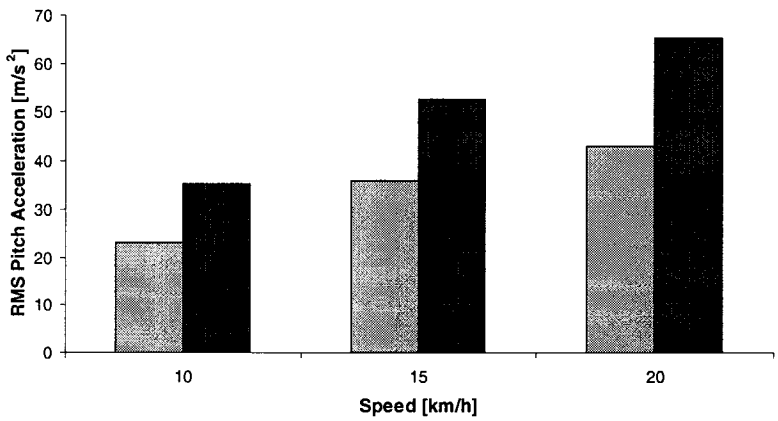

(c) Pitch acceleration

Figure 6.11: Model results vs. mean measured RMS accelerations on the Touring bicycle (Speeds: 10, 15 and 20 km/h; Pattern: Round I): (a) Handle bar acceleration; (b) Seat post acceleration; (c) Pitch acceleration.

6.4 PARAMETRIC STUDY

A parametric study is conducted to investigate the influence of the rumble strip geometry on the vertical and pitch acceleration responses of the bicycle-rider system. A series of computer based simulations is carried out in order to obtain model results subject to different rumble strip geometries, traversing speeds and suspension properties. The influence of rumble strip geometry on acceleration responses of the bicycle-rider system is investigated using the Touring bicycle-rider model. The influence of the front suspension stiffness and damping coefficients on acceleration response subject to excitations arising from the rumble strip pattern is conducted on the Hybrid bicycle-rider model. As described in section 6.2.2, the rumble strip is characterized as a pattern of equally spaced rectangular grooves superimposed by the randomly distributed pavement roughness. Moreover, an assumption is made that the width of the grooves is not large enough to allow the contact between the tire and the bottom of the groove. Therefore, the following set of the rumble strip geometry parameters is considered for the analysis: the width of the groove and the center to center distance, as illustrated in Figure 6.12. The evaluation of the model simulation results is conducted in terms of the overall RMS vertical and pitch accelerations responses. The analysis is conducted for three traversing speeds: 10, 15 and 20 km/h.

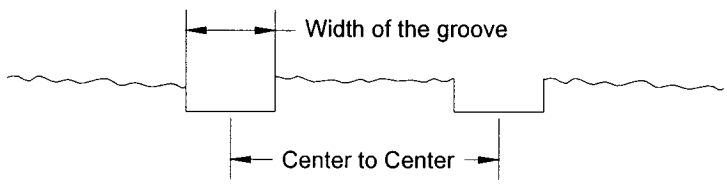

Figure 6.12: Geometrical parameters of the Rumble Strip.

6.4.1 Influence of center to center distance

The influence of the center to center distance of the grooved portions in the rumble strip pattern on the acceleration responses of the Touring bicycle-rider model is examined through a series of computer simulations, by considering different center to center distances. The center to center distance is varied, starting from 0.2 m and gradually increasing to 0.55 m while keeping the width of the grooves at 0.11 m. Figures 6.13 to 6.15 illustrate the RMS vertical and pitch accelerations obtained from the model results for different center to center distance.

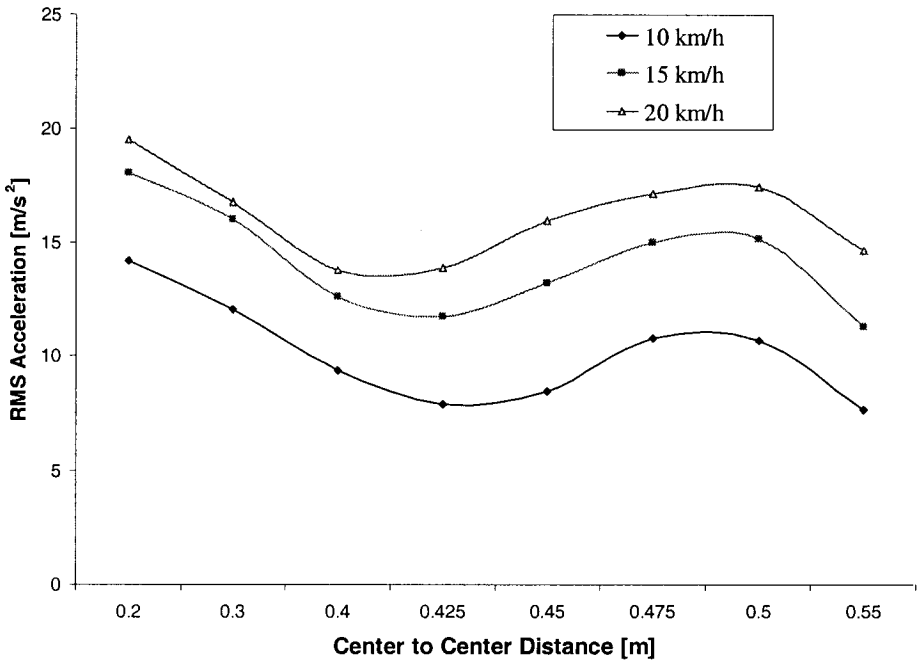

Figure 6.13: Influence of rumble strip pattern center on center distance on the RMS acceleration at the handle bar (Speed: 10, 15 and 20 km/h; Bicycle: Touring).

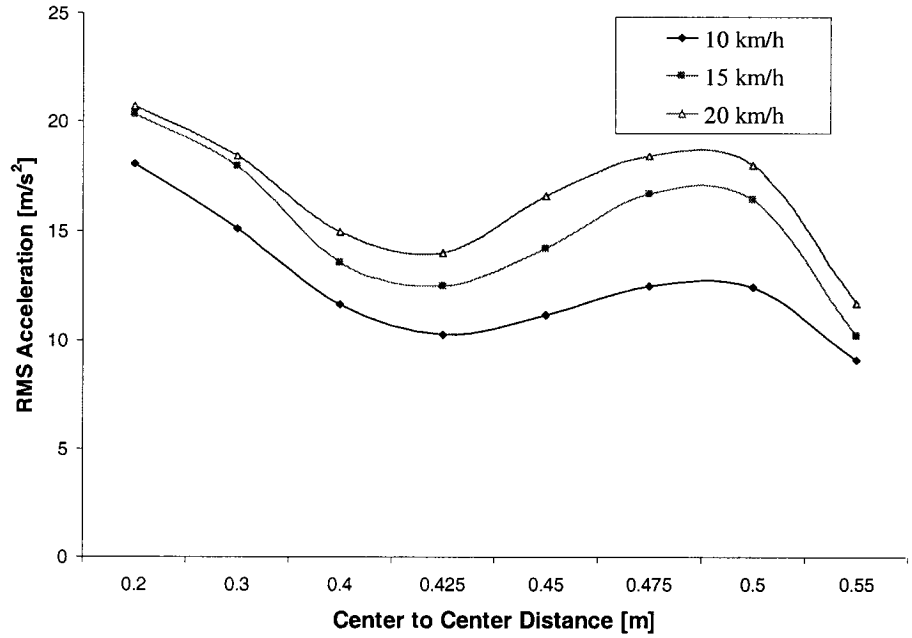

Figure 6.14: Influence of rumble strip pattern center on center distance on the RMS acceleration at the seat post (Speed: 10, 15 and 20 km/h; Bicycle: Touring).

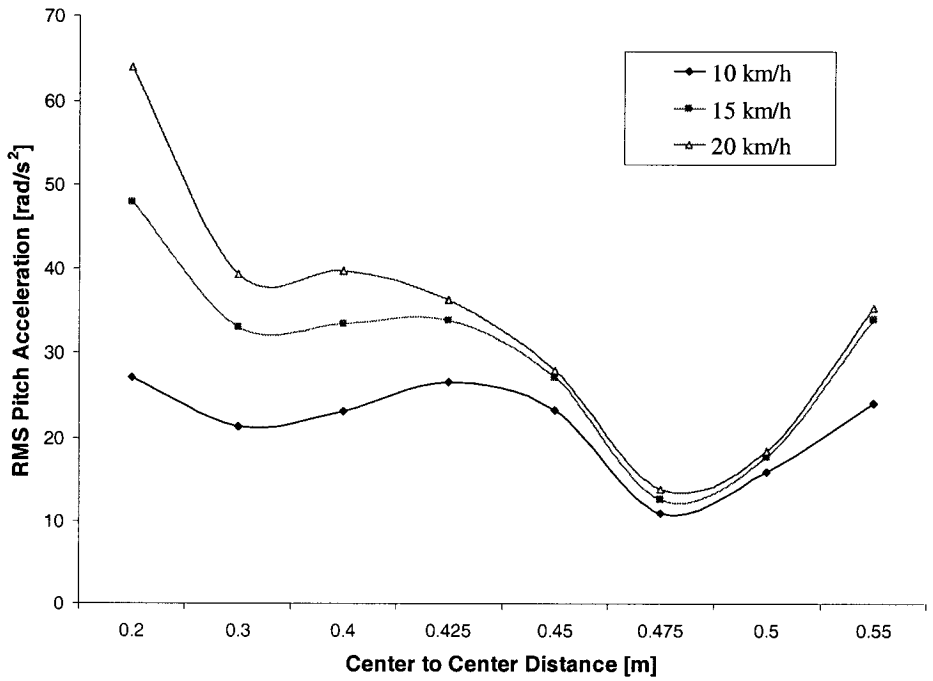

Figure 6.15: Influence of rumble strip pattern center on center distance on the RMS pitch acceleration (Speed: 10, 15 and 20 km/h; Bicycle: Touring; Pattern).

The results for the RMS accelerations at the handle bar and the seat post reveal that with the increase of the center to center distance the overall RMS accelerations are initially decreasing until the center to center distance attains a value of 0.425 meters. Thereafter, the RMS accelerations start to rise again and they peak at the vicinity of the center to center distance of 0.5 meters, after which they decrease again. The increase in vertical accelerations around the center to center distance of 0.5 meters can be explained by the wheel base distance coinciding with the double center to center distance, which in this case is one meter. The measured wheel base distance of the Touring bicycle is 1.016 meters, meaning that both wheels will be approximately at the same time on the grooved portions of the rumble strip and thus predominantly exciting the bounce motion of the bicycle-rider system. The pitch acceleration has somewhat opposite trend. After the initial decrease, the RMS pitch acceleration exhibits a tendency to rise in the range between 0.4 and 0.425 meters. The pitch acceleration is expected to peak when the wheels and the grooves are "out of phase", consequently exhibiting the smallest values of the RMS pitch acceleration in the vicinity of 0.475 to 0.5 meters. After the center to center distance of 0.5 meters, pitch acceleration sharply rises again, by going again "out of phase" with the bicycle wheels. The influence of the riding speed on the responses is also clearly noticeable. The increase in vertical acceleration responses as a function of forward speed seems to be constant, except for the between the speeds of 15 and 20 km/h in the vicinity of 0.2 to 0.4 meters where it appears to be smaller in comparison with the larger center to center distances. The increase in pitch acceleration response as a function of forward speed is the smallest in the vicinity of 0.475 to 0.5 meters where at the same time the pitch acceleration exhibits the smallest RMS values. However, this discrepancy

may be attributed to the limitations of the dynamic interaction model between the wheel and the rumble strip, as discussed in section 6.3.1.

Based on the previous discussion, it can be concluded that from the point of view of the vertical acceleration responses of the bicycle-rider system the best results correspond to the center to center distance of 0.425 meters. From the point of view of pitch acceleration responses the best results correspond to the center to center distance of 0.475 to 0.5 meters. Moreover, the results show that the pitch accelerations exhibit a considerable increase in the RMS values for the center to center distances in the close surrounding of the 0.475 to 0.5 meters region. This can be important since that the geometry of the rumble strip pattern can vary due to inaccuracy of the fabrication process, as evident from Table 2.4. On the other hand, the RMS vertical accelerations do not show considerable change for the center to center distances smaller or greater than 0.425 meters. Therefore, the center to center distance of 0.425 meters seems to provide the optimal results.

6.4.3 Influence of the width of the groove

The influence of the width of the grooves on vertical and pitch acceleration responses of the Touring bicycle-rider model is further investigated. The responses of the Touring bicycle-rider model on the rumble strips are obtained from computer based simulations, using different groove widths and riding speeds. The width of the grooves is varied, starting from 0.1 meters and gradually increasing while the center to center distance was kept constant. Based on the discussion in the previous section, the center to center distance of 0.425 meters is considered for the analysis. The investigation is

conducted for traversing speeds of 10, 15 and 20 km/h. Figures 6.16 to 6.18 illustrate the influence of the groove width on the RMS vertical and pitch acceleration responses obtained for the Touring bicycle-rider model.

The model results show that, as expected, the RMS vertical and pitch accelerations are increasing with the increase in width of the grooves. The dependence between the width and the RMS values seems to be close to linear for both vertical and pitch responses. According to the model results, the RMS acceleration at the handle bar and the seat post exhibit an increase of approximately 0.83 m/s^2 for every 5 mm of increase in the groove width. In case of the RMS pitch acceleration, the increase is approximately 2.5 rad/s^2 for the increase of 5 mm in the groove width.

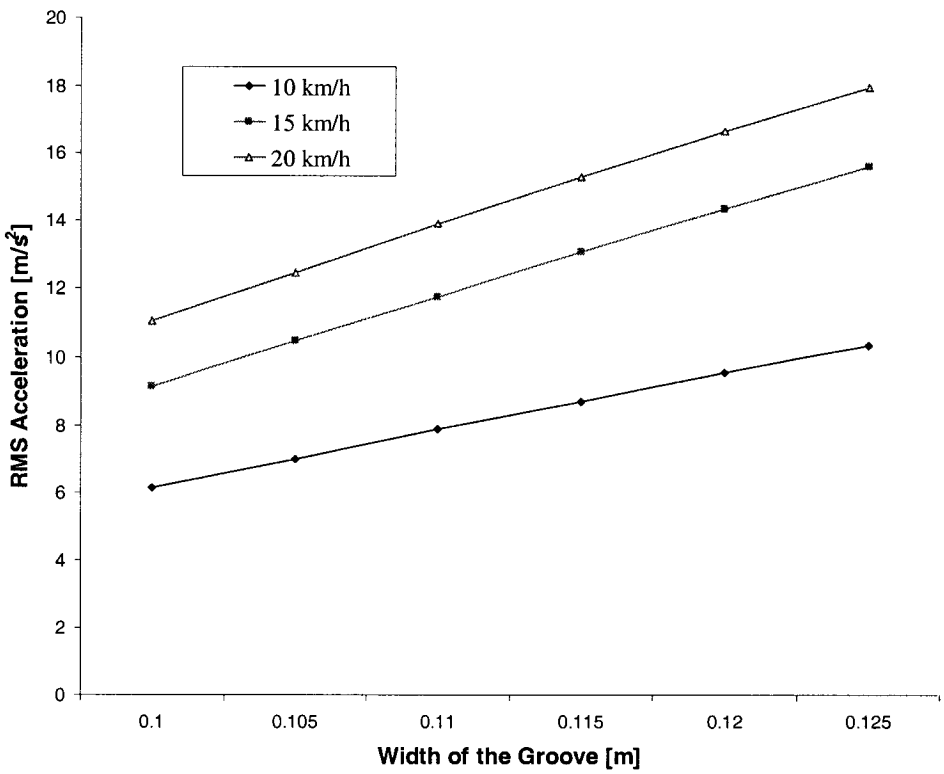

Figure 6.16: Influence of the width of the grooves on the RMS acceleration at the handle bar (Speed: 10, 15 and 20 km/h; Bicycle: Touring).

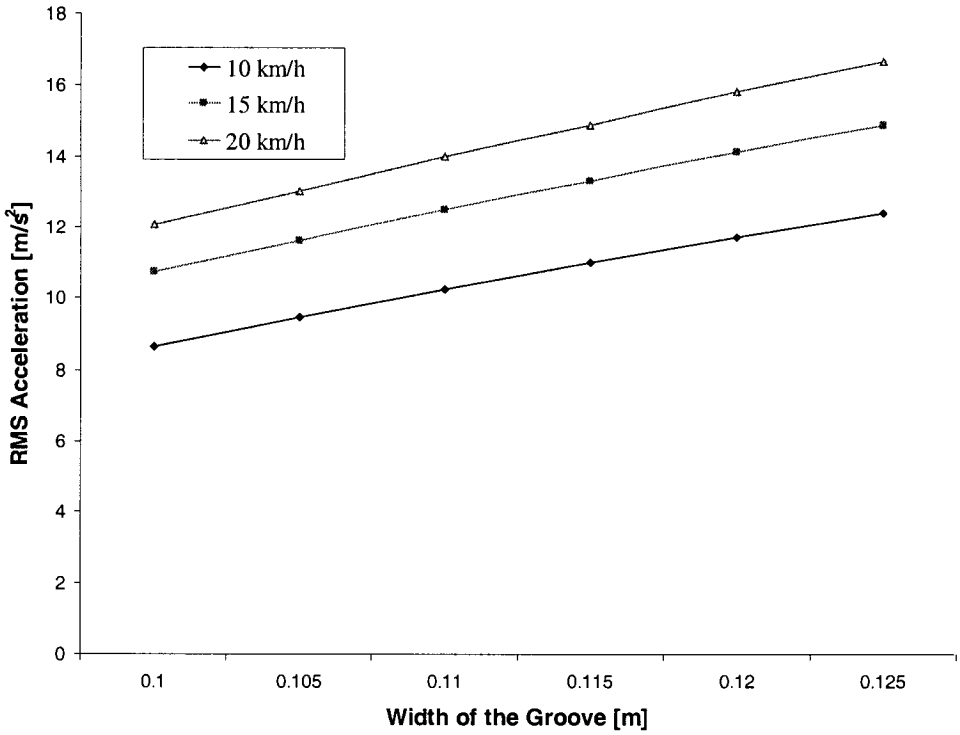

Figure 6.17: Influence of the width of the grooves on the RMS acceleration at the seat post (Speed: 10, 15 and 20 km/h; Bicycle: Touring).

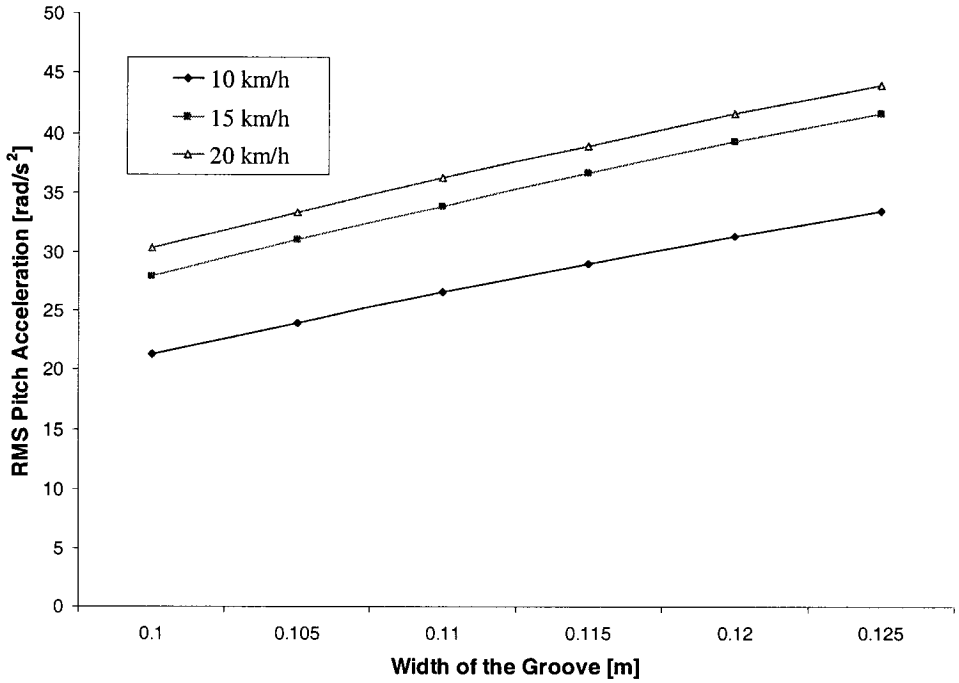

Figure 6.18: Influence of the width of the grooves on the RMS pitch acceleration (Speed: 10, 15 and 20 km/h; Bicycle: Touring).

Traversing speed does not seem to influence the overall trend of the data, and the dependence appears to remain linear, regardless of the riding speed. According to the model results, it is reasonable to assume that the overall RMS values will steadily increase until the width of the grooves becomes large enough to allow for the tire to drop completely inside the groove. After the contact between the bottom of the groove and the tire has been established, further increase of the groove width will not necessarily results in increase in the overall RMS values since further tire drop will be limited by the depth of the groove.

Based on the previous discussion, it can be concluded that if the center to center distance of 0.425 meters is used, it is possible to increase the width of the grooves while keeping the overall RMS values reasonably low. According to literature review, the width of the groove is a single most important parameter from the point of view of motor vehicles. For a given rumble strip geometry, wider grooves provide higher vibration and noise levels and therefore better warning to drowsy and inattentive drivers. Compared to results obtained using the geometry pattern Round I, the center to center distance of 0.425 m allows wider grooves up to 10 mm while at the same time yielding lower values of the RMS vertical acceleration by 23 % at the handle bar and by 23 % at the seat at the speed of 10 km/h. The difference is getting smaller with the increase in speed, and for the speed of 20 km/h the RMS acceleration at the handle bar is smaller by 3 % and at the seat post by 15 %. However, according to previous dissuasion, the overall RMS pitch acceleration is higher compared to that of the pattern Round I. According to model results, the increase in pitch acceleration is 30 % for the speed of 10 km/h, while for the speeds of 15 and 20 km/h the increase is 14 % and 2 %, respectively.

6.4.3 Influence of the front suspension stiffness

The influence of the front suspension stiffness on the acceleration responses of the bicycle-rider system traversing the rumble strip pattern is further investigated through computer based simulations, as previously described. The random responses of the Hybrid bicycle-rider model are obtained from the computer based simulations by considering different stiffness coefficients of the front suspension. The rumble strip geometry Round I is considered for the investigation which includes the center to center distance of 0.3 meters and width of the grooves of 0.115 meters. The analysis is conducted for a range of traversing speeds: 10, 15 and 20 km/h. The bicycle acceleration responses are examined for a range of suspension stiffnesses clustered around the measured stiffness of the Hybrid bicycle's front suspension stiffness of 22.12 kN/m, as obtained from the laboratory tests. The front suspension stiffness coefficients that are considered for the investigation are: 15, 22.12, 30, 40 and 50 kN/m while the suspension damping coefficient is kept constant at 104 Ns/m, which is the equivalent damping coefficient for the front suspension estimated from Equation (5.27), by considering measured magnitude of Coulomb damping of 150 N. Figures 6.19 to 6.21 illustrate the influence of the front suspension stiffness coefficient on the RMS vertical and pitch acceleration responses of the Hybrid bicycle-rider model.

The results show that higher spring rate of the front suspension yield higher RMS vertical and pitch acceleration responses, for given rumble strip pattern. Moreover, the results suggest that the relationship is not a linear one. It appears that softer suspension spring rates (in the range between 15 and 30 kN/m) do not significantly influence the acceleration responses at the handle bar and seat post.

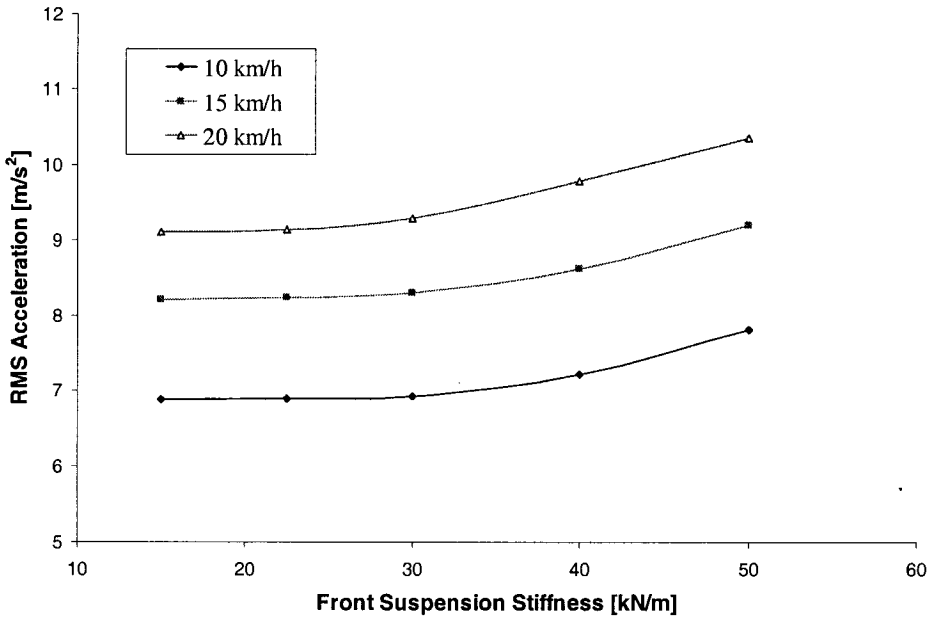

Figure 6.19: Influence of the front suspension stiffness coefficient on the RMS acceleration at the handle bar (Speed: 10, 15 and 20 km/h; Bicycle: Hybrid; Pattern: Round I).

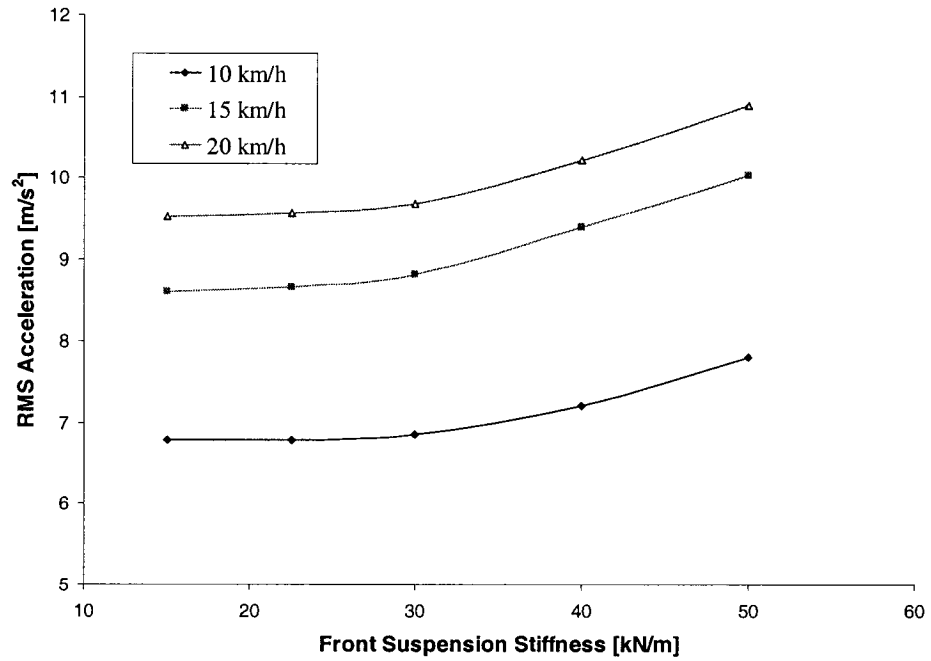

Figure 6.20: Influence of the front suspension stiffness coefficient on the RMS acceleration at the seat post (Speeds: 10, 15 and 20 km/h; Bicycle: Hybrid; Pattern: Round I).

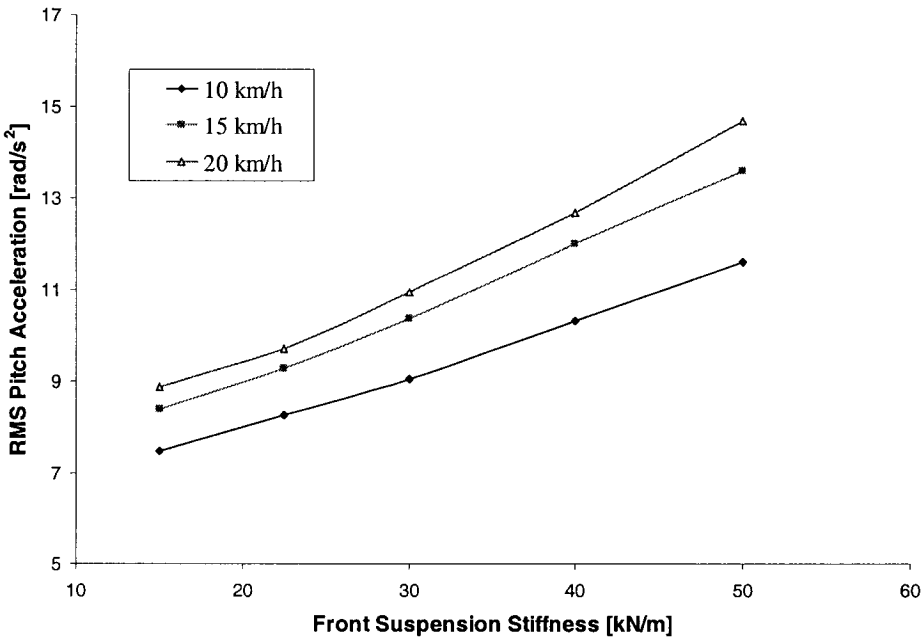

Figure 6.21: Influence of the front suspension stiffness coefficient on the RMS pitch acceleration (Speed: 10, 15 and 20 km/h; Bicycle: Hybrid; Pattern: Round I).

As the suspension becomes stiffer the influence of the suspension spring rate on vertical acceleration responses becomes more significant. On the other hand, the results show that the pitch acceleration response of the Hybrid bicycle exhibits more significant increase as the suspension becomes stiffer. The RMS pitch acceleration steadily increases as the suspension becomes stiffer. It appears that the front suspension stiffness has more influence on pitch than on the vertical acceleration, irrespective of the traversing speed. For instance, the overall RMS pitch acceleration exhibits increase of 22 %, between suspension stiffnesses of 30 and 50 kN/m, while at the same time the overall RMS vertical acceleration exhibits increase of 11 % and 12 % at the handle bar and seat post, respectively.

6.4.4 Influence of the front suspension damping

The influence of the front suspension damping coefficient on the acceleration responses of the bicycle-rider system is further investigated. The random responses of the Hybrid bicycle-rider model are obtained from the computer based simulations by considering different front suspension damping coefficients while keeping the suspension's spring rate constant at 22.12 kN/m. The geometrical parameters of the rumble strip pattern Round I are considered for the analysis while the results for each damping coefficient are obtained for speeds of 10, 15 and 20 km/h. The bicycle acceleration responses are examined for a range of suspension damping coefficients: 50, 104, 150, 200 and 250 Ns/m where suspension damping of 104 Ns/m is the equivalent viscous damping estimated from Equation (5.27), by considering measured magnitude of Coulomb damping of 150 N. Figures 6.22 to 6.24 illustrate the influence of the front suspension damping coefficient on the RMS vertical and pitch acceleration responses of the Hybrid bicycle-rider model.

The results show that the acceleration responses of the Hybrid bicycle-rider model show the largest sensitivity for front suspension damping coefficients between 50 and 150 Ns/m. The damping coefficients larger than 150 Ns/m would yield smaller change in the magnitudes of the acceleration responses, especially for the handle bar and the seat accelerations. The pitch acceleration response exhibits a decrease in magnitudes, at all three speeds, as the damping coefficient increases.

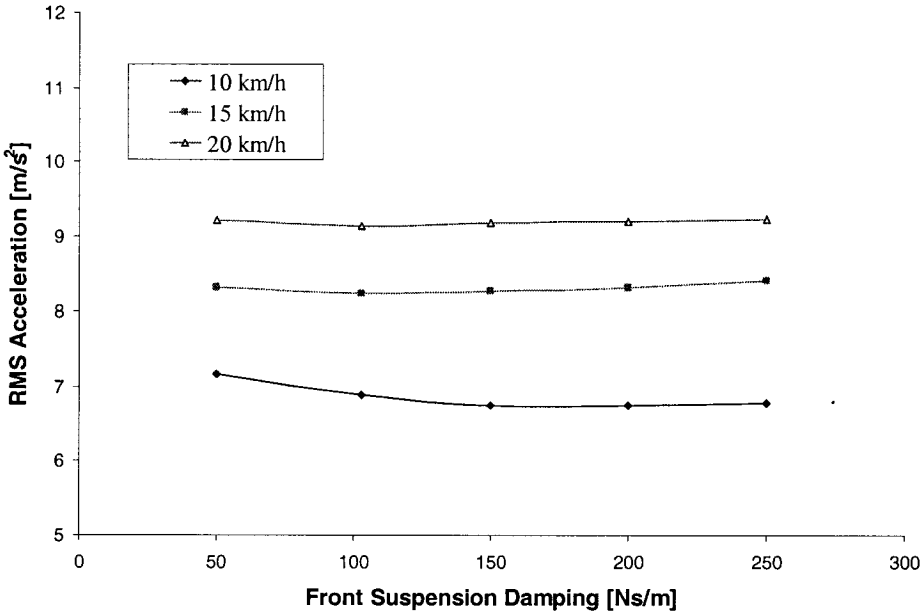

Figure 6.22: Influence of the front suspension damping coefficient on the RMS acceleration at the handle bar (Speed: 10, 15 and 20 km/h; Bicycle: Hybrid; Pattern: Round I).

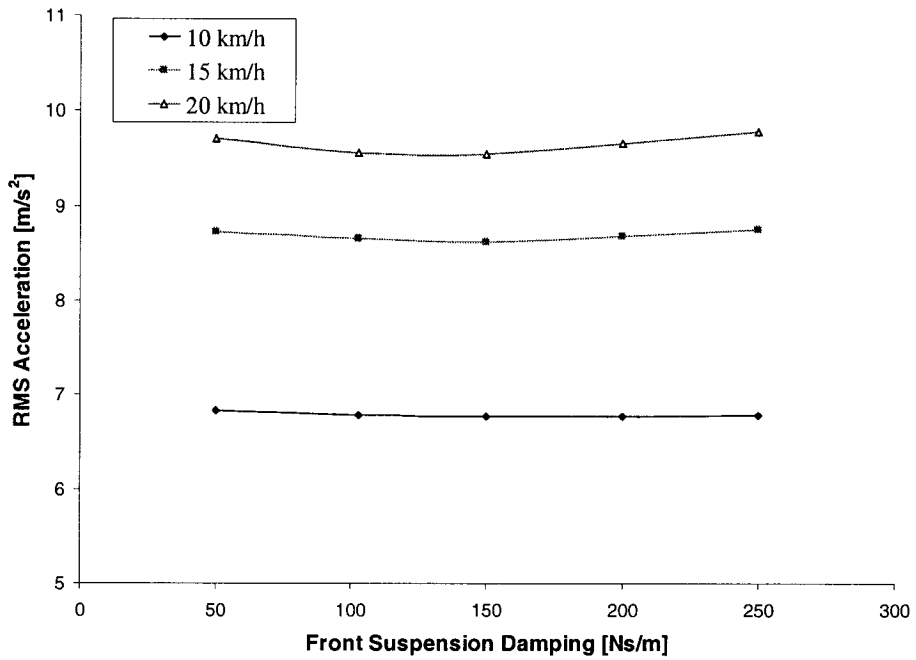

Figure 6.23: Influence of the front suspension damping coefficient on the RMS acceleration at the seat post (Speed: 10, 15 and 20 km/h; Bicycle: Hybrid; Pattern: Round I).

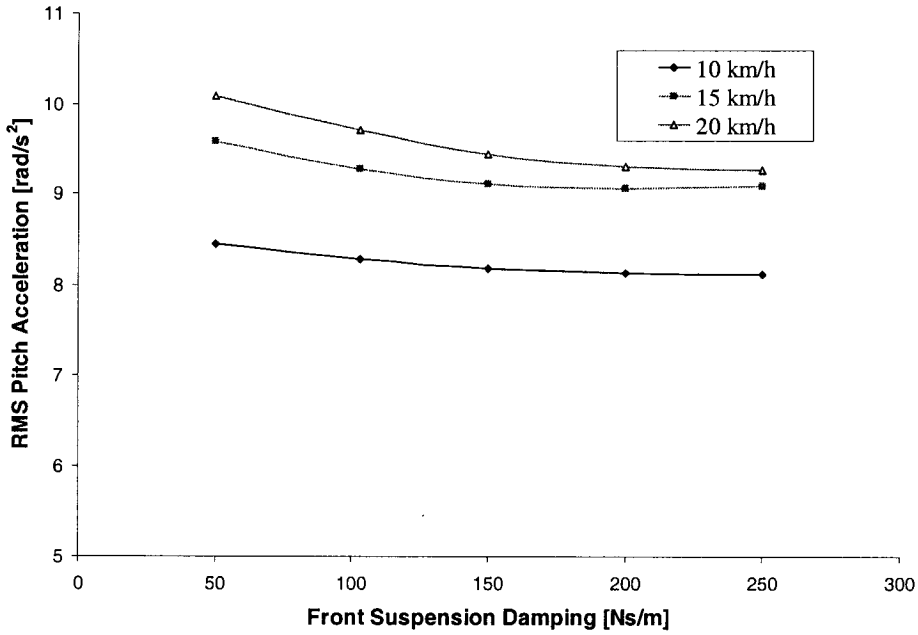

Figure 6.24: Influence of the front suspension damping coefficient on the RMS pitch acceleration (Speed: 10, 15 and 20 km/h; Bicycle: Hybrid; Pattern: Round I).

6.6 SUMMARY

In this Chapter, the Touring and the Hybrid bicycle-rider models, developed in Chapter 5, are validated against the respective measured data. The random responses of the analytical models subject to excitations arising from the surface roughness are obtained from the computer based simulation model. Also a dynamic interaction between the wheel and the rumble strip model is developed in order to carry out computer based simulation of the random responses of bicycle-rider model subject to rumble strip pattern. The influence of the rumble strip geometry on the bicycle acceleration responses is investigated and, it is concluded that the center to center distance of 0.425 meters yields the optimal results. It is also concluded that the relationship between the width of the groove and the overall RMS vertical and pitch acceleration is a linear one. Also the

influence of front suspension stiffness and damping coefficients on vertical and pitch acceleration responses is investigated on the Hybrid bicycle-rider model.

CHAPTER 7

CONCLUSIONS AND RECOMMENDATIONS FOR FUTURE WORK

7.1 HIGHLITES OF THE INVESTIGATION

The objective of this thesis, set in the first Chapter, was to investigate the ride discomfort and controllability of a bicycle traversing the rumble strips and, if possible, to find the geometry of the rumble strip that would be more bicycle-friendly. The research work initially included the field measurements of the ride discomfort and controllability through objective and subjective means. The research was than extended to the development of an analytical model in order to study the dynamic properties of the coupled bicycle-rider system. The major highlights of this study can be summarized as follows:

1. Objective and subjective measurements of the ride discomfort and controllability of a bicycle traversing different rumble strip configurations. The test matrix included: two different types of bicycles; four different rumble strip patterns; three traversing speeds; multiple trials and a population of seven test subjects. The objective assessment of ride discomfort and controllability included the measurements of the acceleration responses of the bicycle frame and the measurements of the yaw oscillations of the bicycle's handle bar. The measurements were conducted on the bicycles instrumented with the acceleration transducers, mounted at the handle bar and the seat post, and with a servo potentiometer mounted on the bicycle's handle bar to measure the oscillations of

the yaw angle. The subjective measurements included subjective ratings of the ride discomfort and controllability based on a comprehensive questioner.

2. A comprehensive data analysis was conducted to derive the magnitudes and the spectral components of the measured accelerations responses as well as to derive the RMS and VDV accelerations and the RMS of the measured yaw angle oscillations. The results were further analyzed to study the ride discomfort and controllability as a function of bicycle type, traversing speed and rumble strip geometry.
3. Laboratory tests were designed and performed to characterize the dynamic properties of the test bicycle components. The characterization of bicycle's inertial and geometrical properties included: bicycle mass, pitch moment of inertia and bicycle's center of gravity. Also laboratory tests were conducted to obtain the force-deflection characteristics of the bicycle suspension components such as: front and rear tires; front suspension and the seat post suspension.
4. A coupled Touring bicycle-rider system was characterized by a five-DOF to describe its motion in the vertical and pitch planes. The Hybrid bicycle-rider models was then further developed as an in-plane six-DOF system. Parameters of the proposed models were identified from the laboratory measured data and from the data reported in the literature.
5. A dynamic interaction between the wheel and the rumble strip model was developed to study the acceleration responses of the Touring and the Hybrid bicycle-rider systems subject to excitations arising from the rumble strip patterns.

6. Developed analytical models of the Touring and Hybrid bicycle-rider systems were validated against the respective measured data.
7. A parametric study was carried out to study the influence of the rumble strip geometry on the acceleration responses of the Touring bicycle-rider model as well as to study the influence of the dynamic properties of the front suspension on the acceleration responses of the Hybrid bicycle-rider model.

7.2 CONCLUSIONS

The following major conclusions are drawn from the experimental and analytical studies performed in this dissertation:

1. The measured data showed that the ride on the rumble strip patterns Round I and Round II generates a significant increase in RMS and VDV vertical and pitch accelerations in comparison with the ride on the flat pavement.
2. The subjective measurements showed that the ride on the rumble strip pattern Round I causes a significant decrease in comfort and controllability compared to the flat pavement.
3. Ride comfort and controllability of the bicycle on the rumble strip patterns decreases with the traversing speed which is evident from both the objective and subjective measurements.
4. Irrespective of traversing speed, the ride on the suspended bicycle exhibits less discomfort and decrease in controllability compared with the conventional bicycle which showed both the objective and the subjective measurements.

5. The measured data show less RMS yaw angle oscillations at higher speeds, irrespective of the bicycle type or the rumble strip pattern.
6. The results for the yaw rate, which were considered as a measure of controllability, did not show conclusive enough in order to serve as a measure of bicycle controllability on the rumble strip patterns.
7. The measured data show that the acceleration magnitudes of the bicycle frame under oblique angle of approach to rumble strip of 10 degrees are less than those obtained for a continuous ride on the same rumble strip pattern. However, the acceleration magnitudes are much higher that those obtained on the flat pavement.
8. A coupled bicycle-rider system can be represented by 5-DOF and 6-DOF models, representing the Touring and Hybrid bicycle-rider systems, respectively.
9. The results of the parametric study showed that:
    a. The vertical and pitch acceleration responses of the bicycle increase with the increase in the groove width of the pattern, in a nearly linear manner.
    b. The results suggest that a pattern with center-to-center distance of 0.425 meters could provide improved performance from the point of view of vertical vibration transmitted to the rider.

7.3 RECOMMEDATIONS FOR FUTURE WORK

This dissertation research presents a preliminary attempt in investigation of the influence of rumble strips to cyclist's comfort and controllability. Some of the recommendations for future work can be summarized as follows:

1. The experimental investigation of the rumble strip patterns should be conducted by considering:
    a. Different widths of the grooves while keeping the center to center distance constant.
    b. Different center to center distances while keeping the width of the grooves constant.
2. The experimental data acquisition should be conducted with larger number of subjects. Also, the tests should be conducted with a population of female test subjects.
3. Formulate a simulation model that would consider randomly distributed geometrical dimensions of the rumble strip pattern based on the mean and standard deviation of the measured dimensions of the fabricated rumble strip pattern.

REFERENCES

1. AASHTO Guide for Development of Bicycle Facilities, American Association of State Highway and Transportation Officials, 1999.

2. Ardekani, S. A., Govind, S., Mattingly, S. P., Demers, A., Mahmassani, H. S. and Taylor, D., "Detection and Mitigation of Roadway Hazards for Bicyclists", Report FHWA/TXDOT-96/1394-2F, Texas Department of Transportation, 1996.

3. Bachman, D., "Rumble Strips, Finding a Design for Bicycles and Motor Vehicles." *Research Pays Off*, TR News 215, Pennsylvania Department of Transportation, July-August, 2001.

4. Basso, R., Fabbri, L., and Zagatti, E., "A Method to Analysis the Dynamic Behavior of a Motorcycle Front Suspension Equipped with Sequential Dampers", Vehicle System Dynamics, 1998, pp. 213-230.

5. Boileau, P.-E., "A Study of Secondary Suspensions and Human Driver Response to Whole-Body Vehicular Vibrations and Shock", Ph.D. Thesis, Concordia University, Montreal, Canada, 1995.

6. Boileau, P.-E., Rakheja, S., "Whole-Body Vertical Biodynamic Response Characteristics of the Seated Vehicle Driver Measurement and Model Development", International Journal of Industrial Ergonomics 22, 1998, pp. 449-472.

7. Captain, K.M., Boghani, A.B., and Wormley, D.N., "Analytical Tire Models", Vehicle System Dynamics, Vol. 8, 1979.

8. Cheng, E.Y.C., Gonzalez E., and Christensen. M.O., "Application and Evaluation of Rumble Strips on Highways", Utah Department of Transportation, 1994.

9. Cristiaans, M., Henri, H.C., and Bremner, A., "Comfort on Bicycles and the Validity of a Commercial Bicycle Fitting System", Applied Ergonomics, Vol. 29, No. 3, 1998, pp. 201-211.

10. Dhir, A., and Sankar, S., "Analytical Wheel Models for Ride Dynamic Simulation of Off-road Tracked Vehicles", Vehicle System Dynamics, Vol. 27, 1997, pp. 37-63.

11. Dhir, A., "Ride Dynamics of Heavy Vehicles Using Local Equivalent Linearization Technique", M.A.Sc., Concordia University, 1988.

12. Elefteriadou, L., El-Gindy, M., Torbic, D., Garvey, P., Homan, A., Jiang, Z., Pecheux, B., and Tallon, R., "Bicycle Tolerable Shoulder Rumble Strips", March, 2000.

13. Errol C. Noel., Ziad A. Sabra, Conrad L. Dudek, "Work Zone Traffic Management Synthesis: Use of Rumble Strips in Work Zones", Report No. FHWA-TS-89-037, FHWA, U.S Department of Transportation, July, 1989.

14. FHWA, "Roadway Shoulder Rumble Strips", U.S. Department of Transportation, T 5040.35, December 20, 2001.

15. Garder, P., "Rumble Strip or Not Along Wide Shoulders Designated for Bicycle Traffic", Transportation Research Record 1502:1-7, 1995.

16. Griffin, M. J., "Handbook of Human Vibrations" Academic Press, 1996.

17. Griffith, M.S., "Safety Evaluation of Continuous Shoulder Rumble Strips Installed on Freeways", Paper No. 990162, 78th Annual Meeting of the Transportation Research Board in Washington, D.C., January, 1999.

18. Griffith, M.S., "Safety Evaluation of Rolled-In Continuous Shoulder Rumble Strips Installed on Freeways", Report FHWA-RD-00-032, FHWA, U.S Department of Transportation, December, 1999.

19. Gupta, J., "Development of Criteria for Design, Placement and Spacing of Rumble Strips" Report FHWA/OH-93/022, Ohio Department of Transportation, 1993.

20. Hac, A., "Suspension Optimization of a 2-DOF Vehicle Model Using a Stochastic Optimal Control Technique", Journal of Sound and Vibrations, Vol. 100(3), pp. 343-357, 1985.

21. Harwood, D.W., NCHRP Synthesis 191: "Use of Rumble Strips to Enhance Safety", TRB, National Research Council, Washington, D.C., 1993.

22. Hickey, J.J. Jr., "Shoulder Rumble Strip Effectiveness, Drift-Off-Road Accident Reductions on the Pennsylvania Turnpike", Transportation Research Record 1573: 105-109, 1997.

23. Higgins, J.S., and W. Barbel. "Rumble Strip Noise." Transportation Research Record 983:27-36, 1984.

24. Hull, M.L., Wang, E.L. and Moor, D. F., "An Empirical Model For Determining The Radial Force-Deflection Behavior Of Off-Road Bicycle Tire", Cycling Science, Spring, 1996.

25. International Standard Organization, "Road Surface Profile - Reporting of Measured Data", ISO-8608, 1984.

26. International Standard Organization, "Mechanical vibrations and shock Evaluation of Human Exposure to Whole-Body Vibrations", ISO 2631-1, 1997.

27. Illinois Division of Highways, "Portland Cement Concrete Shoulders", Research and Development Report #27, 1970.

28. Khan A. M., Baccus A., "Economic Feasibility and Related Issues of Highway Shoulder Rumble Strips" Transport research Record No 1498: 92-101, 1994.

29. Lundstrom, R., and Holmlund, P., "Absorption of Energy During Whole-Body Vibration Exposure", Journal of Sound and Vibration, Vol. 214(4), 1998, pp. 780-799.

30. Minetti A., and Belli G., "A Model for the Estimation of Visceral Mass Displacement in Periodic Movements", Journal of Biomechanics, Vol. 27, 1994, pp. 97-101.

31. Morgan, R.L., and D.E. McAuliffe, "Effectiveness of shoulder Rumble Strips: A Survey of Current Practice", Report FHWA/NY/SR-97/127, FHWA, U.S. Department of Transportation, September, 1997.

32. Outcalt, W., "Bicycle-Friendly Rumble Strips", Report No., CDOT-DTD-R-2001-4, FHWA, U.S Department of Transportation, Colorado Department of Transportation Research Branch, May, 2001.

33. Outcalt, W., "Centerline Rumble Strips", Colorado Department of Transportation Research Branch Report No. CDOT-DTD-R-2001-8, August, 2001.

34. Paddan, G. S, and Griffin, M. J., "A Review of the Transmission of Translational Seat Vibration to the Head", Journal of Sound and Vibration, Vol. 215(4), 1998, pp. 863-882.

35. Perrillo, K., "The Effectiveness and Use of Continuous Shoulder Rumble Strips", Federal Highway Administration, August, 1998.

36. Pheasant, S., "Bodyspace: Anthropometry, Ergonomics and Design", Taylor & Francis, London and Philadelphia, 1986.

37. Richard C.M., "Rumble Strip Gap Study", Final Report, Arizona Department of Transportation, May, 1999.

38. Ryan, M.M., "Milled Shoulder Rumble Strips (MSRS), Safety Enhancement", SOL# 470-93-45, Highway Administration, June, 1993.

39. Tchernychouk, V., "Objective Assessment of Static and Dynamic Seat Under Vehicular Vibrations" M.A.Sc Thesis, Concordia University, Canada, 1999.

40. Thomson, W.T., "Theory of Vibration with Applications", Fifth Edition, Prentice Hall, 1998.

41. Torbic, D., "Development of Rumble Strip Configurations that are more Bicycle Friendly", Transportation research record 1773: 23-31, 2001.

42. Torbic, D.J., "Comfort and Controllability of Bicycle as a Function of Rumble Strip Design", Ph.D. Thesis, The Pennsylvania State University, August, 2001.

43. Waechter, M., Riess, F., and Zacharias, N., "A Multibody Model for the Simulation of Bicycle Suspension Systems", Vehicle System Dynamics, 2002, Vol. 37, No. 1, pp. 3-28.

44. Wang, E.L., and Hull, M.L., "A Model for Determining Rider Induced Energy Losses in Bicycle Suspension System", Vehicle System Dynamics, 1996, 25(3): pp. 223-246.

45. Wang, E.L. and Hull, M.L., "A Dynamic System Model of an Off-Road Cyclist", Journal of Biomechanical Engineering, August, 1997, Vol. 119.

46. Watts, G.R., "Development of Rumble Areas as a Driver-Alerting Device", In Supplementary report 291, Transportation and road research laboratory, 1977.

47. Wilczynski H., and Hull. M.L., "A Dynamic System Model for Estimating Surface-Induced Frame Loads During Off-Road Cycling", Journal of Mechanical Design, September, 1994, Vol. 116/817.

48. Wilczynski, H., and Hull, M.L., "A Dynamic System Model of an Off-Road Cycling", Journal of Biomechanical Engineering Design, August, 1997, Vol. 1169/249.

49. Wood, N.E., "Shoulder Rumble Strips: A Method to alert drifting drivers", Pennsylvania Turnpike Commission, January, 1994.

50. Wong. J.Y., "Theory of Ground Vehicles", Second Edition, John Wiley & Sons, INC., 1993.